I N A U G U R A L – D I S S E R T A T I O N

zur

Erlangung der Doktorwürde

der

Naturwissenschaftlichen – Mathematischen
Gesamtfakultät

der

Ruprecht - Karls - Universität
Heidelberg

vorgelegt von

M.Sc. Elisa Thauer

aus Heilbronn

Tag der mündlichen Prüfung: 17.11.2021

Einfluss von Morphologie und Funktionalisierung auf die elektrochemischen Eigenschaften von oxidischen Anodenmaterialien für Lithium-Ionen-Batterien

Gutachter: Prof. Dr. Rüdiger Klingeler

Prof. Dr. Christian Enss

Einfluss von Morphologie und Funktionalisierung auf die elektrochemischen Eigenschaften von oxidischen Anodenmaterialien für Lithium-Ionen-Batterien
In der vorliegenden Arbeit werden potenzielle Anodenmaterialien für Lithium-Ionen-Batterien hinsichtlich ihrer physikalischen und elektrochemischen Eigenschaften untersucht. Dabei im Vordergrund steht der Zusammenhang von Partikelgröße, Morphologie, Funktionalisierung und elektrochemischen Eigenschaften. In diesem Kontext wurden das Interkalationsmaterial Li_3VO_4, die konversionsbasierten Übergangmetalloxide MoO_2, V_2O_3, $CoFe_2O_4$ und Mn_3O_4 sowie ZnO als Vertreter der legierungsbildenden Materialien untersucht. Die physikalische Charakterisierung der Ausgangsmaterialien und elektrochemisch zyklierter Proben erfolgte mittels Röntgendiffraktometrie, Rasterelektronenmikroskopie und Magnetisierungsmessungen. Als elektrochemische Messmethoden kamen die zyklische Voltammetrie und galvanostatische Zyklierung zum Einsatz. Die vorgestellten Ergebnisse zeigen, dass durch morphologische Modifikation sowie den Verbund mit Kohlenstoff Einfluss die elektrochemischen Eigenschaften signifikant verbessert werden können. So weisen im Fall von Li_3VO_4 und MoO_2 kleinere Partikel höhere elektrochemische Aktivitäten auf. Die pseudo-kapazitive Ladungsspeicherung, die für hierarchisch strukturierte V_2O_3/C-Mikrosphären beobachtet wird, erlaubt auch bei hohen Laderaten eine gute Leistung. Im Fall der Komposite mit Kohlenstoffhohlkugeln und -nanoröhren führen die Beiträge der Übergangsmetalloxide zu höheren spezifischen Kapazitäten. Zudem erweist sich die Einkapselung von $CoFe_2O_4$ in Kohlenstoffnanoröhren als erfolgreiche Strategie, um den negativen Auswirkungen der Konversionsprozesse auf die Zyklenstabilität entgegenzuwirken.

Effect of morphology and functionalization on the electrochemical properties of oxide anode materials for lithium-ion batteries.
In the present thesis, potential anode materials for lithium-ion batteries are studied with respect to their physical and electrochemical properties. The focus is on the relationship between particle size, morphology, functionalization and electrochemical properties. In this context, the intercalation material Li_3VO_4, the conversion-based transition metal oxides MoO_2, V_2O_3, $CoFe_2O_4$ and Mn_3O_4 as well as ZnO as a representative of the alloy-forming materials were investigated. The physical characterization of the pristine as well as electrochemically cycled materials was performed by X-ray diffraction, scanning electron microscopy and magnetization measurements. The electrochemical measurement methods used were cyclic voltammetry and galvanostatic cycling. In total, the presented results show, that the electrochemical properties of anode materials can be improved significantly by morphological modification and realising carbon composites. In the case of Li_3VO_4 and MoO_2 smaller particles exhibit higher electrochemical activities. The pseudo-capacitive charge storage observed for hierarchically structured V_2O_3/C microspheres allows good performance even at high charge rates. In the case of the composites with hollow carbon spheres and nanotubes, the contributions of the transition metal oxides lead to higher specific capacities. Moreover, encapsulation of $CoFe_2O_4$ in carbon nanotubes proves to be a successful strategy to counteract the negative effects of conversion processes on cycling stability.

Inhaltsverzeichnis

Kapitel 1 1 Einleitung und Grundlagen

Elektrochemische Energiespeicher gelten als Schlüsseltechnologie auf dem Weg zu einer nachhaltigen, modernen und mobilen Gesellschaft. Mit der Möglichkeit der portablen Stromspeicherung wurde in den letzten Jahrzehnten die Voraussetzung für viele innovative Technologien geschaffen, die zum Wandel zu einer digitalen, vernetzten Informations- und Kommunikationswelt beigetragen haben. In der heutigen Zeit sind portable elektronische Geräte im Alltag und im Berufsleben längst nicht mehr wegzudenken. Darüber hinaus sind Batteriespeichersysteme ein wesentlicher Baustein für das Gelingen der Energiewende, die unumgänglich ist für eine sichere, umweltverträgliche und wirtschaftlich erfolgreiche Zukunft. Der größte Teil der globalen Energieversorgung wird gegenwärtig von fossilen Brennstoffen abgedeckt, die allerdings aufgrund ihrer begrenzten Verfügbarkeit angesichts des stetig wachsenden globalen Energiebedarfs nicht zukunftsfähig sind. Ein weitaus wichtigerer Aspekt, der die Energiewende vorantreibt, ist die Notwendigkeit, die Treibhausgasemissionen zu reduzieren, um das Weltklima zu schützen [1]. Zu den alternativen Energiequellen gehören Solar- und Windenergie, die jedoch tageszeitbedingten und witterungsabhängigen Schwankungen unterliegen. In diesem Zusammenhang sind effiziente stationäre Energiespeicher erforderlich, die die Volatilität der erneuerbaren Energien ausgleichen und somit ein stabiles Stromnetz gewährleisten. Um das von der Deutschen Bundesregierung angestrebte Ziel der Klimaneutralität im Jahr 2045 zu erreichen [2], ist zudem der Umstieg auf Elektromobilität unabdingbar. Hierfür werden leistungsfähige mobile Energiespeicher mit langer Lebensdauer benötigt, die hohen Sicherheitsanforderungen genügen müssen und die gleichzeitig zu niedrigen Herstellungskosten produziert werden können.

Im Vergleich zu anderen Batteriesystemen zeichnen sich Lithium-Ionen-Batterien (LIBs) durch ihre hohe Energie- und Leistungsdichte aus (Abb. 1.1a), was sie bereits zur vorherrschenden Batterietechnologie für tragbare Elektronik und Elektrofahrzeuge werden ließ. Darüber hinaus überzeugen sie durch ihre hohe Langlebigkeit und niedrige Selbstentladung. Lithium-Ionen-Batterien beruhen auf dem Prinzip der reversiblen Ein- und Auslagerung von Li^+-Ionen in Aktivmaterialien durch elektrochemische Redoxreaktionen. Sie bestehen prinzipiell aus zwei Elektroden, welche durch den elektrolytgetränkten Separator räumlich

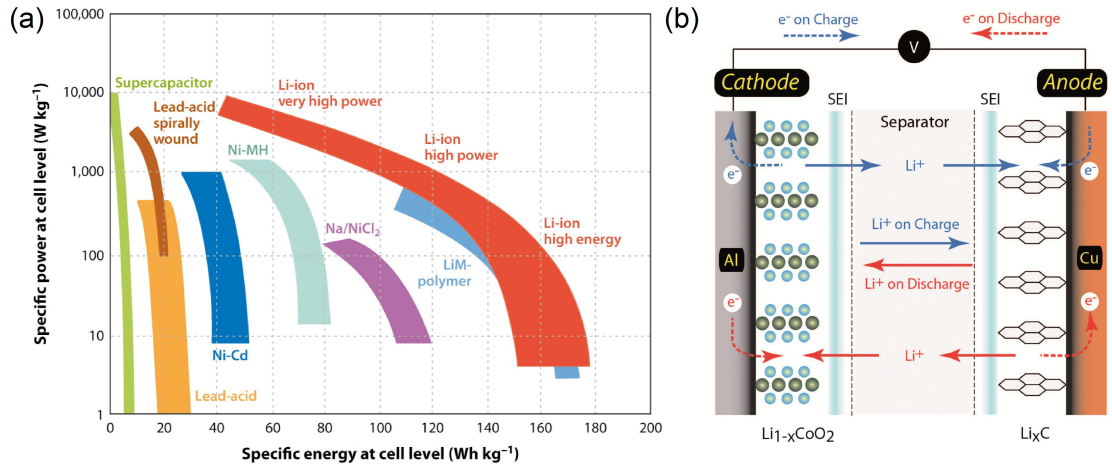

Abbildung 1.1: (a) Übersicht über die spezifische Leistungs- und Energiedichte für konventionelle Batteriesysteme und Lithium-Ionen-Batterien. Aus [3]). (b) Schematische Darstellung der Funktionsweise einer Lithium-Ionen-Batterie. Aus [4])

voneinander getrennt sind. Beim Entladen werden an der negativen Elektrode (Anode) durch Oxidation Li^+-Ionen frei, die durch den Elektrolyten in Richtung der positiven Elektrode (Kathode) wandern, in die sie verbunden mit der Reduktion des Aktivmaterials eingelagert werden (Abb. 1.1b). Beim Laden findet der umgekehrte Prozess statt. Die vergleichsweise kleinen Li^+-Ionen weisen eine hohe Beweglichkeit auf, die für eine hohe Leistungsdichte relevant ist. Die Menge an elektrischer Energie, die eine Batterie speichern kann, wird bestimmt durch die Menge der speicherbaren Ladung, die sogenannte Kapazität, und der Differenz der elektrochemischen Potentiale der Redoxpaare. Die Leistungsfähigkeit einer Batterie wird somit maßgeblich von der Zellchemie bestimmt. Metallisches Lithium gilt als ideales Anodenmaterial, da es von allen Redoxpaaren das negativste Standardelektrodenpotential (-3,05 V gegen Standardwasserstoffelektrode) besitzt und eine hohe spezifische Kapazität von 3860 $mA\,h\,g^{-1}$ aufweist [5]. Zwar finden Lithium-Metall-Anoden Anwendung in nicht wiederaufladbaren Primärbatterien, allerdings verhindern Sicherheistaspekte den Einsatz in Sekundärbatterien. Beim wiederholten Laden kommt es zur Ausbildung von Lithium-Dendriten, die zu einem Kurzschluss führen können [6, 7].

Die Suche nach geeigneten Elektrodenmaterialien ist auch heute noch ein Schwerpunkt der Batterieforschung. Seit der erfolgreichen Markteinführung der ersten Lithium-Ionen-Batterie im Jahr 1991 (Sony, Japan) hat sich Graphit als Anodenmaterial und oxidische Übergangsmetallverbindungen als Kathodenmaterial durchgesetzt [8, 9]. Sowohl Graphit als auch die vielfach eingesetzten Verbindungen mit Steinsalzstruktur besitzen eine schichtartige Kristallstruktur, in die die Li^+-Ionen über reversible topotaktische Redoxreaktionen eingelagert werden (Abb. 1.2a). Die Li^+-Ionen diffundieren an freie Plätze im Kristallgitter, sodass im Idealfall die Wirtsstruktur nicht zerstört wird und die Phasenumwandlungen ohne große

kristallographische Änderungen verbunden sind. Es tritt lediglich eine geringe Dehnung des Kristallgitters auf. Dieser Prozess der Lithiumeinlagerung, auch Interkalation genannt, weist zwar eine hohe Reversibilität auf, allerdings ist die Speicherkapazität auf meist 1 Li^+-Ion pro Formeleinheit (engl. formula unit, f.u.) limitiert [10].

Um die Nutzung von Elektrofahrzeugen, deren Reichweite nach wie vor eines der Hauptkaufkriterien ist, attraktiver zu machen, sind jedoch höhere gravimetrische und volumetrische Energiedichten erforderlich, als die derzeitige Lithiumbatterietechnologie bietet. In diesem Zusammenhang sind in den letzten Jahren Elektrodenmaterialien, die auf alternativen Speichermechanismen basieren, zu denen die Legierungbildung und Konversion (Abb. 1.2b) zählen, zunehmend in den Fokus der Forschung gerückt. Typische Elemente, die mit Lithium bei Raumtemperatur intermetallische Verbindungen eingehen sind Mg, Al, Si, Ge, Sn, Ag, Zn [11]. Übergangsmetallverbindungen MX (M = Fe, Co, Ni etc., X = O, N, F, S, P,) können über eine sogenannte Konversionsreaktion Li^+-Ionen speichern [12]. Dieser Speichermechanismus wurde erstmals im Jahr 2000 von Poizot et al. [13] für Übergangsmetalloxide beschrieben. Bei der Konversionsreaktion wird das Übergangsmetall vollständig reduziert und im Fall oxidischer Verbindungen Li_2O gebildet. Die Struktur der gebildeten metallischen Partikel, die in der amorphen Li_2O-Matrix eingebettet sind, ist entscheidend für die Reversibilität der Reaktion, da die Zersetzung von Li_2O nur durch kleine Metallnanopartikel mit großer Oberfläche und katalytischen Eigenschaften gewährleistet wird [14]. In Bezug auf die Energiedichte sind sowohl die Legierungsbildung als auch die Konversion der Interkalation deutlich überlegen, da pro Formeleinheit mehrere Li^+-Ionen gespeichert werden können. Die Kehrseite der hohen Anzahl an gespeicherten Li^+-Ionen ist allerdings, dass damit auch gravierende strukturelle Veränderungen verbunden sind [10]. So kann die mit starken Volumenänderungen einhergehende mechanische Belastung zur Fraktionierung des Elektrodenmaterials führen [15]. Durch die Zerstörung der Elektrodenstruktur entstehen elektrochemisch inaktive Bereiche, die mit Kapzitätsverlusten verknüpft sind.

In den letzten Jahrzehnten wurde verschiedene vielversprechende Strategien entwickelt, um dieser Problematik entgegenzuwirken. Dazu zählen unter anderem die morphologische Modifikation der Elektrodenmaterialien sowie der Verbund mit Kohlenstoff [9]. Das Ausmaß der strukturellen Schäden hängt zum einen von der Größe der Partikel ab, so ist für nanoskalige Partikel die mechanische Belastung aufgrund der effektiv kleineren Volumenänderungen geringer [16]. Des Weiteren spielt die Morphologie bei anisotroper Ausdehnung des Volumens, wie es zum Beispiel für Silizium beobachtet wird [17], eine wichtige Rolle. Zum anderen kann ein leitfähiges Kohlenstoffnetzwerk die strukturelle Stabilität erhöhen, indem es als Puffer der Volumenänderungen dient. Außerdem verhindert es die Agglomeration der Partikel und kann auch bei strukturellen Schäden die elektrische Kontaktierung innerhalb

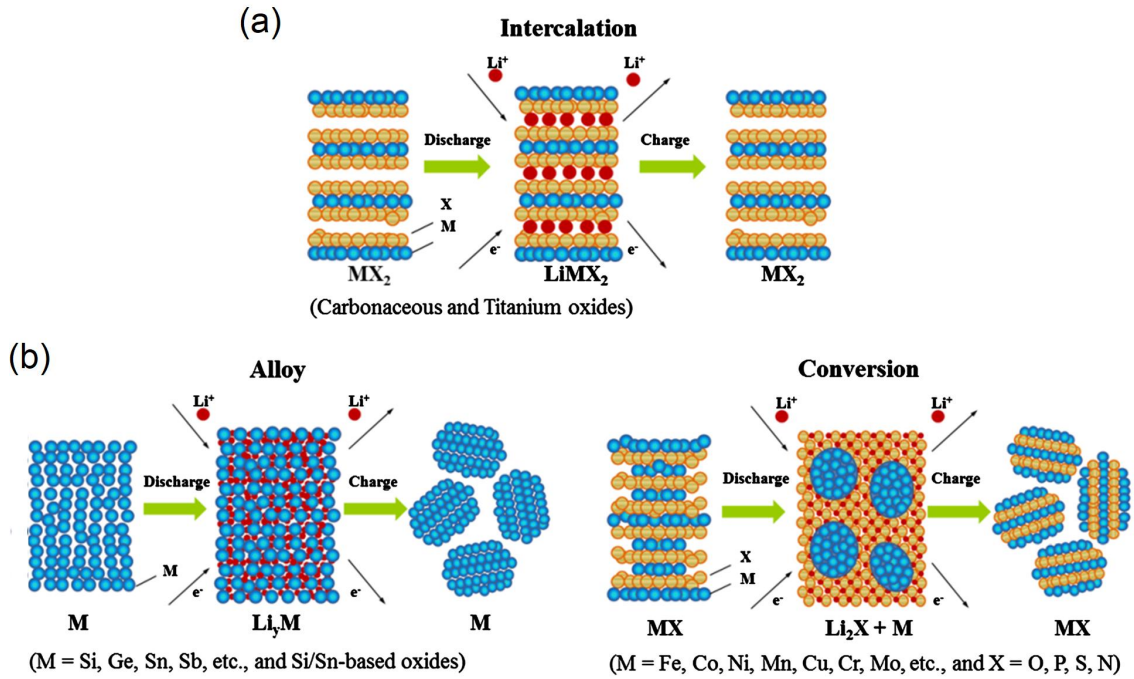

Abbildung 1.2: Schematische Darstellung der verschiedenen Mechanismen zur Speicherung von Li^+-Ionen. Nach [10].

des Elektrodenmaterials weiter aufrechterhalten.[18]

Eine weitere Herausforderung bei der Optimierung der Leistungsfähigkeit von Lithium-Ionen-Batterien stellt die Gewährleistung eines schnellen Ladungstransports dar. Während im Elektrolyten aufgrund dessen hohe Ionen-Diffusivität ein schneller Transfer der Li^+-Ionen garantiert ist sind die Li^+-Ionen-Diffusion im Aktivmaterial und der Elektronentransport innerhalb der Elektrode die limitierenden Faktoren. Ein Paradebeispiel, dass die bereits oben genannten Lösungsstrategien auch in diesem Zusammenhang Erfolg versprechend sind, ist das mittlerweile kommerziell verfügbare Kathodenmaterial Lithiumeisenphosphat. Im Jahr 1997 wurde $LiFePO_4$ zum ersten Mal in der Arbeitsgruppe von J. B. Goodenough als Interkalationsmaterial entdeckt [19]. Um dessen schlechte ionische als auch elektronischen Transporteigenschaften [20] zu überwinden und die kommerzielle Anwendungsreife zu erreichen, wurde auf die Nanoskalierung der Partikel und die Beschichtung mit Kohlenstoff zurückgegriffen [21]. Zum einen verkürzen sich durch die Nanoskalierung die Diffusionswege im Aktivmaterial und zum anderen bildet die Kohlenstoffbeschichtung ein leitfähiges Netzwerk, das das Elektrodenmaterial durchzieht und einen schnellen Elektronentransport gewährleistet [22, 23].

Auf dem Weg zu leistungsfähigeren Lithium-Ionen-Batterien ist neben der Synthese neuer Materialien auch die Aufklärung der komplexen Speichermechanismen und der Transport-

prozesse sowie deren Beziehung zur Elektrodenmorphologie und -struktur erforderlich, um sie gezielt optimieren zu können.

In der vorliegenden Arbeit werden verschiedene interkalationsfähige sowie konversionsbasierte Übergangsmetalloxide als potenzielle Anodenmaterialien in LIBs untersucht. Der Fokus der Untersuchungen liegt auf dem Einfluss der Morphologie und Funktionalisierung mit Kohlenstoff auf die elektrochemischen Eigenschaften.

Die Arbeit ist wie folgt gegliedert: In den folgenden Abschnitten des Kapitels 1 werden im ersten Teil die theoretischen Grundlagen elektrochemischer Systeme erläutert. Anschließend werden die experimentellen Grundlagen und der Versuchsaufbau der im Rahmen der Arbeit eingesetzten elektrochemischen Charakterisierungsmethoden beschrieben. Im zweiten Teil wird eine Einführung in die Thematik der Anodenmaterialien gegeben, die die Anforderungen an diese und die Vorstellung der kommerziell am häufigsten verwendeten Anode Graphit beinhaltet. Anschließend werden die untersuchten Materialien vorgestellt, einschließlich eines kurzen Überblicks über relevante Forschungsarbeiten. Kapitel 2 befasst sich mit den Untersuchungen am Interkalationsmaterial Lithiumorthovanadat Li_3VO_4. Im ersten Teil wird der Einfluss verschiedener morphologischer Modifikationen auf die elektrochemischen Eigenschaften von reinem Li_3VO_4 dargestellt. Es folgen im zweiten Teil die Ergebnisse zu den Untersuchungen an verschiedenen Li_3VO_4-Komposite mit amorphem Kohlenstoff. Kapitel 3 beinhaltet die Untersuchungen an konversionsbasierten Anodenmaterialien im Verbund mit amorphem Kohlenstoff. Hierzu zählen die Übergangsmetalloxide Molybdändioxid MoO_2(Abschnitt 3.2), Vanadiumdioxid V_2O_3 (Abschnitt 3.3 und 3.4) sowie Zinkoxid ZnO (Abschnitt 3.5). Es wird unter anderem mittels kinetischer Analyse für V_2O_3 der Einfluss der Morphologie auf den vorliegenden Speichermechanismus mittels kinetischer Analyse näher betrachtet. Der zweistufige Reaktionsmechanismus von ZnO, bestehend aus einer Konversions- und Legierungsbildung wird anhand von *ex-situ* Studien analysiert. Untersuchungen zu Kompositen von Übergansmetalloxiden mit Kohlenstoffnanostrukturen werden in Kapitel 4 vorgestellt. Hierzu zählt ein Komposit, bestehend aus $CoFe_2O_4$ und Kohlenstoffnanoröhren (Abschnitt 4.1) sowie ein Komposit aus Mn_3O_4 und Kohlenstoffhohlkugeln. In Kapitel 5 findet sich im ersten Teil eine Zusammenfassung der wichtigsten Ergebnisse zu den einzelnen Abschnitten, die im zweiten Teil gegenübergestellt und in einem größeren Kontext diskutiert werden.

1.1 Theoretische und experimentelle Grundlagen

1.1.2 Theoretische Grundlagen elektrochemischer Systeme

Die folgenden Erläuterungen zu den theoretischen Grundlagen elektrochemischer Systeme sind an das Buch „Electrochemical Methods: Fundamentals and Applications“ [24] angelehnt.

Batterien bestehen aus einer oder mehreren galvanischen Zellen, bei denen spontan chemische Energie in elektrische Energie umgewandelt wird. Eine galvanisches Zelle ist aus zwei Elektroden, die durch einen ionenpermeablen elektrolytgetränkten Separator räumlich und elektronisch voneinander getrennt sind, aufgebaut. Über den Elektrolyt, einen elektronischen Isolator, sind die Elektroden ionisch leitend miteinander verbunden. Ihre Funktionsweise beruht auf Redoxreaktionen, die an den Elektroden räumlich voneinander getrennt ablaufenden. Per definitionem wird die Elektrode, an der die Oxidation abläuft, als Anode bezeichnet und diejenige an der die Reduktion stattfindet wird Kathode genannt. Die Reaktionsgleichung für eine der Einzelreaktionen kann wie folgt allgemein beschrieben werden:

$$\mathrm{Ox} + \mathrm{z\,e^-} \rightleftharpoons \mathrm{Red}$$

Wobei Ox für den oxidierten und Red für den reduzierten Zustand der Spezies steht, z bezeichnet die Äquivalenzzahl, die der Anzahl der an der Reaktion beteiligten Elektronen entspricht.

Die Klemmspannung einer galvanischen Zelle ergibt sich aus der Differenz der Potentiale von Kathode und Anode. Üblicherweise wird das Potential eines Redoxpaares im thermodynamischen Gleichgewicht gegenüber der Standardwasserstoffelektrode definiert und wird durch die Nernst-Gleichung beschrieben:

$$E = E_0 + \frac{RT}{zF}\, ln\left(\frac{a_{Ox}}{a_{Red}}\right) \tag{1.1}$$

mit dem Standardelektrodenpotential E^0 gegenüber der Standardwasserstoffelektrode bei Standardbedingungen, universeller Gaskonstante R, absoluter Temperatur T, Äquivalentzahl z, Faraday-Konstante F und die von der Ionenkonzentration abhängigen Aktivitäten a.[25]

Im Betrieb einer elektrochemischen Zelle laufen verschiedene Ladungstransferprozesse ab, die im Folgenden beschrieben werden. Dazu zählen der Ladungstransfer an den Phasengrenzen von Elektrode und Elektrolyt sowie die Diffusion der Ionen.

Ladungstransfer an einer elektrischen Doppelschicht

Im Allgemeinen weisen die Elektrode und der Elektrolytdiese unterschiedliche chemische Potentiale auf, was dazu führt dass sich zur Einstellung eines Gleichgewichts die Ionen im Elektrolyten lösen bzw. an der Elektrode abgeschieden werden. Aufgrund der positiv geladenen Ionen im Elektrolyten und den nicht kompensierten negativ geladenen Elektronen in der Elektrode bildet sich eine elektrochemische Doppelschicht. Für detaillierte Modelle der Struktur der Doppelschicht, wie das Helmholtz-, Chapman- oder Stern-Modell, wird auf die Literatur [26] verwiesen. Der Ladungstransfer an den Phasengrenzen ist ein Prozess mit endlicher Geschwindigkeit und kann somit ein limitierender Faktor in elektrochemischen Systemen sein. Betrachtet man den Ladungstransfer als aktivierten Prozess einer Ein-Elektron-Reaktion mit Arrhenius-Verhalten, so wird der faradaysche Stromfluss J durch die Butler-Volmer-Gleichung beschrieben. Sie entspricht der Superposition der anodischen (oxidativen) und kathodischen (reduktiven) Strombeiträge.

$$J = J_c + J_a = J_0 \cdot (e^{(1-\beta)\cdot\frac{\eta F}{RT}} - e^{-\beta\cdot\frac{\eta F}{RT}}) \tag{1.2}$$

Wobei J_0 der im Gleichgewicht vorliegende Austauschstromdichte entspricht, β dem Transferkoeffizienten und η der angelegten Überspannung.

Diffusiver Massentransport

Sowohl die Ionenleitung im Elektrolyt als auch der Massentransport im Elektrodenmaterial erfolgt unter anderem über Diffusion. Der vom Konzentrationgradienten ∇c getriebene Diffusionsstrom J folgt der durch das erste Fick'sche Gesetz beschriebenen Proportionalität:

$$\vec{J}(\vec{x},t) = -D \cdot \nabla c(\vec{x},t) \tag{1.3}$$

Mit D dem sogenannten Diffusionstensor und c der Konzentration. Durch Einbeziehen der Kontinuitätsgleichung in Form von Massenerhaltung wird aus dem ersten das zweite Ficksche Gesetz abgeleitet, welches im eindimensionalen Fall linearer Diffusion die sich zeitlich und räumlich ändernde Konzentrationsverteilung in der Diffusionsschicht beschreibt.

$$\frac{\partial c}{\partial t} = D\frac{\partial^2 c}{\partial x^2} \tag{1.4}$$

Die Ableitung des zweiten Fick'schen Gesetzes, basierend auf der kinetischen Gastheorie von Einstein, ergibt wiederum den Zusammenhang (Gl. 1.5) zwischen mittlerem Verschiebungsquadrat $\langle x^2 \rangle$ eines linear diffundierenden Teilchens und dem Diffusionskoeffizienten D [27]. Diese dient der Abschätzung der typischen Diffusionslänge ℓ während der Zeitdauer τ

(Gl. 1.6):

$$\left\langle x^2 \right\rangle = 2Dt \tag{1.5}$$

$$\ell = \sqrt{\tau D} \tag{1.6}$$

1.1.3 Elektrochemische Charakterisierungsmessungen

Im Folgenden werden die in der vorliegenden Arbeit genutzten elektrochemischen Messmethoden, die zyklische Voltammetrie und galvanostatische Zyklierung, sowie der Versuchsaubau beschrieben.

Messmethoden

Die Zyklovoltammetrie (CV) ist eine weit verbreitete Methode zur Charakterisierung elektrochemischer Eigenschaften eines Materials hinsichtlich der aktiven Potentialbereiche, der Reversibilität der Prozesse und der Reaktionskinetik. Bei dieser Technik wird an die elektrochemische Zelle eine sich zeitlich linear ändernde Spannung in Dreiecksform angelegt und der fließende Strom gemessen. Die sogenannte Scanrate gibt den Betrag der Spannungsänderung pro Zeit an. Beim Zyklovoltammogramm bei dem der geflossene Strom gegen das Potential aufgetragen ist, treten in den Potentialbereichen, in denen das Elektrodenmaterial elektrochemisch aktiv ist, charakteristische Strompeaks auf. Bei der verwendeten Verkabelung fließt bei einer Oxidation des Elektrodenmaterials ein positiver Strom und bei reduktiven Prozessen ein negativer Strom.

Zur Untersuchung des Lade- bzw. Entladeverhaltens eines Materials dient die galvanostatische Zyklierung. Bei dieser Technik wird an die Messzelle ein konstanter Strom angelegt und der Potentialverlauf gemessen. Die Stromstärke wird in diesem Zusammenhang auch Zyklierrate genannt.

Eine wichtige Messgröße ist die spezifische Kapazität Q_{spez}, die der umgesetzten massennormierten Ladungsmenge entspricht.

$$Q_{spez} = \frac{1}{m} \int_0^{t'} I(t)dt \tag{1.7}$$

Mit dem in der Zeit t' geflossenen Strom I und der Masse m des Aktivmaterials. Die theoretische Obergrenze der Ladung Q_{theo} eines elektrochemisch aktiven Stoffes ist durch

das Faradaysche Gesetz definiert:

$$Q_{theo} = \frac{zF}{M} \tag{1.8}$$

Mit der Faraday-Konstante F, der Äquivalentzahl z und die molare Masse M.

In der vorliegenden Arbeit wurde die Technik „Galvanostatic Cycling with Potential Limitation“ (GCPL) eingesetzt, bei der die Zellspannung auf einen Potentialbereich zwischen Lade- und Entladeschlussspannung beschränkt wird. Dies Gewährleistet die Vergleichbarkeit der Daten und Überladungs- bzw. Tiefentladungseffekte können vermieden werden.

Versuchsaufbau

Die elektrochemischen Messungen wurden mit Hilfe eines mehrkanaligen VMP3-Potentiostats durchgeführt, der über Anschlüsse für Zwei- und Dreielektrodenzellen verfügt. Es gibt drei Abgriffe zur Potentialmessung und zwei Stromanschlüsse.

Die verwendete „EC-Lab“-Software der Firma BioLogic stellt anpassbare Vorlagen für die zuvor beschriebenen Messmethoden bereit und ermöglicht eine automatisierte Durchführung. Zur Gewährleistung stabiler Umgebungsbedingungen befinden sich die Zellen während der Messung in einem Wärmeschrank, dessen Temperatur auf 25 °C gehalten wird.

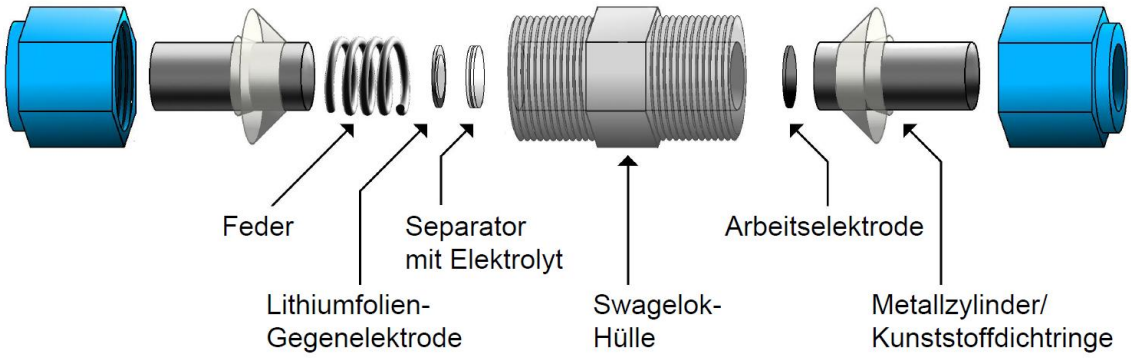

Abbildung 1.3: Schematischer Aufbau der elektrochemischen Zelle mit Zwei-Elektroden-Konfiguration. Nach [28].

Der Aufbau der elektrochemischen Messzellen ist in Abb.1.3 schematisch dargestellt. Als Gehäuse dienen luftdichte Swagelog-Rohrverschraubungen aus Perfluoralkoxylalkan (PFA), die mit Edelstahlstäben verschlossen werden. Der Separator, der sich zwischen Arbeits- und Gegenelektrode befindet, besteht aus 2 Lagen Mikroglasfaser-Filterpapier (Whatman GF/D) und ist mit 200 ţl Elektrolyt (1 M LiPF6 in 1:1 Ehtylenecarbonat (EC) und Dimethylcarbonat (DMC), Electrolyte LP30, Merck) getränkt. Als Gegenelektrode wird eine kreisförmig ausgestanzende Lithium-Folie (Alfa Aesar, 99,9 % Metal basis), die auf eine Nickelscheibe gepresst

ist, verwendet. Die Arbeitselektrode besteht aus 75 wt% aktivem Material, 15 wt% Leitruß (Super C65, Timcal) und wt% Polyvinylidenfluorid-Binder (Solvay Plastics) und wurde wie folgt hergestellt. Zunächst wurden die Pulver in N-Methyl-2-Pyrrolidon (NMP, Sigma-Aldrich) gemischt und mindestens 12 Stunden lang gerührt. Dadurch wird eine homogene Verteilung von Aktivmaterial und Kohlenstoff erreicht. Um eine streichfähige Elektrodenpaste zu erhalten, wurde der größte Teil des NMP unter Vakuum verdampft. Anschließend wurde die Elektrodenpaste auf kreisförmige Cu-Netze (Drahtdurchmesser: 0,115 mm, Nenndurchmesser: 0,14 mm, Drähte/Zoll: 100×100, offene Fläche: 30,3 %, Dicke: 0,25 mm) mit einem Durchmesser von 10 mm aufgebracht. Die präparierten Elektroden wurden unter Vakuum getrocknet und im Anschluss mit einer hydraulischen Presse mit einem Druck von 10 MPa oder mit einer Spindelpresse von Hand gepresst. Vor dem Transfer in die Glovebox mit Argonatmosphäre werden sie nochmals für einige Stunden im unter Vakuum unter gleichen Bedingungen belassen. Aufgrund der hohen Reaktivität von Lithium mit Wasser und Sauerstoff und der Bildung von Flusssäure bei Kontakt des Elektrolyts mit Wasser werden die Zellen in einer Glovebox unter Argonatmosphäre ($O_2 < 1$ ppm, $H_2O < 1$ ppm) zusammengebaut.

Die dominierende Fehlerquelle der Messdaten, die auf die Masse des Aktivmaterials normiert sind, ist die Bestimmung der Probenmasse. Bei der Fehlerabschätzung wird zum einen die Ungenauigkeit der Waage und zum anderen das tatsächlich vorliegende Massenverhältnisses von Aktivmaterial und Kohlenstoff berücksichtigt. Abhängig von der Probenmenge liegt die Ungenauigkeit der Messdaten zwischen 5 % und 10 %. Auf die Reproduzierbarkeit der elektrochemischen Messungen kann sich ebenfalls der händische Zusammenbau der Zellen auswirken.

1.2 Anodenmaterialien

1.2.1 Anforderungen und Stand der Technik

Im Folgenden werden zunächst die relevanten Eigenschaften, die ein Anodematerial mitbringen muss, vorgestellt und anschließend mit denen von Graphit verglichen, das in kommerziell erhältlichen LIBs am häufigsten Verwendung findet.

Um eine hohe Menge an Energie bei möglichst kleinem Eigengewicht und auf möglichst kleinen Raum zu speichern, ist zum einen eine hohe gravimetrische und volumetrische Kapazität erforderlich. Das Anodenmaterial sollte demnach Elemente mit geringer Atommasse

enthalten, eine geringe Dichte aufweisen und eine möglichst große Anzahl an Li^+-Ionen speichern. Als zweites ist für eine hohe Energiedichte relevant, dass das elektrochemische Potential so nah wie möglich zu dem von Li/Li^+ ist, um eine hohe Zellspannung zu gewährleisten. Für eine lange Lebensdauer mit hoher Zyklenstabilität ist eine hohe Reversibilität der elektrochemischen Prozesse sowie strukturelle Stabilität relevant. Außerdem muss eine ideale Anode sowohl gute elektronische als auch ionische Transporteigenschaften besitzen. Des Weiteren sollte das Material nicht schädlich für Mensch und Umwelt sein und möglichst günstig in der Herstellung.

Graphit, das bis dato die Vorherrschaft auf dem Markt eingenommen hat, wird den meisten Anforderungen an ein Anodenmaterial gerecht. Es ist leicht verfügbar, thermisch und chemisch stabil sowie günstig und einfach in der Herstellung. Außerdem überzeugt es durch sein leichtes Atomgewicht, das geringe Potential gegen Li/Li^+ von unter 0,3 V und die gute elektronische Leitfähigkeit der sp^2-hybridisierten Kohlenstoffatome [29]. Da die Li^+-Ionen in Graphit durch Interkalation gespeichert und damit eine Volumenänderung von nur 5-10 % [29, 30] verbunden ist, besitzt es zudem eine hohe Form- und Zyklenstabilität. Allerdings besteht darin auch seine größte Schwäche. Die Li^+-Ionen werden zwischen die Graphitschichten, die durch eher schwache Van-der-Waals-Kräfte zusammengehalten werden, eingelagert und werden dabei an 6 Kohlenstoffatome gebunden [29]. Die Anzahl der speicherbaren Li^+-Ionen ist somit auf 1 Li^+-Ion pro 6 Kohlenstoffatome begrenzt, was dazu führt, dass Graphit trotz des geringen Atomgewichts eine theoretische spezifische Kapazität von lediglich 372 $mA\,h\,g^{-1}$ besitzt. Zwar ist ein niedriges Potential gegen Li/Li^+ wünschenswert in Bezug auf eine hohe Energiedichte, allerdings birgt dies auch Sicherheitsrisiken. Vor allem bei hohen Stromraten kann es dazu kommen, dass sich beim Ladevorgang metallisches Lithium auf der Oberfläche der Anode abscheidet, was auch Lithium-Plating genannt wird, und letztlich zum Kurzschluss führen kann [31, 32]. Ein weiterer Nachteil ist die geringe Li^+-Ionen-Diffusivität von Graphit [33]. Obwohl Graphit als Anodenmaterial in handelsüblichen LIBs durchaus gut geeignet ist, kann es die steigende Nachfrage nach Batterien mit höherer Energiedichte und schnelleren Ladezeiten nicht erfüllen.

1.2.2 Anodenmaterialien der nächsten Generation

1.2.2.1 Interkalationsmaterialien

Aktuell haben nur die beiden Interkalationsmaterialien Graphit und $Li_4Ti_5O_{12}$ die kommerzielle Marktreife erreicht, was auf die hohe Reversibilität der Interkalationsreaktion zurückzuführen ist [34]. Ein Nachteil der Interkalation ist die meist auf 1 Li^+-Ion/f.u. begrenz-

te Speichermenge und damit verbundenen geringen spezifischen Kapazitäten. Das wesentliche Ziel bei der Erforschung neuer Interkalationsmaterialien besteht darin, die speicherbare Ladung zu erhöhen und gleichzeitig die positiven Eigenschaften der Interkalation, wie hohe Form- und Zyklenstabilität, beizubehalten.

Kohlenstoffnanostrukturen

In Anbetracht der vielerlei positiven Eigenschaften von Graphit, gelten andere Kohlenstoffmodifikationen mit sp^2-hybridisierten Kohlenstoffatome, wie Kohlenstoffnanoröhren und Kohlenstoffhohlkugeln, als vielversprechender Ersatz [35]. Kohlenstoffnanoröhren (engl. Carbon Nanotubes, CNTs) sind seit ihrer Entdeckung im Jahr 1991 [36] aufgrund ihrer Eigenschaften auf großes Interesse in vielen verschiedenen Forschungsgebieten gestoßen [37–43]. Dabei handelt es sich um zylinderförmig aufgerollte Graphenschichten, deren Eigenschaften von ihrer genauen Struktur abhängen. Je nach Aufrollrichtung des hexagonalen Graphengitters sind sie entweder halbleitend oder metallisch leitend [4]. Die Enden können offen oder geschlossen sein. Des Weiteren unterscheidet man zwischen einwandigen und mehrwandigen CNTs. Letztere weisen eine ausgezeichnete Zugfestigkeit von 50-200 GPa auf sowie mit 1,2 TPa ein hohes Maß an Elastizität [44]. Damit zählen sie zu den stärksten und härtesten Materialien.

Zahlreiche Forschungsgruppen haben das Potenzial von einwandigen sowie mehrwandigen CNTs als Anodenmaterial in LIBs untersucht [30, 45–49]. Die berichteten spezifischen Kapazitäten variieren je nach Struktur der CNTs stark und reichen von 312 $\mathrm{mA\,h\,g^{-1}}$ bei 40 Ag [50] bis hin zu $\mathrm{mA\,h\,g^{-1}}$ bei 50 $\mathrm{mA\,g^{-1}}$ [51]. Solch hohe Kapazitätswerte, die bei weitem den theoretischen Wert von Graphit unter der Bildung von LiC_6 übertreffen, können auf die zusätzlichen Speicherplätze für Li^+-Ionen in den CNTs zurückgeführt werden. Li^+-Ionen können unter anderem in den Zwischenräumen zwischen CNT-Bündeln oder auch im Fall von offenen Enden oder Defekten im Inneren der CNTs eingelagert werden [30, 52, 53]. Basierend auf einer Stöchiometrie von LiC_2 wurde der maximale theoretische Wert für die reversible Kapazität von einwandigen CNTs auf 1116 $\mathrm{mA\,h\,g^{-1}}$ abgeschätzt [54]. Eine Herausforderung aktueller Forschung stellt allerdings der schlechte Coulomb-Wirkungsgrad von CNTs dar.

Im Verbund mit anderen Aktivmaterialien haben sich CNTs bereits bewährt [30, 55–57]. Einerseits tragen sie im Komposit durch ihr eigenes Vermögen, Li^+-Ionen zu interkalieren, zur Ladungsspeicherung bei. Zum anderen stellen sie ein leitfähiges Netzwerk dar, das aufgrund ihrer guten elektronischen Leiteigenschaften einen schnellen Elektronentransport innerhalb der Elektrode gewährleistet, und erhöhen die strukturelle Stabilität der Elektrode. Bei der gängigen Methode werden die Aktivmaterialien auf den CNTs abgeschieden, was

allerdings dazu führen kann, dass sich die Partikel aufgrund der schwachen Adsorptionskräfte wieder lösen [58]. Vielversprechender ist die Einlagerung der Aktivmaterialien in die Hohlräume der CNTs. Dies hat sich insbesondere als erfolgreich erwiesen, um den Schäden durch die starken Volumenänderungen, die bei der Konversion und Legierungsbildung auftreten, entgegenzuwirken [59]. Ein Übersichtsartikel über Untersuchungen zu gefüllten CNTs als Anodenmaterialien findet sich im Anhang. Die CNTs können sich aufgrund ihrer hervorragenden mechanischen Eigenschaften, wie die hohe Elastizität, den Volumenänderungen anpassen und die dabei einhergehende mechanische Belastung ableiten.

Bei weitem nicht so gut erforscht wie CNTs sind Kohlenstoffhohlkugeln (engl. Hollow carbon spheres, HCS). Dabei handelt es sich um Kugeln aus Kohlenstoff mit Durchmessern von meist wenigen hundert Nanometern, die im Inneren einen Hohlraum aufweisen. Sie zeichnen insbesondere ihre hohe spezifische Oberfläche aus, die zusätzliche Li^+-Ionen-Speicherplätze bietet sowie kurze Diffusionswege [60]. Allerdings zeigen die wenigen Untersuchungen zu reinen HCS als Anodenmaterial keine großen Vorteile gegenüber Graphit [61–63]. Generell führt die geringe Packungsdichte der HCS aufgrund des Hohlraums zu einer niedrigen volumetrischen Energiedichte.

Die Hohlräume eignen sich dagegen ideal zur Einkapselung von anderen Aktivmaterialien, was zu der Entwicklung zahlreicher Komposite geführt hat, die eine hervorragende elektrochemische Perfomance liefern. Dazu zählen unter anderem Komposite mit legierungsbildenden Materialien, wie Silizium [64], Germanium [65] und Zinn [66, 67], sowie mit den Konversionmaterialien Fe_2O_3 [68], CoO [69], Co_3O_4 [70].

Lithiumorthovanadat Li_3VO_4

Das Vanadat Li_3VO_4 ist bereits seit vielen Jahren aufgrund seiner nicht-linearen optischen sowie ionenleitenden Eigenschaften Gegenstand der Forschung [71–73]. Erst die Studien von Li et al. [74] im Jahr 2013, die dessen interkalative Eigenschaften aufdeckten, haben das Interesse an Li_3VO_4 als potenzielles Anodenmaterial geweckt. Unter den verschiedenen Li_3VO_4-Polymorphen ist die sogenannte β-Phase, deren Kristallstruktur (Abb. 1.4) der orthorhombischen Raumgruppe $Pnm2_1$ angehört, bei Raumtemperatur stabil [75].

Die Kristallstruktur besteht aus einem verzerrten Netzwerk hexagonal dicht gepackter Sauerstoffionen, wobei die Hälfte der tetraedrischen Plätze von Li und V besetzt ist. Die über gemeinsamen Kanten verknüpften LiO_4- und VO_4-Tetraeader besitzen die gleiche Orientierung parallel zur kristallographischen c-Richtung. Gerade Tunnel entlang der kristallographischen a- und c-Richtung sowie zickzackförmige Tunnel entlang der kristallographischen b-Richtung bieten potenzielle Diffusionspfade für Li^+-Ionen. Neben den bereits von den drei Lithiu-

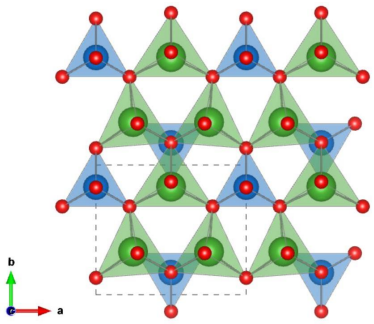

Abbildung 1.4: Schematische Darstellung der Kristallstruktur von β-Li_3VO_4 entlang der c-Achse nach den Stukturdaten aus [76]. Die LiO_4-Tetraeder sind in grün, die PO_4-Tetraeader in blau und die Sauerstoffatome in rot dargestellt.

matomen besetzten Kristallgitterplätze (Li(1) in 1b- und Li(2) in 2c-Wykoff-Positionen), stehen die 2a- (1/2, 1/2, 0,68) und 4b-Positionen (1/4, 0,0028, 1/4) für zusätzliche Lithiumatome zur Verfügung. Neben der hohen ionischen Leitfähigkeit macht vor allem die große Bandbreite möglicher Oxidationsstufen von Vanadium, die die Speicherung von mehr als $1\,Li^+$-Ion/f.u. zulässt, Li_3VO_4 zu einem vielversprechenden Anodenmaterial. Außerdem weist es ein sicheres aber dennoch niedriges Potentialfenster zwischen 0,2 V und 1 V vs. Li/Li^+ aus. Basierend auf *ex-situ* Röntgendiffratometrie-Studien (engl. X-ray diffraction, XRD) in Verbindung mit der spezifischen Kapazität, die mittels galvanostatischer intermittierender Titrationstechnik (GITT) erhalten wurde, wurde von Li et al. [74] folgender Mechanismus der Li^+-Ionen Speicherung in Li_3VO_4 vorgeschlagen:

$$Li_3VO_4 + x\,Li^+ + x\,e^- \rightleftharpoons Li_{3+x}VO_4 \qquad Q_{th(x=2)} = 394\,mA\,h\,g^{-1}$$

Anders als bei typischen Interkalationsmaterialien kann in Li_3VO_4 mehr als $1\,Li^+$-Ion/f.u. eingelagert werden, wobei über die genaue Anzahl Uneinigkeit herrscht. In der Literatur [77–81] finden sich für Li_3VO_4 überwiegend spezifische Kapazitäten unter $400\,mA\,h\,g^{-1}$, entsprechend $x = 2$. Liang et al. [82] und Ni et al. [83] berichten dagegen von reversiblen spezifischen Kapazitäten um $590\,mA\,h\,g^{-1}$, was die Vermutung aufkommen ließ, dass unter der Reduktion von V^{5+} zu V^{2+} bis zu $3\,Li^+$-Ionen/f.u. gespeichert werden können und die theoretische Kapazität somit $591\,mA\,h\,g^{-1}$ beträgt. Zur Bestätigung dieser Annahme demonstrierten Liang et al. [82] mit Hilfe von First-Principle-Berechnungen, dass 3 Li^+-Ionen stabil in die Kristallstruktur von Li_3VO_4 eingelagert werden können. Hier ist anzumerken, dass diese Berechnungen jedoch nur auf Basis der kristallografischen Struktur erfolgten und eine umfassendere Analyse mittels Dichtefunktionaltheorie von Dompablo et al. [84] zu einem anderen Ergebnis kommt. Die Speicherung von $2\,Li^+$-Ionen führt zwar zu einer Verzerrung

der Sauerstoffschichten, die ursprüngliche hexagonale dicht gepackte Struktur bleibt dabei jedoch erhalten. Da die Einlagerung eines dritten Li^+-Ions dagegen mit einer rekonstruktiven Phasenumwandlung zu Li_6VO_4 mit einer Antifluorit-Struktur verbunden ist, wird eine mögliche reversible Speicherung von 3 Li^+-Ionen in Li_3VO_4 ausgeschlossen. Eine Erklärung der hohen gemessenen reversiblen Kapazitäten um 590 $mA\,h\,g^{-1}$ ist möglicherweise eine kapazitive Speicherung von Lithium in oberflächennahen Schichten oder Grenzflächen, zumal es sich bei den untersuchten Materialien um nanoskalierte Kohlenstoffkomposite handelt. Ungeachtet des noch nicht vollständig aufgeklärten Speichermechanismus wäre Li_3VO_4 im Hinblick auf die Energiedichte mit einer derart hohen Kapazität jedoch wettbewerbsfähiger als die kommerziell verfügbaren Interkalationsmaterialien Graphit und $Li_4Ti_5O_{12}$ (Abb.1.5).

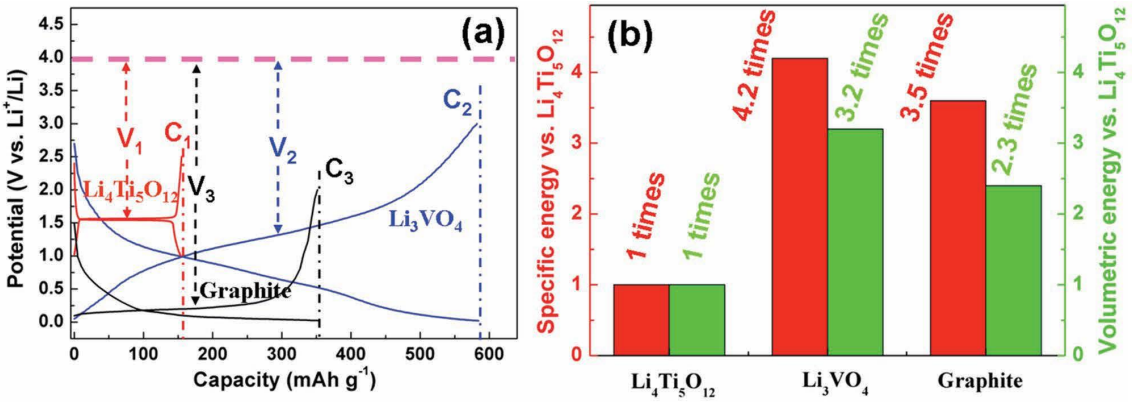

Abbildung 1.5: Vergleich von Li_3VO_4 mit $Li_4Ti_5O_{12}$ und Graphit hinsichtlich (a) der Potentialverläufe während des Ent-/Ladens und die spezifische Kapazität sowie (b) die gravimetrische und volumetrische Energiedichte. Aus [83].

Neben der spezifischen Kapazität und möglichen Li^+-Ionen-Plätze ist die Kenntnis über die strukturellen Änderungen, die während der Li^+-Ionen-Speicherung auftreten, erforderlich, um ein besseres Verständnis über den Speichermechanismus zu erhalten. *Ex-situ* und *in-situ* durchgeführte Untersuchungen mittels XRD verschiedener Forschungsgruppen [73, 74, 85] zeigen, dass die Interkalation zunächst über einen einphasigen Prozess abläuft und sich anschließend eine zweite Phase bildet. Dabei handelt es sich um einen reversiblen Prozess, bei dem nach einem vollen Zyklus die ursprüngliche Li_3VO_4-Phase wieder vorliegt. Einen genaueren Einblick liefern die *in-situ* durchgeführten XRD-Studien von Liu et al. [85] die zeigen, dass sich die Abstände zwischen den (200)- und (002)-Ebenen nach dem ersten Zyklus irreversibel vergrößert haben, was sich positiv auf das weitere Zyklierverhalten auswirkt.

Im Folgenden wird ein kurzer Überblick über die Fortschritte der elektrochemischen Performance von Li_3VO_4 gegeben, seit es erstmals als Anodenmaterial untersucht wurde. Li et al. [74] berichteten von spezifischen Kapazitäten um 300 $mA\,h\,g^{-1}$, die über 25 Zyklus stabil waren, jedoch bei einer relativ geringen Stromdichte von 20 $mA\,g^{-1}$. Mit der Reduk-

tion der Partikelgröße konnte die Leistungsfähigkeit von Li_3VO_4 in den folgenden Jahren verbessert werden, so lieferten Li_3VO_4-Partikel mit einer Durchschnittsgröße von 250 nm nach 100 Zyklen immer noch eine reversible Kapazität von 396 mA h g^{-1} bei einer etwa fünffach größeren Stromdichte von 0,25 C [86]. Es wurden verschiedenste Morphologien entwickelt, wie hohle Li_3VO_4-Mikroboxen [87] und Mikrokugeln [88] mit dem Ziel, die elektrochemischen Eigenschaften zu verbessern. Yang et al. [89] führten Untersuchungen zu verschiedenen Morphologien von Li_3VO_4 durch. Im Vergleich zu den Materialien, deren Ausmaße im Bereich einiger Mikrometer lagen, erwiesen sich die Nanostäbchen mit Durchmessern von 50 - 100 nm und Längen von 100 - 500 nm hinsichtlich spezifischer Kapazität und Hochstromfähigkeit als am Besten. Sie erreichten bei 100 mA g^{-1} eine Kapazität von 370 mA h g^{-1} und selbst bei 4000 mA g^{-1} noch 150 mA h g^{-1}. Durch die nachträgliche Beschichtung mit Kohlenstoff konnte sowohl die spezifische Kapazität, die Zyklenstabilität und die Hochstromfähigkeit weiter optimiert werden, sodass bei 100 mA g^{-1} selbst nach 100 Zyklen noch 430 mA h g^{-1}erzielt wurden und bei einer Stromdichte von 4000 mA g^{-1} noch 250 mA h g^{-1}. Zhang et al. [90] konnten durch die Zugabe der Kohlenstoffquelle schon bei der Synthese das Wachstum der Li_3VO_4-Partikel eindämmen und ein Komposit aus kohlenstoffbeschichteten Li_3VO_4-Nanopartikel herstellen, die eine Größe von 20 - 75 nm aufwiesen. Sie lieferten bei Stromdichten von 1 C, 10 C und 80 C jeweils ausgezeichnete Kapazitäten von 410 mA h g^{-1}, 340 mA h g^{-1} und 106 mA h g^{-1}. Außerdem blieb selbst bei einer hohen Stromdichte von 10 C nach 2000 Zyklen 80 % der Kapazität erhalten. Neben amorphen Kohlenstoff [79, 82, 91] wurden Komposite mit verschiedensten Kohlenstoffallotropen, wie Graphene [92], Graphit [93], Kohlenstoffnanoröhren [94] sowie Kombinationen [95] davon untersucht. Die bis heute höchste gemessene spezifische Kapazität liegt bei 594 mA h g^{-1} bei 150 mA g^{-1} im ersten Delithiierungszyklus [83]. Dabei handelt es sich um ein Komposit bestehend aus Li_3VO_4-Nanokristallen, die homogen verteilt auf C-Nanoflocken eingebettet sind. [85] synthetisierten ein Komposit aus mesoporösen Li_3VO_4/C-Ellipsoiden mit Größen im Submikrometerbereich, die auf reduzierten Graphenoxid eingebettet sind, welches die bis heute längste Lebensdauer (82,5 % Kapazitätserhalt über 5000 Zyklen bei 10 C) aufweist und die beste Hochstromfähigkeit (230 mA h g^{-1} bei 125 C).

1.2.2.2 Konversionsbasierte Materialien

Bei der Entwicklung neuer Anoden für Hochenergie-Lithium-Ionen-Batterien kommen des Weiteren Materialien in Betracht, die auf alternativen Speichermechanismen, wie der Konversion, basieren. Im Gegensatz zur Interkalation können dabei mehrere Li^+-Ionen/f.u. gespeichert werden. Unter diesen Materialien gelten Oxide von Übergangsmetallen, die bis heute am meisten erforscht sind, aufgrund ihrer vielerlei positiven Eigenschaften als

besonders vielversprechend [96, 97].

Einfache Übergangsmetalloxide

Im Gegensatz zu den meisten Übergangsmetalloxiden, die in der Regel eine schlechte elektronische Leitfähigkeit aufweisen [98], besitzt Molybdändioxid MoO_2 einen niedrigen elektrischen Widerstand, was es als Anodenmaterial interessant macht.

MoO_2 kristallisiert in einem monoklinen primitiven Gitter der Raumgruppe $P2_1/c$ (Abb. 1.6). Die verzerrt rutilartige Kristallstruktur kann als Tunnelgerüst beschrieben werden, bei dem die über Kanten verknüpften MoO_6-Oktaedern entlang der kristallographischen a-Richtung eindimensionale Kanäle bilden, die den Li^+-Transport begünstigen.

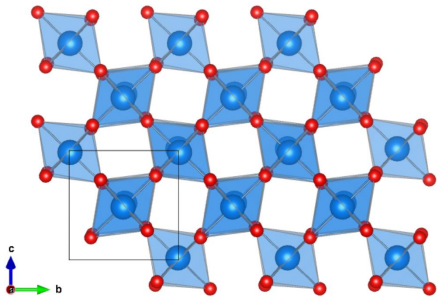

Abbildung 1.6: Schematische Darstellung der Kristallstruktur von MoO_2 entlang der a-Achse nach den Strukturdaten aus [99]. Die MoO_6-Tetraeder sind in blau und die Sauerstoffatome in rot dargestellt.

Bereits im Jahr 1987 veröffentlichte Auborn et al. [100] Untersuchungen zu MoO_2 als potenzielles Anodenmaterial, das auf der Interkalation von Li^+-Ionen basiert. Dahn et al. [101] konnten mittels *in-situ* XRD-Studien nachweisen, dass die ursprüngliche monokline Phase bei der Interkalation von 1 Li^+-Ion/f.u. über eine orthorhombische Phase ($Pnnm$) in eine andere monokline Struktur übergeht und damit eine Volumenänderung von 11 % verbunden ist (Abb. 1.7 a). Die theoretische gravimetrische und volumetrische Kapazität von MoO_2 betragen 209 $mA\,h\,g^{-1}$ und 1357 $mAh\,cc^{-1}$ und liegen damit über denen von $Li_4Ti_5O_{12}$ (Abb. 1.7 b). In den Untersuchungen von Dahn et al. [101] zeigten die mikrometergroßen MoO_2-Partikel jedoch hohe Kapazitätsverluste bei der elektrochemischen Zyklierung über den Phasenübergang hinaus. In den folgenden Jahren gelang es durch die Nanoskalierung die Zyklenstabilität signifikant zu verbessern, so berichtete Sen et al. [102] für MoO_2-Nanobänder hohe stabile Kapazitäten um 150 $mA\,h\,g^{-1}$ für über 200 Zyklen bei 100 $mA\,g^{-1}$. Die ergänzenden *ex-situ* XRD-Studien zur Untersuchung der strukturellen Entwicklung während der De-/Interkalation demonstrierten zudem die Reversibilität des Phasenübergangs, wie auch die *ex-situ* XRD-Studien und Analyse mittels dichte-Funktional-Theorie von Kim et al. [103]

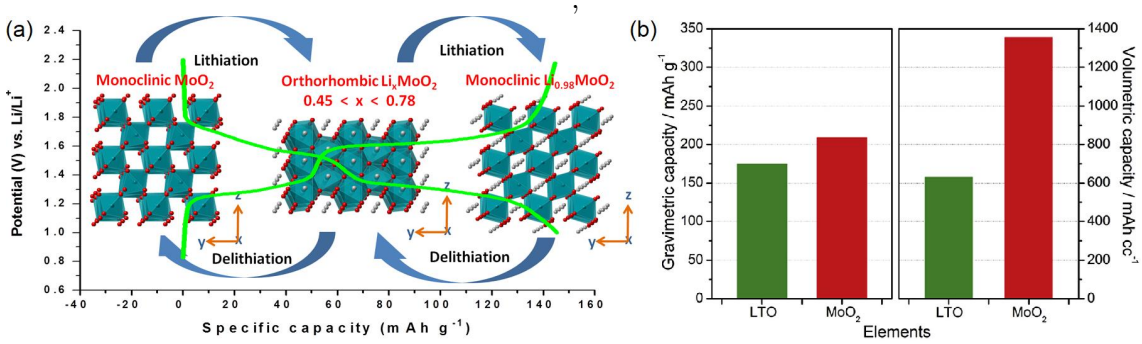

Abbildung 1.7: (a) Schematische Darstellung der Kristallstrukturen und Potentialverläufe von MoO_2 bei der De-/Interkalation von 0,98 Li^+-Ionen. [102].(b) Vergleich der gravimetrischen und volumetrischen Energiedichte von MoO_2 und $Li_4Ti_5O_{12}$ Aus [103].

zeigen. Liu et al. [104] synthetisierten MoO_2-Nanoplättchen, die bei 1 C zwischen dem 1000 und 2000 Zyklus einen Kapazitätsverfall von lediglich 0,015 mA h g^{-1} pro Zyklus. Park et al. [105] demonstrierte mit seinen Untersuchungen, dass durch die Reduktion der Partikelgröße zudem die elektrochemische Aktivität signifikant gesteigert werden kann. Im Vergleich zu MoO_2/C-Mikrostäbchen zeigten die mittels kolloider Vermahlung hergestellten Partikel mit einer Größe unter 200 nm, weitaus höhere spezifische Kapazitäten, so erreichten sie bei 0,5 C eine spezifische Kapazität von 206 mA h g^{-1} und selbst bei einer hohen Stromdichte von 30 C noch 129 mA h g^{-1}. Außerdem wiesen sie mit einem Erhalt von 98,6 % der initialen Delithiierungskapazität nach 100 Zyklen bei 0,5 C eine hervorragende Zyklenstabilität auf.

Zwar wurde bereits in den Jahren zuvor für MoO_2-Nanopartikel berichtet, dass bei der elektrochemischen Zyklierung bis 0,01 V vs. Li/Li^+ eine für interkalations-basierte Speicherung ungewöhnliche hohe Anzahl von über 3 Li^+-Ionen/f.u. reversibel eingelagert werden können [106, 107], doch erst durch die von Ku et al. [108] durchgeführten Röntgenphotoelektronenspektroskopie (engl. X-ray photoelectron spectroscopy, XPS) konnte aufgeklärt werden, dass die Speicherung von mehr als 1 Li^+-Ion/f.u. auf einer Konversionsreaktion beruht, die entweder durch Erhöhung der Raumtemperatur oder Verkleinerung der Partikelgröße begünstigt wird.

$$\text{(A)}\quad MoO_2 + x\,Li^+ + x\,e^- \rightleftharpoons Li_xMoO_2 \qquad (0 \leq x \leq 0{,}98)$$

$$\text{(B)}\quad Li_xMoO_2 + (4-x)\,Li^+ + (4-x)\,e^- \rightleftharpoons 4\,MoO_2 + Li_2O$$

Die hohe theoretische Kapazität von 838 mA h g^{-1} hat in den folgenden Jahren großes Interesse an MoO_2 als Anodenmaterial geweckt. Als Konversionmaterial unterliegt jedoch auch

MoO_2 bei der Zyklierung starken Volumenänderungen, die sich negativ auf die Zyklenstabilität auswirken. Um die elektrochemische Performance zu verbessern, wurden verschiedene morphologische Modifikationen entwickelt, wobei der Fokus insbesondere auf nanoskalierte Materialien [106, 109, 110] lag. Des Weiteren haben sich mesoporöse Strukturen [111], aufgrund der großen Oberfläche, die sie bieten, als vielversprechend erwiesen. Obwohl die elektrochemischen Eigenschaften durch die morphologische Modifikation deutlich optimiert werden konnten, ist für eine kommerzielle Anwendung eine weitere Verbesserung der Zyklenstabilität erforderlich. Dies hat zur Herstellung von Kompositen mit Kohlenstoffallotropen, wie Graphene [112], CNTS [113], amorphen Kohlenstoff [114] geführt. So berichten Sun et al. [115] für MoO_2-Nanopartikel, die in eine Matrix aus Kohlenstoff eingebettet sind, von einer spezifischen Kapazität in Höhe von $734\,\mathrm{mA\,h\,g^{-1}}$ nach über 350 Zyklen bei $50\,\mathrm{mA\,g^{-1}}$. Interessant sind außerdem die Untersuchungen von Shon et al. [116] an mesoporösen MoO_2-Elektroden. Sie liefern bei einer Stromdichte von 0,1 C über 50 Zyklen eine extrem hohe stabile Kapazität um $1500\,\mathrm{mA\,h\,g^{-1}}$, die bis heute höchste Kapazität ist, die für MoO_2 gemessen wurde und den theoretischen Wert basierend auf der Konversionsreaktion deutlich überschreitet. Die Analyse mittels *in-situ* XRD, TEM verbunden mit Elektronen-Energie-Verlust-Spektroskopie (EELS) und Computermodellierung decken auf, dass die Speicherung der Li^+-Ionen nicht über eine Konversionsreaktion stattfindet und stattdessen die nanoskalige Porenstruktur des Materials einen anderen Speichermechanismus ermöglicht, der noch weiter erforscht werden muss, um die Gründe für die hohe Lithium-Speicherfähigkeit zu finden. Dies bietet möglicherweise eine vielversprechende Strategie für das Design von Hochenergie-Anodenmaterialien.

Das Vanadiumsesquioxid V_2O_3 ist vor allem als Mott-Hubbard-Isolator bekannt, der bei einer Temperatur um 160 K einen Metall-Isolator-Phasenübergang erster Ordnung aufweist [117]. Dabei geht mit Abnahme der Temperatur die paramagnetische rhomboedrische Phase mit Korund-Struktur (Raumgruppe $R\bar{3}c$) in eine antiferromagnetische monokline Phase (Raumgruppe $I2/a$) über. Bei Raumtemperatur weist V_2O_3 eine hohe elektronische Leitfähigkeit von $10^3\,\mathrm{S\,cm^{-1}}$ [118] auf, weshalb es bereits erfolgreich als leitfähige Beschichtung von $LiFePO_4$-Partikeln zur Optimierung derer elektrochemischen Eigenschaften eingesetzt wurde [119]. Tranchant et al. [120] untersuchten im Jahr 1980 die elektrochemischen Eigenschaften von V_2O_3 in einem Potentialbereich zwischen 2 V und 3,5 V gegen Li/Li^+ und erklärten es aufgrund der geringen Kapazität ohne erkennbare Plateaus in den Potentialverläufen für ungeeignet als Kathodenmaterial in LIBs. Das Interesse der Forschung an V_2O_3 als Anodenmaterial wurde von Li et al. [121] geweckt, die basierend auf thermodynamischen Berechnungen V_2O_3 eine theoretische spezifische Kapazität von $1073\,\mathrm{mA\,h\,g^{-1}}$ bei Potentialen unterhalb von 1 V gegen Li/Li^+ zuschrieben. Der zugrunde liegende Speichermechanismus

setzt sich aus einer anfänglichen Interkalation und einer anschließenden Konversionsreaktion zusammen:

$$\text{(A)}\ \ V_2O_3 + x\,Li^+ + x\,e^- \rightleftharpoons Li_xV_2O_3$$

$$\text{(B)}\ \ Li_xV_2O_3 + (6-x)\,Li^+ + (6-x)\,e^- \rightleftharpoons 2\,V + 3\,Li_2O$$

Die Ergebnisse der experimentellen Untersuchung von Li et al. [121] lieferten jedoch für V_2O_3 eine Kapazität von nicht einmal der Hälfte des theoretisch erwarteten Werts verbunden mit einer schlechte Reversibilität. In den nachfolgenden Jahren wurden viele Anstrengungen unternommen, um die elektrochemischen Eigenschaften von V_2O_3 zu optimieren. Der Schwerpunkt lag dabei auf der Herstellung von Kompositen mit verschiedenen Kohlenstoffmodifikationen und Morphologien, um die schlechte Zyklenstabilität aufgrund der starken Volumenänderungen bei der Konversionsreaktion zu verbessern. Da die oberflächennahen Vanadiumatome von V_2O_3 aufgrund deren geringer Valenz (V^{3+}), leicht in höhere Valenzzustände (V^{4+} oder V^{5+}) oxidieren, ist eine Beschichtung von V_2O_3 mit Kohlenstoff zudem in Hinblick auf dessen Stabilität an Luft interessant [122]. Jiang et al. [123] synthetisierten *in-situ* mit Kohlenstoff beschichtete Mikrosphären, die mit einer spezifischen Delithiierungskapazität von 437,5 $mA\,h\,g^{-1}$ nach 100 Zyklen bei 100 $mA\,g^{-1}$ 92,6 % des initialen Werts erhalten. XRD-Untersuchungen bestätigen zudem, dass die Kohlenstoffbeschichtung die V_2O_3-Partikel vor Alterung schützt. Dong et al. [124] berichten von einem Komposit aus nanoskaligem V_2O_3und amorphen Kohlenstoff, das nach 100 Zyklen bei 200 $mA\,g^{-1}$ eine reversible Kapazität von 780 $mA\,h\,g^{-1}$ liefert. In Kohlenstoff eingekapselte V_2O_3-Nanofäden weisen bei einer Stromdichte von 100 $mA\,g^{-1}$ stabile spezifische Kapazitäten um 985 $mA\,h\,g^{-1}$ auf und selbst bei 5000 $mA\,g^{-1}$ noch 519 $mA\,h\,g^{-1}$ [125]. Neben amorphen Kohlenstoff wurden weitere Kohlenstoffmodifikationen, wie CNTs [126] und reduziertes Graphenoxid [127, 128] untersucht.

Unter den Konversionsmaterialien gelten Manganoxide aufgrund ihrer hohen Umweltverträglichkeit, Wirtschaftlichkeit und leichten Verfügbarkeit als vielversprechende Anodenmaterialien für LIBs [129]. Fan et al. [130] untersuchte erstmals im Jahr 2010 mit Hilfe von *ex-situ* XRD- und TEM-Studien den Speichermechanismus der Manganoxide MnO, MnO_2, Mn_2O_3 und Mn_3O_4. Die Ergebnisse zeigen, dass nach der ersten vollständigen Lithiierung in allen Oxiden die reversible De-/Lithiierung über denselben Prozess abläuft. Unterschiede liegen in der theoretischen spezifischen Kapazität sowie die Höhe des initialen Kapazitätsverlust aufgrund der irreversiblen Prozesse bei der ersten Lithiierung. Das im Mineral Hausmannit

natürlich vorkommende Manganoxid Mn_3O_4 besitzt nach MnO die höchste theoretische spezifische Kapazität und den geringsten initialen Kapazitätsverlust basierend auf folgendem Reaktionsmechanismus:

$$\text{(A)}\ Mn_3O_4 + Li^+ + e^- \longrightarrow LiMn_3O_4 \qquad Q_{th} = 117\,\text{mA h g}^{-1}$$

$$\text{(B)}\ LiMn_3O_4 + Li^+ + e^- \longrightarrow Li_2O + 3\,MnO \qquad Q_{th} = 117\,\text{mA h g}^{-1}$$

$$\text{(C)}\ 3\,MnO + 6\,Li^+ + 6\,e^- \rightleftarrows 3\,Li_2O + 3\,Mn \qquad Q_{th} = 703\,\text{mA h g}^{-1}$$

Um einen tieferen Einblick in den Speichermechansimus von Mn_3O_4 zu bekommen, führten Lowe et al. [131] *in-situ* XRD- und XAS-Studien, deren Ergebnisse in Abb. 1.8 zusammengefasst sind. Sie konnten zum einen zeigen, dass die Lithiierung zunächst an der Oberfläche von Mn_3O_4 mit simultan ablaufender Reduktion von Mn_3O_4 und $LiMn_3O_4$ stattfindet. Metallisches Mn hingegen ist erst nach der Reduktion von Mn^{2+} in einen durchschnittlichen Oxidationszustand von Mn^{1+} zu finden. Die Ergebnisse zeigen zudem, dass mit der Lithiierung ist sukzessive Amorphisierung des Materials verbunden ist. Des Weiteren wurde gezeigt, dass ein großer Teil der Ladung kapazitivartig gespeichert wird, wobei der zugrundeliegende Prozess jedoch weiter erforscht werden muss.

,

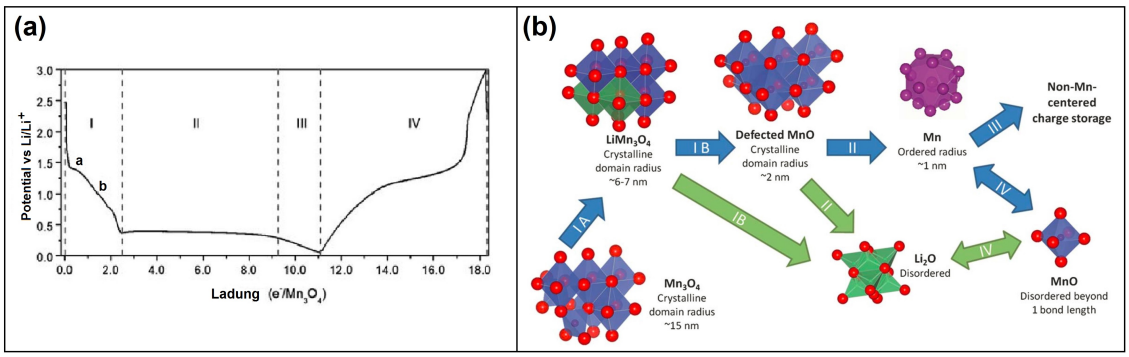

Abbildung 1.8: (a) Potentialverläufe des 1.Zyklus bei der De-/Lithiierung von Mn_3O_4. Der Verlauf während der Lithiierung wurde in drei Bereiche I bis III aufgeteilt. Bereich IV entspricht dem Delithiierungsvorgang. (b) Schema des Reaktionsmechanismus mit den beobachteten auf Manganbasierten Verbindungen. Aus [131].

Mn_3O_4 übertrifft mit einer hohen reversiblen Kapazität von $703\,\text{mA h g}^{-1}$ und einem niedrigen Redoxpotential um 0,3 V Graphit in Bezug auf die gravimetrische Energiedichte bei weitem. Um die Anwendungsreife als Anodenmaterial in kommerziellen LIBs zu erreichen, gilt es jedoch dessen extrem niedrige elektrische Leitfähigkeit (10^{-7} - $10^{-8}\,\text{S cm}^{-1}$) und die schlechte Zyklenstabilität aufgrund der starken Volumenänderung von über 170 % [132] bei der De-/Lithiierung zu überwinden. Zur Verbesserung der elektrochemischen Performance

von Mn_3O_4 als Anodenmaterial wurden verschiedene Ansätze verfolgt, wie die Modifikation der Morphologie und die Herstellung von Kompositen mit Kohlenstoffallotropen. Huang et al. [133] untersuchte den Einfluss der Partikelgröße an verschiedenen Mn_3O_4-Nanooktaeder mit Abmessungen zwischen 40 nm und 350 nm. Die Ergebnisse zeigen einen klaren Zusammenhang zwischen der Partikelgröße und den elektrochemischen Eigenschaften. Je kleiner die Größe der Nanooktaeder und somit größer deren Oberfläche ist, desto höher ist die elektrochemische Aktivität und Hochstromfähigkeit. So erzielen die kleinsten Mn_3O_4-Nanooktaeder mit spezifischen Kapazitäten um 800 mAhg, 500 mA h g^{-1} und 350 mA h g^{-1} bei einer Stromdichte von jeweils 50 mA g^{-1}, 100 mA g^{-1} und 500 mA g^{-1}die höchsten Werte. Aufgrund des stetigen Kapazitätsverlusts, den sie erleiden, bleibt jedoch nach 50 Zyklen bei 50 mA g^{-1} weniger als die Hälfte der Kapazität des ersten Delithiierungszyklus erhalten. Bai et al. [134] synthetisierten mesoporöse Mn_3O_4-Nanoröhrchen mit hervorragender Zyklenstabilität, die über 100 Zyklen bei 500 mA h g^{-1}eine stabile reversible Kapazität um 500 mA h g^{-1}liefert. In den letzten Jahren wurden zahlreiche Komposite von Mn_3O_4mit verschiedensten Kohlenstoffmodifikationen, wie amorphen Kohlenstoff [135–138], Graphen[139–142], reduziertes Graphenoxid [129, 143, 144], Graphit [145, 146], CNTs [59, 147, 148], entwickelt. Erst kürzlich berichteten Cao et al. [149] von einem Komposit, bestehend aus CNTs auf deren Oberfläche Mn_3O_4-Partikel angelagert sind. Es erreicht hohe spezifische Kapazitäten und zeigt ein stabiles Zyklierverhalten; selbst nach 200 Zyklen beträgt die reversible Kapazität 895 mA h g^{-1} bei 500 mA g^{-1}. Wie REM- und TEM-Aufnahmen der zyklierten Elektrode zeigen, ist dies auf die strukturelle Stabilität des Komposits zurückzuführen. Durch die Anlagerung auf die Oberfläche der CNTs kann eine Aggregation der Mn_3O_4-Nanopartikel verhindert werden.

Binäre Übergangsmetalloxide

Neben konversionsbasierten einfachen Übergangsmetalloxide gelten binäre Übergangsmetalloxidverbindungen ebenfalls als vielversprechende Anodenmaterial für LIB [97, 150]. Sie profitieren von der Komplementarität und dem synergetischen Effekt der Mischung zweier Übergangsmetalloxide, die nach der ersten vollständigen Delithiierung vorliegt und das ursprüngliche binäre Metalloxid ersetzt [97, 151]. Zu diesen gehört unter anderem Kobaltferrit $CoFe_2O_4$, das in einer Spinellstruktur der Raumgruppe $Fd\overline{3}m$ kristallisiert. Das größte Interesse der Forschung gilt seiner magnetischer Eigenschaften, wie großer magnetokristallinen Anisotropie und hoher Koerzitivität und Magnetostriktion [152]. Es findet unter anderem Verwendung in der Nanotechnologie als Material für hochkapazitive Magnetspeicher. Erstmals im Jahr 2004 berichteten Alcantaara et al. [153] von seinem potenziellen Nutzen als Anodenmaterial in LIBs. Kurz darauf ist es Chu et al. [154] gelungen, mittels *ex-situ* XPS und

XRD-Studien die zugrunde liegenden Reaktionen der Li^+-Ionen-Speicherung aufzuklären.

$$\text{(A)}\ \ CoFe_2O_4 + 8\,Li^+ + 8\,e^- \longrightarrow 4\,Li_2O + 2\,Fe + Co \qquad Q_{th} = 914\,mA\,h\,g^{-1}$$

$$\text{(B)}\ \ 4\,Li_2O + 2\,Fe + Co \rightleftarrows Fe_2O_3 + CoO + 8\,Li^+ + 8\,e^- \qquad Q_{th} = 914\,mA\,h\,g^{-1}$$

In-situ XRD- und *ex/in-situ* Röntgenabsorptionsspektroskopie (engl. X-ray absorption spectroscopy, XAS) von Permien et al. [155] liefern einen tieferen Einblick in die Prozesse, die während der Konversion ablaufen, und führen damit zu einem besseren Verständnis des Speichermechanismus von $CoFe_2O_4$. Sie beobachten zum einen während der Lithiierung die Umwandlung der ursprünglichen Spinellstruktur der Raumgruppe $Fd\bar{3}m$ in eine NaCl-Struktur der Raumgruppe $Fm\bar{3}m$, bei der die Kationen von den Tetraeder-Plätzen zu benachbarte leere Oktaeder-Plätzen wandern (Abb. 1.9 a). Außerdem weisen sie nach, dass nach der Lithiierung nanoskalierte metallische Co- und Fe-Partikel vorliegen, die in einer Li_2O-Matrix eingebettet sind, und nach der Delithiierung zu Co^{2+} und Fe^{3+} oxidiert sind (Abb. 1.9 b). Sie identifizieren zudem als eine Ursache für Kapazitätsverluste die Abnahme der Oxidation von Co^0 zu Co^{2+}, wohingegen die Reaktion $Fe^0 \rightleftarrows Fe^{3+}$ über viele Zyklen reversibel abläuft (Abb. 1.9 b).

Aufgrund der hohen theoretischen Kapazität von $918\,mA\,h\,g^{-1}$bei der Speicherung von $8\,Li^+$-Ionen ist $CoFe_2O_4$ auf großes Interesse in der Batterieforschung gestoßen. Die Ergebnisse der Untersuchungen von Chu et al. [154] verdeutlichen, dass durch Nanoskalierung die elektrochemischen Eigenschaften, insbesondere die Zyklenstabilität, von $CoFe_2O_4$ signifikant verbessert werden kann. Nach einer initialen Delithiierungskapazität von $910\,mA\,h\,g^{-1}$ bei 1 C stabilisiert sich der Wert nach 20 Zyklen auf $610\,mA\,h\,g^{-1}$. Die Untersuchungen von Lavela et al. [156] zeigen einen klaren Zusammenhang zwischen Synthesebedingungen,

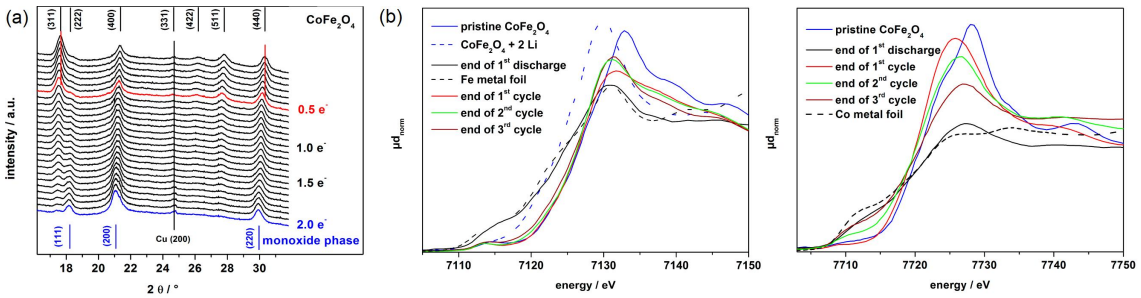

Abbildung 1.9: (a)*In-situ* Röntgendiffraktogramme von $CoFe_2O_4$ während der Einlagerung von $2\,Li^+$-Ionen. (b) *Ex-situ* XAS-Scans an der Fe K-Kante (links) und an der Co K-Kante (rechts) von unzykliertem $CoFe_2O_4$ jeweils nach der ersten Lithiierung und nach ein, zwei und drei Zyklen zusammen mit Spektren von metallischen Fe- bzw. Co-Folien zum Vergleich. Nach [155].

Morphologie und elektrochemischer Perfomance. So zeigen geschichtete flockenartige Aggregate, die ein makroporöses System bilden, die beste Zyklenstabilität und erreichen bei 1 C nach 75 Zyklen noch bis zu 739 mA h g^{-1}. $CoFe_2O_4$ mit dreidimensionaler makroporöser Struktur liefert bei 0,2 mA cm^{-2} in den ersten Zyklen zwar sehr hohe Kapazitäten über 1000 mA h g^{-1}, allerdings zeigen sich bereits nach 30 Zyklen Verluste von über 40 % [157]. REM-Aufnahmen einer zyklierten Elektrode zeigen, dass die Struktur der mechanischen Belastung aufgrund der starken Volumenänderungen während der De-/Lithiierung nicht standhalten konnte und zerbrochen ist. Weitere Morphologien, die untersucht wurden, sind unter anderem Nanostäbchen [158], hierarchisch strukturierte Mikrosphären [159] oder hohle Nanosphären [160]. Die Ergebnisse der Untersuchungen von Wu et al. [161] an reinen $CoFe_2O_4$-Fäden sowie einem Komposit mit Kohlenstoff demonstrieren, dass durch den Verbund mit Kohlenstoff die Zyklenstabilität und Hochstromfähigkeit verbessert werden kann. Letzteres ist auf den geringeren Ladungstransferwiderstand der $CoFe_2O_4$/C-Elektrode zurückzuführen, wie impedanzspektroskopische Untersuchungen zeigen. Ren et al. [162] ist es gelungen durch Einkapselung von $CoFe_2O_4$ in Kohlenstofffäden die Agglomeration der bei der elektrochemischen Zyklierung entstandenen metallischen Nanopartikel zu verhindern, wie *ex-situ* XRD-Studien bestätigen. Dies resultiert in einer hervorragenden Zyklenstabilität des $CoFe_2O_4$/C-Komposits mit spezifischen Kapazitäten über 700 mA h g^{-1} nach 250 Zyklen bei 100 mA g^{-1}. Zhang et al. [163] untersuchten verschiedene Komposite mit Kohlenstoffnanoröhren. Im Vergleich zu den $CoFe_2O_4$-Nanosphären, die lediglich mit CNTs vermischt wurden, zeigen sich bei Verknüpfung mit CNTs bessere elektrochemische Eigenschaften, wie eine höhere Kapazität und Zyklenstabilität. Nach über 100 Zyklen bei 200 mA g^{-1} liefern sie eine Kapazität von 1045,6 mA h g^{-1}, was 93 % der Kapazität des ersten Delithiierungszyklus entspricht. Der zusätzliche Beitrag, der zu einer spezifischen Kapazität führt, die den theoretischen Wert übertrifft, beruht auf pseudo-kapazitiver Ladungsspeicherung. REM-Aufnahmen zyklierter Elektroden demonstrieren, dass die CNTs die strukturelle Stabilität verbessern; so ist ursprüngliche Struktur des verknüpften $CoFe_2O_4$/CNT-Komposits auch nach 100 Ent-/Ladezyklen noch erhalten. Für reine $CoFe_2O_4$-Nanosphären wird hingegen nach 50 Zyklen ein deutliches Größenwachstum beobachtet, was deren schlechte Zyklenstabilität erklärt.

Legierungsbildende Übergangsmetalloxide

Nach einer Abschätzung von Badway et al. [164] können konversionsbasierte Materialien in Bezug auf die Energiedichte nur dann mit Graphit konkurrieren, wenn sie unter Annahme eines initialen Kapazitätsverlustes von 25 % spezifische Kapazitäten um 1000 mA h g^{-1} liefern und bei Potentialen unter 0,6 V mit Lithium reagieren. Im Gegensatz zu den meisten Konversionsmaterialien werden diese Bedingungen von legierungsbildenen Verbindungen

erfüllt. So beträgt beispielsweise die theoretische Kapazität von Silizium bei der Bildung von $Li_{15}Si_4$ 3579 mA h g^{-1} bei einem Potential unter 0,4 V gegen Li/Li$^+$. Die dabei auftretenden erheblichen Volumenänderung bei der De-/Lithiierung von bis zu etwa 300 % [165] hat ihre Anwendung in kommerziellen LIBs bisher ausgeschlossen. Ein vielversprechender Ansatz ist es, die beiden Speichermechanismen zu kombinieren und statt der reinen Metalle die entsprechenden Oxide zu verwenden, sodass bei der Lithiierung zunächst eine Konversionreaktion abläuft bei der sich metallische Nanopartikel und Li_2O bilden und anschließend die metallischen Nanopartikel mit Lithium eine Legierung eingehen. Die Idee basiert auf dem Konzept, dass das bei der Konversionreaktion entandene Li_2O eine elektrochemisch inaktive Matrix bildet. Diese dient einerseits als Puffer für die bei der nachfolgenden Legierungsbildung auftretenden Volumenänderungen und und zum anderen als Haftmittel für die metallischen Nanopartikel, um deren Aggregation zu verhindern [166]. Die Reversibiltät der Konversionsreaktion ist abhängig von der Größe der Übergangsmetallpartikel und ist daher nicht mehr gegeben, wenn diese aggregieren [13], da die Rückbildung von Li_2O nur ablaufen kann, wenn die metallischen Nanopartikel ein leitfähiges Netz bilden [167].

Ein bekannter Vertreter dieser Klasse, der in den letzten Jahren in der Forschung große Beachtung erfahren hat, ist ZnO. Fu et al. [168] gelang es erstmals im Jahr 2007 mit Hilfe von *ex-situ* XRD-Studien den Speichermechanismus von ZnO nachzuweisen und die zuvor angenommene Irreversibilität der Konversionreaktion zu widerlegen [169].

(A) $ZnO + 2\,Li^+ + 2\,e^- \rightleftarrows Li_2O + Zn$ $\qquad Q_{th} = 659\,\text{mA h g}^{-1}$

(B) $Zn + Li^+ + e^- \rightleftarrows LiZn$ $\qquad Q_{th} = 329\,\text{mA h g}^{-1}$

Auch anschließende Untersuchungen anderer Forschungsgruppen mittels *ex/in-situ* XRD [170, 171] und *ex/in-situ* XAS [172, 173] bestätigen die Reversibilität der Konversionreaktion, allerdings nur für die ersten Zyklen. *In-situ* TEM-Studien zeigen, dass die Li_2O-Matrix nicht, wie angenommen, die sukzessive Aggregation der metallischen Nanopartikel verhindern kann, sondern sich große Zink-Partikel mit einer Größe von bis zu einigen hundert Nanometern bilden [174, 175]. Basierend auf den Untersuchungen von Park et al. [172] ist die Reversibilität der Konversionsreaktion jedoch nur für Partikelgrößen unter 3 nm gewährleistet.

Ein erfolgreicher Ansatz, um diese Problematik zu lösen und gleichzeitig die geringe elektronische Leitfähigkeit von ZnO zu überwinden ist der Verbund von nanoskaligen ZnO-Partikel mit Kohlenstoff [172]. Im Gegensatz zu reinem ZnO, das trotz einer initialen spezifischen Delithiierungskapazität um 600 mA h g^{-1} bei 100 mA g^{-1} bereits nach 50 Zyklen nahezu keine Ladung speichert, liefert das ZnO/C-Komposit selbst nach 200 Zyklen 570 mA h g^{-1},

was einem Kapazitätserhalt von 81 % gegenüber dem ersten Zyklus entspricht. Neben Kompositen mit amorphen Kohlenstoff [176–178] wurden weitere Kohlenstoffmodifikationen, wie CNTs [179, 180], Graphit [181] und Graphen [182–184], entwickelt.

Kapitel 2

Interkalationsverbindung

Li_3VO_4

2.1 Hydrothermal microwave-assisted synthesis of Li_3VO_4 as an anode for lithium-ion battery

Autoren:

G.S. Zakharova, E. Thauer, S.A. Wegener, J.-H. Nölke, Q. Zhu, R. Klingeler

veröffentlicht in Journal of Solid State Electrochemistry 23, 2019, 2205-2212

abgedruckt mit freundlicher Genehmigung des Springer Nature Verlags

E. Thauer führte die Rasterelektronenmikroskopie (REM) sowie alle elektrochemischen Messungen und deren Analyse gemeinsam mit den Bachelorstudenten S.A. Wegener und J.-H. Nölke unter ihrer Anleitung durch. E. Thauer konzipierte und verfasste die zugehörigen Teile des Manuskripts und erstellte die Abbildungen Abb. 5 und Abb. S1 - S3. E. Thauer übernahm die Gesamtkorrektur des Manuskripts und war an der Finalisierung beteiligt. Die Korrespondenz mit den Gutachtern sowie die Überarbeitung des Manuskripts wurde von E. Thauer zusammen mit G.S. Zakharovs und R. Klingeler übernommen.

G.S. Zakharova ist die Erst- und Korrespondenzautorin dieses Artikels. G.S. Zakharova konzipierte und verfasste das Manuskript mit Ausnahme der Teile zu den elektrochemischen Untersuchungen und erstellte die Abb. 1 - 4. Die Synthese der Materialien, die Analyse der XRD-Daten und die BET-Messung erfolgten von G.S. Zakharova. Q. Zhu führte die Transmissionelektronenmikroskopie (TEM) durch. R. Klingeler betreute das Projekt, stand beratend zur Seite und war an der Finalisierung des Manuskripts beteiligt. Alle Autoren haben das Manuskript korrekturgelesen.

Journal of Solid State Electrochemistry (2019) 23:2205–2212
https://doi.org/10.1007/s10008-019-04315-4

ORIGINAL PAPER

Hydrothermal microwave-assisted synthesis of Li_3VO_4 as an anode for lithium-ion battery

G. S. Zakharova[1] · E. Thauer[2] · S. A. Wegener[2] · J.-H. Nölke[2] · Q. Zhu[3] · R. Klingeler[2,4]

Received: 6 March 2019 / Revised: 3 May 2019 / Accepted: 3 June 2019 / Published online: 17 June 2019

Abstract

Li_3VO_4 with various morphologies has been synthesized by a microwave-assisted hydrothermal method. It is shown that the crystal size and morphology of Li_3VO_4 are determined by the type of solvent in the reaction solution and possible reasons of the solvent-type effect are discussed. Electrochemical studies of as-prepared Li_3VO_4 as anode materials for Li-ion batteries demonstrate a clear influence of the materials' morphology and surface properties on the electrochemical performance. Li_3VO_4 nanocrystals with a porous structure exhibit an enhanced electrochemical activity with an initial discharge capacity of 163 mAh g^{-1}.

Keywords Li_3VO_4 · Hydrothermal synthesis · Anode material · Lithium-ion batteries

Introduction

Lithium-ion rechargeable batteries have high current and power densities compared with other rechargeable batteries. The major challenges in designing next-generation lithium-ion batteries (LIB) include the need to increase their energy density, cycling life, and charge/discharge rate capability. This demands the design of improved electrode materials with favored properties, e.g., fast Li-ion diffusion and small volume changes upon electrochemical cycling [1]. In this respect, among the different reaction mechanisms, intercalation-type anodes are particularly promising [2, 3]. The commercially widely used graphite features a high theoretical capacity of 372 $mAhg^{-1}$ [4, 5]. However, it exhibits a low voltage plateau (below 0.3 V vs. Li/Li^+) near to the potential to that of deposition of Li metal which involves the risk of dendrite formation [6]. Alternative materials LIBs are $Li_4Ti_5O_{12}$ and TiO_2. In particular, the spinel $Li_4Ti_5O_{12}$ is used in niche applications as it can accommodate three Li-ions with a, however, low theoretical specific capacity of 175 $mAhg^{-1}$ at a flat potential of 1.55 V [7, 8]. TiO_2 demonstrates double theoretical specific capacity (335 $mAhg^{-1}$ at $x = 1$ in Li_xTiO_2) and high Li insertion potential (1.5–1.8 V vs. Li/Li^+) [9]. However, the maximum value of Li insertion is limited to $x = 0.5$, corresponding to the theoretical capacity of 167.5 $mAhg^{-1}$ [10]. Additionally, this material has low electrical conductivity and poor cycling performance. Good electrochemical performance was reported for elongated TiO_2 nanostructures such as rods or tubes [11, 12]. Due to high aspect ratio and porous morphology, TiO_2 nanostructures allow efficient transport of lithium ions and a high charge/discharge capacity (about 250 $mAhg^{-1}$).

Recently, lithium orthovanadate, Li_3VO_4, has been suggested as another promising intercalation-type anode material for lithium-ion batteries [13–19]. In comparison with graphite, $Li_4Ti_5O_{12}$, and TiO_2, lithium orthovanadate could be intercalated by Li-ions in the voltage range of 0.2–1.0 V (vs. Li/Li^+). Its high working voltage offers a save operating potential and allows to effectively avoid the deposition of lithium metal on the electrode. In addition, it demonstrates a large theoretical reversible specific capacity comparable to that of graphite (394 $mAhg^{-1}$) corresponding to $x = 2$ in $Li_{3+x}VO_4$. Low

Electronic supplementary material The online version of this article (https://doi.org/10.1007/s10008-019-04315-4) contains supplementary material, which is available to authorized users.

✉ G. S. Zakharova
gszakharova@mail.ru

[1] Institute of Solid State Chemistry, Ural Division, Russian Academy of Sciences, Yekaterinburg, Russia

[2] Kirchhoff Institute of Physics, Heidelberg University, Heidelberg, Germany

[3] School of Material Science and Engineering, Wuhan University of Technology, Wuhan, China

[4] Centre for Advanced Materials, Heidelberg University, Heidelberg, Germany

and safe voltage combined with a large specific capacity permit to claim that Li_3VO_4 might play a promising role as a new insertion anode for LIB.

There are two known Li_3VO_4 polymorphs: the low-temperature β-form and the high-temperature γ-form. Its crystal structure belongs to the Li_3PO_4-type which is composed of a 3D network of corner-sharing LiO_4 and VO_4 tetrahedrons (Fig. 1). The empty sites of the crystalline framework generate straight channels along the *a*- and *c*-axes, and zigzag channels along the *b*-axis, both of which providing potential intercalation paths for Li-ions.

Various methods have been attempted to synthesize Li_3VO_4, including solid-state reaction [14, 20, 21], hydrothermal [22–24], aerosol spray [25], sol-gel [26, 27], precipitation [20], and self-template [28] methods. Solid-state synthesis and precipitation are the most conventional and widely used chemical syntheses. Nevertheless, they lead to broad particle size distributions of the final product. Besides, it is hard to prevent the agglomeration of the primary nanoparticles, which may cause poor electrochemical performance. Whereas, sol-gel and conventional hydrothermal methods can promote precursors to achieve mixing and homogenizing up to the nanometer level. Both procedures, however, usually require a long and time-consuming sintering process. Similarly, as the aerosol spray method is also costly in terms of time and requires sophisticated equipment, it is not advantageous for large-scale production. Compared with conventional methods, hydrothermal microwave-assisted synthesis is quite faster, simpler, and more energy-efficient providing the production of the final product with a smaller particle size and improving its electrochemical performance [29].

In this paper, the hydrothermal microwave-assisted route is introduced to synthesize Li_3VO_4. The study is focused on the results of the structure, morphology, and electrochemical performance of Li_3VO_4.

Experimental

The starting materials used in the experiment were of analytical grade and purchased from Sigma–Aldrich. In a typical procedure, 0.234 g NH_4VO_3 and 0.252 g $LiOH{\cdot}H_2O$ (the molar ration of NH_4VO_3 to $LiOH{\cdot}H_2O$ = 1:3) were dissolved in 30 ml distilled water. After stirring for 20 min, the clear solution was poured into a sealed glass vial and then transferred into a microwave reactor (Monowave 300, Anton Paar). On a ramping time of 10 min, the vial was heated at 180 °C, held at this temperature for 20 min, and cooled by compressed air up to 40 °C. The product was collected by centrifugation and washed with deionized water several times. The as-prepared material is labeled as Li_3VO_4-W. For the purpose of comparison, Li_3VO_4 was also prepared in an ethanol-assisted route using a volume ratio of C_2H_5OH to H_2O = 1:1. The resulting material is denoted as Li_3VO_4-E. To investigate the effect of pounding on the electrochemical activity, Li_3VO_4-E powder was grinded using a mortar for 15 min; this sample is labeled as Li_3VO_4-E(G).

The structure and morphology of the resulting product were characterized by X-ray powder diffraction (Shimadzu XRD-7000S, Cu K_α radiation, $\lambda = 1.540$ Å), ZEISS Leo 1530 scanning electron microscopy (SEM), and JEOL JEM 2100 *transmission electron microscopes* (TEM). The specific surface area and pore volume of the samples were measured by a surface area and porosity analyzer (Gemine VII, Micromeritics).

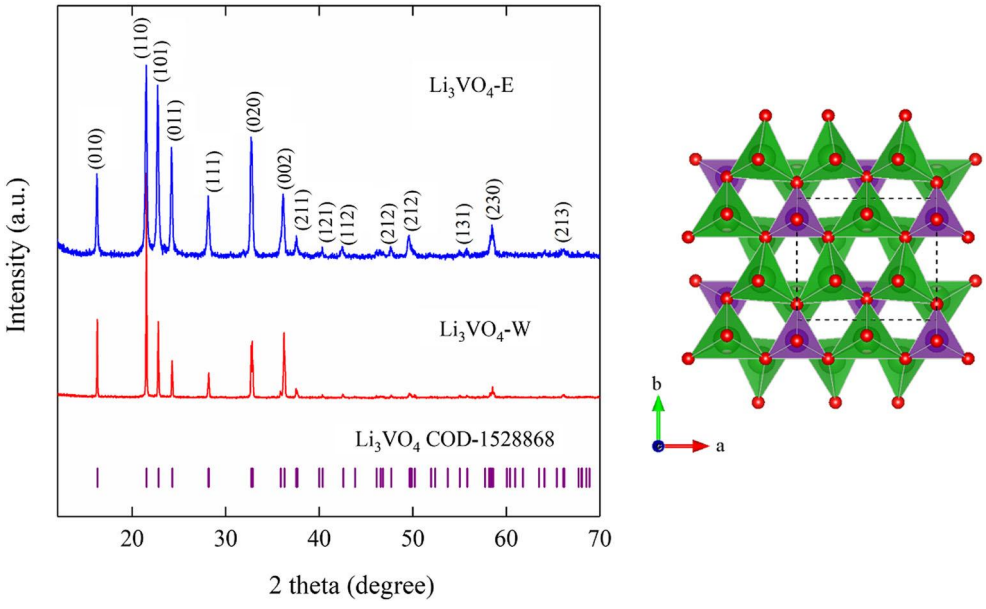

Fig. 1 XRD patterns of Li_3VO_4 synthesized in the presence of ethanol (blue line), in water without ethanol (red line), and the expected Bragg positions for the Li_3VO_4 structure (left). Crystal structure of Li_3VO_4 along (001) direction (right). Oxygen atoms are denoted by red balls, and LiO_4 and VO_4 tetrahedra are marked by green and violet color, respectively

Electrochemical studies were performed in Swagelok-type two electrode cells using a VMP3 potentiostat (Bio-Logic SAS) at 25 °C (see [30]). The working electrodes were prepared by mixing Li_3VO_4, carbon black (Timcal), and polyvinylidene fluoride binder (PVDF, Solvay Plastics) dissolved in N-methyl-2-pyrrolidone (NMP, Sigma–Aldrich) in a weight ratio of 75:20:5. In order to ensure a homogeneous distribution, the mixture was stirred for at least 12 h. Afterwards, most of the NMP was evaporated to obtain a spreadable slurry that was applied on circular Cu-meshes with a diameter of 10 mm. The electrodes were dried in a vacuum oven at 80 °C, mechanically pressed with 8 MPa, and then dried again. The loading density was about 2 mg cm^{-2}. As counter electrode, a lithium metal foil disk (Alfa Aesar) pressed on a nickel current collector was used. Both electrodes were separated by two layers of glass fiber separator (Whatman GF/D), which was soaked with 200 μl electrolyte (Merck Electrolyte LP30), a 1 M $LiPF_6$ salt solution in 1:1 ethylene carbonate (EC) and dimethyl carbonate (DMC). The cells were assembled in a glove box under an argon atmosphere ($O_2/H_2O < 5$ ppm).

Results and discussion

Lithium orthovanadate, Li_3VO_4, was synthesized by the following reaction:

$$3LiOH + NH_4VO_3 \rightarrow Li_3VO_4 + NH_3 + 2H_2O. \quad (1)$$

In Fig. 2, the XRD pattern of the material prepared using pure water as solvent (marked W) is shown in comparison to the one synthesized in the presence of ethanol (marked E). All diffraction peaks of the patterns can be indexed in the orthorhombic β-Li_3VO_4 phase with the space group $Pnm2_1$ according to the standard pattern of COD-1528868. Lattice parameters determined by means of full-profile analyses with the FullProf Suite are in a good agreement with reference data (Table S1). As shown in Fig. 1, Li_3VO_4-W exhibits sharper diffraction peaks which we associate to the larger crystal size in comparison with samples synthesized in the presence of ethanol. The crystallite sizes of the as-synthesized samples are calculated using Scherrer equation:

$$D = K\lambda/\Delta(2\theta)\cos\theta, \quad (2)$$

where D is the average grain size based on the particular reflecting crystal face (hkl) direction, K is a shape factor which can be approximated to 0.93, λ is the wavelength of the applied Cu Kα radiation, $\Delta(2\theta)$ is the full width at half-maximum of the diffraction peak, and θ is the Bragg angle. The analysis of the 110 and 101 peaks yields average crystallite sizes of 68 ± 5 nm for both Li_3VO_4-E and Li_3VO_4-E(G) samples. In contrast, Li_3VO_4-W is a bulk material with an average crystallite size of more than 100 nm which renders Scherrer's formula non-applicable. This indicates that the crystal size decreases with the addition of ethanol to the reactive system.

The influence of the solvent type on the morphology of the synthesized samples is further examined by SEM as illustrated in Fig. 2. As shown in Fig. 2a, Li_3VO_4-W which is hydrothermally synthesized with water as solvent mainly possesses irregular aggregates. Some particles exhibit a truncated tetragonal pyramid-like shape with sharp corners and well-defined edges of 1–4 μm in length. These particles show smooth surfaces. In the presence of ethanol as solvent in the reactive system, self-assembled hierarchical porous microspheres with a size of around 1 μm are formed (Fig. 2b). The surface of Li_3VO_4-E is very rough and consists of numerous flake-like nanoparticles which sizes range from 40 to 200 nm. Between these particles, the large holes are distinctly exhibited (Fig. 2c). Similar Li_3VO_4 particles of sphere-like shape have been also fabricated with the usage of ethanol as solvent under conventional hydrothermal conditions by other researchers [31]. As seen in Fig. 2d, grinding of Li_3VO_4-E yields breaking of the sphere-like particles and formation of weakly agglomerated of about 50–70-nm-sized nanocrystals (Li_3VO_4-E(G)). Note that according to Scherrer's analysis, it does not significantly affect the primary particles size but mainly affects agglomerates.

Additionally, TEM investigation was applied to further study the morphology of Li_3VO_4-E in detail. As shown in a low-magnification TEM image in Fig. 3a, the Li_3VO_4-E compounds are composed of sphere-like microparticles which size ranges from 0.9 to 1.5 μm. As seen, these particles show uneven surfaces with cavities. The high-resolution TEM (HRTEM) image of Li_3VO_4-E in Fig. 3b exhibits lattice fringes with spacing of 0.35 nm, which corresponds well with the (011) plane of the orthorhombic Li_3VO_4.

Our data highlight the crucial role of solvent in the synthesis process. The morphology of samples prepared using a mixture of water and ethanol as solvents significantly differs from that of Li_3VO_4 synthesized in H_2O only. It is known that the polarity and the saturated vapor pressure of the solvents during the hydrothermal (solvothermal) treatment are relevant solvent parameters which determine the morphology and size of the final product [32]. The polarity of the solvent is proportional to the dielectric constant, which for water and alcohol is 80.1 and 25.3 at 25 °C, respectively [33]. Chen et al. have determined the correlation between particle size and dielectric constant of alcohol/water solution [34]. There is a linear relationship between the reciprocal of particle size and the reciprocal of the dielectric constant for various kinds of alcohols which implies that the polarity of the solvents affects the nucleation rate and particle size of the prepared nanoparticles. In general, more polar solvents facilitate nucleation and tend to result in bigger particles according to the Ostwald ripening

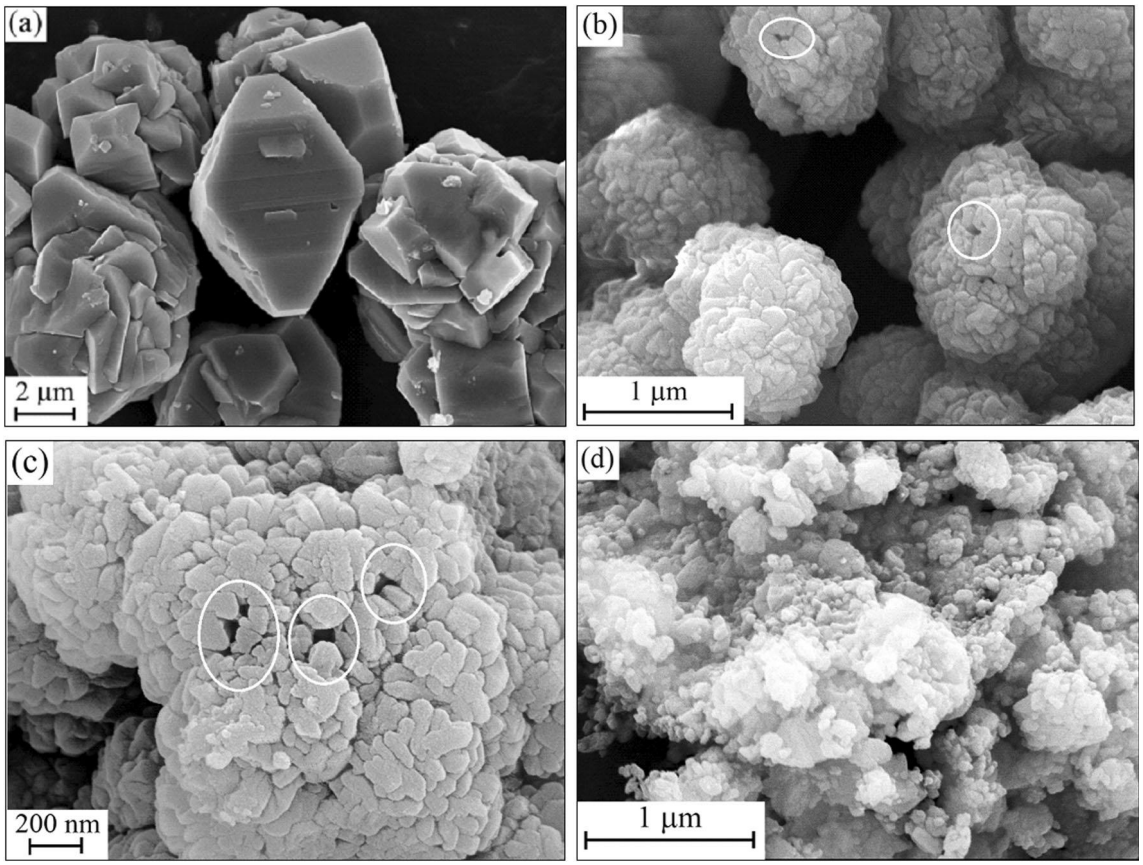

Fig. 2 SEM images of Li_3VO_4-W (**a**), Li_3VO_4-E at low (**b**) and high (**c**) magnifications, and Li_3VO_4-E(G) (**d**). Large holes in Li_3VO_4-E particles are shown by white circles

process [35]. The saturated vapor pressure influences not only the nucleation of the crystals but also the morphology of the materials since it is inversely proportional to the boiling point of the solvents [36]. For water and ethanol at ambient pressure, the boiling points of water and ethanol amount to 100 and 78.29 °C, respectively [33]. Accordingly, larger Li_3VO_4 crystals with faceted morphologies were obtained in water which possesses lower vapor pressure. This implies that the lower saturated vapor pressures assist more rapid growth of the Li_3VO_4 nuclei, resulting in larger particles. In contrast, the saturated vapor pressure of ethanol is high, so that growth of the Li_3VO_4 nuclei is limited, leading to the predominant nucleation of nanosized particles. Aggregation of these nanoparticles to the observed clusters and assemblies of various morphology takes place to reduce the overall surface area and thus to lower the surface energy of the compound.

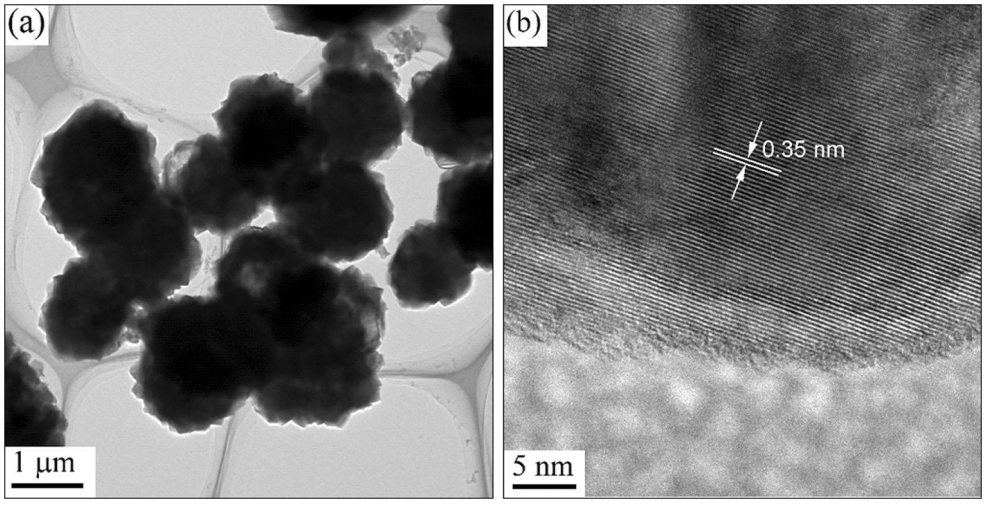

Fig. 3 (**a**) TEM and (**b**) HRTEM images of Li_3VO_4-E

In addition to size of primary and secondary particles, electrochemical activity of a material is influenced by surface properties such as specific surface area and pore size distribution. Both properties have been investigated on the Li_3VO_4 samples at hand by physisorption of nitrogen using the Brunauer–Emmett–Teller (BET) method. The specific surface area, average pore size, and total pore volumes for the samples are summarized in Table S1, indicating that the use of different solvents has substantial effects on the textural properties of the materials. The nitrogen adsorption–desorption isotherms of Li_3VO_4-W (data not shown) imply a very low surface area of roughly 0.02 $m^2\ g^{-1}$ as expected for a typical bulk material with a non-porous structure. The similar value of the specific surface was obtained by G. Yang et al. [22]. In contrast, application of ethanol as solvent during the hydrothermal treatment increases the specific surface area of the sample to 2.36 $m^2\ g^{-1}$. Additionally, grinding of Li_3VO_4-E further increases the BET surface area by nearly four times (8.91 $m^2\ g^{-1}$). According to the classification of IUPAC [37], sorption isotherms (Fig. 4a) obtained on Li_3VO_4-E prepared with ethanol as solvent feature a type IV behavior with a type H3 hysteresis, which is a characteristic for particles with rather uniform particle size distribution and a slit-shaped mesoporous structure. Analysis of the pore size distribution (Fig. 4b) shows that both Li_3VO_4-E and Li_3VO_4-E(G) samples exhibit a wide pore size distribution from 2 to more than 120 nm. Li_3VO_4-E mainly features mesopores which sizes are centered at around 11 and 17 nm. Grinding, which yields the abovementioned partial breaking of agglomerates, also affects the porosity: the pore-size distribution of Li_3VO_4-E(G) is rather broad and has two distinct maxima. One of which is associated with mesopores of about 5 nm. According to the literature, these pores may be attributed to the presence of interstices between the primary particles [38]. The larger pores (concentrated around ~ 36 nm) of Li_3VO_4-E(G) are supposed to result from aggregation of the nanosized crystals. To summarize, the obtained textural parameters show that use of ethanol as solvent and grinding of the final product yields increase of surface area and porosity which both may enhance applicability of the materials for electrodes in LIB.

In order to assess the effects of modified materials parameters on the electrochemical performance, Li_3VO_4-based electrodes have been investigated by means of cyclic voltammetry and galvanostatic cycling with potential limitation (GCPL) in the range 0.2–3.0 V. Figure 5 a shows the first, second, and tenth cycle of the cyclic voltammogram (CV) of Li_3VO_4-E recorded at a scan rate of 0.1 mV/s. The first reductive sweep shows a weak peak R_1 at 1.19 V and three pronounced ones at 0.67 V (R_2), 0.37 V (R_3), and at the lower limit 0.2 V (R_4). The peaks R_2 and R_3 can be assigned to intercalation of Li^+ into Li_3VO_4 [39]. During the first cycle, formation of the SEI contributes to the electrochemical activity in the same voltage range [23]. As of the second cycle, a shift of the peaks R_2 and R_3 to slightly higher potentials 0.82 V or rather 0.56 V is observable which is attributed to structural changes caused by an irreversible phase transformation during initial cycling [39, 40]. The first oxidative scan shows the main peak O_2 around 1.18 V, which corresponds to the delithiation of Li_3VO_4 [39], and a weak peak O_3 around 2.5 V. Upon further cycling, O_2 gets broader and the oxidation peak O_1 around 0.3 V shows up. The redox pair O_1/R_4 corresponds to the de−/lithiation processes related to carbon [41]. However, the underlying processes of the weak peaks R_1 and O_3 that are observed also by Ni et al. [23] remain unclear.

In order to investigate the cycling performance and rate capability of Li_3VO_4 with different morphologies, GCPL

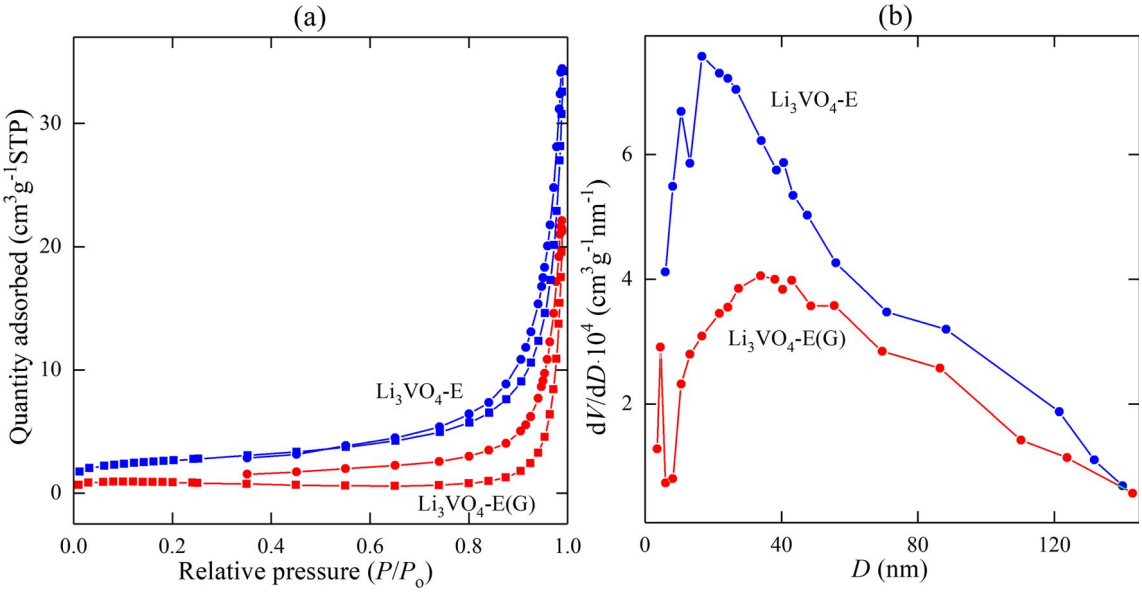

Fig. 4 (**a**) Nitrogen sorption isotherms and (**b**) corresponding pore size distribution curve of Li_3VO_4-E and Li_3VO_4-E(G) samples

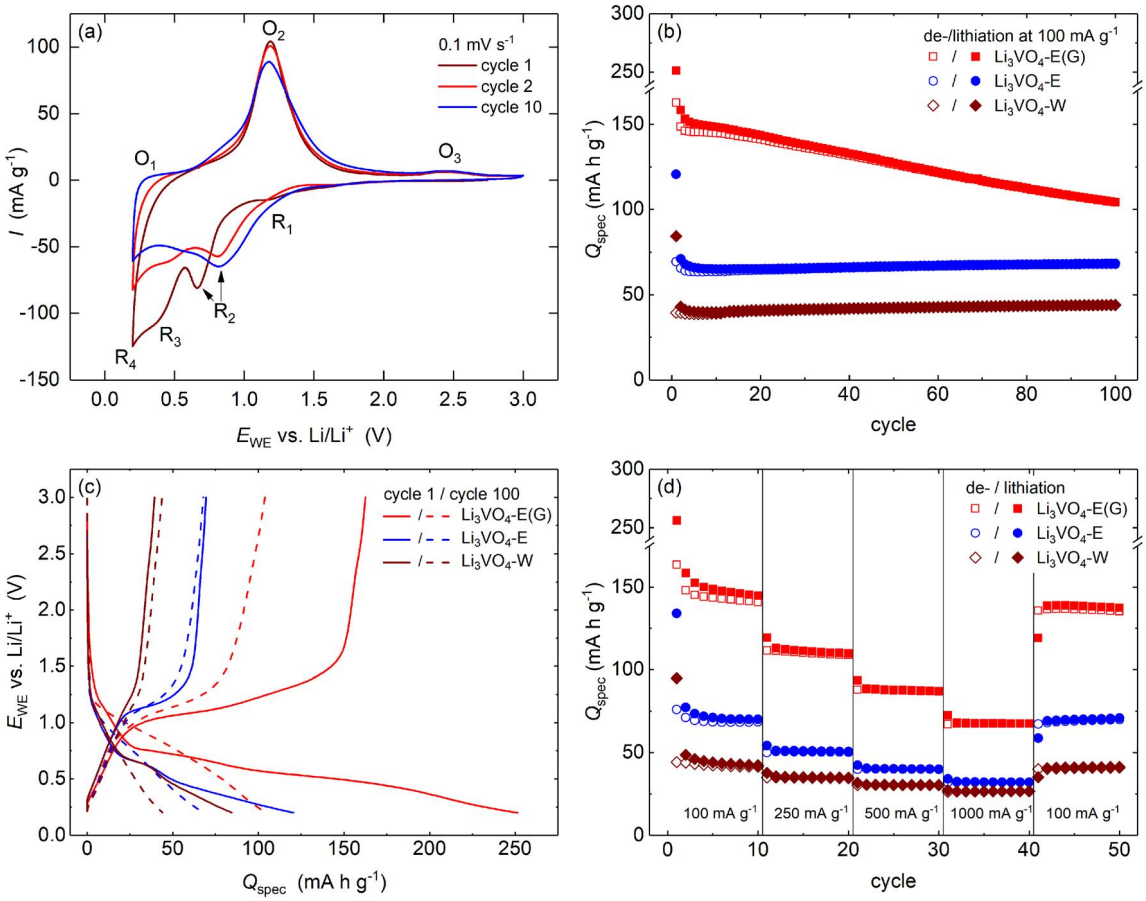

Fig. 5 (**a**) CV of Li_3VO_4-E studied at a scan rate of 0.1 mV s^{-1}. Specific charge/discharge capacities (**b**) and (**c**) potential profiles of the first and hundred cycles of Li_3VO_4-W, Li_3VO_4-E, and Li_3VO_4-E(G) for galvanostatic cycling at 100 mA g^{-1}. (**d**) Capability test with different cycling rates between 100 and 1000 mA g^{-1}

measurements have been performed. Figure 5 b shows the evolution of charge/discharge capacities during long-term measurements at a current density of 100 mA g^{-1} for 100 cycles. The belonging potential profiles in Fig. 5c exhibit plateaus corresponding to the peaks that are visible in the CV (Fig. 5a). For each sample, there is a large irreversible contribution in the first half cycle due to the SEI formation and structural changes [21, 39]. It is noticeable that the nanocrystals (Li_3VO_4-E(G)) reach the highest capacity over all cycles. In the first and the hundredth cycle, a charge capacity of 163 and 104 mAh g^{-1} is measured, respectively, while for the porous hierarchical microspheres (Li_3VO_4-E) just 69/68 mAh g^{-1} and for the bulk material with non-porous structure (Li_3VO_4-W) 39/44 mAh g^{-1} are reached. Comparing the samples that have been synthesized with and without ethanol shows that Li_3VO_4-E, which features more than 100 times larger surface, achieves about 60% higher capacity than Li_3VO_4-W. Grinding of sample Li_3VO_4-E results in a more than three times larger surface area and yields an increase of the capacity of around two times for Li_3VO_4-E(G). As expected, larger reaction surface leads to a higher electrochemical activity of Li_3VO_4 as on the one hand electrolyte diffusion is facilitated, and on the other hand, a large contact area with the conductive additive enables good electron transport pathway [22]. However, regarding the relative cycling stability, the grinded sample Li_3VO_4-E(G) delivers the least results with a discharge capacity loss of 36% between the first and hundredth cycle. In contrast, the other materials exhibit a more stable behavior. In case of Li_3VO_4-E, a small capacity loss of 1% and for Li_3VO_4-W even an increase of 13% is observable. The lower cycling stability of Li_3VO_4-E(G) may be attributed to huge charge depth yielding to structure damage caused by distortion and expansion upon cycling [21].

Furthermore, the rate capability of the different samples was studied at cycling rates between 100 and 1000 mA g^{-1}. The specific charge/discharge capacities are shown in Fig. 5d and the potential profiles in Fig. S1-S3. Again, the nanocrystals Li_3VO_4-E(G) show enhanced rate performance. Even at a high current density of 1000 mA g^{-1}, a discharge capacity of 67 mAh g^{-1} is still achieved, which is more than twice of that of the other materials. Moreover, it is observable that the capacity of Li_3VO_4-E(G), Li_3VO_4-E, and Li_3VO_4-W can regain to about 96%, 97%, and 95% when the current density returns to the initial value of 100 mA g^{-1}. Notably,

Table 1 Summary of the electrochemical performance of Li_3VO_4 electrodes prepared via different synthesis methods

Method	Current density 1 C ≈ 394 mA g^{-1} (mA g^{-1})/rate	Discharge capacity (mAh g^{-1})/cycle no.	Ref.
Solid-state reaction	20	283/25	[14]
Precipitation	1 C	190/100	[20]
Solid-state reaction	20	116/50	[21]
Hydrothermal	100	200/100	[22]
Aerosol-assisted	400	150/5	[25]
Hydrothermal	100	350/100	[31]
Solid-state reaction	20	143/50	[42]
Sol-gel	4000	52/1000	[43]
Sol-gel	30 C	160/60	[44]

in case of a constant current density of 100 mA g^{-1} (Fig. 5b), the capacity loss between cycle 41 and 10 is even larger (e.g., Li_3VO_4-E(G) 10%). This observation can be also traced back to higher degradation effects of a more comprehensive de−/lithiation process as it is in the case of lower cycling rates [21]. Table 1 illustrates the electrochemical performance of Li_3VO_4 prepared via different synthesis methods. It is obvious that the electrochemical performance of Li_3VO_4 mainly depends on morphological features as particle size and surface texture. These parameters determine the specific surface of the material which is related to the transport path lengths.

Conclusions

In conclusion, a facile and low-cost approach was developed for the synthesis of Li_3VO_4 with different morphology by means of the hydrothermal microwave-assisted method. In particular, using a mixture of water and ethanol used as solvent yields hierarchically structured Li_3VO_4 microspheres assembled from stacked nanoflakes, while without ethanol, the procedure yields a rather bulk-like material with micro-sized primary particles. The electrochemical performance of the produced materials highlights the relevance of hierarchical structure and morphology for application in LIB. In comparison with the Li_3VO_4 bulk material, the hierarchical sphere-like particles show enhanced cycling performance which is associated with porous structure and large reaction area for the de−/insertion of Li-ions. The electrochemical activity is further boosted by grinding of the microspheres which significantly breaks the hierarchical structure while in general maintaining the size of the primary nanoparticles. The grinded material features a significantly improved specific capacity of 163 mAh g^{-1} which is straightforwardly explained by short Li-ion diffusion length and large surface area enabling good electronically conductive network by additives. Boosted capacity is however associated with lower cycling stability of the grinded nanocrystals which most presumingly is caused by the huge charge depth that leads to more pronounced degradation effects. In view of further optimization, a promising approach to suppress the pulverization upon cycling may be coating of the surface with carbon.

Acknowledgments The authors thank I. Glass for experimental support.

Funding information This work was supported by the Deutsche Forschungsgemeinschaft through project KL 1824/14-1. G.Z. acknowledges support of the state order via the Ministry of Science and High Education of Russia. E.T. acknowledges support by the BMWi through project 03ET6095C (HiKoMat).

References

1. Zhao B, Ran R, Liu M, Shao Z (2015) Mater Sci Eng R 98:1–71
2. Aravindan V, Lee Y-S, Madhavi S (2015) Adv Energy Mater 5(13): 1402225
3. Liu Y, Yang Y (2016) J Nanomater 2016:8123652
4. Croguennec L, Palacin MR (2015) J Am Chem Soc 137(9):3140–3156
5. Eftekhari A (2017) Energy Storage Mater 7:157–180
6. Xu Y, Wang L, Jia W, Yu Y, Zhang R, Li T, Fu X, Niu X, Li J, Kang Y (2019) Electrochim Acta 301:251–257
7. Zhu G-N, Wang Y-G, Xia Y-Y (2012) Energy Environ Sci 5(5): 6652–6667
8. Wang L, Wang F, Zhu J, Zhang X, Tang Y, Wang X (2018) Ceram Int 44(2):1296–1303
9. Chen Z, Belharouak I, Sun Y-K, Amine K (2013) Adv Funct Mater 23(8):959–969
10. Song T, Paik U (2016) J Mater Chem A 4(1):14–31
11. Wang Z, Zhang F, Xing H, Gu M, An J, Zhai B, Ana Q, Yu C, Li G (2017) Electrochim Acta 243:112–118
12. Xu J, Jia C, Cao B, Zhang WF (2007) Electrochim Acta 52(28): 8044–8047
13. Mo J, Zhang X, Liu J, Yu J, Wang Z, Liu Z, Yuan X, Zhou C, Li R, Wu X, Wu Y (2017) Chin J Chem 35(12):1789–1796
14. Li H, Liu X, Zhai T, Li D, Zhou H (2013) Adv Energy Mater 3(4): 428–432
15. Ni S, Zhang J, Ma J, Yang X, Zhang L, Li X, Zeng H (2016) Adv Mater Interfaces 3(1):1500340

16. Wang F, Liu Z, Yuan X, Mo J, Li C, Fu L, Zhu Y, Wu X, Wu Y (2017) J Mater Chem A 5(28):14922–14929
17. Li Q, Wei Q, Sheng J, Yan M, Zhou L, Luo W, Sun R, Mai L (2015) Adv Sci 2(12):1500284
18. Shen L, Chen S, Maier J, Yu Y (2017) Adv Mater 29(33):1701571
19. Shi Y, Wang J-Z, Chou S-L, Wexler D, Li H-J, Ozawa K, Liu H-K, Wu Y-P (2013) Nano Lett 13(10):4715–4720
20. Kim W-T, Jeong YU, Lee YJ, Kim YJ, Song JH (2013) J Power Sources 244:557–560
21. Liao C, Wen Y, Shan B, Zhai T, Li H (2017) J Power Sources 348: 48–56
22. Yang G, Zhang B, Feng J, Lu Y, Wang Z, Aravindan V, Aravind M, Liu J, Srinivasan M, Shen Z, Huang Y (2018) J Mater Chem A 6: 456–463
23. Ni S, Lv X, Ma J, Yang X, Zhang L (2014) J Power Sources 248: 122–129
24. Shi Y, Gao J, Abruña HD, Li H-J, Liu H-K, Wexler D, Wang J-Z, Wu Y (2014) Chem Eur J 20(19):5608–5612
25. Tartaj P, Amarilla JM, Vazquez-Santos MB (2016) Chem Mater 28(3):986–993
26. Song X, Jia M, Chen R (2002) J Mater Process Technol 120(1-3): 21–25
27. Du C, Wu J, Liu J, Yang M, Xu Q, Tang Z, Zhang X (2015) Electrochim Acta 152:473–479
28. Li Q, Wei Q, Wang Q, Luo W, An Q, Xu Y, Niu C, Tang C, Mai L (2015) J Mater Chem A 3(37):18839–18842
29. Zakharova GS, Ottmann A, Ehrstein B, Klingeler R (2016) Mater Res Bull 83:225–229
30. Ottmann A, Zakharova GS, Ehrstein B, Klingeler R (2015) Electrochim Acta 174:682–687
31. Yang G, Feng J, Zhang B, Aravindan V, Peng D, Cao X, Yu H, Madhavi S, Huang Y (2017) Int J Hydrog Energy 42(34):22167–22174
32. Xu L, Hu Y-L, Pelligra C, Chen C-H, Jin L, Huang H, Sithambaram S, Aindow M, Joesten R, Suib SL (2009) Chem Mater 21(13): 2875–2885
33. Lide DR (2004-2005) Handbook of chemistry and physics. CRC Press, New York
34. Chen H-I, Chang H-Y (2004) Colloids Surf A Physicochem Eng Asp 242(1-3):61–69
35. Ostwald W (1900) Z Phys Chem 34:495–503
36. Biswas S, Kar S, Chaudhuri S (2007) Mater Sci Eng B 142(2-3): 69–77
37. Sing KSW, Everett DH, Haul RAW, Moscou L, Pierotti RA, Rouquerol J, Siemieniewska T (1985) Pure App Chem:603–619
38. Sun P, Wang W, Liu Y, Sun Y, Ma J, Lu G (2012) Sensors Actuators B 173:52–57
39. Zhou L, Shen S, Peng X, Wu L, Wang Q, Shen C, Tu T, Huang L, Li J, Sun S (2016) ACS Appl Mater Interfaces 8(36):23739–23745
40. Iwama E, Kawabata N, Nishio N, Kisu K, Miyamoto J, Naoi W, Rozier P, Simon P, Naoi K (2016) ACS Nano 10(5):5398–5404
41. Ottmann A, Scholz M, Haft M, Thauer E, Schneider P, Gellesch M, Nowka C, Wurmehl S, Hampel S, Klingeler R (2017) Sci Rep 7: 23914
42. Shao G, Gan L, Ma Y, Li H, Zhai T (2015) J Mater A 3:11253–11260
43. Zhang C, Liu C, Nan X, Song H, Liu Y, Zhang C, Cao G (2016) ACS Appl Mater Interfaces 8(1):680–688
44. Liu J, Lu P-J, Liang S, Liu J, Wang W, Lei M, Tang S, Yang Q (2015) Nano Energy 12:709–724

Supplement Information:
Hydrothermal microwave-assisted synthesis of Li_3VO_4 as an anode for lithium-ion battery

G.S. Zakharova[1], E. Thauer[2], S.A. Wegener[2], J.-H. Nölke[2], Q. Zhu[3], R. Klingeler[2,4]

[1]*Institute of Solid State Chemistry, Ural Division, Russian Academy of Sciences, Yekaterinburg, Russia*

[2]*Kirchhoff Institute of Physics, Heidelberg University, Heidelberg, Germany*

[3]*School of Material Science and Engineering, Wuhan University of Technology, Wuhan, China*

[4]*Centre for Advanced Materials, Heidelberg University, Heidelberg, Germany*

Table S1. Rietveld refinement and results of BET analysis for Li_3VO_4 synthesized at lack and presence of ethanol

Sample	Lattice parameters			S_{BET} ($m^2\ g^{-1}$)	Total pore volume ($cm^3\ g^{-1}$)	Main pore diameter (nm)
	a (Å)	*b* (Å)	*c* (Å)			
Li_3VO_4-W	6.326(1)	5.449(1)	4.954(1)	0.02	-	-
Li_3VO_4-E	6.322(2)	5.452(2)	4.965(1)	2.36	0.03	11 and 17
Li_3VO_4-E(G)	6.317(3)	5.448(2)	4.961(1)	8.91	0.05	5 and 36
Li_3VO_4 [COD-1528868]	6.3259	5.446	4.9469			

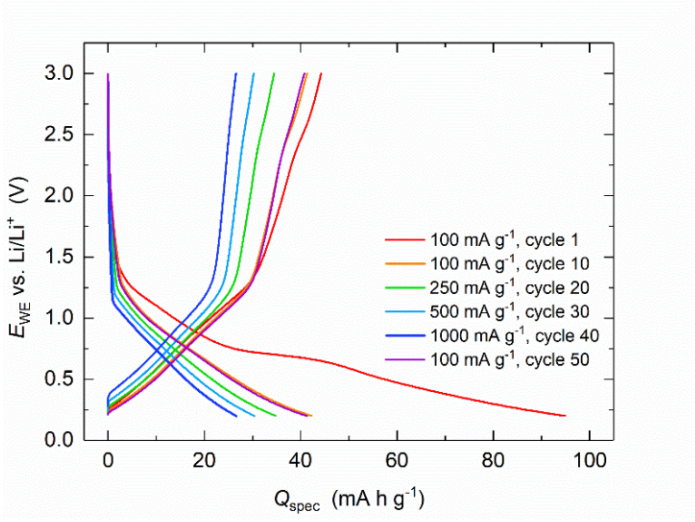

Fig. S1. Potential profile of Li_3VO_4-W at different current densities.

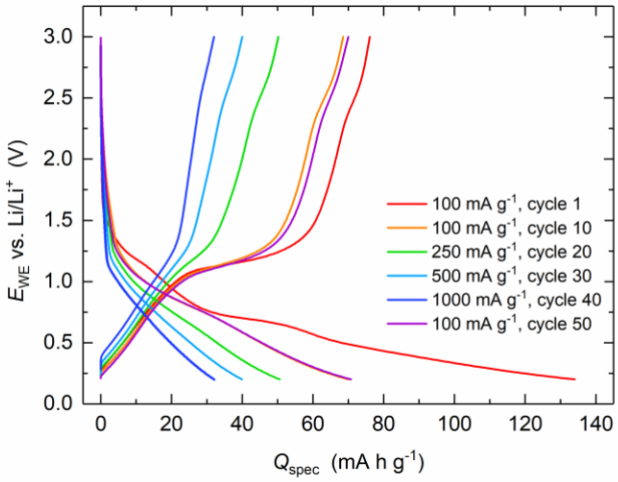

Fig. S2. Potential profile of Li_3VO_4-E at different current densities.

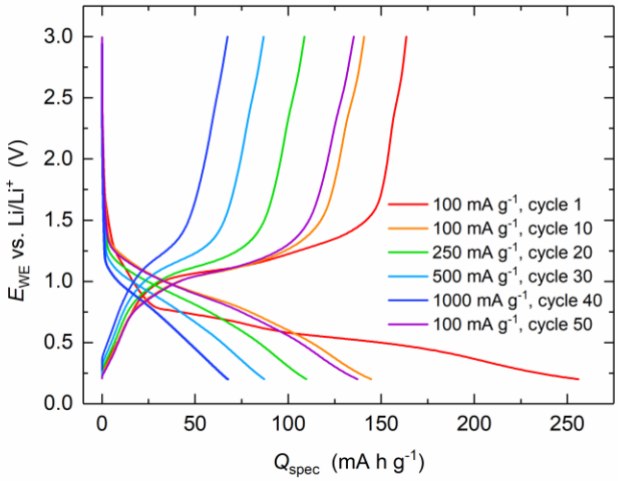

Fig. S3. Potential profile of Li_3VO_4-E(G) at different current densities.

2.2 Sol-gel synthesis of Li_3VO_4/C composites as anode materials for lithium-ion batteries

Autoren:

E. Thauer, G.S. Zakharova, S.A. Wegener, Q. Zhu, R. Klingeler

veröffentlicht in Journal of Alloys and Compounds 853, 2021, 157364

abgedruckt mit freundlicher Genehmigung des Elsevier Verlags

E. Thauer ist die Erst- und Korrespondenzautorin dieses Artikels. E. Thauer konzipierte und verfasste das Manuskript mit Ausnahme des experimentellen Teils zur Synthese und der Diskussion zu den Raman-, TEM- und BET-Messungen und erstellte die Abbildungen Abb. 1 a, Abb. 3a - c, Abb. 5 - 7, Abb. S1 - S2. Die Charakterisierung mittels XRD und REM sowie alle elektrochemischen Untersuchungen, einschließlich der -itex-situ XRD-Studien, wurden gemeinsam von E. Thauer und dem Bachelorstudent S.A. Wegener unter ihrer Anleitung durchgeführt. Die Korrespondenz mit den Gutachtern sowie die Überarbeitung des Manuskripts wurde von E. Thauer zusammen mit G.S. Zakharova und R. Klingeler übernommen.

G.S. Zakharova führte die Synthese der Materialien sowie die Raman-spektroskopischen (Abb. 1 b), thermogravimetrischen (TGA) (Abb. 2) und BET-Messungen (Abb. 4) durch und verfasste die zugehörigen Teile sowie die Diskussion zu den TEM-Aufnahmen (Abb. 3 d - f). Q. Zhu führte die TEM-Messung durch. R. Klingeler betreute das Projekt, stand beratend zur Seite und war an der Finalisierung des Manuskripts beteiligt. Alle Autoren haben das Manuskript korrekturgelesen.

Journal of Alloys and Compounds 853 (2021) 157364

Contents lists available at ScienceDirect

Journal of Alloys and Compounds

journal homepage: http://www.elsevier.com/locate/jalcom

Sol-gel synthesis of Li_3VO_4/C composites as anode materials for lithium-ion batteries

E. Thauer [a, *], G.S. Zakharova [b], S.A. Wegener [a], Q. Zhu [c], R. Klingeler [a, d, **]

[a] Kirchhoff Institute of Physics, Heidelberg University, Heidelberg, Germany
[b] Institute of Solid State Chemistry, Ural Division, Russian Academy of Sciences, Yekaterinburg, Russia
[c] Institute of Material Science and Engineering, Wuhan University of Technology, Wuhan, PR China
[d] Centre for Advanced Materials, Heidelberg University, Heidelberg, Germany

ARTICLE INFO

Article history:
Received 22 June 2020
Received in revised form
17 September 2020
Accepted 26 September 2020
Available online 28 September 2020

Keywords:
Li_3VO_4/C composite
Sol-gel thermolysis synthesis
Anode material
Lithium-ion batteries

ABSTRACT

Li_3VO_4/C composites have been synthesized by a sol-gel method and post-annealing at 650 °C for 1 h in N_2 flow using either tartaric acid, malic acid, or glucose as both chelating agents and carbon source. The presence of these organic additives crucially affects morphology and crystallite size of the final product. It is found that the electrochemical properties of Li_3VO_4/C as anode material for Li-ion batteries (LIBs) are influenced by the morphology, texture and carbon content of the material. When using carboxylic acids as carbon source composites with mesoporous structure and a high surface area are obtained that display an enhanced electrochemical activity. Initially, reversible capacity of about 400 mAh g^{-1} is obtained. In contrast, Li_3VO_4/C synthesized with glucose outperforms in terms of cycling stability. It exhibits a discharge capacity of 299 mAh g^{-1} after 100 cycles corresponding to an excellent capacity retention of 96%. The favorable effect of carbon composites on the electrochemical performance of Li_3VO_4 is shown.

1. Introduction

An ideal Li-ion battery for commercial application has to meet a variety of requirements such as high energy density, high safety performance, a long lifetime and a good rate capability. One approach to achieve these goals is the development of advanced anode materials. The common commercial anode materials for Li-ion batteries, i.e., graphite, suffers from a low insertion potential coming along with security risks due to the formation of lithium dendrites and its moderate rate capability caused by its low Li^+ diffusion coefficient [1]. In general, three types of Li^+ storage mechanism may be distinguished: intercalation, conversion and alloying [2]. The key advantages of intercalation materials for commercial use are superior reversibility and good stability due to small volume changes during the insertion and extraction of Li-ions into a host lattice. Despite the development of successful strategies for improving the cycle stability of conversion and alloy-based anode materials made in recent years, they cannot compete with intercalation anodes [3]. Among these, especially the zero-strain material $Li_4Ti_5O_{12}$ has attracted much attention due to its excellent cycle stability and its high Li^+ insertion potential of 1.55 V [4]. Although beneficial in terms of safety the high operating voltage along with a low specific capacity of only 175 mAh g^{-1} result in a low energy density. Thus, $Li_4Ti_5O_{12}$ finds proper use as anode material only in niche applications [5]. Li_3VO_4 is another promising intercalation material which was first studied by Li et al. as anode material for Li-ion batteries [6]. In contrast to $Li_4Ti_5O_{12}$ it exhibits a higher theoretical capacity of 397 mAh g^{-1} corresponding to $x = 2$ in $Li_{3+x}VO_4$, which, that is comparable to that of graphite (372 mAh g^{-1}), and the insertion of Li-ions occurs at a safe but still low-potential window between 0.2 and 1 V [7]. Another advantage of Li_3VO_4 is its high mobility of Li-ions [8]. However, to become a high-performance anode material one has to overcome its low electronic conductivity resulting in large resistance polarization and poor rate capability. Composites of Li_3VO_4 with carbon-based materials has been demonstrated as an effective strategy to solve this problem [7,9–16]. A number of different carbon materials, such as carbon nanotubes [17,18], graphite [19,20], graphene [11,12,21,22] and graphene oxide [23,24], as well as various synthesis methods have been utilized to prepare Li_3VO_4/C composites. Besides promoting

* Corresponding author.
** Corresponding author. Kirchhoff Institute of Physics, Heidelberg University, Heidelberg, Germany.
E-mail addresses: elisa.thauer@kip.uni-heidelberg.de (E. Thauer), klingeler@kip.uni-heidelberg.de (R. Klingeler).

https://doi.org/10.1016/j.jallcom.2020.157364
0925-8388/

fast electron transfer, the carbon network can act as buffer of the volume changes and provides the structural stability of the electrode during cycling. Moreover, attributed to its stable chemical characteristics [25], carbon as surface layer can protect the material from side reactions at the electrode/electrolyte interface [26–28]. Surface coating is a promising approach to boost the structural stability of electrode materials and a hotspot research field for cathodes [29–32]. The electrochemical properties of Li_3VO_4/C are significantly influenced by the carbon component and the preparation method. For example, Li_3VO_4/C composite with a capacity of 245 mAh g^{-1} after 50 cycles at 20 mA g^{-1} were prepared via solid-state synthesis combined with chemical vapor deposition (CVD) coating by Shao et al. [28]. The *in-situ* carbon-encapsulated Li_3VO_4 nanoparticles synthesized via solid-state method by Zhang et al. [15] show a reversible capacity of 340 mAh g^{-1} at a current density of 4 A g^{-1} and a capacity retention of 80% after 2000 cycles. Ni et al. report the hydrothermal synthesis of Li_3VO_4/C composite using citric acid as carbon source which delivers after 1000 cycles at 2 A g^{-1} a specific discharge capacity of 422 mAh g^{-1} [33]. Qin et al. [26] used electrospinning to prepare Li_3VO_4/C nanofibers which exhibits a capacity of 405 mAh g^{-1} at 40 mA g^{-1}. Among different fabrication techniques, the sol–gel method provides a molecular level mixing of the starting materials which enhances chemical homogeneity of the final products. Additionally, low temperature of the preparation facilitates the formation of mesopores on the material surface, thereby improving the electrochemical properties. For example, carbon-coated Li_3VO_4 nanoparticles fabricated by citric acid-assisted sol-gel route achieved a high reversible capacity of 480 mAh g^{-1} at 0.1 A g^{-1} [34]. In the sol-gel process, the chelating agent takes part in hydrolysis and condensation reactions of metal-oxide precursor, forming M-O-M bridging bonds by the chelation between metal ions and polar functional groups of the chelating agent.

In the present study, three different organic additives, i.e., glucose, malic acid and tartaric acid, are used to synthesize Li_3VO_4/C composites through a facile sol-gel thermolysis method. Malic acid and tartaric acid, having carboxyl COOH-functional groups, belong to the acid chelating agents and tend to diminish the pH of the metal-oxide precursor solution to lower values. The use of tartaric and malic acid as a chelating agent for the synthesis of Li_3VO_4/C composites has not been reported so far. On the contrary, glucose has a ring structure with hydroxyl OH-groups and can be a chelating agent only in acidic ambient, turning into gluconic acid. In this work, in base medium, glucose serves as a capping agent to prevent the cations from agglomerating generating a highly viscous and stable sol [35]. Additionally, all these additives are carbon-rich materials which can be used as carbon sources to produce composite materials and enhance the crystallization process during the calcination as well. Here, we report the influence of different type of organic additives on the phase composition, morphology and electrochemical properties of the Li_3VO_4/C composites.

2. Experimental

2.1. Materials preparation

Ammonium metavanadate NH_4VO_3, lithium hydroxide monohydrate $LiOH \cdot H_2O$, glucose $C_6H_{12}O_6$, malic acid $C_4H_6O_5$, tartaric acid $C_4H_6O_6$ purchased from Sigma–Aldrich were used for the synthesis. First, 0.585 g NH_4VO_3 and 0.630 g $LiOH \cdot H_2O$ (with the molar ratio of NH_4VO_3 to $LiOH \cdot H_2O$ being 1:3) were dissolved under stirring in 50 ml distilled water to form a clear solution. Afterwards, glucose (with the molar ratio of glucose to vanadium metal of 1:1) was employed as carbon source and was added to the solution. To get a gel, the solution was heated at 60 °C under continuous stirring. The resulting gel was dried at 60 °C in air to get precursor, and later, calcined at 650 °C for 1 h in N_2 flow to yield the Li_3VO_4/C composite. The as-prepared product is labeled as Li_3VO_4/C-G. For comparison, Li_3VO_4/C was produced with malic acid and tartaric acid at the same molar ratio of V: carboxylic acid = 1 : 1. These samples are denoted as Li_3VO_4/C-M and Li_3VO_4/C-T, respectively. The bare Li_3VO_4 sample was prepared by annealing of the Li_3VO_4/C-M composite at 650 °C for 1 h in air flow.

2.2. Materials characterization

X-ray powder diffraction (XRD) patterns were taken with a Bruker AXS D8 Advance Eco using Cu Kα radiation ($\lambda = 1.540$ Å). The morphology of the samples was investigated by a ZEISS Leo 1530 scanning electron microscope (SEM) and a JEOL JEM 2100 transmission electron microscope (TEM). Thermogravimetric analysis (TG-DSC-MS) with a heating rate of 10 K min^{-1} under flowing air was carried out using STA 449 F_3 Jupiter thermoanalyzer (Netzsch) coupled with a QMS 403 mass spectrometer. The examination of the carbon content was carried out by chemical analysis (CA) using Vario MICRO Cubes (Elementar). Raman spectra were measured with a Renishaw in Via Reflex spectrometer at a laser wavelength of 532 nm. Nitrogen sorption isotherms were determined on a Micromeritics Gemini VII 2390 Surface Area Analyzer. The specific surface area, pore size distribution and pore volumes were obtained by means of the Brunauer-Emmett-Teller (BET) method and the Barrett-Joyner-Halenda model from the desorption branches of the isotherms.

2.3. Electrochemical measurements

The electrochemical measurements were carried out with a VMP3 potentiostat (Bio-Logic SAS) at 25 °C using Swagelok-type cells (see Ref. [36]). For the preparation of the working electrodes 80 wt% Li_3VO_4/C, 15 wt% carbon black (Super C65, Timcal) and 5 wt % polyvinylidene fluoride binder (PVDF, Solvay Plastics) dissolved in *N*-methyl-2-pyrrolidone (NMP, Sigma-Aldrich) were mixed and stirred for at least 12 h. The spreadable slurry obtained by evaporating most of the NMP was applied on circular Cu meshes with a diameter of 10 mm. Afterwards, the electrodes were dried at 80 °C under vacuum, mechanically pressed with 8 MPa and dried again. The loading density was about 4 mg cm^{-2}. A lithium metal foil (Alfa Aesar) pressed on a nickel disk served as counter electrode. Two layers of glass fiber (Whatman GF/D) that was soaked with 200 µl electrolyte (Merck Electrolyte LP30), a 1 M $LiPF_6$ salt solution in 1:1 ethylene carbonate and dimethyl carbonate were used as separator. The cells were assembled in a glove box under argon atmosphere (O_2/H_2O < 5 ppm). For *ex-situ* XRD measurements the cells were disassembled in a glovebox and the electrodes were washed in DMC. The XRD measurements were performed using an airtight sample carrier. The calculation of the specific capacity is based on the total mass weight of the composites Li_3VO_4/C or of bare Li_3VO_4, respectively.

3. Results and discussion

The XRD patterns of the Li_3VO_4/C composites shown in Fig. 1a confirm that by heating the precursors up to 650 °C composites based on Li_3VO_4 are formed. All diffraction peaks can be assigned to Li_3VO_4 with an orthorhombic structure according to the reference COD-1528868 [37]. As shown in Table 1, the lattice parameters of Li_3VO_4 in the composites are in a good agreement with reference data. The estimated average crystallite size of Li_3VO_4 calculated by Scherrer's formula based on the (110), (101) and (111) crystal planes indicates diameters of 30–50 nm.

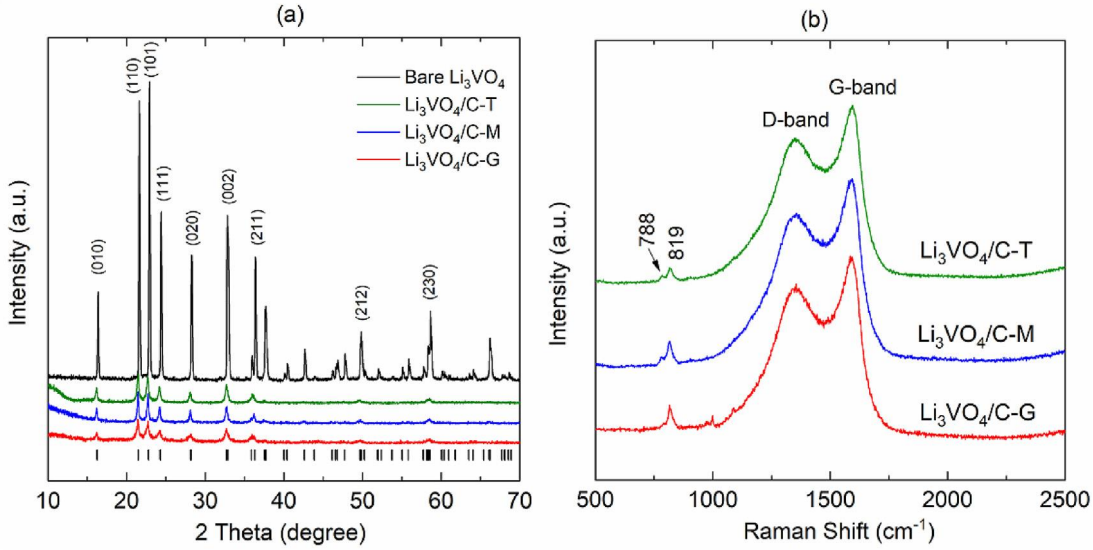

Fig. 1. (a) XRD patterns of the Li_3VO_4/C composites synthesized with glucose (G), malic acid (M), and tartaric acid (T) as carbon source as well as of bare Li_3VO_4. Black bars mark the Bragg peak position of Li_3VO_4 according to COD #1528868 [37]. (b) Raman spectra of the Li_3VO_4/C composites.

Table 1
Lattice parameters from Rietveld refinement, average crystallite size from analyzing the XRD peak width of the (110), (101) and (111) reflections, carbon content, and BET surface area for Li_3VO_4/C composites. The last two lines show parameters of Li_3VO_4 studied here and from the literature [37].

Sample	Lattice parameters			D_{XRD} (nm)	Carbon content (wt%)		S_{BET} (m^2 g^{-1})
	a (Å)	b (Å)	c (Å)		TGA	CA	
Li_3VO_4/C-G	6.350(1)	5.460(2)	4.959(4)	25(9)	25.6	18.0(5)	12
Li_3VO_4/C-M	6.346(3)	5.462(4)	4.964(2)	41(7)	13.7	10.7(5)	42
Li_3VO_4/C-T	6.341(8)	5.461(9)	4.973(8)	34(8)	14.1	9.6(5)	32
Bare Li_3VO_4	6.329(1)	5.448(1)	4.949(1)	61(5)		0	
Li_3VO_4 [COD-1528868]	6.3259	5.446	4.9469				

To confirm and to quantify the presence of carbon in the Li_3VO_4/C composites, Raman spectra and DSC-TG-MS curves were measured. The Raman spectra of all samples show two broad peaks at about 1340 and 1593 cm^{-1} (Fig. 1b). The Raman-active E_{2g} mode at 1593 cm^{-1} (G-band) is characteristic of sp^2-hybridized carbon atoms resulting from in-plane vibrations, whereas the D-band at around 1340 cm^{-1} can be attributed to the presence of structural defects or disorder [38]. The ratio of the maximal intensities of the D- and G-band (I_D/I_G) was calculated as 0.87, 0.82, 0.82 for Li_3VO_4/C-G, Li_3VO_4/C-T, and Li_3VO_4/C-M composites, respectively, indicating a small fraction of sp^3-hybridized carbon atoms [39]. A high graphitization degree is supposed to enhance the electron transport and thus the electrochemical cycling performance [22]. The peaks located around 788 and 819 cm^{-1} are attributed to the asymmetric and symmetric stretching vibrations of VO_4-tetrahedra in Li_3VO_4, respectively [17,40]. These results confirm the successful preparation of Li_3VO_4/C composites.

In order to determine the carbon content of Li_3VO_4/C composites, TG-DSC-MS measurements of as-prepared materials were carried out under air flow. It can be observed that several steps emerge from the TG-curves of the Li_3VO_4/C composites (Fig. 2). In all samples, the first step starts from about 70 °C and ends at 200 °C. It can be mainly attributed to the loss of water absorbed on the material's surface. The process is accompanied by a weak and broad endothermic peak centered at about 104 °C. Additionally, the MS-curve of the Li_3VO_4/C-T composite (ion current versus temperature) also implies a weight loss in the range of 70–170 °C ascribed to evaporation of surface-adsorbed gaseous carbon dioxide ($m/z = 44$ a.m.u.). The next weight loss from 250 °C to 700 °C is caused by oxidation of the carbon component of Li_3VO_4/C composites and the emission of CO_2 gases as also corroborated by analysis of the MS curves. This process is accompanied by a broad and complex exothermal peak. The MS curves exhibit maxima at the same temperatures where exothermic peaks appear. For Li_3VO_4/C-G and Li_3VO_4/C -T composites, the stepped combustion of carbonaceous material can be attributed to the realization of different reactions (e.g., carbonization of glucose and tartaric acid, burning of amorphous carbon and the rest of carbon component, graphitization). In contrast, for Li_3VO_4/C-M composite the data imply only one intensive peak around 405 °C which is associated with removal of CO_2 gases upon heating without visible satellite peaks attributed to multistage carbon oxidation. Based on the assumptions made above, the calculated carbon contents in Li_3VO_4/C-G, Li_3VO_4/C-M and Li_3VO_4/C-T composites are 25.6, 13.7, and 14.1 wt%, respectively (see Table 1). According to the CA, the bare Li_3VO_4 sample contains no carbon.

As can be seen from the SEM images (Fig. 3 and Fig. S1), the carbon source added during synthesis has a pronounced influence on the morphology of the resulting product. There are clear differences between Li_3VO_4/C-G, synthesized with glucose, and both samples which have been synthesized with carboxylic acids, i.e., Li_3VO_4/C-M and Li_3VO_4/C-T. Li_3VO_4/C-G composite consists of irregularly shaped particles of several tens of micrometers decorated with smaller particles which sizes are below 1 μm (Fig. 3a). In contrast, the powders Li_3VO_4/C-M and Li_3VO_4/C-T are composed of large sponge-like particles with partly smooth and partly

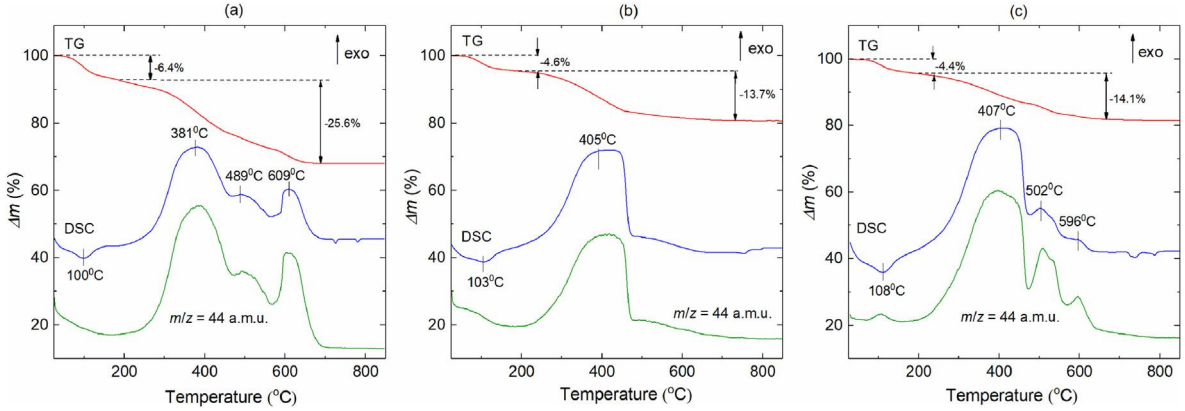

Fig. 2. Thermogravimetric (red), DSC (blue), and mass spectroscopy (green) curves of (a) Li_3VO_4/C-G, (b) Li_3VO_4/C-M, and (c) Li_3VO_4/C-T composites. (For interpretation of the references to colour in this figure legend, the reader is referred to the Web version of this article.)

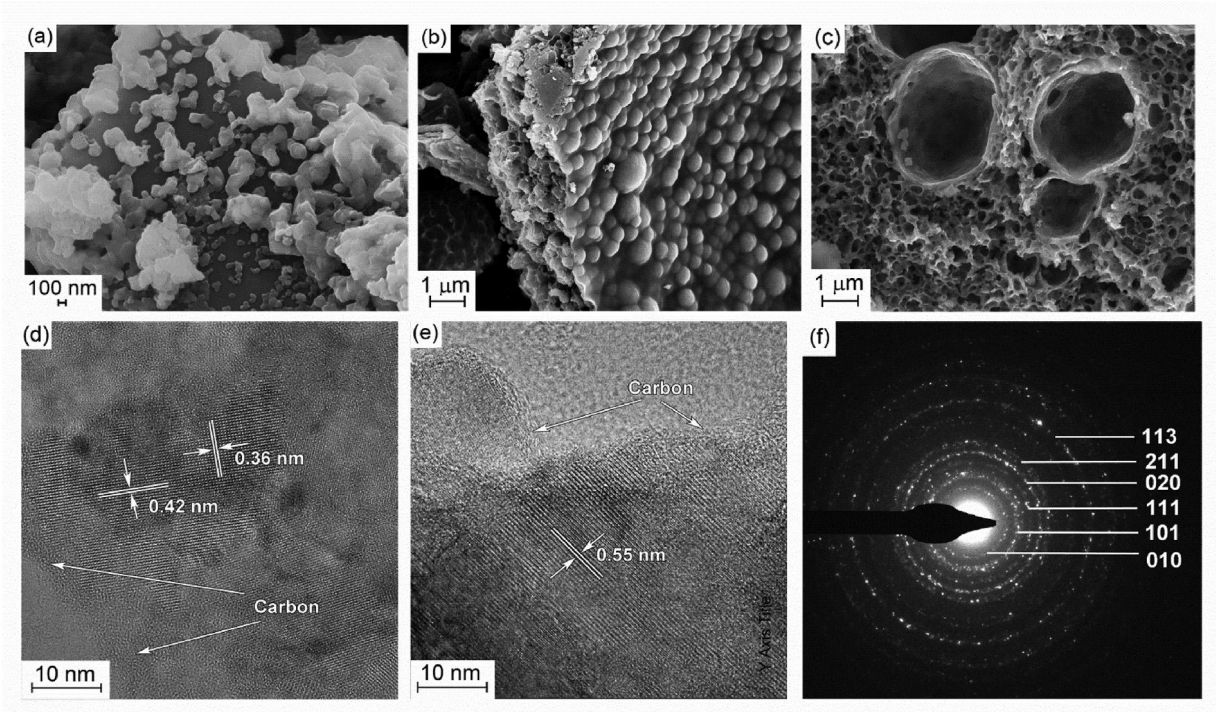

Fig. 3. SEM images of (a) Li_3VO_4/C-G, (b) Li_3VO_4/C-M, and (c) Li_3VO_4/C-T composites; HRTEM images of (d) Li_3VO_4/C-G and (e) Li_3VO_4/C-T composites with the corresponding (f) SAED pattern.

mesoporous surface (Fig. 3b–c). In addition, micrometer sized round hollows are visible. The bare Li_3VO_4 sample consists of primary particles with sizes between 100 nm and few micrometers that are arranged to secondary particles of several tens of micrometers (Fig. S1).

A high resolution TEM (HRTEM) was used for further study the microstructure of the Li_3VO_4/C composites. Fig. 3d–e shows lattice fringes with interplanar spacing of 0.36, 0.42, and 0.55 nm, assigning to the (011), (110), and (010) planes of orthorhombic Li_3VO_4, respectively. Amorphous carbon layers with thickness of about 10 and 1 nm are observed on the surface of Li_3VO_4/C-G and Li_3VO_4/C-T. The results show that the thickness of the carbon layer covering the Li_3VO_4 particles is greater when glucose is used as carbon source as compared to tartaric acid. This observation complies with the results of thermogravimetric analysis. The selected-area electron diffraction (SAED) pattern of Li_3VO_4/C-T (Fig. 3f) indicate the polycrystalline nature of Li_3VO_4 with diffraction rings associated with the (010), (101), (111), (020), (211), and (113) crystal planes from inner to exterior, respectively.

Nitrogen sorption isotherms were generated to investigate the BET surface area and the porous structure of the Li_3VO_4/C composites (Fig. 4). All samples display a type-IV isotherm, based on the IUPAC classification, with an H3 hysteresis loop [41]. The BET specific surface area of the Li_3VO_4/C composites are displayed in Table 1 and are in the range of several 10 $m^2\ g^{-1}$. In comparison with pure Li_3VO_4 [42], the BET surface area of the Li_3VO_4/C composites is rather high due to the presence of mesopores. Among the here reported composites, Li_3VO_4/C-M and Li_3VO_4/C-T show distinctly higher BET surfaces than the one produced by virtue of glucose. This is attributed to a highly porous structure and the presence of

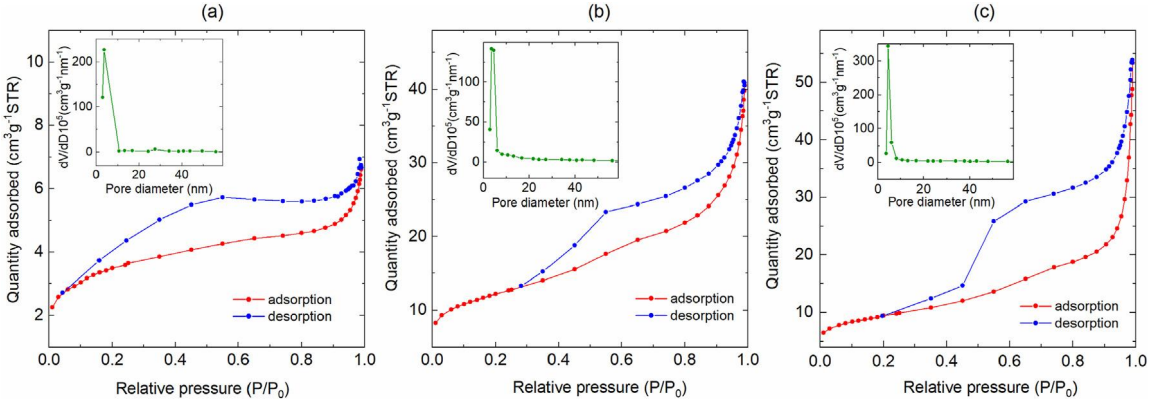

Fig. 4. Nitrogen sorption isotherms and corresponding pore-size distributions of (a) Li_3VO_4/C-G, (b) Li_3VO_4/C-M, and (c) Li_3VO_4/C-T composites.

smaller particles as seen in the SEM images (Fig. 3b–c). The pore-size distribution curves demonstrate that the Li_3VO_4/C composites exhibit mesopores with a narrow pore size distribution of about 4 nm.

In order to study the effects of various material parameters on the electrochemical properties of Li_3VO_4/C, cyclic voltammetry (CV) and galvanostatic cycling with potential limitation in the range 0.2–3 V are used. In addition, studies on bare Li_3VO_4 provide additional information about the effect of the carbon composite. In Fig. 5 the cyclic voltammograms of the Li_3VO_4/C composites recorded at a scan rate of 0.1 mV s^{-1} are shown. Exemplarily, Fig. 5a shows the first, second, fifth and twentieth cycle of the CV curves of Li_3VO_4/C-T. In the first reductive half-cycle two peaks at 0.64 V (R1) and 0.50 V (R2) occur that can be ascribed to the intercalation of Li^+ into Li_3VO_4 [43]. Additionally, in the first cycle the formation of the solid electrolyte interface (SEI) contributes in the same voltage range [6]. The lithiation and delithiation of the contained carbon gives rise to the redox peaks Rc and Oc at the lower cycling limit 0.2 V [44]. In the first oxidative scan two peaks at 1.36 V (O1) and 1.6 V (O2) are observable that correspond to the delithiation processes in Li_3VO_4 [43]. Upon further cycling the reduction peaks R2 and R3 are notably enlarged and shifted to higher potentials up to the 5th cycle. In oxidative sweep, besides a shift of the peaks O1 and O2 to lower potentials up to the 5th cycle, a third broad peak appears around 0.8 V (O3). Similar observations in the literature were associated with structural changes [33]. Iwama et al. [45] and Zhou et al. [43] showed that during the first lithiation there is an irreversible structure transformation. For comparison of the various Li_3VO_4/C composites reported at hand, the first and tenth cycle of the CV curves are shown in Fig. 5b. Despite differences in electrochemical activity between Li_3VO_4/C-G synthesized with glucose as carbon source as compared to Li_3VO_4/C-M and Li_3VO_4/C-T, synthesized with carboxylic acids, the courses of the cyclic voltammograms are almost similar. The electrochemical activity of Li_3VO_4/C-G is overall lower but extends over a wider potential range. For the reductive scan it ranges to lower potentials and for oxidative scans to higher potentials. However, specifically, all CV curves of the various composites exhibit the same general redox features described above for Li_3VO_4/C-T (Fig. 5a). The same applies to bare Li_3VO_4 which, however, features the lowest electrochemical activity.

In Fig. 6 the long-term cycling performances of the three different composites during galvanostatic cycling at 100 mA g^{-1} are shown. The potential profiles (Fig. 6a) are consistent with the results obtained from cyclic voltammetry (Fig. 5) and all redox features discussed above can be observed. In the first cycle the dis-/charge capacities are 430/289 mAh g^{-1}, 537/405 mAh g^{-1}, and 531/396 mAh g^{-1} for Li_3VO_4/C-G, Li_3VO_4/C-M, and Li_3VO_4/C-T, respectively (Fig. 6b). The huge irreversible contribution in the first half cycle is caused by the SEI formation and structural changes [9,27,43]. Except for the first cycles, all samples display high coulombic efficiencies. As of the fifth cycle, the coulombic efficiency of Li_3VO_4/C-G is over 99%. By comparison, the composites Li_3VO_4/C-M and Li_3VO_4/C-T show lower values in the initial 20 cycles and

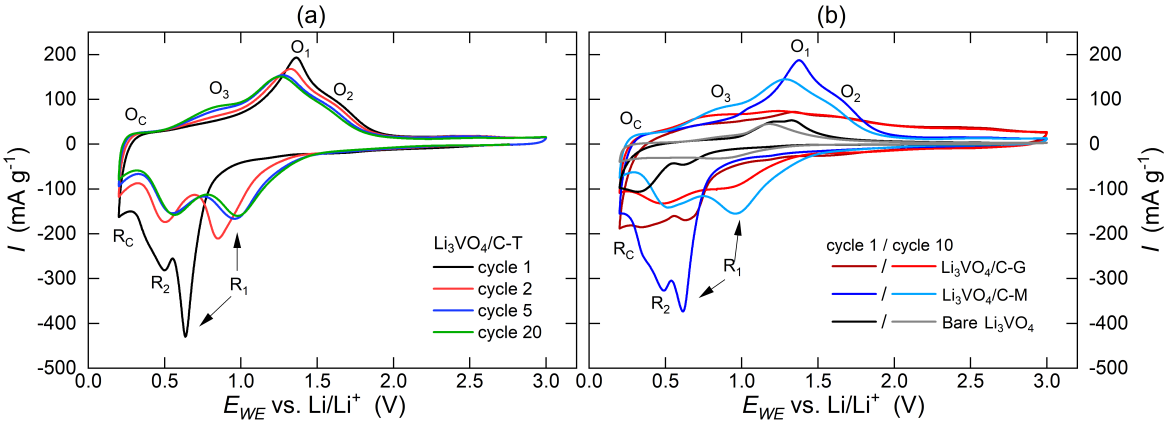

Fig. 5. CV curves recorded at a scan rate of 0.1 mV s^{-1} of Li_3VO_4/C-T (a) and for comparison the first and tenth cycle of the different composites Li_3VO_4/C-G, Li_3VO_4/C-M, and bare Li_3VO_4.

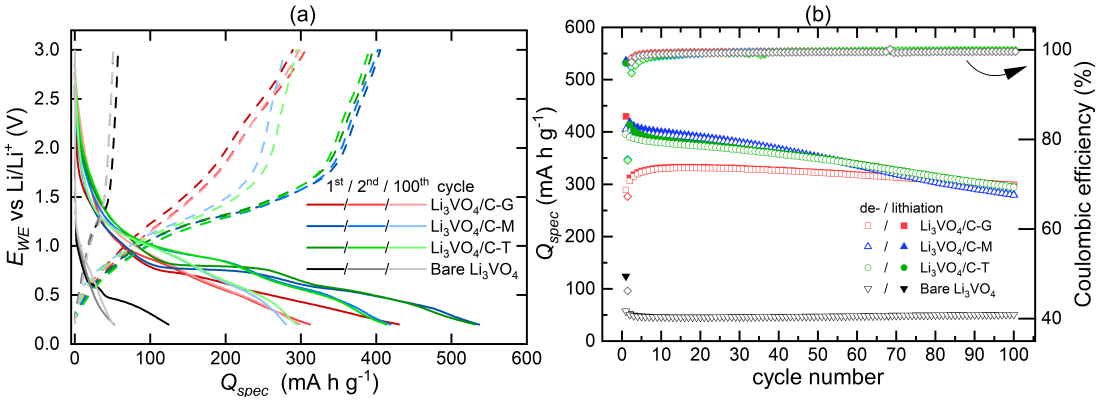

Fig. 6. Potential profiles of the first, second and hundredth cycle (a) and specific dis-/charge capacities and coulombic efficiencies (b) during galvanostatic cycling at 100 mA g^{-1} of Li_3VO_4/C-G, Li_3VO_4/C-M, and Li_3VO_4/C-T composites as well as bare Li_3VO_4.

exceed 99% in cycle 17 and cycle 13, respectively. There are clear differences in the cycle performance between the sample Li_3VO_4/C-G synthesized with glucose and the two composites synthesized with carboxylic acids, Li_3VO_4/C-M and Li_3VO_4/C-T. In the initial 50 cycles, the latter two reach significant higher capacities than Li_3VO_4/C-G. It is noticeable, that with measured values of about 400 mAh g^{-1} the full theoretical capacity for an insertion of 2 Li$^+$/f.u. is gained. Up to the hundredth cycles the discharge capacities continuously decrease to 281 mAh g^{-1} (Li_3VO_4/C-M) or rather 295 mAh g^{-1} (Li_3VO_4/C-T) corresponding to 67% and 71% relative to the second cycle. In contrast, Li_3VO_4/C-G reaches indeed only a maximal discharge capacity of 333 mAh g^{-1} in cycle 21 but it exhibits an excellent cycle stability. After 100 cycles a discharge capacity of 299 mAh g^{-1} is measured, which corresponds to a retention of 96% relative to the second cycle. The initial superior electrochemical activity of the samples Li_3VO_4/C-M and Li_3VO_4/C-T can be explained by their larger surface area compared to Li_3VO_4/C-G (Table 1). It provides an enhanced Li-ion diffusion and a high contact area with the carbon, which offers favorable electron transfer [28,40,42]. However, on the other side, the larger exposed electrode surfaces yield enhanced degradation due to corrosion and electrolyte dissolution, thus resulting in worse cycling stability [27,28]. Moreover, the cycle life is strongly influenced by the depth of discharge. The storage of a larger amount of Li-ions is accompanied with more serious structural damages. Crystal distortion and volume expansion by Li-ion insertion generate stress, which can lead to particle cracking. Such cracking in the electrode material has been considered to be one of the major mechanism for performance degradation [27,46]. This is in accordance with the observations made for the composite Li_3VO_4/C-G. It has the smallest surface area (Table 1), reaches initially the lowest capacity but is least affected by the degradation mechanisms discussed above. In addition, the high carbon content of Li_3VO_4/C-G is possibly another important factor that explains the enhanced cycling stability. The carbon plays an important role in inhibiting the degradation processes. On the one hand it protects the surface of the Li_3VO_4 particles for side reactions at the electrode-electrolyte interface [9,26–28]. Secondly, the carbon matrix can serve as a buffer for the volume changes during electrochemical cycling and prevents the electrode material from pulverization and aggregation [7,26]. A high and uniform distribution of the carbon in the electrode reduces the possibility of electrical contact loss and the formation of inactive regions in the material leading to performance degradation. The comparison of the Li_3VO_4/C composites with bare Li_3VO_4 clearly demonstrates the beneficial effect of the carbon composite. The specific capacity of bare Li_3VO_4 is far below those of the composite materials. In the first cycle the dis-/charge capacities are only 124/57 mAh g^{-1} exhibiting low first columbic efficiency of 46% due to side reactions at the unprotected Li_3VO_4/electrolyte interface [9]. The low specific capacity of bare Li_3VO_4 can be explained by limited access and inactive regions of the material due to its low electronic conductivity. *Ex-situ* XRD studies (Fig. S2) indeed suggest that a large part of Li_3VO_4 is not involved in the lithiation process. While after discharging to 0.2 V at 20 mA g^{-1} the XRD pattern of Li_3VO_4/C-T electrode exhibits no more Bragg peaks associated with Li_3VO_4, for the discharged bare Li_3VO_4 electrode just a slight decrease in the intensity of the Li_3VO_4 Bragg peaks can be observed.

To test the rate capability the samples were cycled with rates between 100 and 1000 mA g^{-1}. The specific dis-/charge capacities are shown in Fig. 7a and the potential profiles of cycle 10 at 100 mA g^{-1}, cycle 40 at 1000 mA g^{-1} and cycle 50 again at 100 mA g^{-1} in Fig. 7b. The composite Li_3VO_4/C-T reaches even at a high current density of 1000 mA g^{-1} an excellent capacity of about 325 mAh g^{-1}. Furthermore, for all samples the charge capacity can regain to about 97% when the current density returns to 100 mA g^{-1}. Obviously, high cycling rates do not cause irreversible damage detrimental for the electrochemical processes. In fact, the cycle stability is even worse for a constant low current density of 100 mA g^{-1} (Fig. 6a). During the long-term cyclability test the capacity loss between cycle 10 and 41 of Li_3VO_4/C-M is 8% and 6% for Li_3VO_4/C-T. We attribute this to higher degradation effects of a huge discharge depth in case of low cycling rates. As demonstrated by the potential profiles, the worse rate capability of the sample Li_3VO_4/C-G and Li_3VO_4/C-M compared to Li_3VO_4/C-T can be explained by a larger resistance polarization. The potential gap between charge and discharge is significantly enlarged at a rate of 1000 mA g^{-1} due to kinetic effects.

In Table 2 the electrochemical performances of various Li_3VO_4-based anodes reported in literature are collected. In comparison to bare Li_3VO_4 the carbon composites exhibit enhanced Li$^+$ storage properties, especially in terms of electrochemical activity. The differences of the various composites can be traced back to differences in the carbon component on the one hand and morphological features on the other hand. In addition, the mere content of carbon and its structure plays an important role.

4. Conclusion

In summary, various Li_3VO_4/C composites with differences in morphology were prepared by a sol-gel method and subsequent annealing using different carbon sources. It is demonstrated that

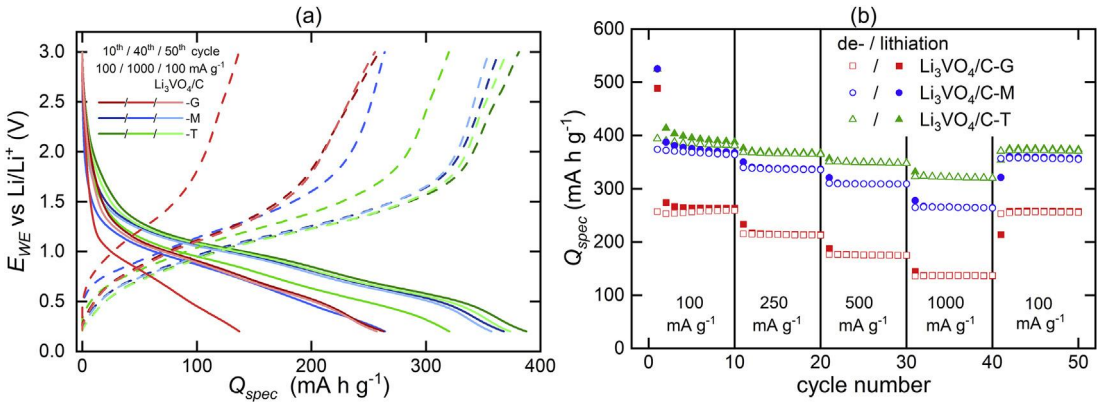

Fig. 7. Specific dis-/charge capacities (a) and potential profiles (b) for rate capability test with different cycling rates between 100 and 1000 mA g^{-1} of Li_3VO_4/C-G, Li_3VO_4/C-M and Li_3VO_4/C-T composites.

Table 2
Summary of the electrochemical performance of Li_3VO_4-based electrodes prepared via different synthesis methods.

Synthesis Method	Composite	Current 1C ≈ 394 mA g^{-1} (mA g^{-1})	1st charge capacity (mAh g^{-1})	Specific capacity (mAh g^{-1}) /cycle	Ref
Microwave-assisted hydrothermal	Li_3VO_4/C nanoparticles	100	163	104/100	[42]
Hydrothermal*	Li_3VO_4/C nanoparticles	150	594	542/300	[33]
Solid-state combining with CVD*	Li_3VO_4/C nanospheres	20	295**	245/50	[28]
Spray-drying*	Li_3VO_4/C hollow spheres	80	429	400*/100	[16]
Electrospinning*	Li_3VO_4/C nanofibers	40	451	394/100	[26]
Sol-gel*	Li_3VO_4/C nanoparticles	100	491	408/100	[19]
Citric acid-assisted sol-gel*	Li_3VO_4/C nanoparticles	0.8C	400**	363/40	[34]
Glucose-assisted sol-gel*	Li_3VO_4/C microparticles	100	289	299/100	This work
Malic acid-assisted sol-gel*	Li_3VO_4/C mesoporous particles	100	405	281/100	This work

Synthesis methods marked with an asterisk include post-synthesis heat treatment.
Values marked with a double asterisk (**) are estimated from the graphs.

the electrochemical properties of Li_3VO_4/C as anode material for Li-ion batteries depend on morphology, surface texture and carbon content. In the initial 50 cycles, the mesoporous composites Li_3VO_4/C-M and Li_3VO_4/C-T synthesized with carboxylic acids excels in enhanced reversible electrochemical capacity which we attribute to their high surface area. However, both materials display slightly stronger fading effects which can be as well ascribed to adverse effects of the high surface area as a to huge charge depth upon the beginning cycles. While displaying slightly smaller initial reversible capacity, Li_3VO_4/C-G synthesized with glucose exhibits an excellent cycling stability. It is much less affected by the degradation mechanisms due to the smaller surface area and higher carbon content. Comparison with bare Li_3VO_4 clearly demonstrates the beneficial effect of carbon composites on the electrochemical performance. The data show that it significantly enhances specific capacity and improves first coulombic efficiency. A promising approach for further optimization may be the complete encapsulation of single Li_3VO_4 particles with carbon to protect the surface for side reactions at the electrode-electrolyte interface and suppress the pulverization upon cycling.

CRediT authorship contribution statement

E. Thauer: Conceptualization, Methodology, Investigation, Writing - original draft, Visualization. **G.S. Zakharova:** Conceptualization, Methodology, Investigation, Writing - original draft, Visualization, Materials Synthesis. **S.A. Wegener:** Investigation. **Q. Zhu:** Investigation. **R. Klingeler:** Conceptualization, Writing - review & editing, Supervision.

Declaration of competing interest

The authors declare that they have no known competing financial interests or personal relationships that could have appeared to influence the work reported in this paper.

Acknowledgements

This work was supported by the Deutsche Forschungsgemeinschaft through project KL 1824/14-1. G.Z. acknowledges support of the state order via the Ministry of Science and High Education of Russia (Theme no. AAAA-A19-119031890025-9). E.T. and R.K acknowledges support by the BMWi through project 03 ET6095C (HiKoMat). The authors thank I. Glass for experimental support.

Appendix A. Supplementary data

Supplementary data to this article can be found online at https://doi.org/10.1016/j.jallcom.2020.157364.

References

[1] K. Persson, V.A. Sethuraman, L.J. Hardwick, Y. Hinuma, Y.S. Meng, A. van der Ven, V. Srinivasan, R. Kostecki, G. Ceder, Lithium diffusion in graphitic carbon, J. Phys. Chem. Lett. 1 (2010) 1176–1180.
[2] N. Mahmood, T. Tang, Y. Hou, Nanostructured anode materials for lithium ion batteries, Adv. Energy Mater. 6 (2016), 1600374.
[3] V. Aravindan, Y.-S. Lee, S. Madhavi, Research progress on negative electrodes for practical li-ion batteries, Adv. Energy Mater. 5 (2015), 1402225.
[4] G. Xu, P. Han, S. Dong, H. Liu, G. Cui, L. Chen, $Li_4Ti_5O_{12}$-based energy conversion and storage systems, Coord. Chem. Rev. 343 (2017) 139–184.
[5] L. Wang, F. Wang, J. Zhu, X. Zhang, Y. Tang, X. Wang, Synthesis and

electrochemical performance of three-dimensional ordered hierarchically porous $Li_4Ti_5O_{12}$ for high performance lithium ion batteries, Ceram. Int. 44 (2018) 1296–1303.
[6] H. Li, X. Liu, T. Zhai, D. Li, H. Zhou, Li_3VO_4: a promising insertion anode material for lithium-ion batteries, Adv. Energy Mater. 3 (2013) 428–432.
[7] J. Mo, X. Zhang, J. Liu, J. Yu, Z. Wang, Z. Liu, X. Yuan, C. Zhou, R. Li, X. Wu, Y. Wu, Progress on Li_3VO_4 as a promising anode material for Li-ion batteries, Chin. J. Chem. 35 (2017) 1789–1796.
[8] X. Song, M. Jia, R. Chen, Synthesis of Li_3VO_4 by the citrate sol–gel method and its ionic conductivity, J. Mater. Process. Technol. 120 (2002) 21–25.
[9] C. Liao, Q. Zhang, T. Zhai, H. Li, H. Zhou, Development and perspective of the insertion anode Li_3VO_4 for lithium-ion batteries, Energy Storage Mater 7 (2017) 17–31.
[10] Z. Liang, Z. Lin, Y. Zhao, Y. Dong, Q. Kuang, X. Lin, X. Liu, D. Yan, New understanding of Li_3VO_4/C as potential anode for Li-ion batteries, J. Power Sources 274 (2015) 345–354.
[11] Z. Jian, M. Zheng, Y. Liang, X. Zhang, S. Gheytani, Y. Lan, Y. Shi, Y. Yao, Li_3VO_4 anchored graphene nanosheets for long-life and high-rate lithium-ion batteries, Chem. comm. 51 (2015) 229–231.
[12] Y. Shi, J.-Z. Wang, S.-L. Chou, D. Wexler, H.-J. Li, K. Ozawa, H.-K. Liu, Y.-P. Wu, Hollow structured Li_3VO_4 wrapped with graphene nanosheets in situ prepared by a one-pot template-free method as an anode for lithium-ion batteries, Nano Lett. 13 (2013) 4715–4720.
[13] W. Lv, Z. Li, Y. Deng, Q.-H. Yang, F. Kang, Graphene-based materials for electrochemical energy storage devices, Energy Storage Mater 2 (2016) 107–138.
[14] M. Zhao, S. Kariuki, H.D. Dewald, F.R. Lemke, R.J. Staniewicz, E.J. Plichta, R.A. Marsh, Electrochemical stability of copper in lithium-ion battery electrolytes, J. Electrochem. Soc. 147 (2000) 2874.
[15] C. Zhang, H. Song, C. Liu, Y. Liu, C. Zhang, X. Nan, G. Cao, Fast and reversible Li ion insertion in carbon-encapsulated Li_3VO_4 as anode for lithium-ion battery, Adv. Funct. Mater. 25 (2015) 3497–3504.
[16] Y. Yang, J. Li, X. He, J. Wang, D. Sun, J. Zhao, A facile spray drying route for mesoporous Li 3 VO 4/C hollow spheres as an anode for long life lithium ion batteries, J. Mater. Chem. A 4 (2016) 7165–7168.
[17] Q. Li, J. Sheng, Q. Wei, Q. An, X. Wei, P. Zhang, L. Mai, A unique hollow Li_3VO_4/carbon nanotube composite anode for high rate long-life lithium-ion batteries, Nanoscale 6 (2014) 11072–11077.
[18] Y. Yang, J. Li, D. Chen, J. Zhao, Spray drying-assisted synthesis of Li_3VO_4/C/CNTs composites for high-performance lithium ion battery anodes, J. Electrochem. Soc. 164 (2017) A6001–A6006.
[19] S. Ni, X. Lv, J. Zhang, J. Ma, X. Yang, L. Zhang, The electrochemical performance of lithium vanadate/natural graphite composite material as anode for lithium ion batteries, Electrochim. Acta 145 (2014) 327–334.
[20] S. Hu, Y. Song, S. Yuan, H. Liu, Q. Xu, Y. Wang, C.-X. Wang, Y.-Y. Xia, A hierarchical structure of carbon-coated Li_3VO_4 nanoparticles embedded in expanded graphite for high performance lithium ion battery, J. Power Sources 303 (2016) 333–339.
[21] J. Liu, P.-J. Lu, S. Liang, W. Wang, M. Lei, S. Tang, Q. Yang, Ultrathin Li_3VO_4 nanoribbon/graphene sandwich-like nanostructures with ultrahigh lithium ion storage properties, Nano Energy 12 (2015) 709–724.
[22] X. Jin, B. Lei, J. Wang, Z. Chen, K. Xie, F. Wu, Y. Song, D. Sun, F. Fang, Pomegranate-like Li_3VO_4/3D graphene networks nanocomposite as lithium ion battery anode with long cycle life and high-rate capability, J. Alloys Compd. 686 (2016) 227–234.
[23] Q. Li, Q. Wei, J. Sheng, M. Yan, L. Zhou, W. Luo, R. Sun, L. Mai, Mesoporous Li_3VO_4/C submicron-ellipsoids supported on reduced graphene oxide as practical anode for high-power lithium-ion batteries, Adv. Sci. 2 (2015), 1500284.
[24] Q. Li, Q. Wei, Q. Wang, W. Luo, Q. An, Y. Xu, C. Niu, C. Tang, L. Mai, Self-template synthesis of hollow shell-controlled Li_3VO_4 as a high-performance anode for lithium-ion batteries, J. Mater. Chem. A 3 (2015) 18839–18842.
[25] H. Li, H. Zhou, Enhancing the performances of Li-ion batteries by carbon-coating, Chem. Commun. 48 (2012) 1201–1217.
[26] R. Qin, G. Shao, J. Hou, Z. Zheng, T. Zhai, H. Li, One-pot synthesis of Li_3VO_4@C nanofibers by electrospinning with enhanced electrochemical performance for lithium-ion batteries, Sci. Bull. 62 (2017) 1081–1088.
[27] C. Liao, Y. Wen, B. Shan, T. Zhai, H. Li, Probing the capacity loss of Li_3VO_4 anode upon Li insertion and extraction, J. Power Sources 348 (2017) 48–56.
[28] G. Shao, L. Gan, Y. Ma, H. Li, T. Zhai, Enhancing the performance of Li_3VO_4 by combining nanotechnology and surface carbon coating for lithium ion batteries, J. Mater. Chem. A 3 (2015) 11253–11260.
[29] C. Xu, W. Xiang, Z. Wu, Y. Xu, Y. Li, Y. Wang, Y. Xiao, X. Guo, B. Zhong, Highly stabilized Ni-rich cathode material with Mo induced epitaxially grown nanostructured hybrid surface for high-performance lithium-ion batteries, ACS Appl. Mater. Interfaces 11 (2019) 16629–16638.
[30] J. Xia, W. Wu, K. Fang, X. Wu, Enhancing the interfacial stability of P2-type cathodes by polydopamine-derived carbon coating for achieving performance improvement, Carbon 157 (2020) 693–702.
[31] C. Li, H.P. Zhang, L.J. Fu, H. Liu, Y.P. Wu, E. Rahm, R. Holze, H.Q. Wu, Cathode materials modified by surface coating for lithium ion batteries, Electrochim. Acta 51 (2006) 3872–3883.
[32] R. Qian, Y. Liu, T. Cheng, P. Li, R. Chen, Y. Lyu, B. Guo, Enhanced surface chemical and structural stability of Ni-rich cathode materials by synchronous lithium-ion conductor coating for lithium-ion batteries, ACS Appl. Mater. Interfaces 12 (2020) 13813–13823.
[33] S. Ni, J. Zhang, J. Ma, X. Yang, L. Zhang, X. Li, H. Zeng, Approaching the theoretical capacity of Li_3VO_4 via electrochemical reconstruction, Adv. Mater. Interfaces 3 (2016), 1500340.
[34] Z. Liang, Y. Zhao, L. Ouyang, Y. Dong, Q. Kuang, X. Lin, X. Liu, D. Yan, Synthesis of carbon-coated Li_3VO_4 and its high electrochemical performance as anode material for lithium-ion batteries, J. Power Sources 252 (2014) 244–247.
[35] F. Heshmatpour, R.B. Aghakhanpour, Synthesis and characterization of nanocrystalline zirconia powder by simple sol–gel method with glucose and fructose as organic additives, Powder Technol. 205 (2011) 193–200.
[36] G.S. Zakharova, C. Täschner, T. Kolb, C. Jähne, A. Leonhardt, B. Büchner, R. Klingeler, Morphology controlled $NH_4V_3O_8$ microcrystals by hydrothermal synthesis, Dalton Trans. 42 (2013) 4897–4902.
[37] G. Vanhoyland, F. Bourée, M.K. van Bael, J. Mullens, L.C. van Poucke, Structure determination and refinement of acid strontium oxalate from X-ray and neutron powder diffraction, J. Solid State Chem. 157 (2001) 283–288.
[38] A.C. Ferrari, J. Robertson, Interpretation of Raman spectra of disordered and amorphous carbon, Phys. Rev. B 61 (2000) 14095–14107.
[39] A.C. Ferrari, J. Robertson, Raman spectroscopy of amorphous, nanostructured, diamond-like carbon, and nanodiamond, Philos. Trans. Royal Soc. A, Mathematical, physical, and engineering sciences 362 (2004) 2477–2512.
[40] G. Yang, B. Zhang, J. Feng, Y. Lu, Z. Wang, V. Aravindan, M. Aravind, J. Liu, M. Srinivasan, Z. Shen, Y. Huang, Morphology controlled lithium storage in Li_3VO_4 anodes, J. Mater. Chem. A 6 (2018) 456–463.
[41] J. Rouquerol, D. Avnir, C.W. Fairbridge, D.H. Everett, J.M. Haynes, N. Pernicone, J.D.F. Ramsay, K.S.W. Sing, K.K. Unger, Recommendations for the characterization of porous solids (Technical Report), Pure Appl. Chem. 66 (1994) 1739–1758.
[42] G.S. Zakharova, E. Thauer, S.A. Wegener, J.-H. Nölke, Q. Zhu, R. Klingeler, Hydrothermal microwave-assisted synthesis of Li_3VO_4 as an anode for lithium-ion battery, J. Solid State Electrochem. 23 (2019) 2205–2212.
[43] L.L. Zhou, S.-Y. Shen, X.-X. Peng, L.N. Wu, Q. Wang, C.-H. Shen, T.-T. Tu, L. Huang, J.-T. Li, S.-G. Sun, New insights into the structure changes and interface properties of Li_3VO_4 anode for lithium-ion batteries during the initial cycle by in-situ techniques, ACS Appl. Mater. Interfaces 8 (2016) 23739–23745.
[44] S. Flandrois, B. Simon, Carbon materials for lithium-ion rechargeable batteries, Carbon 37 (1999) 165–180.
[45] E. Iwama, N. Kawabata, N. Nishio, K. Kisu, J. Miyamoto, W. Naoi, P. Rozier, P. Simon, K. Naoi, Enhanced electrochemical performance of ultracentrifugation-derived nc-Li_3VO_4/MWCNT Composites for Hybrid Supercapacitors, ACS Nano 10 (2016) 5398–5404.
[46] P. Yan, J. Zheng, M. Gu, J. Xiao, J.-G. Zhang, C.-M. Wang, Intragranular cracking as a critical barrier for high-voltage usage of layer-structured cathode for lithium-ion batteries, Natu. commun 8 (2017), 14101.

Supplementary Information

Sol-gel synthesis of Li_3VO_4/C composites as anode materials for lithium-ion batteries

E. Thauer[1], G.S. Zakharova[2], S.A. Wegener[1], Q. Zhu[3], R. Klingeler[1,4]

[1] *Kirchhoff Institute of Physics, Heidelberg University, Heidelberg, Germany*

[2] *Institute of Solid State Chemistry, Ural Division, Russian Academy of Sciences, Yekaterinburg, Russia*

[3]*Institute of Material Science and Engineering, Wuhan University of Technology, Wuhan, PR China*

[4]*Centre for Advanced Materials, Heidelberg University, Heidelberg, Germany*

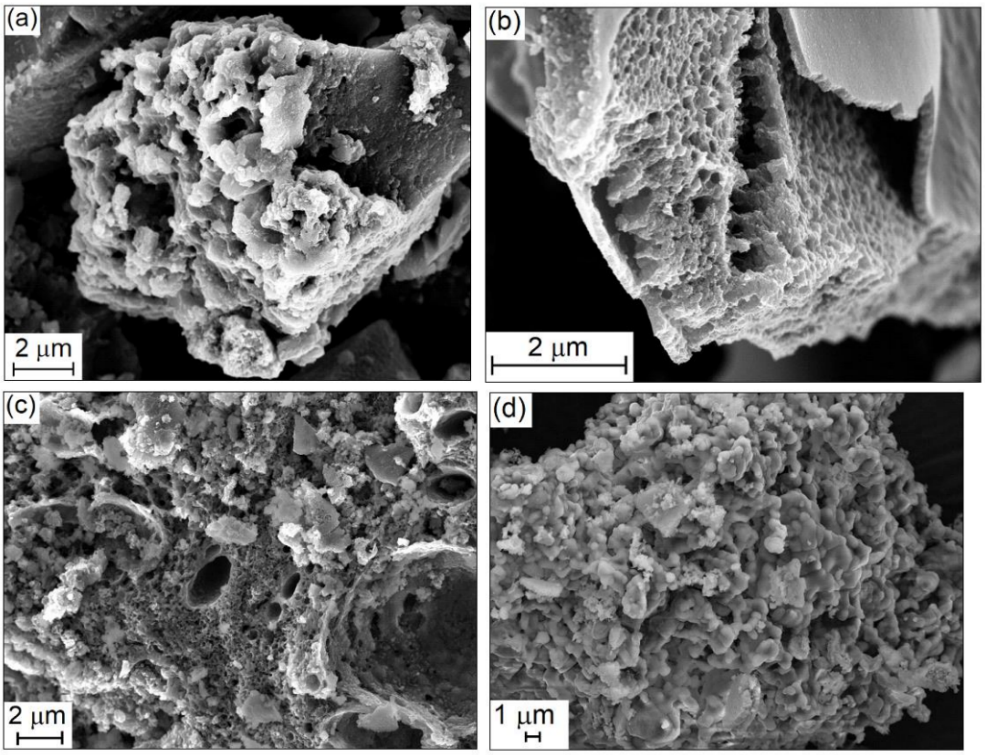

Fig. S1. SEM images of (a) Li_3VO_4/C-G, (b) Li_3VO_4/C-M, and (c) Li_3VO_4/C-T composites as well as of (d) bare Li_3VO_4.

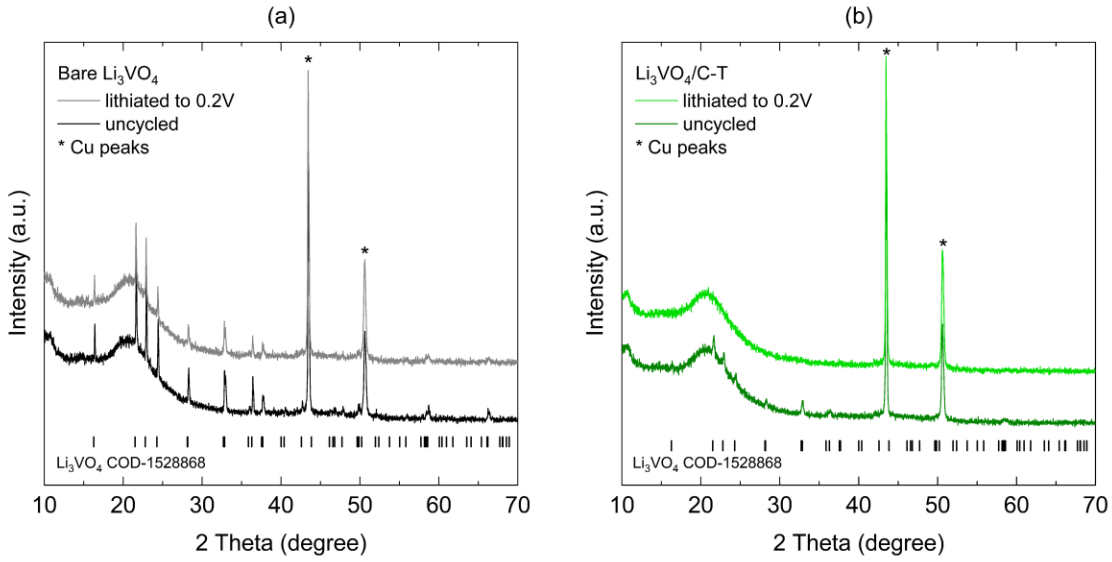

Fig. S2. *Ex-situ* XRD patterns (a) of a bare Li_3VO_4 electrode and (b) of a Li_3VO_4/C-T electrode (b) in uncycled and discharged state, respectively. The peaks marked with * originate from the Cu current collector.

Kapitel 3

Konversionsbasierte Übergangsmetalloxide

3.1 MoO_2/C composites prepared by tartaric acid and glucose-assisted sol-gel processes as anode materials for lithium-ion batteries

Autoren:

G.S. Zakharova, L. Singer, Z.A. Fattakhova, S.A. Wegener, E. Thauer, Q. Zhu, E.V. Shalaeva, R. Klingeler

veröffentlicht in Journal of Alloys and Compounds 863, 2021, 158353

abgedruckt mit freundlicher Genehmigung des Elsevier Verlags

E. Thauer führte gemeinsam mit dem Bachelorstudent S.A. Wegener unter ihrer Anleitung die Untersuchung mittels REM sowie die elektrochemische Charakterisierung der unbehandelten Materialien durch und übernahm die finale Korrektur des Manuskripts.

G.S. Zakharova und L. Singer teilen sich die Erstautorenschaft zu gleichen Teilen. Das Manuskript wurde mit Ausnahme der Teile zu den elektrochemischen Untersuchungen von G.S. Zakharova konzipiert und verfasst. G.S. Zakharova führte die Charakterisierung mittels XRD, Raman- und Infrarot-Spektroskopie sowie die TGA durch und erstellte die Abb. 1 - 5. L. Singer verfasste den Teil zu den elektrochemischen Messungen, erstellte die Abb. 6 - 7 sowie Abb. S1 - S4 und übernahm die Gesamtkorrektur des Manuskripts. L. Singer führte die REM- und elektrochemischen Messungen der nachbehandelten Probe, einschließlich der *ex-situ* REM-Messungen. Z.A. Fattakhova führte die Synthese durch. Q. Zhu und E.V. Shalaeva übernahmen die TEM-Messungen. R. Klingeler ist der Korrespondenzautor, betreute das Projekt und war an der Finalisierung des Manuskripts beteiligt. Die Korrespondenz mit den Gutachtern sowie die Überarbeitung des Manuskripts wurde von G.S. Zakharova, L. Singer und R. Klingeler übernommen. Alle Autoren haben das Manuskript korrekturgelesen.

Journal of Alloys and Compounds 863 (2021) 158353

Contents lists available at ScienceDirect

Journal of Alloys and Compounds

journal homepage: www.elsevier.com/locate/jalcom

MoO_2/C composites prepared by tartaric acid and glucose-assisted sol-gel processes as anode materials for lithium-ion batteries

G.S. Zakharova[a,1], L. Singer[b,1], Z.A. Fattakhova[a], S. Wegener[b], E. Thauer[b], Q. Zhu[c], E.V. Shalaeva[a], R. Klingeler[b,d,*]

[a] Institute of Solid State Chemistry, Ural Division, Russian Academy of Sciences, Yekaterinburg, Russia
[b] Kirchhoff Institute of Physics, Heidelberg University, Heidelberg, Germany
[c] Institute of Material Science and Engineering, Wuhan University of Technology, Wuhan, PR China
[d] Centre for Advanced Materials (CAM), Heidelberg University, Heidelberg, Germany

ARTICLE INFO

Article history:
Received 28 October 2020
Received in revised form 10 December 2020
Accepted 11 December 2020
Available online 9 January 2021

Keywords:
Molybdenum dioxide
Composite
Tartaric acid
Glucose
Sol-gel method
Lithium-ion battery

ABSTRACT

MoO_2/C-composites have been fabricated for the first time by a tartaric acid/glucose-assisted sol-gel method with post-annealing at 500 °C for 1 h in N_2 flow. The synthesized materials were fully characterized with respect to structure, morphology, and electrochemical properties. Compared with tartaric acid-assisted products, the adoption of glucose as carbon source effectively increases the carbon content in the composites. Irrespective of the organic component, the composites exhibit low crystallinity and small grain size. This results in good electrochemical performance of the anode materials as confirmed for the glucose-assisted materials which after additional post treatment delivers a competitive electrochemical capacity.

1. Introduction

Molybdenum dioxide (MoO_2), as an important semiconductor, has great potential applications in the production of chemical sensors [1], catalysts [2], field emission devices [3,4], and solar cells [5]. Additionally, MoO_2 has attracted considerable attention as electrode material for lithium ion batteries (LIB) because of its relatively large theoretical capacity (838 mA h g^{-1}) [6] and its high metallic conductivity ($6.04 \cdot 10^3$ S cm^{-1} for the individual rods) [7]. However, several of its intrinsic material properties limit the practical application of bulk MoO_2, namely strong capacity fading and poor cycling stability originated by the huge volume changes during the charge/discharge processes as well as poor rate performance caused by the slow kinetics [8,11]. A variety of strategies have been employed to overcome this issue such as preparation of nanosized materials with different morphologies [9], doping with nitrogen [10], copper [11], and design of 3D hierarchically structures nanomaterials providing shorter lithium ion/electron diffusion distances and accommodating strain associated with strong volume changes upon cycling [12,13]. Additionally, incorporating MoO_2 with functional conductive carbonaceous materials like hollow carbon spheres [14], graphene [15], graphite oxide [16], is regarded as an effective strategy. A further way which advantageously yields homogeneous distribution of the carbon component, thereby increasing cycling stability of the materials is to introduce the carbonaceous phase during calcination of many different organic precursors such as aniline [17], dopamine [18,19], polyethylene glycol [20], alginate [21], ascorbic acid [22], glucose [23], or sucrose [24]. All functionalized materials display enhanced Li-retention performance in comparison with bulk MoO_2, based on their higher surface areas, more actives sites, shorter ion diffusion paths, and functioning carbon buffer which accommodate the strain.

Various techniques, such as a hydrothermal method [25,26], thermolysis [27], and electrospinning [28], have been developed to prepare composites based on MoO_2. Herein, we present a new sol-gel synthesis approach to obtain MoO_2/C composites. This method provides a molecular level-mixing of the starting materials and leads to better chemical homogeneity of the final products. Carbon coated MoO_2 particles have been produced by using glucose or tartaric acid

* Corresponding author at: Kirchhoff Institute of Physics, Heidelberg University, Heidelberg, Germany.
E-mail address: r.klingeler@kip.uni-heidelberg.de (R. Klingeler).
[1] Both authors contributed equally.

https://doi.org/10.1016/j.jallcom.2020.158353
0925-8388/

as both reducing agents and carbon sources and the electrochemical performance of the resulting MoO_2/C composites as electrodes for Li-ion batteries was investigated.

2. Experimental

Molybdenum powder Mo (99.95% metal, Alfa Aesar), hydrogen peroxide H_2O_2 (30%, Merck), tartaric acid $C_4H_6O_6$ (AppliChem), and glucose $C_6H_{12}O_6$ (Sigma-Aldrich) were utilized for the synthesis. Firstly, 1.0 g of Mo powder was dissolved in 35 ml H_2O_2 at 10–15 °C to form a clear yellow solution of peroxomolybdic acid. Secondly, tartaric acid was dissolved in distilled water and stirred for 10 min. The molar ratio of tartaric acid to molybdenum metal was 1: 1. Then, the solution of tartaric acid was slowly added into the solution of peroxomolybdic acid. To get a gel, the solution was heated at 60 °C under continuous stirring. The resulting gel was dried at 60 °C in air and calcinated at 500 °C for 1 h in N_2 flow to yield the MoO_2/C composite. At lower annealing temperatures, the materials were amorphous while annealing at 500 °C yields crystalline samples. The as-prepared product is labeled as MoO_2/C-T. For comparison, MoO_2/C was produced in a glucose-assisted process at a molar ratio of Mo: glucose = 1: 1 and denoted as MoO_2/C-G. To study the effect of pounding on the electrochemical activity, MoO_2/C-G powder was colloidally grinded (300 Us^{-1}) in ethanol using **Ø** 1 mm ZrO_2 balls in a PM 100 planetary mill (Retsch) for 6 h, later annealed at 500 °C for 1 h in N_2 and afterwards hand grinded in a mortar for 15 min; this sample is labeled as MoO_2/C-G(M).

X-ray diffraction (XRD) patterns were obtained on a Bruker AXS D8 Advance Eco using Cu Kα radiation with a step size of Δ2θ = 0.02°. The morphology of the powder was determined by a ZEISS Leo 1530 and a JEOL JSM-7610F scanning electron microscope (SEM), a JEOL JEM 2100 and a JEMe200 CX transmission electron microscope (TEM), respectively. In order to monitor the microstructural changes of MoO_2 upon cycling, ex-situ SEM studies were performed using a JEOL JSM-7610F scanning electron microscope. The cycled electrodes were disassembled in an Argon glove box, washed with ethylene carbonate and then dried overnight.

Fourier transform infrared (FT-IR) spectra were recorded using Spectrum One B (Perkin-Elmer) with an automatic diffuse reflectance accessory. A thoroughly ground sample was applied as a thin layer to a purpose-designed holder plate. Thermogravimetric analysis (TG-DSC-MS) with a heating rate of 10 K min^{-1} starting from room temperature up to 750 °C under flowing air was carried out using STA 449 F_3 Jupiter thermoanalyzer (Netzsch) coupled with a QMS 403 mass spectrometer. Raman spectra were measured with a Renishaw U1000 spectrometer at a laser wavelength of 532 nm.

Electrochemical measurements were carried out in Swagelok-type cells (see [29]). Working electrodes were prepared by mixing the active material, carbon black and polyvinylidene fluoride (PVDF) in N-methyl-2-pyrrolidinone (NMP) and stirred for 24 h before the resulting slurry was pasted on copper net current collectors. The as-prepared electrodes were dried in a vacuum oven (80 °C, 10 mbar) overnight, pressed and dried again. Fiberglass (Whatman GF/D) was used as separator and pure lithium metal foil (Aldrich) as counter electrode. The electrolyte was 1 M $LiPF_6$ in a mixture of ethylene carbonate and diethyl carbonate (1: 1 by weight). Cell assembly was carried out in an Ar-filled glovebox with controlled moisture and oxygen concentration. Cyclic voltammetry (CV) at a scan rate of 0.1 mV s^{-1} and galvanostatic cycling with potential limitation (GCPL) at specific currents of 100 mA g^{-1}, both in the voltage range of 0.01–3.0 V vs. Li/Li^+, were carried out on a VMP3 potentiostat (Bio-Logic) at 25 °C.

3. Results and discussion

Fig. 1 shows X-ray diffractograms of the synthesized materials, i.e., MoO_2/C-G, MoO_2/C-G(M), and MoO_2/C-T. All observed peaks correspond to monoclinic MoO_2 and are accordingly indexed in a monoclinic lattice system with space group $P2_1/c$. The post treatment of the as-prepared composite does not change its structure. The experimentally determined lattice parameters of MoO_2 in the composite MoO_2/C materials are in a good agreement with theoretical values from JCSD no. 72-4534 (cf. Table 1).

The XRD data exhibit broad diffraction peaks with rather weak intensity which suggests that MoO_2 formed in the composites displays poor crystallinity and small crystal size. The mean primary crystallite size of the as-synthesized samples can be estimated using Scherrer's equation [30]:

$$D = K\lambda/\Delta(2\theta)\cos\theta, \quad (1)$$

where D is the average grain size based on the particular reflecting crystal face (hkl) direction, K is a shape factor which can be approximated to 0.9, λ is the wavelength of the applied Cu Kα radiation, $\Delta(2\theta)$ is the full width at half-maximum of the diffraction peak, and θ is the Bragg angle. Analysis[2] of the (011), (200), and (022) peaks yield to a mean primary crystallite size of around 6 nm for MoO_2/C-G, MoO_2/C-G(M), and MoO_2/C-T composites under study. The crystal structure of monoclinic MoO_2 is depicted in Fig. 1. It consists of

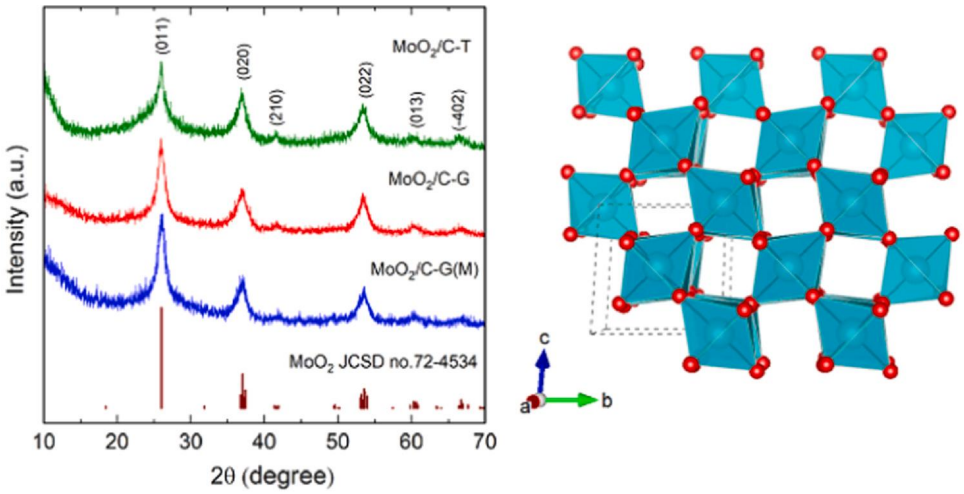

Fig. 1. XRD patterns of the MoO_2/C-G and the MoO_2/C-T composites (left), and a schematic of the corresponding crystal structure of MoO_2 (right).

Table 1
Experimentally determined lattice parameters of MoO_2 in MoO_2/C-G, MoO_2/C-G(M), and MoO_2/C-T as well as values from JCSD no. 72-4534.

	a (Å)	*b* (Å)	*c* (Å)	*β* (deg.)	*V* (Å^3)
MoO_2/C-G	5.652(6)	4.832(5)	5.594(7)	120.39(6)	131.7(3)
MoO_2/C-G(M)	5.679(5)	4.808(9)	5.619(8)	120.48(2)	132.2(3)
MoO_2/C-T	5.648(3)	4.912(6)	5.609(1)	119.24(7)	135.8(2)
MoO_2	5.6109	4.8562	5.6285	120.95	131.53

MoO_6 octahedrons which form channels along the *a*-axis which are supposed to facilitate Li^+ transport during electrochemical cycling.

Scanning electron microscopy images in Fig. 2 show the morphology of the as-prepared composites. Both as-prepared composite materials MoO_2/C-T and -G consist of irregular micro-sized agglomerates (Fig. 2a, c). The underlying primary particles, which are well visible in the high-magnification SEM images in Fig. 2b and d, in both composites consist of round grains with an average particle size of less than 20 nm. A further post treatment of the sample results in a visible size reduction of the agglomerates (Fig. 2e-f).

Additional detailed information on MoO_2/C-G is obtained from the TEM images in Fig. 3a. The images show the presence of MoO_2/C-G nanocrystallites forming large agglomerates that are dispersed in an amorphous carbon matrix. Lattice fringes visible in the high-resolution TEM (HR-TEM) image (Fig. 3b) indicate lattice display spacings of approximately 0.35 nm. This value corresponds well with the (011) plane of MoO_2 which according to our XRD analysis has a plane distance of 0.3417(3) nm in MoO_2/C-G. Fig. 3b also shows carbon layers of around 10 nm in thickness around the crystallites. Selected area electron diffraction (SAED) confirms the crystalline structure of MoO_2 in the MoO_2/C-G nanocomposite (Fig. 3c). Debye rings from the SAED pattern demonstrate the ultrafine structure of crystalline MoO_2 without any preferred orientation of the individual crystallites. The Debye rings can be attributed to the monoclinic phase of MoO_2 with $P2_1/c$ space group symmetry, which agrees with the XRD results.

Raman spectra of the MoO_2/C composites shown in Fig. 4a provide information on both the MoO_2 and the carbon components of the nanocomposite as the observed Raman peaks refer to Mo-O as well as carbon modes. The prominent carbon modes are the G-band which corresponds to the sp^2-bonded carbon atoms and the D-band associated with defects or disorder mainly due to sp^3-hybridization of carbon atoms [31]. The D- and G-bands of MoO_2/C-G composite arise at 1372 cm^{-1} and 1586 cm^{-1}, respectively. In comparison, the G- and D-bands of MoO_2/C-T are at slightly lower wavenumbers of 1365 and 1575 cm^{-1}. The ratio of the maximum intensities of these peaks, I_D/I_G, was calculated as 0.78 and 0.71 for MoO_2/C-G and MoO_2/C-T composites, respectively. This indicates that in comparison with tartaric acid, glucose promotes the formation of defects and disorder in the carbon component of the composite. In comparison with the pure MoO_2 phase [32], a richer Raman spectrum of MoO_2/C composites with intensive bands below 1000 cm^{-1} resulting from different vibration modes of Mo-O is observed. The presence of the peaks located at 819 and 993 cm^{-1} corresponding to the stretching vibrations of Mo=O bonds indicates the formation of the layered structure of the compounds similar to MoO_3 [33]. This phenomenon has been reported by Camacho-Lopez et al. [34] who associated it with the oxidation of MoO_2 to $MoO_{2+\delta}$ by laser irradiation.

FT-IR spectra of the MoO_2/C composites are shown in Fig. 4b. There are two typical vibration modes belonging to the MoO_2 phase [35]. The stretching vibrations of Mo=O bonds are demonstrated by the characteristic bands at 957 and 955 cm^{-1} for MoO_2/C-T and MoO_2/C-G composites, respectively. The bridge stretching vibration of Mo-O-Mo bonds are displayed by the bands at 718 and 693 cm^{-1} for MoO_2/C-T and MoO_2/C-G composites, respectively. The peaks at 1598 cm^{-1} (MoO_2/C-T) and 1600 cm^{-1} (MoO_2/C-G) are assigned to the C–O stretching vibration in the carboxylic group which may result from incomplete decomposition of the organic groups in the carbon component. The weak bands located at around 3400 cm^{-1} and 1640 cm^{-1} are associated with the stretching and bending vibrations of O–H, respectively, originating from trace amounts of adsorbed water in the powder. It is worth noting that the peaks which are attributed to pure glucose [36] and tartaric acid [37] are not part of the respective spectra.

In order to determine the thermal stability of MoO_2/C composites in air and to quantify the amount of carbon within the materials, TG-DSC-MS studies of as-prepared materials were carried out (Fig. 5). The TG curve of the MoO_2/C-G composite evidences two steps of weight loss (Fig. 5a). We attribute the first weight loss of 5.7 wt% in the temperature regime from 70 °C to 300 °C mainly to evaporation of water. It appears as a weak and broad endothermic process centered at 115 °C. The second weight loss of 23.7 wt% from 300 °C to 690 °C is caused by oxidation of carbon components and the release of CO_2 gases. The mass spectrometry curve (ion current versus temperature) indicates that the main gaseous product of MoO_2/C-G decomposition is CO_2 ($m/z = 44$ a.m.u.). However, the carbon component of MoO_2/C-G was not completely oxidized to CO_2 at 690 °C. Despite the appearance of a two-step process somehow similar to what is observed in MoO_2/C-G, the TG curve of MoO_2/C-T shown in Fig. 5b shows several differences. Again, a first stage from 25 to 300 °C with corresponding weight loss of 3.6 wt% can be assigned to evaporation of surface-adsorbed water. The second region of mass loss (2.4 wt%) from 300 to 514 °C is accompanied by a broad exothermal peak. It is attributed to the decomposition and full oxidation of organics. From the mass spectrometry curve, it can be revealed that the main gaseous product of MoO_2/C-T decomposition is CO_2 ($m/z = 44$ a.m.u.). Additionally, the three steps observed in TGA suggest that the carbon component in the MoO_2/C-T composite has three states differently bound to the main phase (MoO_2). At around 550 °C, the TG data indicate an increase of sample weight by 2.9 wt%. This process is attributed to the oxidation of Mo^{4+} to Mo^{6+} and results in the formation of MoO_3 as a final thermolysis product. Based on the assumptions made above, the calculated carbon contents in MoO_2/C-T and MoO_2/C-G composites are 2.4 and more than 23.7 wt %, respectively.

The electrochemical properties of the composite materials obtained as described are investigated with respect to their applicability as electrode materials in LIB by means of CV and GCPL. Fig. 6 displays the first, second, fifth CV curve of MoO_2/C-G and MoO_2/C-T. The reversible reactions of MoO_2 with lithium are described by the following electrochemical reactions [16,38]:

$$MoO_2 + xLi^+ + xe^- \leftrightarrow Li_xMoO_2, \quad (0 \le x \le 0.98) \tag{2}$$

$$Li_xMoO_2 + (4 - x)Li^+ + (4 - x)e^- \leftrightarrow Mo + 2Li_2O. \tag{3}$$

Due to the deliberate low crystallinity of the samples, mainly extended areas of electrochemical activity instead of well-defined peaks are visible in the CV. In the first reductive sweep of MoO_2/C-G, four different cathodic features are observed. The elevation at around 1.25 V (R1) can be attributed to the phase transition between the orthorhombic and the monoclinic phase upon lithium insertion (Eq. (2)) as suggested by Dahn et al. [39]. Due to the absence of the peak R2 at around 0.6 V in further cycles, it is most likely assigned to the solid electrolyte interface (SEI) formation which is consistent with reports by Luo et al. [40] and Xu et al. [41]. The reversible conversion reaction (Eq. (3)) can be assigned to the reduction peak R3, parts of R4 and the elevation O3 [38]. The two overlapping oxidation peaks O2 and O1 can be ascribed to the phase transitions (monoclinic-orthorhombic-monoclinic) in partially lithiated

[2] Additional contributions to peak broadening are neglected.

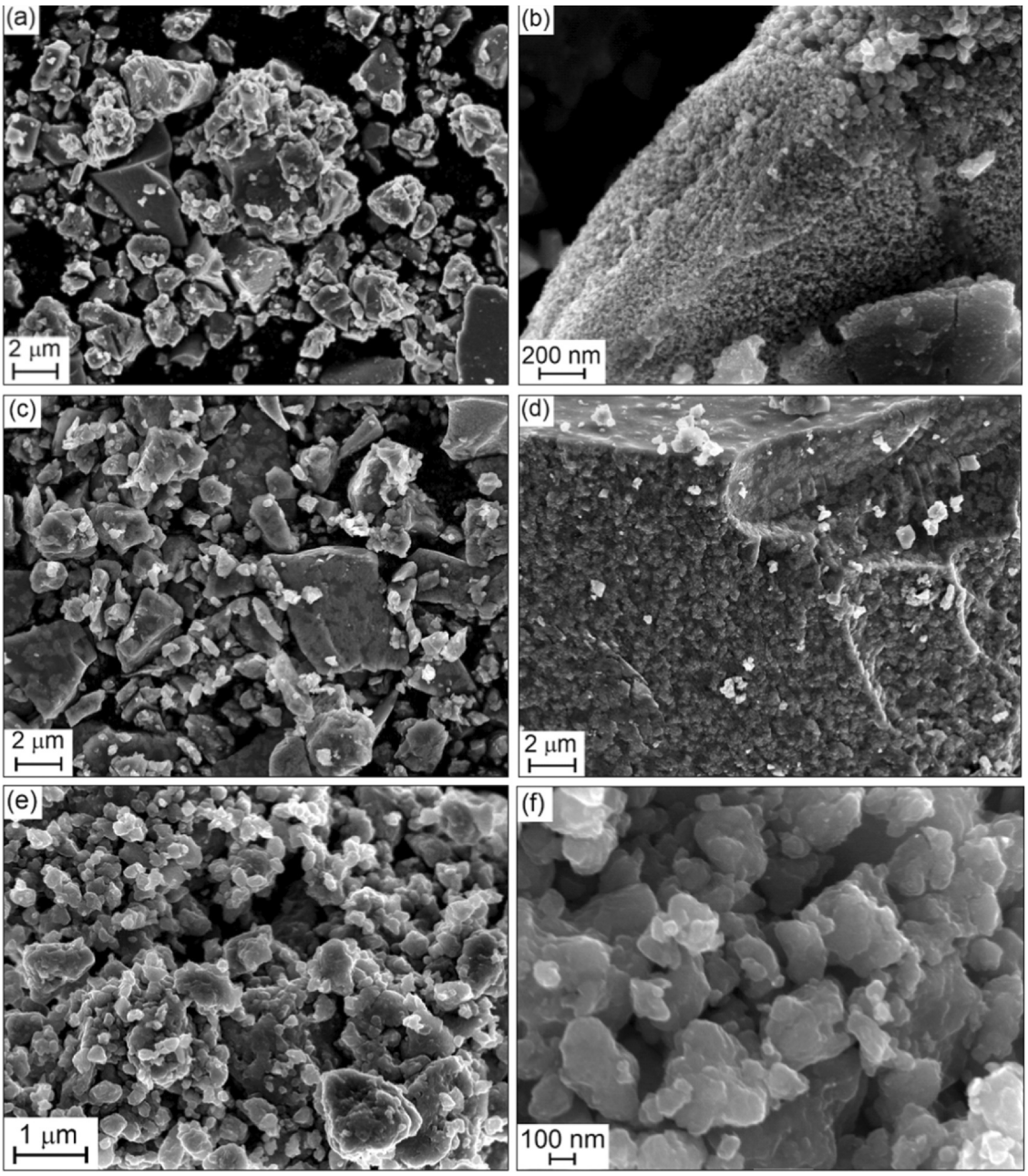

Fig. 2. SEM and high-magnification SEM images of (a, b) MoO_2/C-T, (c, d) MoO_2/C-G, and (e, f) MoO_2/C-G(M) obtained by a post treatment (see the text).

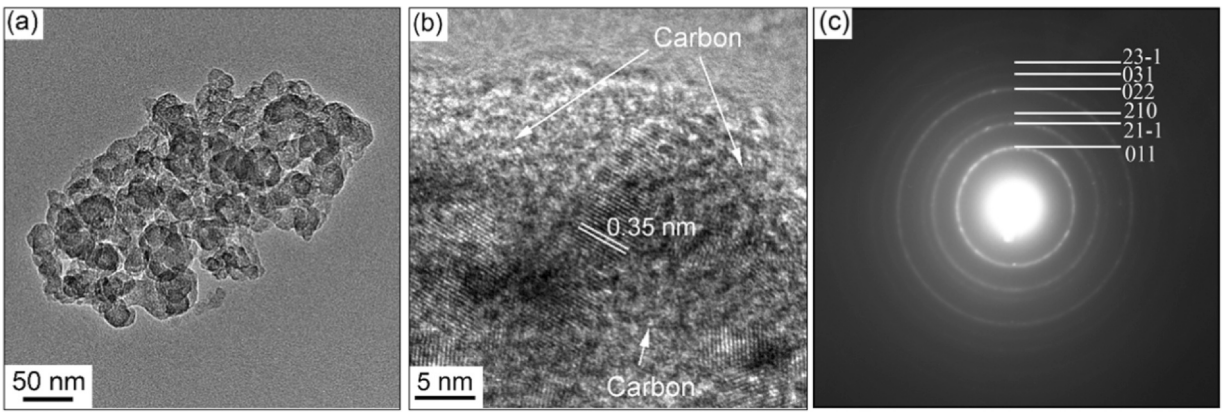

Fig. 3. (a) TEM image, (b) HRTEM image, and (c) SAED pattern of MoO_2/C-G composite.

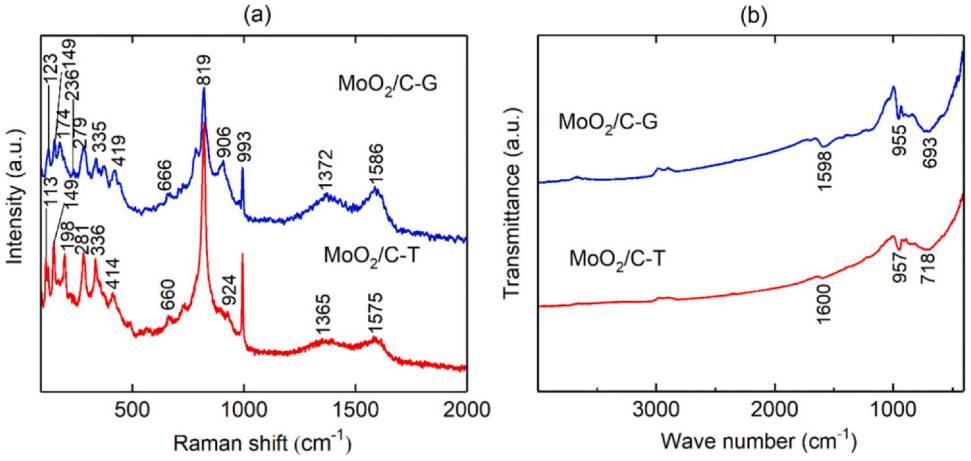

Fig. 4. (a) Raman and (b) FT-IR spectra of MoO_2/C-G and MoO_2/C-T composites.

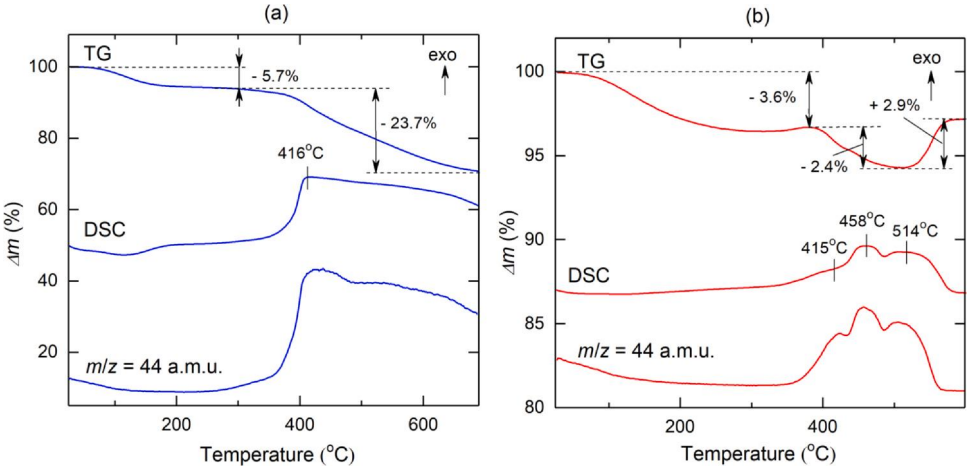

Fig. 5. Thermogravimety, DSC, and mass spectroscopy curves of (a) MoO_2/C-G and (b) MoO_2/C-T composites.

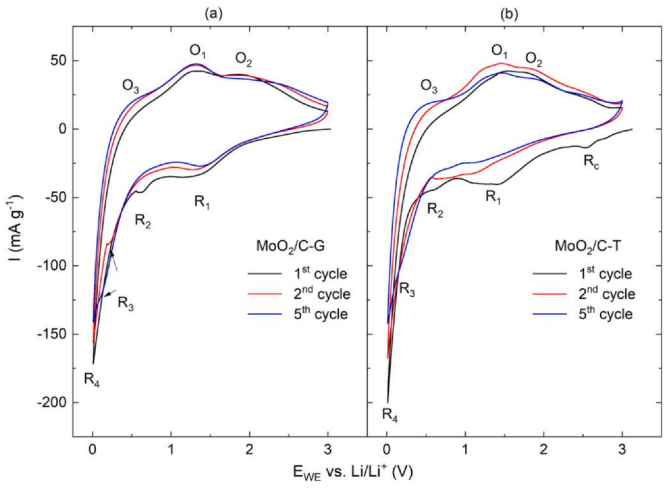

Fig. 6. Cyclic voltammograms of (a) MoO_2/C-G and (b) MoO_2/C-T composites recorded at a scan rate of 0.1 mV s^{-1}.

Li_xMoO_2 [42]. The main difference between the CV of MoO_2/C-G (Fig. 6a) and MoO_2/C-T (Fig. 6b) is the presence of the feature Rc at around 2.5 V in the first reductive sweep of the latter. In the literature, Rc is sometimes observed [27,43] and sometimes not [42,44] and its origin is yet unclear.

The cycling performance of as-prepared MoO_2/C-G- and MoO_2/C-T- as well as of MoO_2/C-G(M)-based electrodes is presented in Fig. 7a. The corresponding potential profiles are shown in Figs. S1-S3. The electrochemical performance of the MoO_2/C composites show strong differences. The highest discharge capacity in the first and twentieth cycle of 928 mAh g^{-1} and 610 mAh g^{-1} is reached by the post treated sample MoO_2/C-G(M). In contrast, the as-prepared material MoO_2/C-G achieves 516/195 mAh g^{-1}, respectively. Coulombic efficiencies also shown in Fig. 7a confirm significant irreversible effects not only for MoO_2/C-T but also for MoO_2-/C-G. All materials display reduced Coulombic efficiency in the first cycles which is attributed to common irreversible processes as electrolyte decomposition and formation of the SEI [22,40,41]. Similarly to what is concluded from the evolution of capacity upon cycling, Coulombic efficiencies for MoO_2/C-G(M) are highest and amount to about 98%. MoO_2/C-T has in comparison to MoO_2/C-G a high initial discharge capacity of 617 mAh g^{-1} but shows a much severe drop in capacity already in the second cycle. We attribute this to the much lower (i.e., by more than 20%) carbon content. Such a low carbon content may result in an increased contact loss between the active material and the current collector during cycling. This degeneration process is well known for conversion-type materials and occurs due to the volume expansion and the associated induced pulverization during the conversion reaction [45–47]. Comparison of the treated and untreated MoO_2/C-G samples shows that the post treated sample MoO_2/C-G(M), which features a reduced size of the agglomerates (Fig. 2e-f), achieves nearly 2 times the capacity of MoO_2/C-G over all

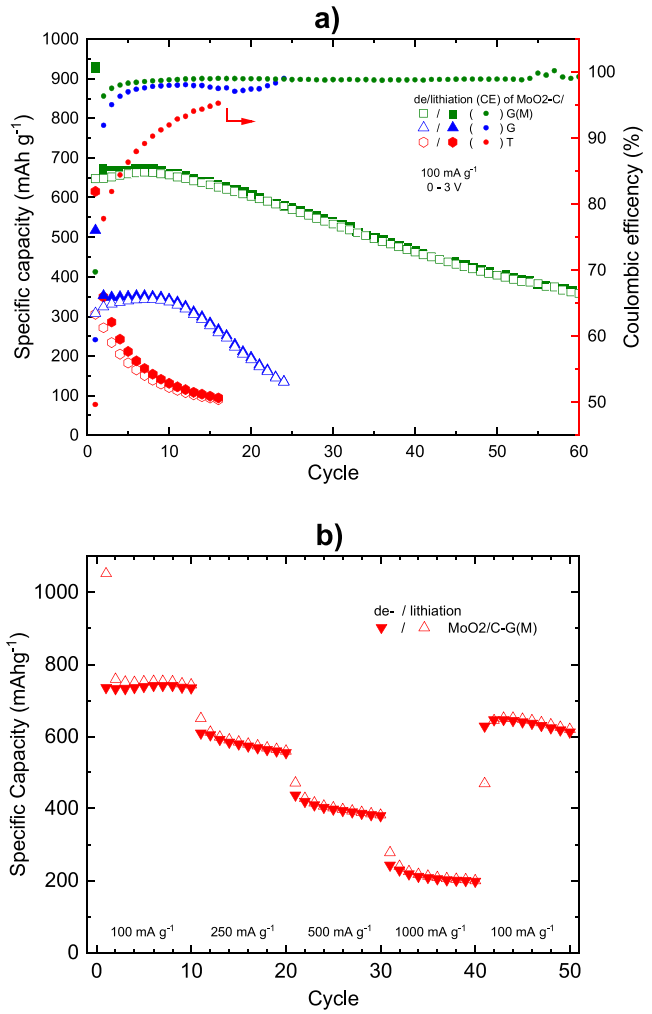

Fig. 7. a) Specific charge/discharge capacities and associated coulombic efficiencies of MoO_2/C electrodes and b) rate capability test with different cycling rates of MoO_2/C-G(M) electrode measured by GCPL between 0.01 V and 3 V.

cycles. As expected, the size reduction of the agglomerates by the post treatment and the associated surface enlargement leads to an increased electrochemical activity of MoO_2/C-G as electrolyte diffusion is facilitated [48]. The initial increase in capacity of the MoO_2/C-G samples may be attributed to a gradual decomposition of Li_xMoO_2 in the conversion reaction during cycling, the formation of crystalline defects which is a common phenomenon in oxide anodes resulting in increasing capacity, and/or a reaction including the SEI [43,49,50]. The rate capability of MoO_2/C-G(M) at cycle rates between 100 and 1000 mA g^{-1} displayed in Fig. 7b implies a reversible capacity of 740, 580, 400, and 210 mA h g^{-1}, at a current density of 100, 250, 50 and 1000 mA g^{-1}, respectively. The reversible capacitance reaches 650 mA h g^{-1} when the current density is set again to 100 mA g^{-1}, which proves good reversibility of the electrode. To characterize the microstructure details of the MoO_2/C-G(M) based electrode before and after galvanostatic cycling, *ex-situ* SEM measurements were performed (Fig. S4). The comparison of the SEM images before (Fig. S4a) and after (Fig. S4b) cycling reveals that the individual particles change their surface texture, which is likely due to the known degeneration mechanisms such as SEI formation [51] and/or agglomeration. Pulverization as a possible degeneration phenomenon for MoO_2/C-G(M) seems to be less critical as the high-resolution SEM images show that even after 60 cycles the binder network is intact and no clear cracks are visible.

To relate the electrochemical performance of the here presented MoO_2/C-G(M) composite to the literature, Table 2 lists the discharge capacities of various MoO_2/C composite anodes. The MoO_2/C-G(M)-based electrode studied at hand exhibits a superior electrochemical capacity compared to the materials obtained by Che *et al.* [21], Yoon *et al.* [52] and Luo *et al.* [40] and is slightly better than the materials reported by Sun et al. [53] and Hu *et al.* [54]. However, MoO_2/graphene oxide composite materials generally show higher capacities [16,41,55]. In contrast to these materials, the MoO_2/C-G(M) composite reported here benefits from a straightforward, environment-friendly, and well-controllable synthesis process, which is based on cost-effective starting materials. Evidently, the electrochemical performance of MoO_2/C composites mainly depends on morphological features as carbon coating, particle size and surface texture which are directly affecting the transport path length of electrons as well as Li-ions.

4. Conclusions

In summary, a tartaric acid and glucose based sol–gel method combined with thermal reduction has been utilized to synthesize hybrid MoO_2/C nanocomposites. This synthetic strategy is simple, cost-effective, and promising for large-scale industrial production of MoO_2/C composites. In the as-prepared composites, MoO_2 nanoparticles with a size of about 20 nm are embedded into a ~10 nm thick amorphous carbon matrix, which serves as a buffer layer preventing the degradation of MoO_2 nanoparticles during charge/discharge processes.

The observed electrochemical performances of the prepared materials underline the relevance of the used carbon source and the received morphology for the application in LIB. Compared to untreated MoO_2/C-G, post treated MoO_2/C-G(M) shows a clearly improved capacity. The post treated MoO_2/C-G(M) features a remarkably enhanced, competitive specific capacity of 660 mAh g^{-1} at 100 mA g^{-1} in the tenth cycle. Therefore, the results show that this simple and cost-effective synthesis approach may also be successfully applied to other metal oxides.

Table 2
Comparison of the electrochemical cycling performance of MoO_2 -based composites obtained by various synthesis methods.

Material	Synthesis method	Current (mA g^{-1})	Discharge capacity (mAh g^{-1})/cycle no[a]	Ref.
MoO_2/C-G(M) nanoparticles	Glucose-assisted sol-gel	100	660/10	this work
MoO_2/C nanoparticles	Alginate-assisted sol-gel	200	300/10	[21]
Nitrided MoO_2	hydrothermal	120	310/10	[52]
MoO_2/C nanofibers	Electrospinning	100	500/10	[40]
MoO_2/C nanoparticles	Impregnation of carbon matrix	100	600/10	[53]
MoO_2/graphite oxide nanoparticles	Solvothermal	100	620/10	[54]
MoO_2/graphite oxide nanoparticles	Solvothermal	100	800/10	[16]
MoO_2/C cage-like particle	Hydrothermal reduction	200	800/10	[22]
MoO_2/exfoliated graphene oxide	Solid-state graphenothermal reduction	100	850/10	[55]
MoO_2/graphene oxide	Decomposition	100	1200/10	[41]

[a] For better comparison, data from the same cycle number are shown as read-off from reported figures.

CRediT authorship contribution statement

G.Z.: Conceptualization, Investigation, Methodology, Writing - original draft, Writing - review & editing. **L.S.:** Investigation, Methodology, Writing - original draft, Writing - review & editing. **Z.F.**: Investigation. **S.W.**: Investigation. **E.T.**: Writing - review & editing. **Q.Z.**: Investigation. **E.V.:** Investigation. **R.K.:** Conceptualization, Supervision, Writing - review & editing.

Declaration of Competing Interest

The authors declare that they have no known competing financial interests or personal relationships that could have appeared to influence the work reported in this paper.

Acknowledgements

This work was supported by the Deutsche Forschungsgemeinschaft through projects KL 1824/12-1 and KL 1824/14-1. G.Z. acknowledges support of the state order via the Ministry of Science and High Education of Russia (Theme no. AAAA-A19-119031890025-9). Partial support by the BMWi through project 03ET6095C (HiKoMat) is acknowledged. The authors thank I. Glass for experimental support.

Appendix A. Supporting information

Supplementary data associated with this article can be found in the online version at doi:10.1016/j.jallcom.2020.158353.

References

[1] T. Yunusi, C. Yang, W. Cai, F. Xiao, J. Wang, X. Su, Synthesis of MoO_3 submicron belts and MoO_2 submicron spheres via polyethylene glycol-assisted hydrothermal method and their gas sensing properties, Ceram. Int. 39 (2013) 3435–3439.
[2] A. Bento, A. Sanches, E. Medina, C.D. Nunes, P.D. Vaz, MoO_2 nanoparticles as highly efficient olefin epoxidation catalysts, Appl. Catal. A 504 (2015) 399–407.
[3] J. Liu, Z. Zhang, C. Pan, Y. Zhao, X. Su, Y. Zhou, D. Yu, Enhanced field emission properties of MoO_2 nanorods with controllable shape and orientation, Mater. Lett. 58 (2004) 3812–3815.
[4] S.T. Nishanthi, A. Baruah, K.K. Yadav, D. Sarker, S. Ghosh, A.K. Ganguli, M. Jha, New low temperature environmental friendly process for the synthesis of tetragonal MoO_2 and its field emission properties, Appl. Surf. Sci. 467–468 (2019) 1148–1156.
[5] L. Li, H. Sui, K. Zhao, W. Zhang, X. Li, S. Liu, K. Yang, M. Wu, Y. Zhang, Preparation of carbon nanofibers supported MoO_2 composites electrode materials for application in dye-sensitized solar cells, Electrochim. Acta 259 (2018) 188–195.
[6] G. Xu, P. Liu, Y. Ren, X. Huang, Z. Peng, Y. Tang, H. Wang, Three-dimensional MoO_2 nanotextiles assembled from elongated nanowires as advanced anode for Li ion batteries, J. Power Sources 361 (2017) 1–8.
[7] Q. Xie, X. Zheng, D. Wu, X. Chen, J. Shi, X. Han, X. Zhang, G. Peng, Y. Gao, H. Huang, High electrical conductivity of individual epitaxially grown MoO_2 nanorods, Appl. Phys. Lett. 111 (2017) 093505.
[8] L.C. Yang, Q.S. Gao, Y. Tang, Y.P. Wu, R. Holze, MoO_2 synthesized by reduction of MoO_3 with ethanol vapor as an anode material with good rate capability for the lithium ion battery, J. Power Sources 179 (2008) 357–360.
[9] Y. Liang, Z. Yi, S. Yang, L. Zhou, J. Sun, Y. Zhou, Hydrothermal synthesis and lithium-intercalation properties of MoO_2 nano-particles with different morphologies, Solid State Ion. 177 (2006) 501–505.
[10] Huanhuan Sun, Yu Zhang, Huanyan Liu, Xingyuan Zhang, Jian-Gan Wang, Constructing hierarchical MoO2/N-doped carbon hydrangea-like spheres with superior lithium storage properties, J. Alloy. Compd. 787 (2019) 45–52.
[11] L. Zhang, W. He, M. Ling, K. Shen, Y. Liu, S. Guo, Cu@MoO_2@C nanocomposite with stable yolk-shell structure for high performance lithium-ion batteries, J. Alloy. Compd. 768 (2018) 714–721.
[12] X. Li, Q. Xiao, Y. Gao, H. Zhang, H. Xu, Y. Zhang, Hierarchical MoO_2/C microspheres: preparation and application as anode materials for lithium ion batteries, J. Alloy. Compd. 723 (2017) 1113–1120.
[13] P. Zhang, L. Zou, H. Hu, M. Wang, J. Fang, Y. Lai, J. Li, 3D hierarchical carbon microflowers decorated with MoO_2 nanoparticles for lithium ion batteries, Electrochim. Acta 250 (2017) 219–227.
[14] Xingyuan Zhanga, Jian-Gan Wanga, Wei Huaa, Hongzhen Liua, Bingqing Weiaa, Hierarchical nanocomposite of hollow carbon spheres encapsulatingnano-MoO_2 for high-rate and durable Li-ion storage, J. Alloy. Compd. 787 (2019) 301–308.
[15] K.H. Seng, G.D. Du, L. Li, Z.X. Chen, H.K. Liu, Z.P. Guo, Facile synthesis of graphene–molybdenum dioxide and its lithium storage properties, J. Mater. Chem. 22 (2012) 16072–16077.
[16] Y. Xu, R. Yi, B. Yuan, X. Wu, M. Dunwell, Q. Lin, L. Fei, S. Deng, P. Andersen, D. Wang, H. Luo, High capacity MoO_2/graphite oxide composite anode for lithium-ion batteries, J. Phys. Chem. Lett. 3 (2012) 309–314.
[17] Q. Gao, L. Yang, X. Lu, J. Mao, Y. Zhang, Y. Wu, Y. Tang, Synthesis, characterization and lithium-storage performance of MoO_2/carbon hybrid nanowires, J. Mater. Chem. 20 (2010) 2807–2812.
[18] Y. Qi, B. Zhou, X. Yang, Y. Zhou, W. Jin, J. Zhou, W. Chen, 3D microstructures with MoO_2 nanocrystallines embedded into interpenetrated carbon nanosheets for lithium ion batteries, J. Mater. Sci. Mater. Electron. 29 (2018) 11521–11528.
[19] P. Zhang, L. Zou, H. Hu, M. Wang, J. Fang, Y. Lai, J. Li, 3D hierarchical carbon microflowers decorated with MoO_2 nanoparticles for lithium ion batteries, Electrochim. Acta 250 (2017) 219–227.
[20] X. Li, Q. Xiao, Y. Gao, H. Zhang, H. Xu, Y. Zhang, Hierarchical MoO_2/C microspheres: preparation and application as anode materials for lithium ion batteries, J. Alloy. Compd. 723 (2017) 1113–1120.
[21] Y. Che, X. Zhu, J. Li, J. Sun, Y. Liu, C. Jin, C. Dong, Simple synthesis of MoO_2/carbon aerogel anodes for high performance lithium ion batteries from seaweed biomass, RSC Adv. 6 (2016) 106230–106236.
[22] B. Liu, X. Zhao, Y. Tian, D. Zhao, C. Hu, M. Cao, A simple reduction process to synthesize MoO_2/C composites with cage-like structure for high performance lithium-ion batteries, Phys. Chem. Chem. Phys. 15 (2013) 8831–8837.
[23] J. Ni, Y. Zhao, L. Li, L. Mai, Ultrathin MoO_2 nanosheets for superior lithium storage, Nano Energy 11 (2015) 129–135.
[24] W. Cho, J.H. Song, J. Kim, G. Jeong, E.Y. Lee, Y. Kim, Electrochemical characteristics of nano-sized MoO_2/C composite anode materials for lithium-ion batteries, J. Appl. Electrochem. 42 (2012) 909–915.
[25] J. Jiang, W. Yang, Hao Wang, Y. Zhao, J. Guo, J. Zhao, M. Beidaghi, L. Gao, Electrochemical performances of MoO_2/C nanocomposite for sodium ion storage: an insight into rate dependent charge/discharge mechanism, Electrochim. Acta 240 (2017) 379–387.
[26] K. Palanisamy, Y. Kim, H. Kim, J.M. Kim, W. Yoon, Self-assembled porous MoO_2/graphene microspheres towards high performance anodes for lithium ion batteries, J. Power Sources 275 (2015) 351–361.
[27] L. Guo, Y. Wang, Standing carbon-coated molybdenum dioxide nanosheets on graphene: morphology evolution and lithium ion storage properties, J. Mater. Chem. A 3 (2015) 4706–4715.
[28] J. Xianga, Z. Wu, X. Zhang, S. Yao, Enhanced electrochemical performance of an electrospun carbon/MoO_2 composite nanofiber membrane as self-standing anodes for lithium-ion batteries, Mater. Res. Bull. 100 (2018) 254–258.
[29] A. Ottmann, G.S. Zakharova, B. Ehrstein, R. Klingeler, Electrochemical performance of single crystal belt-like $NH_4V_3O_8$ as cathode material for lithium-ion batteries, Electrochim. Acta 174 (2015) 682–687.
[30] A.L. Patterson, The Scherrer formula for X-Ray particle size determination, Phys. Rev. Lett. 56 (1939) 978–982.
[31] V. Wang, D.C. Alsmeyer, R.L. McCreery, Raman spectroscopy of carbon materials: structural basis of observed spectra, Chem. Mater. 2 (1990) 557–563.
[32] L. Kumari, Y.-R. Ma, C.-C. Tsai, Y.-W. Lin, S.Y. Wu, K.-W. Cheng, Y. Liou, X-ray diffraction and Raman scattering studies on large-area array and nanobranched structure of 1D MoO_2 nanorods, Nanotechnology 18 (2007) 115717.
[33] G.S. Zakharova, Ch Schmidt, A. Ottmann, E. Mijowska, R. Klingeler, Microwave-assisted hydrothermal synthesis and electrochemical studies of α- and h-MoO_3, J. Solid State Electrochem. 22 (2018) 3651–3661.
[34] M.A. Camacho-Lypez, L. Escobar-Alarcyn, M. Picquart, R. Arroyo, G. Cyrdoba, E. Haro-Poniatowski, Micro-Raman study of the m-MoO_2 to α-MoO_3 transformation induced by cw-laser irradiation, Opt. Mater. 33 (2011) 480–484.
[35] X. Wang, Y. Liu, J. Zeng, C. Peng, R. Wang, MoO_2/C hollow nanospheres synthesized by solvothermal method as anode material for lithium-ion batteries, Ionics 25 (2019) 437–445.
[36] F.O. Libnau, A.A. Christy, O.M. Kvalheim, Resolution of infrared spectra and kinetic analysis of mutarotation of D-glucose in water by sequential rank analysis, Vib. Spectrosc. 7 (1994) 139–148.
[37] N. Chumha, S. Kittiwachana, T. Thongtem, S. Thongtem, S. Kaowphong, Synthesis and characterization of $GdVO_4$ nanostructures by a tartaric acid-assisted sol–gel method, Ceram. Int. 40 (2014) 16337–16342.
[38] L. Yang, X. Li, Y. Ouyang, Q. Gao, L. Ouyang, R. Hu, J. Liu, M. Zhu, Hierarchical MoO_2/Mo_2C/C hybrid nanowires as high-rate and long-life anodes for lithium-ion batteries, ACS Appl. Mater. Interfaces 8 (2016) 19987–19993.
[39] J. Dahn, W. Mckinnon, Structure and electrochemistry of Li_xMoO_2, Solid State Ion. 23 (1987) 1–7.
[40] W. Luo, X. Hu, Y. Sun, Y. Huang, Electrospinning of carbon-coated MoO_2 nanofibers with enhanced lithium-storage properties, Phys. Chem. Chem. Phys. 13 (2011) 16735–16740.
[41] Z. Xu, K. Yao, H. Fu, X. Shen, X. Duan, L. Cao, J. Huang, H. Wang, Constructing MoO_2 porous architectures using graphene oxide flexible supports for lithium ion battery anodes, Glob. Chall. 1 (2017) 1700050.
[42] L. Zhou, H. Wu, Z. Wang, X. Lou, Interconnected MoO_2 nanocrystals with carbon nanocoating as high-capacity anode materials for lithium-ion batteries, ACS Appl. Mater. Interfaces 3 (2011) 4853–4857.
[43] B. Guo, X. Fang, B. Li, Y. Shi, C. Ouyang, Y. Hu, Z. Wang, G. Stucky, L. Chen, Synthesis and lithium storage mechanism of ultrafine MoO_2 nanorods, Chem. Mater. 24 (2012) 457–463.

[44] Y. Sun, X. Hu, W. Luo, Y. Huang, Self-assembled hierarchical MoO_2/graphene nanoarchitectures and their application as a high-performance anode material for lithium-ion batteries, ACS Nano 5 (2011) 7100–7107.
[45] J. Li, S. Hwang, F. Guo, S. Li, Z. Chen, R. Kou, K. Sun, C. Sun, H. Gan, A. Yu, E. Stach, H. Zhou, D. Su, Phase evolution of conversion-type electrode for lithium ion batteries, Nat. Commun. 10 (2019) 2224.
[46] M. Ebner, F. Marone, M. Stampanoni, V. Wood, Visualization and quantification of electrochemical and mechanical degradation in Li ion batteries, Science 342 (2013) 716–720.
[47] A. Ottmann, M. Scholz, E. Thaue, P. Schneider, M. Gellesch, C. Nowka, S. Wurmehl, S. Hampel, R. Klingeler, Electrochemical magnetization switching and energy storage in manganese oxide filled carbon nanotubes, Sci. Rep. 7 (2017) 13625.
[48] C. Delacourt, P. Poizot, S. Levasseur, C. Masquelier, Size effects on carbon-free $LiFePO_4$ powders: the key to superior energy density, Electrochem. Solid State Lett. 9 (2006) A352–A355.
[49] Kun Chang, Dongsheng Geng, Xifei Li, Jinli Yang, Yongji Tang, Mei Cai, Ruying Li, Xueliang Sun, Ultrathin MoS_2/nitrogen-doped graphene nanosheets with highly reversible lithium storage, Adv. Energy Mater. 3 (2013) 839–844.
[50] Yan-Yan Hu1, Zigeng Liu, Kyung-Wan Nam, Olaf J. Borkiewicz, Jun Cheng, Xiao Hua1, Matthew T. Dunstan, Xiqian Yu, Kamila M. Wiaderek, Lin-Shu Du, Karena W. Chapman, Peter J. Chupas, Xiao-Qing Yang2, Clare P. Grey, Origin of additional capacities in metal oxide lithium-ion battery electrodes, Nat. Mater. 12 (2013).
[51] Fanyan Zeng, Maohui Yu, Wanting Cheng, Wenxiu He, Yang Pan, Yaohui Qu, Cailei Yuan, Tunable surface selenization on MoO_2-based carbon substrate for notably enhanced sodium-ion storage properties, Small 16 (2020) 2001905.
[52] Sukeun Yoon, Kyu-Nam Jung, Chang Soo Jin, Kyung-Hee Shin, Synthesis of nitrided MoO_2 and its application as anode materials for lithium-ion batteries, J. Alloy. Compd. 536 (2012) 179–183.
[53] Y. Sun, X. Hu, W. Luo, Y. Huang, Ultrafine MoO_2 nanoparticles embedded in a carbon matrix as a high-capacity and long-life anode for lithium-ion batteries, J. Mater. Chem. 22 (2012) 425–431.
[54] S. Hu, F. Yin, E. Uchaker, W. Chen, M. Zhang, J. Zhou, Y. Qi, G. Cao, Facile and green preparation for the formation of MoO_2-GO composites as anode material for lithium-ion batteries, J. Phys. Chem. C 118 (2014) 24890–24897.
[55] S. Petnikota, K.W. Teo, L. Chen, A. Sim, S.K. Marka, M.V. Reddy, V.V.S.S. Srikanth, S. Adams, B.V.R. Chowdari, Exfoliated graphene oxide/MoO_2; composites as anode materials in lithium-ion batteries: an insight into intercalation of Li and conversion mechanism of MoO_2, ACS Appl. Mater. Interfaces 8 (2016) 10884–10896.

Supplement Information:

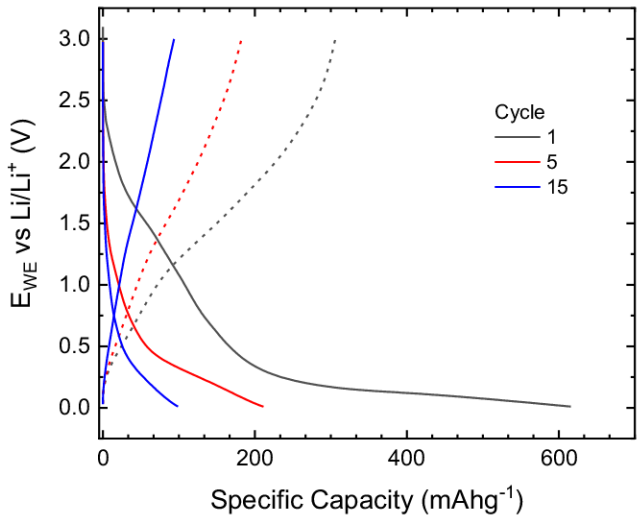

Fig. S1. Potential profile of MoO_2/C-T at current densities of 100 mA g^{-1}.

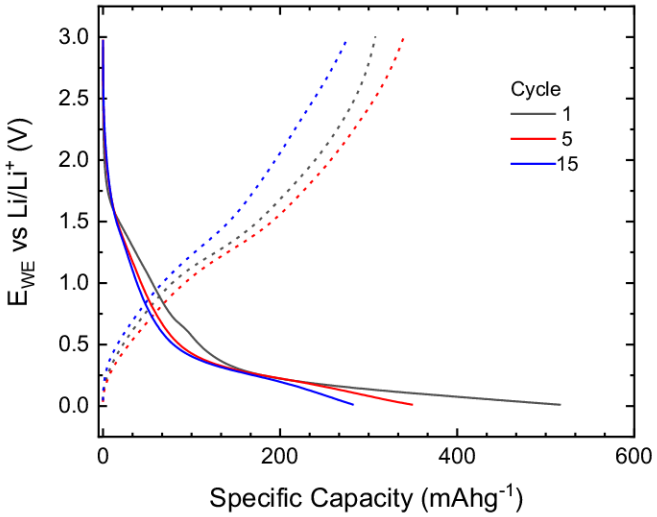

Fig. S2. Potential profile of MoO_2/C-G at current densities of 100 mA g^{-1}.

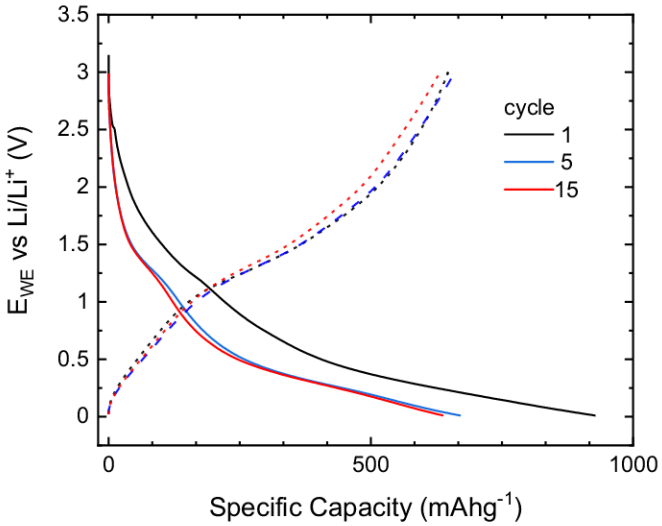

Fig. S3. Potential profile of MoO_2/C-G(M) at current densities of 100 mA g^{-1}.

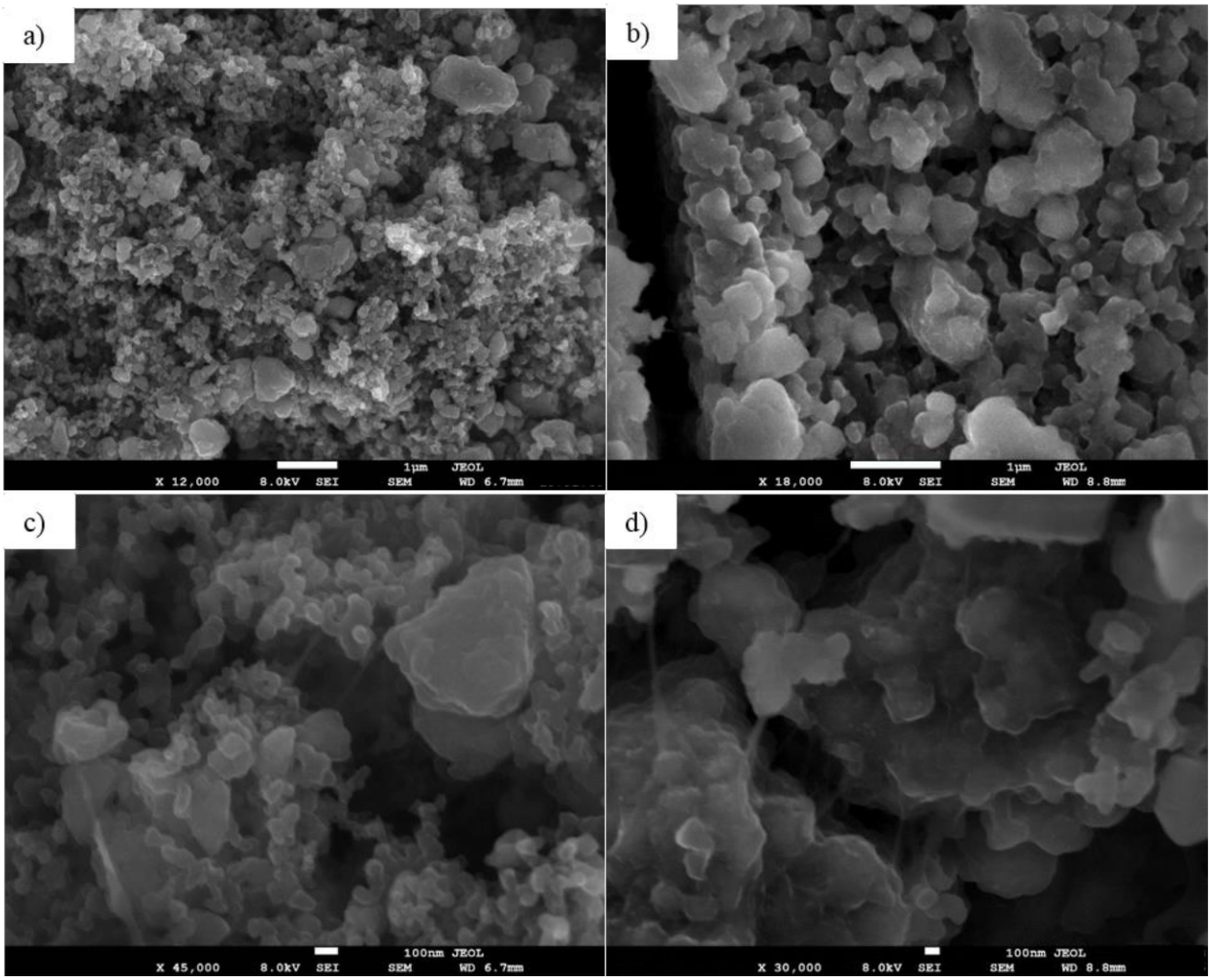

Fig. S4. Ex-situ SEM pictures of a MoO2-C/G(M) electrode after OCV (a,c) and after 60th times galvanostatically cycled at 100 mA/g (b,d).

3.2 V_2O_3/C composite fabricated by carboxylic acid-assisted sol-gel synthesis as anode material for lithium-ion batteries

Autoren:

G.S. Zakharova, E.Thauer, A.N. Enyashin, L.F. Deeg, Q. Zhu, R. Klingeler

veröffentlicht in Journal of Sol-Gel Science and Technology, 2021

E. Thauer ist die Korrespondenzautorin. Die Charakterisierung mittels XRD und REM sowie alle elektochemischen Messungen und deren Analyse erfolgten gemeinsam von E. Thauer und dem Masterstudent L.F. Deeg unter ihrer Anleitung. E.Thauer konzipierte und verfasste die zugehörigen Teile des Manuskripts und erstellte die Abb. 1 a, Abb. 5 und Abb. S1 - S3. E. Thauer übernahm die Gesamtkorrektur des Manuskripts und war an der Finalisierung beteiligt. Die Korrespondenz mit den Gutachtern sowie die Überarbeitung des Manuskripts wurde von E. Thauer zusammen mit G.S. Zakharovs und R. Klingeler übernommen.

G.S. Zakharova ist die Erstautorin dieses Artikels. G.S. Zakharova konzipierte und verfasste das Manuskript mit Ausnahme der Teile zu den elektrochemischen Untersuchungen sowie zu den Dichtefunktionaltheorie-Kalkulationen und erstellte die Abb. 1 - 4 und Abb. S1 - S2. Die Synthese der Materialien und die Untersuchungen mittels Raman-Spektroskopie, TGA und BET-Messung erfolgte von G.S. Zakharova. Q. Zhu führte die TEM-Messungen durch. A.N. Enyashin übernahm die Kalkulationen auf Basis der Dichtefunktionaltheorie (DFT) und verfasste den zugehörigen Teil im Manuskript (Abb. S3). R. Klingeler betreute das Projekt, stand beratend zur Seite und war an der Finalisierung des Manuskripts beteiligt. Alle Autoren haben das Manuskript korrekturgelesen.

Journal of Sol-Gel Science and Technology
https://doi.org/10.1007/s10971-021-05523-z

ORIGINAL PAPER: NANO-STRUCTURED MATERIALS (PARTICLES, FIBERS, COLLOIDS, COMPOSITES, ETC.)

V_2O_3/C composite fabricated by carboxylic acid-assisted sol–gel synthesis as anode material for lithium-ion batteries

G. S. Zakharova[1] · E. Thauer[2] · A. N. Enyashin[1] · L. F. Deeg[2] · Q. Zhu[3] · R. Klingeler[2,4]

Received: 15 February 2021 / Accepted: 10 March 2021

Abstract

The potential battery electrode material V_2O_3/C has been prepared using a sol–gel thermolysis technique, employing vanadyl hydroxide as precursor and different organic acids as both chelating agents and carbon sources. Composition and morphology of resultant materials were characterized by X-ray diffraction, Raman spectroscopy, scanning and transmission electron microscopies, physical sorption, and elemental analysis. Stability and electronic properties of model composites with chemically and physically integrated carbon were studied by means of quantum-chemical calculations. All fabricated composites are hierarchically structured and consist of carbon-covered microparticles assembled of polyhedral V_2O_3 nanograins with intrusions of amorphous carbon at the grain boundaries. Such V_2O_3/C phase separation is thermodynamically favored while formation of vanadium (oxy)carbides or heavily doped V_2O_3 is highly unlikely. When used as anode for lithium-ion batteries, the nanocomposite V_2O_3/C fabricated with citric acid exhibits superior electrochemical performance with an excellent cycle stability and a specific charge capacity of 335 mAh g^{-1} in cycle 95 at 100 mA g^{-1}. We also find that the used carbon source has only minor effects on the materials' electrochemical performance.

Graphical Abstract

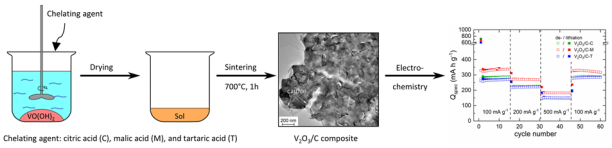

Keywords Anode material · Composites · Lithium-ion batteries · Sol–gel processes · V_2O_3

Supplementary information The online version contains supplementary material available at https://doi.org/10.1007/s10971-021-05523-z.

✉ E. Thauer
elisa.thauer@kip.uni-heidelberg.de

[1] Institute of Solid State Chemistry, Ural Division, Russian Academy of Sciences, Yekaterinburg, Russia

[2] Kirchhoff Institute of Physics, Heidelberg University, Heidelberg, Germany

[3] School of Material Science and Engineering, Wuhan University of Technology, Wuhan, China

[4] Centre for Advanced Materials, Heidelberg University, Heidelberg, Germany

Published online: 01 April 2021

Highlights

- V_2O_3/C composites were synthesized by a facile sol–gel thermolysis method.
- Citric acid, malic acid, and tartaric acid have been applied as both the chelating agents and as carbon source to produce V_2O_3/C composites for the first time.
- DFT calculations confirmed preference of phase separation in C-doped V_2O_3.
- V_2O_3/C composites as anode material exhibit an excellent cycle stability.

1 Introduction

Vanadium trioxide V_2O_3 has been widely studied in fundamental research since the first reports on its metal-to-insulator transition [1]. Regarding application, due to its high theoretical capacity (1070 mAh g^{-1}), low cost, and non-toxicity V_2O_3 is well recognized as a promising anode material for rechargeable lithium-ion batteries (LIBs) [2–4]. However, the practical use of the bulk V_2O_3 as anode materials in LIBs is greatly hindered due to huge volume changes appearing upon electrochemical cycling [5]. A variety of functionalization options has been explored to overcome this issues: incorporation of carbon containing compounds yielding composite materials including the preparation of nanosized materials with the different morphology [6, 7], doping with nitrogen and sulfur [8–10], as well as a design of three-dimensional nanostructures providing shorter lithium-ion/electron diffusion distances as well as more stable structures preventing deterioration of electrodes during the discharge/charge processes [11–16].

Both the preparation process and the post-treatment conditions have a significant influence on the electrochemical performances of V_2O_3/C hybrid materials as an anode material. For example, V_2O_3/C composites prepared by a NaCl template-assisted freeze-drying strategy deliver a capacity of 706 mAh g^{-1} at 5 A g^{-1}, after 2000 cycles [17], while electrospun materials show 100 mAh g^{-1} at 5000 A g^{-1} after 5000 cycles [18]. Among different kinds of carbon materials, there is a variety of reports using graphene oxide (rGO) as the carbon source [5, 19, 20], among them a polymer-pyrolysis made material with ~780 mAh g^{-1} over 100 cycles at 200 mA g^{-1} [21] and V_2O_3/rGO with 823 mAh g^{-1}, at 0.1 A g^{-1} [22]. Other V_2O_3/C composites have been fabricated by solvothermal synthesis using ethylene glycol as the carbon source (474 mAh g^{-1} at 0.5 A g^{-1} after 400 cycles) [23], a hydrothermal route and subsequent calcinations (283 mAh g^{-1} at 25 A g^{-1}) [24].

Here we report for the first time a sol–gel process with post-annealing treatment to synthesize a V_2O_3/C composite material using citric acid, tartaric acid, and malic acid as both the chelating agents and the carbon sources. In general, the sol–gel method has been extensively used to synthesize electrode materials due to their unique advantages such as low synthesis temperature, high purity and high homogeneous structure, and good electrochemical property of the synthesized product [25–28]. Our work shows that it can be exploited as facile method to synthesize hierarchically structured V_2O_3/C nanocomposite and we investigate in detail the influence of different carboxylic acids on the phase composition, morphology, and electrochemical properties of the products.

2 Experimental

2.1 Materials

Vanadyl sulfate hydrate $VOSO_4{\cdot}nH_2O$ (97% $VOSO_4$), ammonium hydroxide solution (28% NH_3 in H_2O), tartaric acid ($C_4H_6O_6$), malic acid ($C_4H_6O_5$), and citric acid ($C_6H_8O_7$) with analytical grade were purchased from Sigma-Aldrich and used without any further purification.

2.2 Synthesis of V_2O_3/C composites

V_2O_3/C composites were prepared using the sol–gel thermolysis process. The typical synthesis process is briefly described as follows. First, vanadyl hydroxide $VO(OH)_2$ precursor was prepared. According to the synthetic procedure, 7.95 g $VOSO_4{\cdot}nH_2O$ was dissolved in 400 mL of deionized H_2O using the magnetic stirring at room temperature, then ammonium hydroxide solution was added dropwise to adjust the pH value of the mixture so that it equals to 4. The brown precipitate was collected by centrifugation and washed several times with water, ethanol, and dried in air to obtain the $VO(OH)_2$ powder products. Second, $VO(OH)_2$ and carboxylic acid (citric acid, malic acid or tartaric acid) were weighed according to the molar ration of 1:1 and mixed well with each other in deionized 60 mL water under constantly stirring. The mixture then came to be a blue solution. The blue solution was evaporated at 80 °C for ~4 h, with a magnetic stirrer sequentially stirring to obtain a clear viscous sol and was subsequently dried to form a gel. The gel was further dried in a vacuum oven at 50 °C for 16 h, which led to a blue powder. Finally, the powder was sintered under a flow of N_2 gas at 400–700 °C for 1 h to obtain the V_2O_3/C composites. Depending on the type of the carboxylic acids, the resulting materials are denoted henceforth as V_2O_3/C-C, V_2O_3/C-M,

and V_2O_3/C-T, where carboxylic acid is citric acid, malic acid, and tartaric acid, respectively.

2.3 Characterization

X-ray diffraction (XRD) patterns were obtained using a Bruker AXS D8 Advance Eco diffractometer using CuKα radiation and applying the step size of $\Delta 2\theta = 0.02°$. The morphology of the powder was determined by a ZEISS Leo 1530 scanning electron microscope (SEM) as well as JEOL JEM 2100 and JEMe200 CX high-resolution transmission electron microscopes (HRTEM). The thermogravimetric analysis with the heating rate of 10 K min^{-1} under flowing air was carried out using a STA 449 F_3 Jupiter thermoanalyzer (Netzsch) coupled with a QMS 403 mass spectrometer (TG-DSC-MS). The specific surface area and pore volume of the samples were measured by a surface area and porosity analyzer (Gemine VII, Micromeritics). The content of carbon was examined by elemental chemical analysis (CA) using Vario MICRO Cubes (Elementar). Prior to N_2 physisorption data collection, the samples were degassed at 100 °C under vacuum for 1.5 h. The specific surface area, pore size distribution, and pore volumes were obtained by means of the Brunauer–Emmett–Teller (BET) method and the Barrett–Joyner–Halenda model from the adsorption branches of the isotherms. Raman spectra were measured with a Renishaw U1000 spectroscope at a laser wavelength of 532 nm.

2.4 Computational details

All quantum-chemical calculations of the V_2O_3/C composite systems were performed within the framework of the self-consistent-charge density-functional tight-binding method (SCC-DFTB) [29, 30]. Atomic positions in both the supercells of the bulk V_2O_3 doped by carbon and the supercells of a slab V_2O_3(0001) contacting with graphene were optimized using the conjugate gradient algorithm within periodic boundary conditions in Γ-point approximation. Self-consistent calculations were performed until the maximal residual components for the total energy of 10^{-3} eV $atom^{-1}$ and for the interatomic force component of 10^{-2} eV $Å^{-1}$. The lattice parameters optimized within these conditions for the bulk V_2O_3 are in a fair agreement with the experimental values, being overestimated by 3% ($a = 5.07$ Å, $c = 14.25$ Å).

As the progenitor of all the model V_2O_3/C composites the pre-optimized supercell $2a \times 2a \times 1c$ of bulk V_2O_3 was selected. Several possible variants for distribution of carbon impurities within V_2O_3 lattice have been accounted: substitutional single C atoms within V or O sublattices; substitutional C_2 dimers at neighbor sites within V or/and O sublattices; interstitial single C atoms or C_2 dimers; graphene sheet on a V_2O_3 surface. The relative stability of these V_2O_3/C composites with relaxed internal geometry was analyzed using the energy of formation ΔE relative to corresponding mechanistic mixture of the bulk V_2O_3, graphite and molecular CO. Positive and negative ΔE values point to endo- and exothermic formation reaction, respectively.

2.5 Electrochemical measurements

The electrochemical measurements of the samples were performed with a VMP3 potentiostat (Bio-Logic SAS) at 25 °C using Swagelok-type half cells with lithium metal foil (Alfa Aesar) as counter electrode [31]. The electrodes were separated by two layers of glass fiber separator (Whatman GF/D) that was soaked with 200 µL of a 1 M $LiPF_6$ salt solution in 1:1 ethylene carbonate and dimethyl carbonate (Merck Electrolyte LP30). The working electrode consists of active material, carbon black (Super C65, Timcal) and polyvinylidene fluoride binder (Solvay Plastics) in a weight ratio of 75:15:10. The powders were mixed in N-methyl-2-pyrrolidone (NMP, Sigma-Aldrich) and stirred for at least 12 h. After evaporating most of the NMP under vacuum the spreadable slurry was deposited on circular Cu meshes (diameter 10 mm) with a mass loading of about 0.4–0.5 mg cm^{-2}. Afterward, the electrodes were dried under vacuum, pressed with a spindle press by hand and then dried again. The preparation of the electrodes and the cell assembly were done in a glovebox filled with argon ($O_2/H_2O < 5$ ppm). The calculation of the specific capacity is based on the total mass weight of the composites V_2O_3/C.

3 Results and discussion

XRD patterns of the V_2O_3/C composites prepared using different carboxylic acids at different temperatures are depicted in Fig. 1a. All samples obtained after annealing at temperatures below 700 °C are amorphous according to the XRD patterns as demonstrated by the example of the V_2O_3/C-C composite. Annealing at 700 °C leads to the appearance of distinguished XRD patterns, which can be undoubtedly attributed to V_2O_3 without any impurities. The lattice of V_2O_3 within the as-prepared V_2O_3/C composites has rhombohedral crystalline structure and belongs to the R-3c space group. For all crystalline V_2O_3/C materials reported here, the lattice parameters derived from the XRD data are listed in Table 1. The results are found close to the reported values for V_2O_3 [ICSD No. 94768]. The XRD patterns however display rather broad and low-intense diffraction peaks, which may be attributed to both a poor crystallinity or/and to a small crystal size of primary V_2O_3 particles present in the composites. Using Scherrer's equation enables estimating the average crystallite sizes of V_2O_3

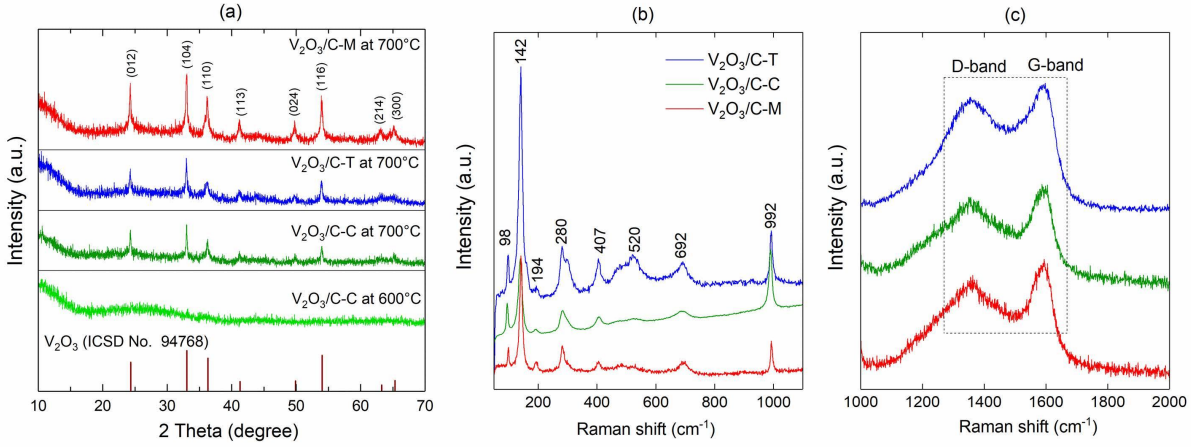

Fig. 1 **a** XRD patterns and Raman spectra in the range of **b** 50–1100 cm^{-1} and **c** 1000–2000 cm^{-1} of the V_2O_3/C composites fabricated using different carboxylic acids: citric acid (V_2O_3/C-C), tartaric acid (V_2O_3/C-T), and malic acid (V_2O_3/C-M)

Table 1 Lattice parameters, crystallite sizes from XRD, results of BET analysis, and carbon content of the V_2O_3/C composites synthesized at 700 °C. The last row shows lattice parameters from the literature

Samples	Lattice parameters		Crystallite size (nm)	S_{BET} ($m^2 g^{-1}$)	Carbon content (wt%)	
	a (Å)	*c* (Å)			TG	CA
V_2O_3/C-C	4.9907	13.8858	34 (10)	1.8	27.0	26.3 (5)
V_2O_3/C-M	4.9659	13.9956	28 (5)	5.8	20.6	20.3 (5)
V_2O_3/C-T	4.9533	14.0280	31 (8)	6.7	16.8	19.6 (5)
V_2O_3 (ICSD No. 94768)	4.95254	14.0038	–	–	–	–

particles:

$$D_{hkl} = K\lambda/\Delta(2\theta_{hkl})\cos 2\theta_{hkl}, \quad (1)$$

where D_{hkl} is the extent of the crystal perpendicular to the reflecting *hkl*-crystal plane, K is a constant depending on the crystal shape which can be approximated to 0.9, λ is the wavelength of the applied CuKα radiation, $\Delta(2\theta_{hkl})$ is the full width at half-maximum of the diffraction peak, and θ_{hkl} is the Bragg angle. The average crystallite sizes of V_2O_3 particles obtained from the analysis of the (012), (104), (110), and (116) reflexes are presented in Table 1. All materials exhibit nanosized primary particles with similar size. Obviously, the crystallite size does not seem to be affected by the chelating agent, which was also observed for other oxide systems, for example, $Y_3Fe_5O_{12}$ and Y_2O_3 synthesized by sol–gel technique with citric, malic, or tartaric acid [32, 33]. This phenomenon is attributed to the space steric effect of the organic acids playing the role of the chelating agent [34]. The chelating ability of carboxylic acids depends on the presence of the carboxylic –COOH groups. Citric acid in comparison with both malic acid and tartaric acid has three –COOH groups, which promote the formation of vanadium-ligand bonds, the formation of a chelate complex, and the growth of crystallites. However, the intermolecular steric hindrances are formed between the citric acid molecules and metal oxide due to the large molecular weight of the citric acid. A large space steric effect hinders close contact between the chelating agent and vanadium oxide that does not favor the growth of V_2O_3 particles. The main difference in the XRD patterns of the three composites is the relative intensity of the V_2O_3 reflexes. For the composite prepared using malic acid the ratio of the area of all crystalline peaks to the total area of the diffractogram is slightly higher than those for V_2O_3/C-C and V_2O_3/C-T indicating higher crystallinity of V_2O_3. This shows that malic acid is an eminent chelating agent to synthesize V_2O_3/C composite with higher crystallinity. Similar results were also observed in the synthesis of LiV_3O_8 prepared by sol–gel method and post-annealing treatment with citric, malic, and tartaric acid as chelating agents [35].

Raman spectroscopy provides further information about the structure of V_2O_5 and also on the carbon in the V_2O_3/C composites. All peaks shown in Fig. 1b located below 1000 cm^{-1} can be attributed to V–O vibrations of V_2O_5 in agreement with the literature values [36]. Evidently, V_2O_3 is partially oxidized to V_2O_5 under the laser irradiation during the Raman measurement in air [37] and therefore, the spectra also show characteristic Raman modes of the V_2O_5 phase. In addition, two broad peaks at ~1350 cm^{-1} and ~1600 cm^{-1} are clearly observed in the spectra of V_2O_3/C composites (Fig. 1c). The band at ~1600 cm^{-1} labeled as the G-band is related to the in-plane vibration of sp^2 hybridized carbon atoms [38–40], while the one at about 1350 cm^{-1} labeled as the D-band is associated to the breathing mode of sp^2 atoms in rings and only becomes active in the presence of defects [38–40]. The peaks of D- and G-bands are broad implying that carbon possesses high structural disorder [39, 41, 42]. The ratio of the

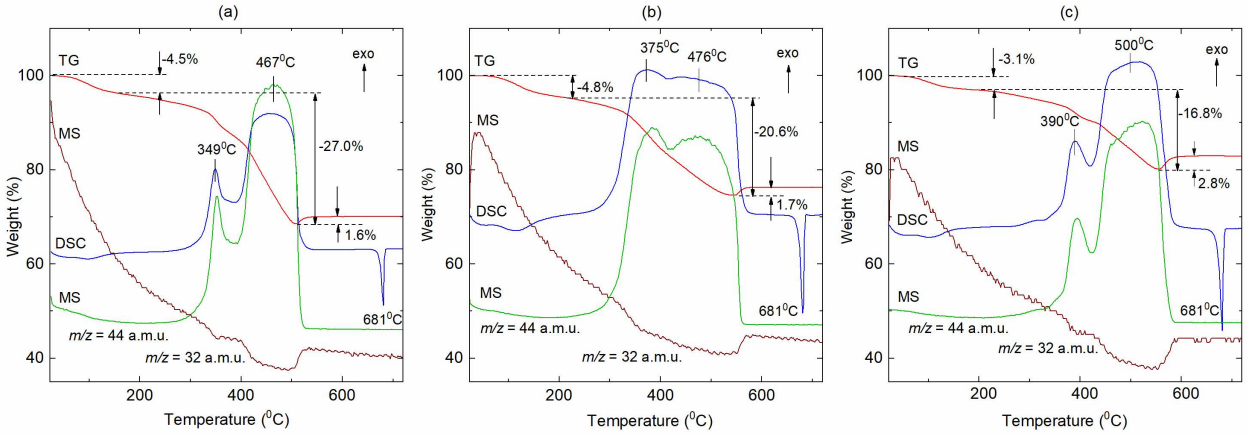

Fig. 2 Thermogravimetric (red), DSC (blue), and mass-spectroscopy (green, brown) curves of V_2O_3/C composites prepared using **a** citric acid, **b** malic acid, and **c** tartaric acid

maximum intensity of both peaks (I_D/I_G) of the V_2O_3/C composites, obtained by using citric acid, malic acid, and tartaric acid, are calculated to be 0.82, 0.83, and 0.87, respectively. In comparison with citric acid and malic acid as the chelating agent, this ratio is for V_2O_3/C-T composite slightly higher indicating less defects and disorder in the carbon component [38].

Thermogravimetric analyses coupled with mass-spectroscopy confirm the presence of carbon and allow to derive the carbon content in the V_2O_3/C composites under study (Fig. 2). The TG-DSC-MS curves of the composites prepared by citric acid (Fig. 2a), malic acid (Fig. 2b), and tartaric acid (Fig. 2c) are very similar. For all three composites, the weight loss proceeds stepwise. In the first step ranged from room temperature to about 180 °C, there is a weak endothermic peak signaling the vaporization of adsorption water. The corresponding weight loss is about 3.1−4.8 wt%. A second step ranging from 200 to 560 °C implies two strong exothermic peaks, which are associated with the vigorous combustion reactions of the carbon component in the composites and the completion of the crystallization reaction. The release of carbon dioxide CO_2 is confirmed by two intense peaks from molecular ion CO_2^+ with $m/z = 44$ a.m.u. in the mass spectra. Seemingly, the existence of this double exotherm with well-resolvable temperature maxima is due to the different states of carbon in the composites. A last feature is observed from ~500 to 730 °C. Here, there is a weight gain of 1.6, 1.7 and 2.8 wt% for V_2O_3/C-C, V_2O_3/C-M, V_2O_3/C-T samples, respectively, upon heating. This process is attributed to the oxidation of V^{3+} ions to V^{5+} and results in the formation of V_2O_5 as a final thermolysis product. The mass-spectroscopy curves reveal that the main gaseous product in this temperature regime is the molecular ion O_2^+ with $m/z = 32$ a.m.u. The endothermic peak at 681 °C is attributed to the melting of V_2O_5. According to the thermogravimetric analysis, the content of carbon in the samples amounts to 27.0, 20.6, 16.8 wt% for V_2O_3/C-C, V_2O_3/C-M, V_2O_3/C-T, respectively. The results of the TG analyses fully agree with carbon content determined by CA (Table 1).

The morphologies of the V_2O_3/C powders synthesized from citric acid, malic acid, and tartaric acid as carbon source are similar. All of them show micrometer sized chunks (Fig. S1) that are decorated with flake-like particles with the average flake size of 100–300 nm and 30–40 nm in thickness (Fig. 3a–c). In addition, the detailed microstructure of the V_2O_3/C-C composite studied by TEM (Fig. 3d) displays a block-like architecture of particles on the nanometer scale. The TEM images also show an amorphous carbon layer of up to 100 nm in thickness. Nanoparticles with the shape of edge-shared polyhedra are uniformly and tightly anchored to an amorphous carbon matrix (Fig. 3e). The lattice fringes with spacing of 0.37 nm corresponds to the (012) plane of the rhombohedral V_2O_3 phase. The corresponding ring-like selected-area electron diffraction (SAED) pattern (Fig. 3f) indicates that the as-synthesized composite is a polycrystalline phase indexed to V_2O_3, which is consistent with the XRD results presented above. Textural properties of the differently prepared V_2O_3/C composites as obtained from nitrogen adsorption and desorption studies and their analysis are shown in Fig. S2 and in Table 1. According to the IUPAC classification, the nitrogen adsorption/desorption isotherms display a type IV behavior [43].

In summary, analysis of XRD, SEM, TEM, and BET data provides solid evidence that the materials exhibit tightly bound, yet, separated V_2O_3 and carbon phases. However, doping of carbon into the V_2O_3 lattice cannot be completely excluded, since it remains undetectable by these methods. Therefore, quantum-chemical DFTB calculations have been employed to estimate tendency of the V_2O_3 lattice to host substitutional and/or interstitial carbon impurities. Several model variants of single and paired carbon atoms hosted at O- or V sites or as

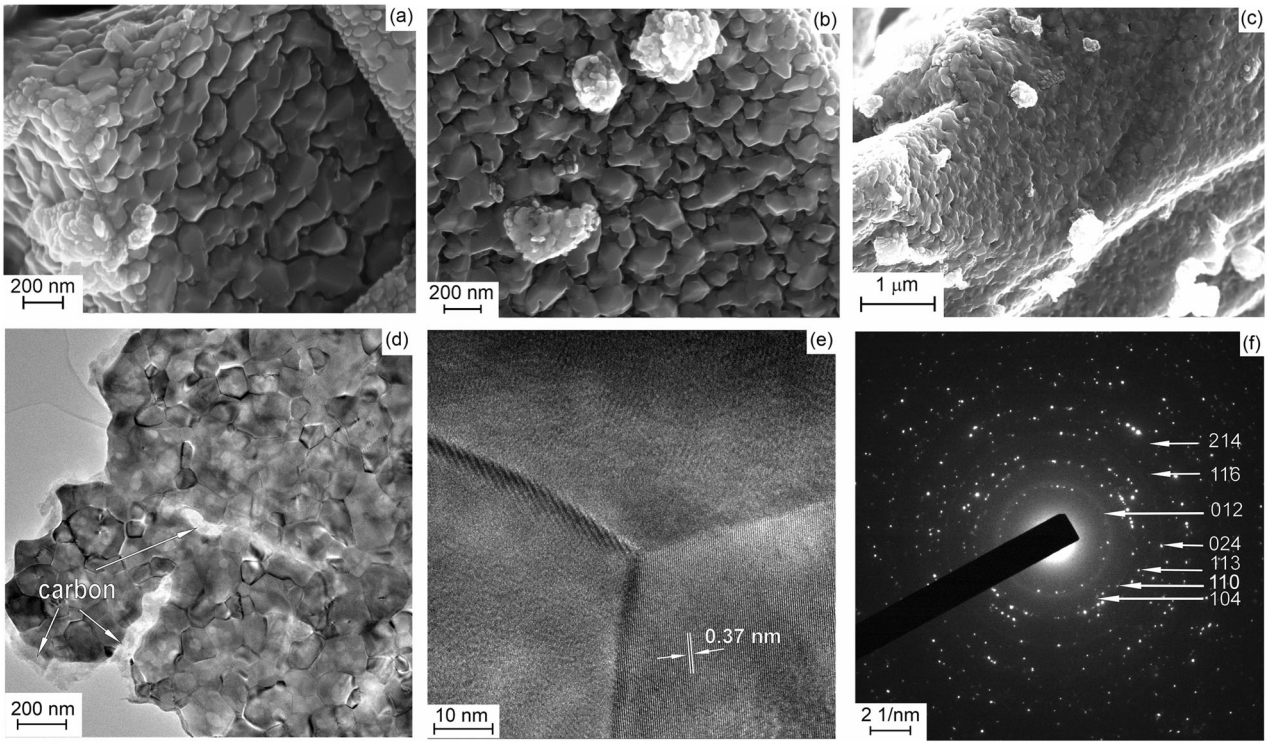

Fig. 3 SEM images of V_2O_3/C composites prepared with the different carboxylic acids: **a** citric acid, **b** malic acid, and **c** tartaric acid. **d** TEM, **e** HRTEM images, and **f** corresponding SAED pattern of V_2O_3/C-C composite

interstitials have been accounted (Table S1). An essential difference in their relative thermodynamic stabilities is established after comparison of their formation energies ΔE. There are a few important inferences. Namely, substitution of single O atoms by C atoms within V_2O_3, accompanied by emergence of carbide-like V–C bonding, is endothermic. Moreover, clusterization of such C atoms is even less favorite. Implantation of interstitial C atoms is also characterized by endothermic energies irrespective of the carbons' mutual distribution.

The energetically most beneficial and even exothermic carbon distribution has been found for the variants of cooperative substitution of either two neighboring V atoms or an VO unit (see Table S1). Optimized structures including these defects undergo a considerable evolution, compared to their initial geometries, which is accompanied by a contraction in the neighborhood of the defect, i.e., by the appearance of a nanoscopic cavity within the bulk of V_2O_3. Particularly, substitution of neighboring V and O atoms leads to the formation of acetylide-like dimers bound via an atom to two V atoms (Table S1, defect type 8). Though, the energetically most beneficial cooperative substitution is found to be on two neighboring V sites, which results in the formation of CO molecules within nanoscopic cavity. Depending on the initial positions of substituting C atoms, the final structure contains either two CO molecules (Table S1, defect type 10) or a single CO molecule and a carbonate-like group (Table S1, defect type 11, and Fig. S3).

Beside the formation of molecular-like carbon species or carbon oxides, the release of free carbon in bulk quantities like a graphene sheet on the $V_2O_3(0001)$ surface should be also an exothermic reaction (Table S1, defect type 14, and Fig. S3). Noteworthy, the in-plane lattice parameters of a $V_2O_3(0001)$ surface and graphene commensurate very well with a ratio close to $a_{V2O3} \approx 2a_C$. According to our calculations, the only stable type of $V_2O_3(0001)$ surface appears as stoichiometric surface with the V atoms moved inward to the surface layer. The graphene sheet can stay 3.1 Å away from this reconstructed surface.

Despite the exclusively thermodynamic characterization, the calculations are capable to explain the origin of several morphological features established in the experimentally fabricated V_2O_3/C composites. Irrespective of the mechanism for reduction of V^{5+} from metal-organic precursors, the formation of any vanadium carbides, vanadium oxycarbides or stable $(V,C)_2O_3$ solid solutions within the V_2O_3/C system should be not expected. Any possible $(V,C)_2O_3$ intermediate should decompose into a thermodynamically more stable state, namely, the nanocavernous bulk V_2O_3 with CO or C_2 species residing in the caverns. Such structural faults do not promote the mechanical stability of the lattice and can serve as the origins of cracks with degassing of fugitive components. The higher the content of the faults, the smaller domains of forming V_2O_3 should be observed. After all, the most likely forms of carbon in the V_2O_3/C

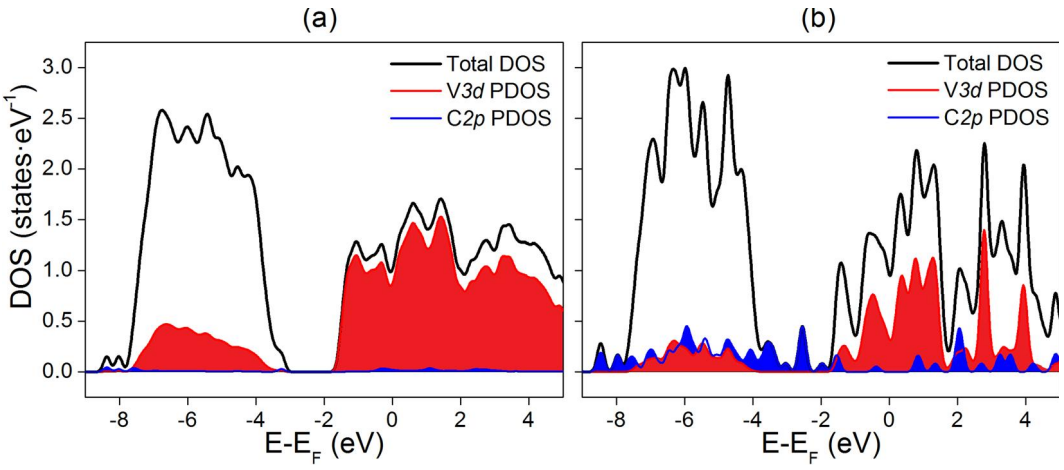

Fig. 4 Total and selected partial electronic densities-of-states (DOS) for a couple of V_2O_3/C composites: **a** the bulk V_2O_3 with a nanocavern hosting CO molecules (initially, carbon was hosted in the V sublattice); **b** model interface of stoichiometric V_2O_3(0001) surface and graphene, the DOS of V3*d* states is depicted only for the surface atoms. DFTB calculations

composites are represented at the particles' surface either as carbonate groups or as elemental carbon like graphene or carbyne assembled from acetylide species.

In addition, the calculations give a preliminary estimate of the electronic structure of V_2O_3/C composites. The electronic densities-of-states (DOS) are typical for the metal-like compounds, and the origin of the DOS near the Fermi level remains similar irrespective of the carbon type in a composite. It is contributed mostly from the V3*d*-states of the V_2O_3 part. The examples for the most thermodynamically stable V_2O_3/C composites—with either chemically integrated or elemental carbon—are depicted in Fig. 4. Similarly to the pristine V_2O_3, the Fermi level is hosted in a local DOS minimum of the wide V3*d*-band, hence, all composites should have a metal-like conductivity. Valence O2*p* states form the wide band at $-8\ldots-4$ eV below the Fermi level. Chemically integrated carbon (like molecular-like CO or C_2) donates also occupied C2*p* states to both the top and the bottom of the main valence band (Fig. 4a). In the case of physisorbed carbon like graphene in contact to the V_2O_3(0001) surface, the valence C2*p* states demonstrate an essential dispersion, though, they are missing at the Fermi level (Fig. 4b). Here, V3*d* states near the Fermi level are presented by both the bulk and the surface V atoms. Thus, all V_2O_3/C composites should preserve a metal-like type of conductivity like parent V_2O_3.

Electrochemical properties of the V_2O_3/C composites synthesized with different carbon sources are investigated by cyclic voltammetry (CV) and galvanostatic cycling with potential limitation (GCPL) in the voltage range between 0.01 V and 3.2 V. Exemplary for all samples, Fig. 5a shows the first, second, and fifth cycle of the cyclic voltammogram of V_2O_3/C-M recorded at a scan rate of 0.05 mV s^{-1}. As shown in Fig. S4, the CV curves of the other two composites, V_2O_3/C-C and V_2O_3/C-T, exhibit the same features. Starting with a reductive scan in the first cycle a peak R_{SEI} at around 0.75 V occurs mainly due to the irreversible formation of a solid electrolyte interface (SEI) [21]. The redox peak pair R_C/O_C around the lower limit 0.01 V corresponds to the lithiation and delithiation of the carbon [44]. All other features, the reduction peaks R_1 and R_2 as well as the oxidation peaks $O1$ and $O2$, can be assigned to the electrochemical reactions of V_2O_3. The Li^+ storage of V_2O_3 initially runs via intercalation (Eq. 2) and, subsequently, conversion of $Li_xV_2O_3$ to metallic V and Li_2O (Eq. 3) as follows [2, 45]:

$$V_2O_3 + xLi^+ + xe^- \leftrightarrow Li_xV_2O_3, \quad (2)$$

$$Li_xV_2O_3 + (6-x)Li^+ + (6-x)e^- \leftrightarrow 2V + 3Li_2O. \quad (3)$$

In the CV curve, there are two broad reduction peaks at 0.9 and 1.75 V and two oxidation peaks at 1.25 and 2.5 V. The absence of much more pronounced peaks implies that the de-/lithiation process smoothly proceeds with several transition species originating from the multivalence of vanadium [21, 46].

The cycling performances of the different samples are studied by GCPL measurements. In Fig. 5b, the dis-/charge capacities at 100 mA g^{-1} are shown. The first dis-/charge capacities of V_2O_3/C-C, V_2O_3/C-M, and V_2O_3/C-T are 769/302, 763/358, and 612/257 mAh g^{-1}, respectively. The huge discrepancy between the first discharge and charge capacity is caused by the irreversible SEI formation and structural changes during the first lithiation [2, 7, 24]. Upon further cycling, the capacity initially rises slightly, which can be attributed to an activation process as a result of electrochemical grinding. This phenomenon has been observed in literature for V_2O_3-based electrodes [7, 21] as

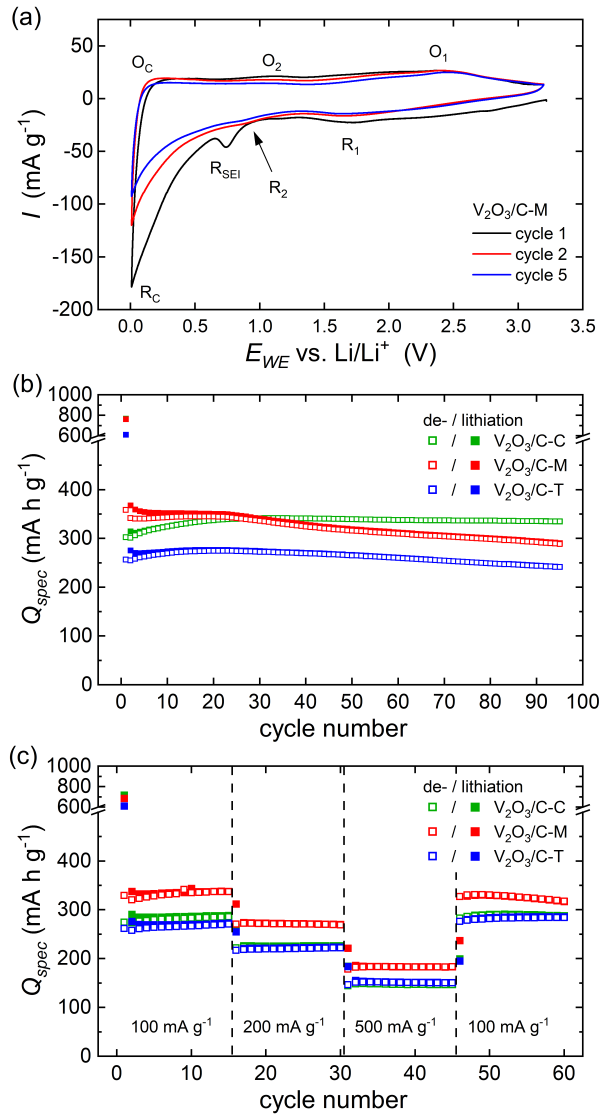

Fig. 5 **a** CV curves of V_2O_3/C-M recorded at a scan rate of 0.05 mV s^{-1}. **b** Specific dis-/charge capacities during galvanostatic cycling at 100 mA g^{-1} and **c** rate capability at various current densities of 100, 200, and 500 mA g^{-1} of the composites fabricated using citric acid (V_2O_3/C-C), malic acid (V_2O_3/C-M), and tartaric acid (V_2O_3/C-T)

well as other anode materials [47, 48]. During the whole measurement the samples exhibit a high cycle stability, whereas especially V_2O_3/C-C stands out. It convinces with a capacity retention of 98% in cycle 95 relative to cycle 33, where the maximal charge capacity of 342 mAh g^{-1} is obtained. By comparing the composites among each other no clear differences of the electrochemical performance can be observed. As expected, due to the quite similar physical properties of the different composites, the used carbon source (citric acid, malic acid or tartaric acid) does not strongly affect the electrochemical properties. In Fig. 5c, the specific dis-/charge capacities are shown at different current rates between 100 and 500 mA g^{-1}. The composite V_2O_3/C-M is superior and exhibits specific charge capacities of 337, 269, and 183 mAh g^{-1} at current densities of 100, 200, and 500 mA g^{-1} after 15 cycles each. When the current density is returned to 100 mA g^{-1} a charge capacity of 327 mAh g^{-1} is regained, demonstrating excellent capacity retention. The other two samples also exhibit high rate performance. The dis-/charge profiles (Fig. S5b) reveal no significant differences of the overpotential due to polarization effects for the different composites. The slightly better rate capacity of V_2O_3/C-M compared to V_2O_3/C-T may be due to an improved electronic conductivity of the material. The percolation threshold for forming a conductive network in a randomly packed three-dimensional body consisting of conductive and insulating particles is exceeded by the higher carbon content, which ensures higher conductivity in the V_2O_3/C-M composite, and thus achieves superior performance [49, 50]. The fact that the composite V_2O_3/C-C with the highest carbon content shows lower rate capacity as V_2O_3/C-M might be due the less amount of the active material, V_2O_3, in the anode material that comes along with it [49].

For a comparison, the electrochemical performances of V_2O_3/C composites prepared via different synthesis methods are collected in Table 2. It can be concluded that the composites presented in this work lie in the midfield. The outstanding performance of V_2O_3/C nanocomposites prepared through the thermolysis of a polymer matrix-based metal precursor can possibly be explained by the good distribution of both components.

4 Conclusions

In summary, we demonstrate a facile, low cost, and scalable two-step route to fabricate pure vanadium-based V_2O_3/C composites of polynanocrystalline V_2O_3 microparticles encapsulated in an amorphous carbon matrix. The absence of foreign phases is confirmed by means of several physical and analytical methods, while the existence of the few-atom impurities has been criticized using quantum-chemical calculations. Based on theoretical analysis, the formation mechanism of such structured composites might include formation of molecular CO, carbonate ions and progressive growth of C–C chains all upon carbonization of precursors. Diffusion out of decomposing precursor and outgassing of these species leads to extensive fracturing of emerging V_2O_3 lattice and to the elemental carbon remained at surface of V_2O_3.

A slight regulation of the carbon content, the typical size of V_2O_3 nanocrystallites and, consequently, the accessible physical surface of the product can be attained using different precursors—vanadyl complexes with citric, tartaric, or malic acids. However, electrochemical performance of

Table 2 Comparison of the electrochemical performance of V_2O_3/C electrodes prepared via different synthesis methods as reported in the literature

Material	Method of synthesis[a]	Current density ($mA\ g^{-1}$)	1st charge capacity ($mAh{\cdot}g^{-1}$)	Specific capacity ($mAh\ g^{-1}$)/cycle no.	Ref.
V_2O_3/C particles	Polymer-pyrolysis	200	800	780/100	[21]
V_2O_3 nanoplatelets/C with core-shell structure	Hydrothermal	100	360[b]	260/100	[4]
Yolk-shell V_2O_3/C microspheres	Solvothermal	100	470[b]	437.5/100	[13]
3D V_2O_3/C networks	Freeze-drying	1000	450[b]	580/500	[17]
V_2O_3/C nanoparticles	Solvothermal	200	380	525/200	[7]
Dandelion-like V_2O_3/C spheres	Solvothermal	500	280[b]	474/400	[23]
Peapod-like V_2O_3/C nanowires	Hydrothermal	100	230	186/125	[11]
V_2O_3/C microparticles	Sol–gel thermolysis	100	302	335/95	This work

[a]All mentioned synthesis methods include a post heat treatment

[b]Values are estimated from the graphs

the final products as anode materials for LIBs are not strongly affected by the type of carbon source. Slight differences in the rate capacity may be due to different carbon contents. All our V_2O_3/C composites exhibit an excellent cycle stability at a medium-range reversible capacity in-line with formerly known V_2O_3/C composites.

Acknowledgements The authors thank I. Glass for experimental support.

Funding This work was supported by the Deutsche Forschungsgemeinschaft through projects KL 1824/12-1 and KL 1824/14-1. GSZ acknowledges support of the state order via the Ministry of Science and High Education of Russia (Theme no. AAAA-A19-119031890025-9). Partial support by the BMWi through project 03ET6095C (HiKoMat) is acknowledged. Open Access funding enabled and organized by Projekt DEAL.

Compliance with ethical standards

Conflict of interest The authors declare no competing interests.

References

1. Adler D, Feinleib J (1964) Semiconductor-to-metal transition in V_2O_3. Phys Rev Lett 12:700
2. Li H, Balaya P, Maier J (2004) Li-storage via heterogeneous reaction in selected binary metal fluorides and oxides. J Electrochem Soc 151:A1878–A1885
3. Sun Y, Jiang S, Bi W, Wu C, Xie Y (2011) Highly ordered lamellar V_2O_3-based hybrid nanorods towards superior aqueous lithium-ion battery performance. J Power Sources 196:8644–8650
4. Cheng W, Zeng G, Niederberger M (2015) Design of vanadium oxide core–shell nanoplatelets or lithium ion storage. J Mater Chem A 3:2861–2868
5. Leng J, Mei H, Zhan L, Wang Y, Yang S, Song Y (2017) V_2O_3 nanoparticles anchored onto the reduced graphene oxide for superior lithium storage. Electrochim Acta 231:732–738
6. Zeng L, Zheng C, Xi J, Fei H, Wei M (2013) Composites of V_2O_3–ordered mesoporous carbon as anode materials for lithium-ion batteries. Carbon 62:382–388
7. Huan C, Zhao X, Xiao X, Lu Y, Qi S, Zhan Y, Zhang L, Xu G (2019) One-step solvothermal synthesis of V_2O_3@C nanoparticles as anode materials for lithium-ion battery. J Alloys Compd 776:568–574
8. Gou W, Kong X, Wang Y, Ai Y, Liang S, Pan A, Cao G (2019) Yolk-shell structured V_2O_3 microspheres wrapped in N, S co-doped carbon as pea-pod nanofibers for high-capacity lithium ion batteries. Chem Eng J 374:545–553
9. Zhang D, Li G, Li B, Fan J, Liu X, Chen D, Li L (2019) A facile strategy to fabricate V_2O_3/porous N-doped carbon nanosheet framework as high-performance anode for lithium-ion batteries. J Alloy Compd 789:288–294
10. Han C, Liu F, Liu J, Li Q, Meng J, Shao B, He Q, Wang X, Liu Z, Mai L (2018) Facile template-free synthesis of uniform carbon-confined V_2O_3 hollow spheres for stable and fast lithium storage. J Mater Chem A 6:6220–6224
11. Li X, Fu J, Pan Z, Su J, Xu J, Gao B, Peng X, Wang L, Zhang X, Chu PK (2016) Peapod-like V_2O_3 nanorods encapsulated into carbon as binder-free and flexible electrodes in lithium-ion batteries. J. Power Sources 331:58–66
12. Liu H, Wang Y, Li H, Yang W, Zhou H (2010) Flowerlike vanadium sesquioxide: solvothermal preparation and electrochemical properties. ChemPhysChem 11:3273–3280
13. Jiang L, Qu Y, Ren Z, Yu P, Zhao D, Zhou W, Wang L, Fu H (2015) In situ carbon-coated yolk-shell V_2O_3 microspheres for lithium-ion batteries. ACS Appl Mater Interfaces 7:1595–1601
14. Wang J, Liu Z, Yang W, Han L, Wei M (2018) A one-step synthesis of porous V_2O_3@C hollow spheres as a high-performance anode for lithium-ion batteries. Chem Commun 54:7346–7349
15. Bai Y, Tang Y, Liu L, Li X, Gao Y (2018) Peapod-like CNT@V_2O_3 with superior electrochemical performance as an

anode for Li-ion batteries. ACS Sustain Chem Eng 6:14614–14620
16. Yu P, Liu X, Wang L, Tian C, Yu H, Fu H (2017) Urchin-like V_2O_3/C hollow nanosphere hybrid for high-capacity and long-cycle-life lithium storage. ACS Sustain Chem. Eng 5:11238–11245
17. Ren X, Ai D, Zhan C, Lv R, Kang F, Huang Z-H (2019) NaCl-template-assisted freeze-drying synthesis of 3D porous carbon encapsulated V_2O_3 for lithium-ion battery anode. Electrochim Acta 318:730–736
18. Gao S, Zhang D, Zhu K, Tang JA, Gao Z, Wei Y, Chen G, Gao Y (2017) Flexible V_2O_3/carbon nano-felts as free-standing electrode for high performance lithium ion batteries. J Alloy Compd 702:13–19
19. Zhang Y, Pan A, Liang S, Chen T, Tang Y, Tan X (2014) Reduced graphene oxide modified V_2O_3 with enhanced performance for lithium-ion battery. Mater Lett 137:174–177
20. Liu X, Zhang D, Li G, Xue C, Ding J, Li B, Chen D, Li L (2018) In situ synthesis of V_2O_3 nanorods anchored on reduced graphene oxide as high-performance lithium ion battery anode. Chem Select 3:12108–12112
21. Dong Y, Ma R, Hu M, Cheng H, Lee J-M, Yang Li Y, Zapien JA (2014) Polymer-pyrolysis assisted synthesis of vanadium trioxide and carbon nanocomposites as high performance anode materials for lithium-ion batteries. J Power Sources 261:184–187
22. Xiao B, Zhang B, Tang L, An C, He Z, Tong H, Yu W, Zheng J (2018) V_2O_3/rGO composite as a potential anode material for lithium ion batteries. Ceram Int 44:15044–15049
23. Xun L, Gao S, Xu Y, Cheng X, Zhang X, Zhao H, Huo L (2018) Synthesis of dandelion-like V_2O_3/C composite with bicontinuous 3D hierarchical structures as an anode for high performance lithium ion batteries. Ceram Int 44:14128–14135
24. Shi Y, Zhang Z, Wexler D, Chou S, Gao J, Abruňa HD, Li H, Liu H, Wu Y, Wang J (2015) Facile synthesis of porous V_2O_3/C composites as lithium storage material with enhanced capacity and good rate capability. J Power Sources 275:392–398
25. Priyadharsini N, Kasturi PR, Shanmugavani A, Surendran S, Shanmugapriya S, Selvan RK (2018) Effect of chelating agent on the sol–gel thermolysis synthesis of $LiNiPO_4$ and its electrochemical properties for hybrid capacitors. J Phys Chem Solids 119:183–192
26. Yin Y, Zhang B, Zhang X, Xu J, Yang S (2013) Nano $MgFe_2O_4$ synthesized by sol–gel auto-combustion method as anode materials for lithium ion batteries. J Sol–Gel Sci Technol 66:540–543
27. Mączk M, Pasier P (2019) Sol–gel synthesis of metal (V, W, Zn) oxide - Carbon nanocomposites as cathode materials for Al-ion batteries. Ceram Int 45:11041–11049
28. Gangulibabu, Bhuvaneswari D, Kalaiselvi N, Jayaprakash N, Periasamy P (2009) CAM sol–gel synthesized $LiMPO_4$ (M=Co, Ni) cathodes for rechargeable lithium batteries. J Sol–Gel Sci Technol 49:137–144
29. Porezag D, Frauenheim TH, Köhler TH, Seifert G, Kaschner R (1995) Construction of tight-binding-like potentials on the basis of density-functional theory: application to carbon. Phys Rev B 51:12947
30. Elstner M, Porezag D, Jungnickel G, Elsner J, Haugk M, Frauenheim TH, Suhai S, Seifert G (1998) Self-consistent-charge density-functional tight-binding method for simulations of complex materials properties. Phys Rev B 58:7260
31. Jähne C, Neef C, Koo C, Meyer H-P, Klingeler R (2013) A new $LiCoPO_4$ polymorph via low temperature synthesis. J Mater Chem A 1:2856–2862
32. Vaqueiro P, López MA (1997) Quintela, Influence of complexing agents and pH on yttrium-iron garnet synthesized by the sol–gel method. Chem Mater 9:2836–2841
33. Dupont A, Parent C, Le Garrec B, Heintz JM (2003) Size and morphology control of Y_2O_3 nanopowders via a sol–gel route. J Solid State Chem 171:152–160
34. Zheng F, Ou X, Pan Q, Xiong X, Yang C, Liu M (2017) The effect of composite organic acid (citric acid & tartaric acid) on microstructure and electrochemical properties of $Li_{1.2}Mn_{0.54}Ni_{0.13}Co_{0.13}O_2$ Li-rich layered oxides. J Power Sources 346:31–39
35. Wang D, Cao L, Huang J, Wu J (2013) Effects of different chelating agents on the composition, morphology and electrochemical properties of LiV_3O_8 crystallites synthesized via sol–gel method. Ceram Int 39:3759–3764
36. Ramana CV, Smith RJ, Hussain OM, Julien CM (2004) Growth and surface characterization of V_2O_5 thin films made by pulsed-laser deposition. J Vac Sci Technol A 22:2453–2458
37. Xu G, Wang X, Chen X, Jiao L (2015) Facile synthesis and phase transition of V_2O_3 nanobelts. RSC Adv 5:17782–17785
38. Ferrari AC, Robertson J (2000) Interpretation of Raman spectra of disordered and amorphous carbon. Phys. Rev. B 61:14095–14107
39. Ferrari AC, Basko DM (2013) Raman spectroscopy as a versatile tool for studying the properties of graphene. Nature nanotechnology 8:235–246
40. Merlen A, Buijnsters J, Pardanaud C (2017) A guide to and review of the use of multiwavelength Raman spectroscopy for characterizing defective aromatic carbon solids: from graphene to amorphous carbons. Coatings 7:153
41. Ferreira EHM, Moutinho MVO, Stavale F, Lucchese MM, Capaz RB, Achete CA, Jorio A (2010) Evolution of the Raman spectra from single-, few-, and many-layer graphene with increasing disorder. Phys Rev B 82:125429
42. Cancado LG, Jorio A, Ferreira EHM, Stavale F, Achete CA, Capaz RB, Moutinho MVO, Lombardo A, Kulmala TS, Ferrari AC (2011) Quantifying defects in graphene via Raman spectroscopy at different excitation energies. Nano Lett 11:3190–3196
43. Sing KSW, Everett DH, Haul RAW, Moscou L, Pierotti RA, Rouquerol J, Siemieniewska T (1985) Pure Appl Chem 57:603–619
44. Ottmann A, Scholz M, Haft M, Thauer E, Schneider P, Gellesch M, Nowka C, Wurmehl S, Hampel S, Klingeler R (2017) Electrochemical magnetization switching and energy storage in manganese oxide filled carbon nanotubes. Sci Rep 7:13625
45. Tranchant A, Messina R, Perichon J (1980) Mechanism of electrochemical reduction of vanadium oxides. J Electroanalyt Chem Interfacial Electrochem 113:225–232
46. Wang Y, Zhang HJ, Admar AS, Luo J, Wong CC, Borgna A, Lin J (2012) Improved cyclability of lithium-ion battery anode using encapsulated V_2O_3 nanostructures in well-graphitized carbon fiber. RSC Adv 2:5748–5753
47. Dong Y, Ma R, Hu M, Cheng H, Yang Q, Li YY, Zapien JA (2013) Thermal evaporation-induced anhydrous synthesis of Fe_3O_4-graphene composite with enhanced rate performance and cyclic stability for lithium ion batteries. Phys Chem Chem Phys 15:7174–7181
48. Zhu T, Chen JS, Lou XW(D) (2011) Glucose-assisted one-pot synthesis of FeOOH nanorods and their transformation to Fe_3O_4@carbon nanorods for application in lithium ion batteries. J Phys Chem C 115:9814–9820
49. Wang C, Sawicki M, Emani S, Liu C, Shaw LL (2015) Na3MnCO3PO4—a high capacity, multi-electron transfer redox cathode material for sodium ion batteries. Electrochim Acta 161:322–328
50. Rajkumar P, Diwakar K, Subadevi R, Gnanamuthu RM, Wang F-M, Liu W-R, Sivakumar M (2021) Graphene sheet-encased silica/sulfur composite cathode for improved cyclability of lithium-sulfur batteries. J. Solid State Electrochem 25:939–948

Supplementary Information

V_2O_3/C composite fabricated by carboxylic acid-assisted sol-gel synthesis as anode material for lithium-ion batteries

G.S. Zakharova[1], E. Thauer[2], A.N. Enyashin[1], L. Deeg,[2] Q. Zhu[3], R. Klingeler[2,4]

[1]*Institute of Solid State Chemistry, Ural Division, Russian Academy of Sciences, Yekaterinburg, Russia*

[2]*Kirchhoff Institute of Physics, Heidelberg University, Heidelberg, Germany*

[3]*School of Material Science and Engineering, Wuhan University of Technology, Wuhan, China*

[4]*Centre for Advanced Materials, Heidelberg University, Heidelberg, Germany*

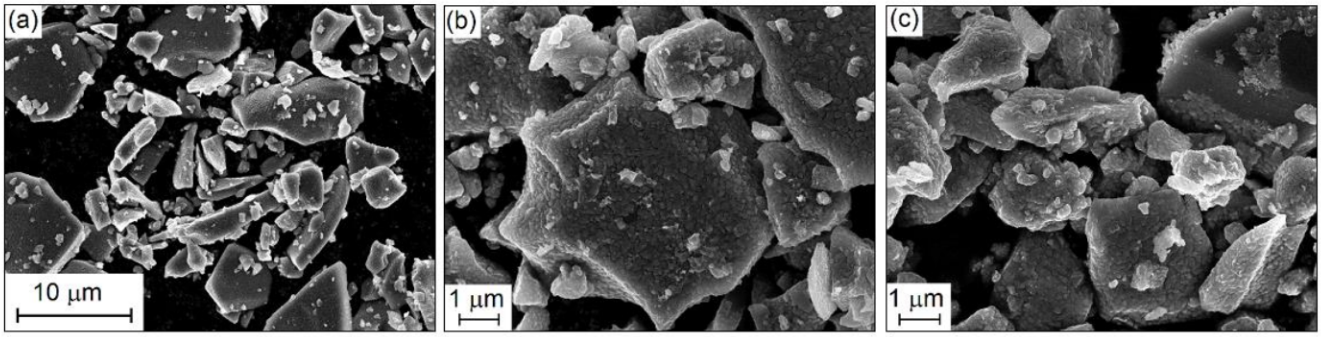

Fig. S1. SEM images of V_2O_3/C composites prepared using (a) citric acid, (b) malic acid, and (c) tartaric acid.

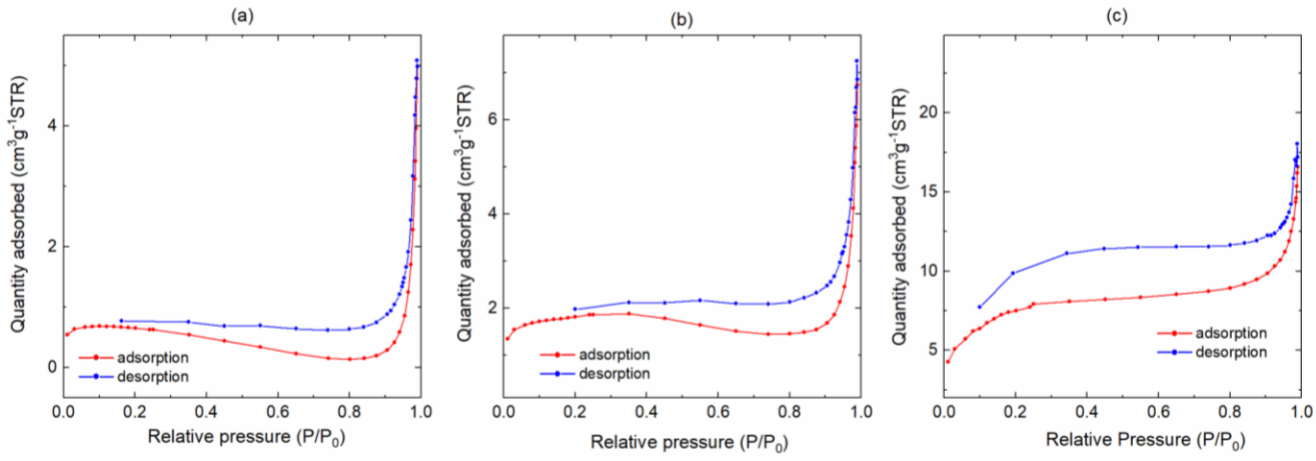

Fig. S2. Nitrogen adsorption/desorption isotherms of V_2O_3/C composites prepared using (a) citric acid, (b) malic acid, and (c) tartaric acid.

Table S1. Formation energies (ΔE) for different V_2O_3/C composites depending on carbon content and its distribution in the V_2O_3 lattice obtained from DFTB calculations. The energies are given relative to the energy of a mechanistic mixture of V_2O_3, graphite and molecular CO. Negative values of ΔE correspond to exothermic reaction.

Type	Composition of the cell	ΔE (eV/C-atom)	Description
1	$V_{48}O_{71}C_1$	+1.78	substitution of single O atom by C atom
2	$V_{47}O_{72}C_1$	+1.30	substitution of single V atom by C atom
3	$V_{48}O_{72}C_1$	+1.99	interstitial C atom
4	$V_{48}O_{70}C_2$	+3.46	substitution of two neighboring O atoms by two C atoms (aslant to c-axis, as common edge of two neighboring VO_6 octahedra)
5	$V_{48}O_{70}C_2$	+2.58	substitution of two neighboring O atoms by two C atoms (across c-axis)
6	$V_{48}O_{70}C_2$	+3.37	substitution of two neighboring O atoms by two C atoms (aslant to c-axis)
7	$V_{48}O_{70}C_2$	+2.81	substitution of two neighboring O atoms by two C atoms (across c-axis, as common edge of two neighboring VO_6 octahedra)
8	$V_{47}O_{71}C_2$	-1.11	substitution of neighboring V and O atoms by two C atoms
9	$V_{46}O_{72}C_2$	+1.90	substitution of two neighboring V atoms by two C atoms (along c-axis)
10	$V_{46}O_{72}C_2$	-2.26	substitution of two neighboring V atoms by two C atoms (across c-axis)
11	$V_{46}O_{72}C_2$	-1.82	substitution of two neighboring V atoms by two C atoms (aslant to c-axis)

3.3 Hierarchically structured V_2O_3/C microspheres: Synthesis, characterization, and their electrochemical properties

Autoren:

E. Thauer, G.S. Zakharova, L.F. Deeg, Q. Zhu, R. Klingeler

veröffentlicht in Journal of Sol-Gel Science and Technology, 2021

abgedruckt mit freundlicher Genehmigung des Springer Nature Verlags

E. Thauer ist die Erst- und Korrespondenzautorin dieses Artikels. E. Thauer konzipierte und verfasste das Manuskript mit Ausnahme der Teile zur Synthese sowie zu den Raman-, TGA- und BET-Messungen und erstellte die Abb. 1 - 2, Abb. 5 - 7, Abb. S4 - S7. Die Charakterisierung mittels XRD und REM sowie alle elektochemischen Messungen, einschließlich der *ex-situ* XRD-Messungen erfolgte von E. Thauer teilweise gemeinsam mit dem Masterstudent L.F. Deeg unter ihrer Anleitung. Die Korrespondenz mit den Gutachtern sowie die Überarbeitung des Manuskripts wurde von E. Thauer zusammen mit G.S. Zakharovs und R. Klingeler übernommen.

G.S. Zakharova führte die Synthese der Materialien, die Untersuchungen mittels XRD (Abb. S1 a) und Raman-Spektroskopie (Abb. 1 b und S1 b) sowie die TGA- (Abb. 3) und BET-Messungen (Abb. 4) durch und verfasste die zugehörigen Teile des Manuskripts sowie den Teil zu den TEM-Aufnahmen (Abb. S2). Q. Zhu führte die TEM-Messungen durch. R. Klingeler betreute das Projekt und stand beratend sowie bei der Finalisierung des Manuskripts zur Seite. Alle Autoren haben das Manuskript korrekturgelesen.

Electrochimica Acta 390 (2021) 138881

Contents lists available at ScienceDirect

Electrochimica Acta

journal homepage: www.elsevier.com/locate/electacta

Hierarchically structured V_2O_3/C microspheres: Synthesis, characterization, and their electrochemical properties

E. Thauer[a,*], G.S. Zakharova[b], L.F. Deeg[a], Q. Zhu[c], R. Klingeler[a,d]

[a] Kirchhoff Institute of Physics, Heidelberg University, Heidelberg, Germany
[b] Institute of Solid State Chemistry, Ural Division, Russian Academy of Sciences, Yekaterinburg, Russia
[c] School of Material Science and Engineering, Wuhan University of Technology, Wuhan, China
[d] Centre for Advanced Materials, Heidelberg University, Heidelberg, Germany

ARTICLE INFO

Article history:
Received 15 March 2021
Revised 1 July 2021
Accepted 1 July 2021
Available online 8 July 2021

Keywords:
Anode material
Composite
Hydrothermal synthesis
Lithium-ion battery
Sphere

ABSTRACT

The V_2O_3/C composites have been successfully synthesized by a facile hydrothermal thermolysis method, employing vanadyl hydroxide as precursor and different carboxylic acids as both a carbon source and reducing agents. The morphology, structure, and composition of the obtained V_2O_3/C composites were investigated by X-ray diffraction, Raman spectroscopy, scanning and transmission electron microscopies, physical sorption, thermogravimetric analysis coupled with mass-spectrometry, and elemental analysis. The as-prepared V_2O_3/C composites consist of hierarchically structured microspheres, either with core-shell or solid architecture depending on the used carboxylic acid. When used as anode for lithium-ion batteries, the V_2O_3/C spheres deliver very good electrochemical performance with high specific capacity, great cyclic stability, and high rate capability. The large capacitive current contribution favors superior lithium storage kinetics compared to more compact chunk-shaped V_2O_3/C materials. In particular, the composite prepared with tartaric acid exhibits a high reversible capacity of 454 mAh g^{-1} after 100 cycles at 100 mA g^{-1}.

1. Introduction

Nowadays, rechargeable lithium-ion batteries (LIB) are the most promising energy storage systems for mobile applications, including electric vehicles, due to their high energy density, high energy efficiency and long cycle life [1–5]. It is well-known that the electrode materials play a decisive role in determining the LIBs performance. Graphite, the predominant commercial anode material, has a rather low theoretical capacity of 372 mA h g^{-1}, that cannot meet the ever-growing demand for next generation high energy LIBs [6,7]. Thus, in recent years, many endeavours have been placed on exploring alternative anode materials for LIBs, especially transition metal oxides have attracted intense research in view of their high theoretical capacities [8–13]. Among them, vanadium trioxide (V_2O_3) is favoured for its high theoretical capacity (1070 mA h g^{-1}), low working potential, low cost, natural abundance, and environment friendliness [14–17]. Particularly, it undergoes a first order metal-to-insulator transition at 150–160 K accompanied by a change from a paramagnetic rhombohedral phase into an antiferromagnetic monoclinic phase [18,19]. So, V_2O_3 exhibits moderate electronic conductivity at room temperature, which is much higher than that of other transition metal oxides, such as MnO_2, Fe_2O_3, Co_3O_4 [20]. However, its poor cycling stability seriously hinders its practical application. Vanadium trioxide suffers from large volume change during Li-ion insertion/extraction resulting in cracking and pulverization. To overcome this issue, rational structure design and the preparation of composites with carbonaceous materials have proven to be promising strategies in recent years [21]. Building hierarchical nano-/micro-architectures can combine both the advantageous of nanosized primary particles and micro-sized arrangements [22–24]. Nanomaterials can accommodate large mechanical strain of Li-ion insertion/extraction improving the cycle life and, in addition, possessing high specific surface area and short Li^+ diffusion path leading to high energy and power density [25,26]. Hierarchical structures guarantee structural stability by preventing agglomeration of the nanoparticles, which occurs due to low thermodynamic stability [24,27]. When using carbonaceous materials for the stabilising matrix, carbon can serve, on the one hand, as a buffer to accommodate changes in volume and as a physical barrier to prevent the agglomeration and restacking of V_2O_3 particles on the other [28,29]. Moreover, the carbon can effectively improve the electronic conductivity by forming a conductive network [14,30].

* Corresponding author.
E-mail address: elisa.thauer@kip.uni-heidelberg.de (E. Thauer).

https://doi.org/10.1016/j.electacta.2021.138881
0013-4686/

Table 1
The molecular structure and acid dissociation constant of the selected carboxylic acids.

Carboxylic acid	Chemical formula	Structure	Acidity (pK_{a1})
Citric acid	$C_6H_8O_7$	fx	3.13
Malic acid	$C_4H_6O_5$	fx	3.46
Tartaric acid	$C_4H_6O_6$	fx	3.04

For example, dandelion-like V_2O_3/C composite with bicontinuous 3D hierarchical structures, which was synthesized by a template-free solvothermal method, shows high reversible capacity, outstanding cycling performance and excellent rate capability [31]. Yu et al. [32] reported that urchin-like V_2O_3/C hybrid composed of nanofibers and hollow nanospheres delivered a discharge capacity of 737 mA h g^{-1} after 100 cycles at a current density of 0.1 A g^{-1}. Jiang et al. [33] prepared via a template-free polyol solvothermal method carbon-coated V_2O_3 yolk−shell microspheres. The hierarchically structured V_2O_3/C composite shows superior electrochemical performance compared to bulk V_2O_3. Liu et al. [34] fabricated 3D hierarchical porous V_2O_3@C micro/nanostructures consisting of crumpled nanosheets through self-reduction under annealing from the structurally similar VO_2(B)@C precursor exhibiting a large reversible capacity up to 732 mA h g^{-1} at 100 mA g^{-1} even after 136 cycles.

Herein, we report for the first time the hydrothermal method with the post-annealing treatment to synthesize a V_2O_3/C composite material with a unique hierarchical structure using citric acid, tartaric acid, and malic acid as both the carbon sources and reducing agents. The chosen organic acids possess different molecular structure, acidity affecting the hydrolysis reaction, and different numbers of hydroxyl groups as well as carboxyl groups which can serve as organic ligands in the coordination reaction with vanadium ion. The chemical formula of used carboxylic acids and their molecular structure are summarized in Table 1. The influence of the synthesis conditions on the chemical composition, morphology, texture, and electrochemical properties of V_2O_3/C composites is particularly investigated.

2. Experimental

2.1. Materials

Vanadyl sulfate hydrate $VOSO_4 \bullet nH_2O$ (97% $VOSO_4$), ammonium hydroxide solution (28% NH_3 in H_2O), tartaric acid ($C_4H_6O_6$), malic acid ($C_4H_6O_5$), and citric acid ($C_6H_8O_7$) with analytical grade were purchased from Sigma–Aldrich and used without any further purification.

2.2. Synthesis of V_2O_3/C composites

V_2O_3/C composites were prepared using the hydrothermal thermolysis process. The typical synthesis route is briefly described as follows. Firstly, vanadyl hydroxide $VO(OH)_2$ precursor was prepared. According to the synthetic procedure, 7.95 g $VOSO_4 \bullet nH_2O$ was dissolved in 400 mL of deionized H_2O using magnetic stirring at room temperature, then ammonium hydroxide solution was added dropwise (one drop every ~1 min) to adjust the pH value of the mixture equal to 4 The brown precipitate was collected by centrifugation, washed several times with water and ethanol, and dried at 25 °C in air to obtain the $VO(OH)_2$ powder products. Secondly, $VO(OH)_2$ and the carboxylic acid (citric acid, malic acid or tartaric acid) were weighed in at a molar ratio of 1: 1 and mixed well together in deionized 60 mL water under constant stirring. The mixture became a clear-blue solution, which was then transferred to a 45 mL stainless steel autoclave lined with PTFE. The autoclave was heated at 180 °C for 24 h and then cooled to room temperature naturally. The obtained product was filtered, washed with deionized water, and dried in air under ambient conditions. Finally, the powder was sintered under a flow of N_2 gas at 400–650 °C for 1 h to obtain the V_2O_3/C composites. Depending on the type of the carboxylic acids, the resulting materials are termed below as V_2O_3/C-C (citric acid), V_2O_3/C-M (malic acid), and V_2O_3/C-T (tartaric acid).

2.3. Characterization

Powder X-ray diffraction (XRD) in the 10–70 ° 2θ range with a step size of 0.2 ° was performed on a Bruker AXS D8 Advance Eco diffractometer using CuKα radiation. The morphology of the samples was investigated by a ZEISS Leo 1530 scanning electron microscope (SEM) and a JEOL JEM 2100 transmission electron microscope (TEM). The energy dispersive X-ray analysis was performed on JEOL JSM 6390 LA scanning electron microscopy equipped with an EX-23010BU energy-dispersive X-ray analyzer. Raman spectra were measured with an inVia Reflex spectrometer (Renishaw) using a 100 mW RL532–08 solid state laser with a 532 nm wavelength. To avoid damages of the samples, the emitted power was decreased up to 1%. Thermogravimetric analysis (TG-DSC-MS) with a heating rate of 10 K•min^{-1} starting from room temperature up to 750 °C under flowing air was carried out using STA 449 F_3 Jupiter thermoanalyzer (Netzsch) coupled with a QMS 403 mass spectrometer. The textural characteristics (specific surface area, porosity) of the samples were determined with a Gemini VII (Micromeritics) analyzer on the basis of low-temperature nitrogen adsorption. The samples were prepared by evacuation at 100 °C for 3 h. The specific surface area was calculated by the Brunauer–Emmett–Teller (BET) method using nitrogen adsorption isotherms. The pore-size distribution curves were calculated by the Barrett–Joyner–Halenda method. The content of carbon was determined by CHN elemental analysis (EA) using Vario MICRO Cube (Elementar).

2.4. Electrochemical measurements

Electrochemical studies were performed with a VMP3 potentiostat (Bio-Logic SAS) at 25 °C using Swagelok-type half cells with lithium metal foil (Alfa Aesar) pressed on a nickel current collector as counter electrode (see [35]). The working electrode consists of 75 wt% active material, 15 wt% carbon black (Super C65, Timcal) and 5% polyvinylidene fluoride binder (Solvay Plastics) and were prepared as follows. First, the powders were mixed in N-methyl-2-pyrrolidone (NMP, Sigma-Aldrich) and stirred for at least 12 h. To obtain a spreadable slurry most of the NMP was evaporated under vacuum. Afterwards, the electrode slurry was applied on circular Cu meshes (wire diameter: 0.115 mm, nominal aperture: 0.14 mm, wires/inch: 100 × 100, open area: 30.3%, thickness: 0.25 mm,) with 10 mm diameter and the resulting electrodes were dried under vacuum, pressed with a spindle press by hand and then dried again. The electrodes were separated by two glass fiber layers (Whatman GF/D). As electrolyte 200 μl of a 1 M $LiPF_6$ salt solution in 1:1 ethylene carbonate and dimethyl carbonate (Merck Electrolyte LP30) was used. The preparation of the electrodes and the cell assembly were done in a glovebox filled under argon atmosphere (O_2/H_2O < 5 ppm). For *ex-situ* SEM measurement, the cells were galvanostatically cycled at 100 mA g^{-1} and disassembled in the glove box. The electrodes were washed in DMC and dried under vacuum conditions. The calculation of the specific capacity is based on the total mass weight of the composites V_2O_3/C.

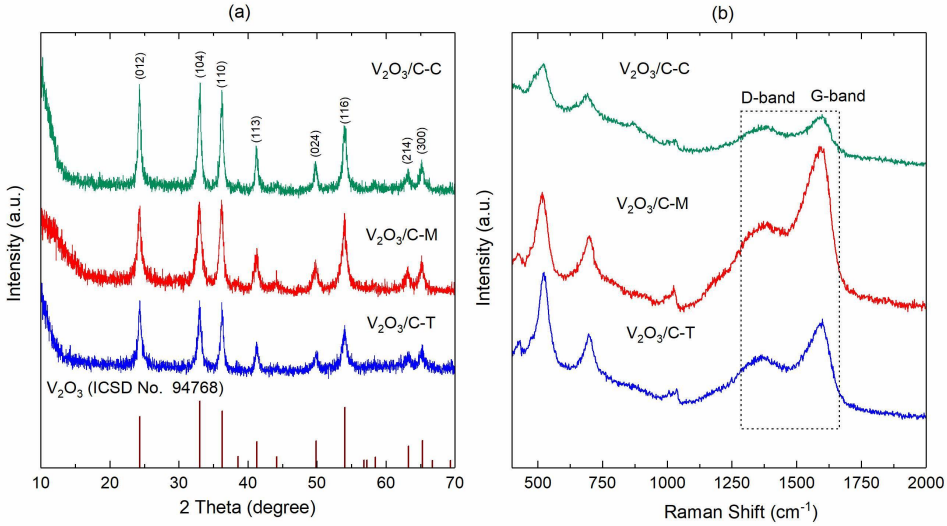

Fig. 1. (a) XRD patterns and (b) Raman spectra of the V_2O_3/C composites fabricated using different carboxylic acids: citric acid (V_2O_3/C-C), tartaric acid (V_2O_3/C-T), and malic acid (V_2O_3/C-M). In addition, the ICSD #94,768 [36] reference pattern of rhombohedral V_2O_3 is shown in (a).

Table 2
Crystallite sizes from XRD, results of the BET analysis, and carbon content of the V_2O_3/C composites.

Samples	Crystallite size (nm)	S_{BET} ($m^2 \bullet g^{-1}$)	Carbon content (wt%) TG	EA
V_2O_3/C-C	17(2)	27.2	6.0	6.5(5)
V_2O_3/C-M	14(2)	34.5	13.0	12.5(5)
V_2O_3/C-T	16(2)	90.0	12.6	12.6(5)

3. Results and discussion

Fig. 1a shows the XRD patterns of the V_2O_3/C composites synthesized using different carboxylic acids. The samples obtained using malic acid and tartaric acid after hydrothermal treatment but before annealing in inert atmosphere are XRD amorphous samples (Fig. S1). On contrary, XRD pattern of the citric acid-assisted sample after hydrothermal treatment shows a low crystallinity of the compound. It can be explained by the stronger redox activity of citric acid. Annealing at 650 °C leads to the appearance of distinguished XRD patterns, which can be assigned to the rhombohedral V_2O_3 phase according to ICSD #94,768 [36]. No impurity peak can be observed, which demonstrates the successful synthesis of phase pure V_2O_3. The average crystallite sizes of V_2O_3 in the V_2O_3/C-composites can be estimated using the Scherrer equation:

$$D_{hkl} = K\lambda / \Delta(2\theta_{hkl}) cos\theta_{hkl}, \quad (1)$$

where D_{hkl} is the average grain size based on the particular reflecting crystal face (hkl) direction, K is a shape factor which can be approximated to 0.9, λ is the wavelength of the applied Cu Kα radiation, $\Delta(2\theta_{hkl})$ is the full width at half-maximum of the diffraction peak, and θ_{hkl} is the Bragg angle. The averaged crystallite sizes of V_2O_3 in the composites V_2O_3/C-C, V_2O_3/C-M and V_2O_3/C-T obtained from the analysis of the (012), (104), (110), and (116) reflexes are listed in Table 2. We conclude that the composites exhibit V_2O_3 nanoparticles which crystallite size does not distinctly depend on the choice of carbon source. In addition, the different Bragg peaks yield very similar results which suggests rather regularly shaped particles.

To confirm the composite formation between V_2O_3 and carbon component, Raman analysis was carried out (Fig. 1b). It can be observed that two typical broad peaks, corresponding to the D- and G-bands, are located at about 1361 and 1595 cm^{-1}. The D-band is associated to the breathing mode of sp^2 hybridized carbon atoms in rings and only becomes active in the presence of defects and disordering atomic arrangements in the hexagonal graphitic layers. The G-bands corresponds to the in-plane vibration of sp^2-bonded carbon atoms [37]. Additionally, the pointed peaks are broad, indicating the presence of amorphous carbon with a low crystallinity. The ratio of the maximum intensities of these peaks, I_D/I_G, was calculated as 0.73, 0.77 and 0.88 for V_2O_3/C-M, V_2O_3/C-T and V_2O_3/C-C composites, respectively. As for the peaks below 1100 cm^{-1}, they are attributed to V–O vibrations as described in previous V_2O_3-based reports [38]. It should be noted that the Raman spectra for samples obtained after hydrothermal treatment but before annealing in inert atmosphere (Fig. S1) do not contain carbon typical vibrational modes.

The elemental chemical analyses of the composites yield a carbon content of 12.5(5)% and 12.6(5)% for V_2O_3/C-M and V_2O_3/C-T, respectively, and thus about twice as much as for the composite prepared with citric acid with 6.5(5)% carbon (see Table 2).

The morphology and topography of the V_2O_3/C composites synthesized using citric acid, malic acid, and tartaric acid as both carbon source and reducing agent were investigated by SEM (Fig. 2) and TEM measurements (Fig. S2). It is observed that all of them show hierarchically structured spheres with diameters about 1–4 µm. Some microspheres are connected to each other. The SEM images of citric acid and malic acid assisted V_2O_3/C composites display core-shell structures filled with a solid core. The thickness of the shells is about 200–300 nm. Obviously, the topography of the samples is affected by the carboxylic acid. The shells of the V_2O_3/C-C composite prepared using citric acid consist of nanoparticles with a size of only a few 10 nm, resulting in a rough surface texture with very fine granulation (Fig. 2 a and b). In the composite V_2O_3/C-M prepared using malic acid the shell has a coarse-grained surface to which particles with varying size up to 300 nm are attached (Fig. 2 c and d). In contrast to V_2O_3/C-C and V_2O_3/C-M composites, the SEM images of the broken microspheres of tartaric acid assisted V_2O_3/C-T composite reveal the solid interior structure (Fig. 2 e and f). It can be seen that the solid microspheres are composed of closely packed nanoparticles with the average size of about 25–40 nm, while the surface is decorated with flake-like nanoparticles. The core-shell structure of the V_2O_3/C composites prepared using citric acid and malic acid is confirmed by TEM measurements (Fig. S2 a–c). In the high resolution TEM image of V_2O_3/C-M composite a lattice spacing of 0.362 nm is mea-

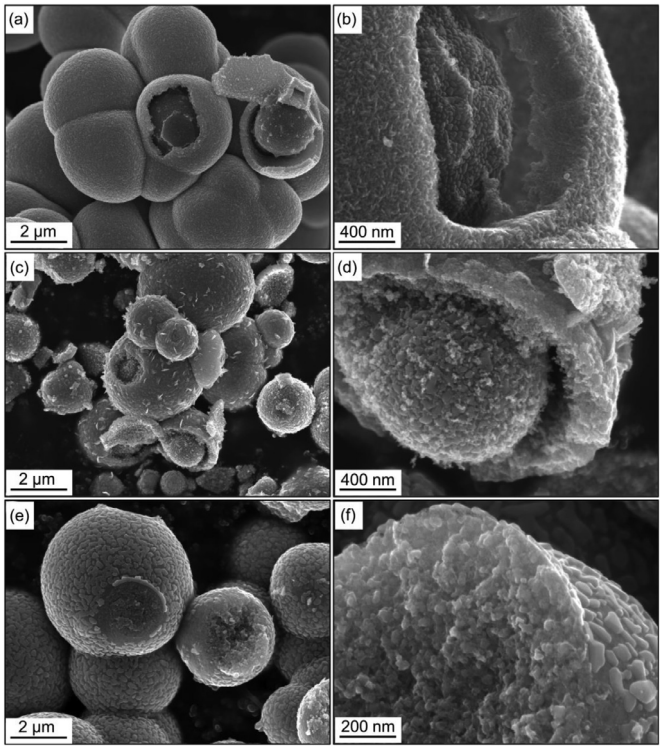

Fig. 2. SEM images of V_2O_3/C composites prepared using the different carboxylic acids: (a,b) citric acid, (c,d) malic acid, and (e,f) tartaric acid.

sured corresponding to the (012) crystal plane of rhombohedral-phase crystalline V_2O_3 (Fig. S2 d). Selected area electron diffraction (SAED) confirms the crystalline structure of V_2O_3 in the V_2O_3/C composite (Fig. S2 e). The observed Debye-rings in the SAED pattern can be indexed to the rhombohedral phase of V_2O_3, with diffraction rings corresponding to the (012), (104), (110), (020), (113), (116), and (300) crystal planes from inner to outer. Our data reveal the crucial role of the carboxylic acids on the morphology and internal microstructure of the resultant V_2O_3/C composites. The morphological structure of the composites prepared using citric acid and malic acid significantly differs from that of V_2O_3/C synthesized using tartaric acid. It is found that the formation the core-shell structure is a time-dependent process [33,39]. In the initial state of the process, the nanoparticles are assembled to spherical solid aggregates by the coordination reaction of the vanadium ion with organic ligand caused by the hydrogen bond and van der Waals interaction [31]. With increasing reaction time, spherical aggregates grow by the deposition of sheet-like particles on the surface of these aggregates. On prolonging the hydrothermal time, the solid microspheres evolve to microspheres with core-shell structure due to an inside-out Ostwald-ripening process that involves the dissolution of the unstable inner core and subsequent recrystallisation at the outer surface to form shells with a more stable phase [40]. The formation mechanism of core-shell structures establishes that the primary seed concentrations play a key role in the crystal nucleation and growth. It is known that the fast hydrolysis rate, which is inversely proportional to the dissociation constant of the compound, produces more primary particles [41]. In the case of V_2O_3/C composites, the primary particles are formed by hydrolysis of VO^{2+}-carboxylic acid complex using the water molecules as solvent. For citric acid, malic acid, and tartaric acid, the negative logarithm of the acid dissociation constant (pK_{a1}) is 3.13, 3.46, and 3.04, respectively. Accordingly, the stronger tartaric acid provides a lower degree of hydrolysis and fewer primary particles obtained. The low density of primary particles requires more time for them to assemble into spherical aggregates with a core-shell structure. In the case of V_2O_3/C-T composite (Fig. 2e), the hydrothermal treatment for 24 h only results in the deposition of the outer shell on the surface of cores which is the second stage of the formation of the core-shell microspheres. The elemental mapping analysis of V_2O_3/C-C composite, selected as an example, confirms the coexistence and homogeneous dispersion of V, O, and C elements (Fig. S3).

In order to determine the carbon content of V_2O_3/C composites, TG-DSC-MS measurements of the as-prepared samples were carried out under air flow. It can be observed that several steps emerge from the TG-curves of the V_2O_3/C composites (Fig. 3). In all samples, the first step starts from about 70 °C and ends at 200 °C. It can be mainly attributed to the loss of water absorbed on the material's surface. The process is accompanied by a very weak and broad endothermic peak centered at about 90 °C. The next weight loss from 200 °C up to ~400 °C is caused by the oxidation of the carbon component of the V_2O_3/C composites and the emission of CO_2 gases (m/z = 44 a.m.u.) as corroborated by the analysis of the MS-curves (ion current versus temperature). For the V_2O_3/C-C composite, this process is described by two distinct steps of weight loss which can be attributed to a successive oxidation of the carbon component, first of the carbon shell and then of the carbon core of the sphere-like particles (Fig. 3a). Additionally, the TG-curve for V_2O_3/C-C composite shows a small mass increase (0.3 wt%) from 357 to 384 °C originating from the oxidation of the outer V_2O_3. While the carbon shell is oxidized, the outer V_2O_3 becomes exposed to air and oxidizes to V_2O_5. The combustion reactions of the carbon component in V_2O_3/C-C composite are accompanied by two broad exothermic peaks in the DSC-curves centered at 354 and 408 °C. A large exothermic peak width indicates that the reactions occur at a low rate. For V_2O_3/C-M composite, the results imply removal of carbon within two distinct steps as indicated by one pronounced peak at around 396 °C and the visible satellite peak at about 360 °C in the MS-curve (Fig. 3b). This process is accompanied by one broad exothermal peak in the DSC-curve at 392 °C. The thermal behavior of the V_2O_3/C-M composite is similar to the one of the acid-assisted composite as it also reflects the particular core-shell morphology (Fig. 2c and d). In contrast, in the case of V_2O_3/C-T composite exhibiting a solid interior structure, the decomposition of the carbon component by oxidation and the release of CO_2 gases occurs within only one stage (Fig. 3c). A strong and sharp exothermal peak with its maximum at 384 °C is observed indicating the vigorous combustion reaction of the carbon. According to the TG-curves, the calculated carbon contents in V_2O_3/C-C, V_2O_3/C-M and V_2O_3/C-T composites amount to 6.0 wt%, 13.0 wt%, and 12.6 wt%, respectively. These results are in a good agreement with the results of the carbon content determination by the EA (Table 2). The last step in the TG curves ranging from ~400 to 750 °C shows a weight gain of about 0.2 wt%, 1.3 wt% and 3.1 wt% for V_2O_3/C-C, V_2O_3/C-M, and V_2O_3/C-T, respectively. This process is attributed to the full oxidation of V^{3+} ions to V^{5+} resulting in the formation of V_2O_5 as a final thermolysis product. From the mass spectroscopy curves it is evident that the main gaseous product is the molecular ion O_2^+ with m/z = 32 a.m.u., whose content changes during this process. A sharp endothermic peak at ~677 °C in the DSC-curves can be ascribed to the melting of V_2O_5.

The texture properties of the composites were investigated by nitrogen sorption isotherms (Fig. 4). All measured curves can be classified as a type-IV isotherm which is typical for mesoporous materials [42]. Unlike V_2O_3/C-M and V_2O_3/C-T, an H3 hysteresis loop occurs in V_2O_3/C-C at high relative pressures (P/P_0 = 0.7–0.9), indicating the presence of macropores (Fig. 4a). Specifically, the H3 hysteresis loop testifies about the presence of the aggregated plate-like particles with slit-shaped pores structure [42]. Both V_2O_3/C-M

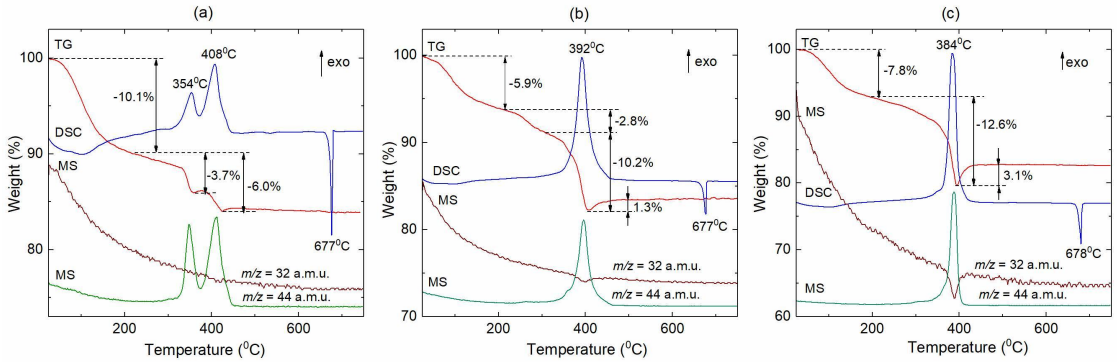

Fig. 3. Thermogravimetric (red), DSC (blue), and mass spectroscopy (brown, green) curves of V_2O_3/C composites prepared using (a) citric acid, (b) malic acid, and (c) tartaric acid (For interpretation of the references to color in this figure legend, the reader is referred to the web version of this article).

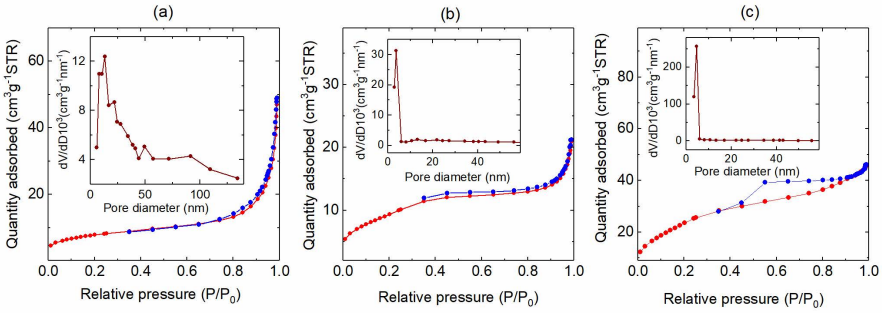

Fig. 4. Nitrogen sorption isotherms and corresponding pore-size distributions (inset) of V_2O_3/C composites prepared using (a) citric acid, (b) malic acid, and (c) tartaric acid.

and V_2O_3/C-T samples exhibit type H4 loops associated with narrow slit-like pores (Fig. 4b and c). The BET specific surface areas of the V_2O_3/C composites are displayed in Table 1. In comparison with V_2O_3/C-C and V_2O_3/C-M, the BET surface area of the V_2O_3/C-T composite is rather high which may be due to the particular morphology of this material (see Fig. 2). For V_2O_3/C-M and V_2O_3/C-T composites, the pore-size distribution is monomodal with the predominant size of about 4 nm (Fig. 4b and c, inset) while, in contrast, V_2O_3/C-C composite exhibits an inhomogeneous pore structure. The pore-size distribution for V_2O_3/C-C composite is observed in a wide range, demonstrating the co-existence of both mesopores and macropores (Fig. 4a, inset). These differences in the textural properties are caused by using of various carboxylic acids as the carbon source. The inhomogeneous pore structure of V_2O_3/C-C might arise from the microcracking of the sample by a large amount of gases generated in the heating of the V-O precursor with citric acid leading to a wide size distribution. Compared to malic acid and tartaric acid, citric acid has the highest molecular mass favoring the release of a large amount of gases during the post-annealing treatment (H_2O, CO_2, O_2, CO).

The electrochemical properties of the V_2O_3/C composites are investigated by cyclic voltammetry (CV) and galvanostatic cycling with potential limitation (GCPL) within the potential window between 0.01 and 3.2 V. Fig. 5a displays the first, second, and fifth cycle of the cyclic voltammogram of V_2O_3/C-C recorded at a scan rate of 0.05 mV s^{-1}. As the comparison of the CV curves of the other two composites V_2O_3/C-M and V_2O_3/C-T (Fig. S4) shows, there are no pronounced differences between the composites prepared with different carboxylic acids. During the first reductive scan, there is a peak at around 0.75 V which disappears in the subsequent cycles, corresponding to the irreversible formation of a solid electrolyte interface (SEI) from the decomposition of electrolyte [14]. The storage of Li-ions in the carbonaceous structures is reflected by the redox activity around the lower voltage limit 0.01 V [43]. The remaining redox activity can be assigned to the electrochemical lithiathion/delithiation mechanism of V_2O_3, that can be described as follows [44,45]:

$$V_2O_3 + xLi^+ + xe^- \leftrightarrow Li_xV_2O_3, \quad (2)$$

$$Li_xV_2O_3 + (6\text{-}x)Li^+ + (6\text{-}x)e^- \leftrightarrow 2\ V + 3Li_2O. \quad (3)$$

During discharge, Li^+ are firstly intercalated into V_2O_3 to form $Li_xV_2O_3$ (Eq. (2)). While more Li-ions are inserted, Li_2O is formed by a conversion reaction accompanied by the total reduction of the vanadium (Eq. (3)). The charge process follows the reverse reactions. Due to the multivalency of vanadium, several transition states can coexist during the dis-/charge process leading to the observed smooth course of the CV curves without pronounced peaks [14,46]. The second and fifth CV cycles are mostly overlapped, implying high reversibility of the Li^+ storage in the hierarchically structured V_2O_3/C sphere electrode.

GCPL measurements enable to investigate the cycling behavior of the V_2O_3/C composites as an anode material for lithium-ion batteries. Fig. 5b shows the dis-/charge capacities at 100 mA g^{-1} for the first 100 cycles. For comparison, the data of V_2O_3/C microparticles with chunk-shaped morphology (V_2O_3/C-C-SG) synthesized by a sol-gel process, which were reported in detail elsewhere [47], are also shown. The potential profiles exemplarily shown for V_2O_3/C-C in Fig. 5c are fully consistent with the CV measurements. During galvanostatic cycling the potential gently decreases and no obvious plateaus appear, indicating that V_2O_3 reacts smoothly with Li-ions. While there are no major differences to the other two composites V_2O_3/C-M and V_2O_3/C-T in the potential profiles (Fig. S5), clear differences can be observed in the reached capacities. In the first cycle, specific dis-/charge capacities of 680/380 mAh g^{-1} and

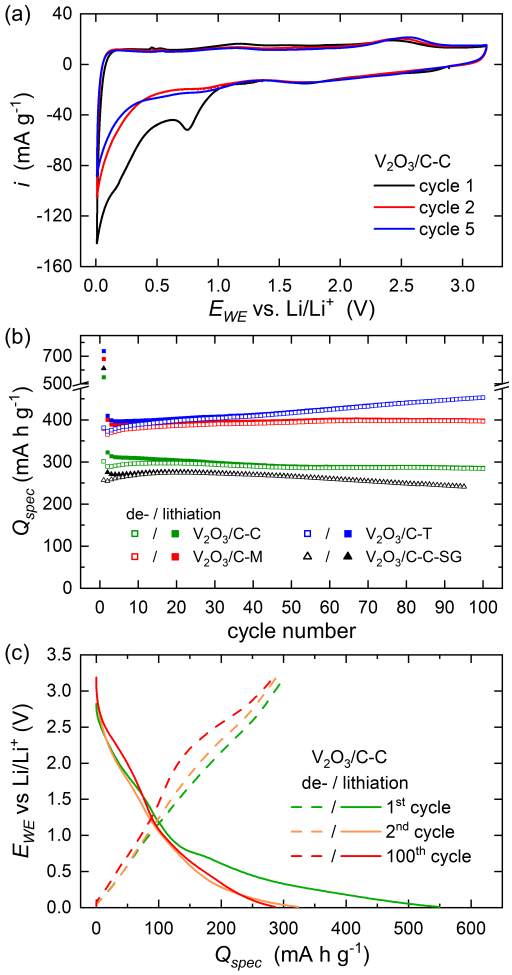

Fig. 5. (a) CV curves of V_2O_3/C-C recorded at a scan rate of 0.05 mV s^{-1}. (b) Specific dis-/charge capacities for the composites fabricated by hydrothermal thermolysis method using citric acid (V_2O_3/C-C), malic acid (V_2O_3/C-M), tartaric acid (V_2O_3/C-T), and by citric acid-assisted sol-gel method (V_2O_3/C-C-SG) during galvanostatic cycling at 100 mA g^{-1} and (c) corresponding potential profiles of the first, second and hundredth cycle for the V_2O_3/C-C composite.

738/381 mAh g^{-1} are measured for V_2O_3/C-M and V_2O_3/C-T, respectively, and only 549/302 mAh g^{-1} for the composite V_2O_3/C-C. The irreversible capacity in the initial cycle originates from the SEI formation and structural changes during the first lithiation as observed in the CV curves [15,16,44]. In comparison to the composites V_2O_3/C-M and V_2O_3/C-T, the composite V_2O_3/C-C has only about half the carbon content and the smallest surface area which might explain the lower capacity. All three composites exhibit excellent capacity retention. After 100 cycles the composites V_2O_3/C-M and V_2O_3/C-T reach discharge capacities of 399 and 454 mAh g^{-1}. The composite V_2O_3/C-C still achieves 284 mAh g^{-1}. Even an increase of the capacity with cycling can be observed for V_2O_3/C-M and V_2O_3/C-T and for the composite V_2O_3/C-C at least in the first twenty cycles. This is also reported in the literature and can be attributed to an activation process resulting from the electrochemical grinding effect [14,16,34,51]. The progressive particle pulverization leads to the exposure of inner inactive regions and thus generates new active sites for electrochemical reactions. The results of the galvanostatic dis-/charge measurements suggest that the morphological structure, core-shell microspheres as for V_2O_3/C-M or solid microspheres as for V_2O_3/C-T, does not seem to affect the electrochemical performance. In addition, it is clearly observed that in comparison to the chunk-shaped composite V_2O_3/C-C-SG (specific

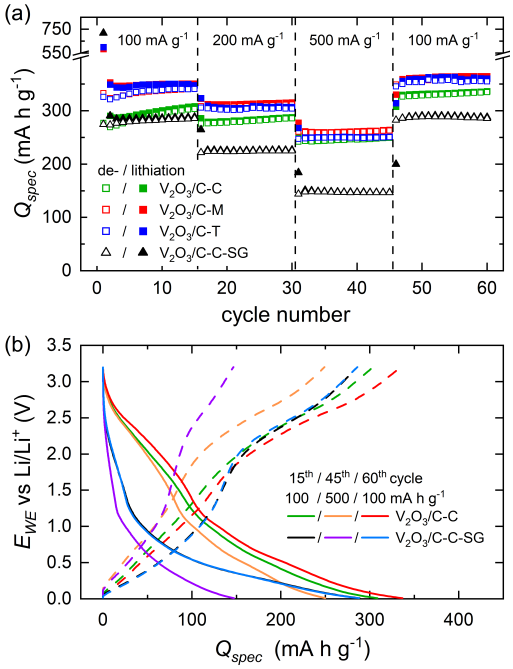

Fig. 6. (a) Specific charge/discharge capacities of rate capability test with different cycling rates between 100 and 500 Ma g^{-1} and (b) corresponding potential profiles of the composites prepared by hydrothermal synthesis using citric acid (V_2O_3/C-C), and the composite V_2O_3/C-C-SG fabricated by citric acid-assisted sol-gel method.

surface area of 1.8 m^2 g^{-1} [47]) fabricated by citric acid-assisted sol-gel method the composites prepared by hydrothermal synthesis exhibit superior electrochemical performance. The composites with sphere-like morphology achieve higher specific capacities with enhanced cycling stability which might be attributed to their special architecture and larger specific surface area. SEM images (Fig. S6) of V_2O_3/C-C electrodes, selected as an example, after 1 cycle and after 200 cycles confirm the structural stability of the hierarchically structured V_2O_3/C microspheres during cycling. The chunk-shaped V_2O_3 may suffer from structural degradation and self-aggregation during cycling, which results in poor cycling stability.

The results of the rate capability studies at current densities from 100 to 500 mA g^{-1} are shown in Fig. 6. Among all samples, the composite V_2O_3/C-M prepared using malic acid, exhibits the best performance with specific discharge capacities of 351 mAh g^{-1}, 316 mAh g^{-1} and 263 mAh g^{-1} at rates of 100 mA g^{-1}, 200 mA g^{-1}, and 500 mA g^{-1} after 15 cycles each, corresponding to a capacity retention of 75% when increasing the current by five times. Moreover, when the current density is returned to 100 mA g^{-1} the original capacity is fully recovered, demonstrating a remarkably high rate capability. The other two samples also show high rate performance while, the composite V_2O_3/C-C-SG exhibits much lower capacities, at all measured current rates in comparison, further confirming the beneficial properties of the sphere-like structure of the samples V_2O_3/C prepared via citric acid, malic acid, or rather tartaric acid-assisted hydrothermal thermolysis method. The potential profiles in Fig. 6b show for the composite V_2O_3/C-C-SG the higher overpotential in terms of lower discharge and higher charge potential with increasing rate which results from kinetic effects.

To explain the superior rate performance of the porous sphere-like composites compared to chunk-shaped V_2O_3/C, the surface-induced capacitive and diffusion-controlled processes were quantified by studying the lithium storage kinetics. Fig. 7a and b show the CV curves of V_2O_3/C-C and V_2O_3/C-C-SG at scan rates ranging

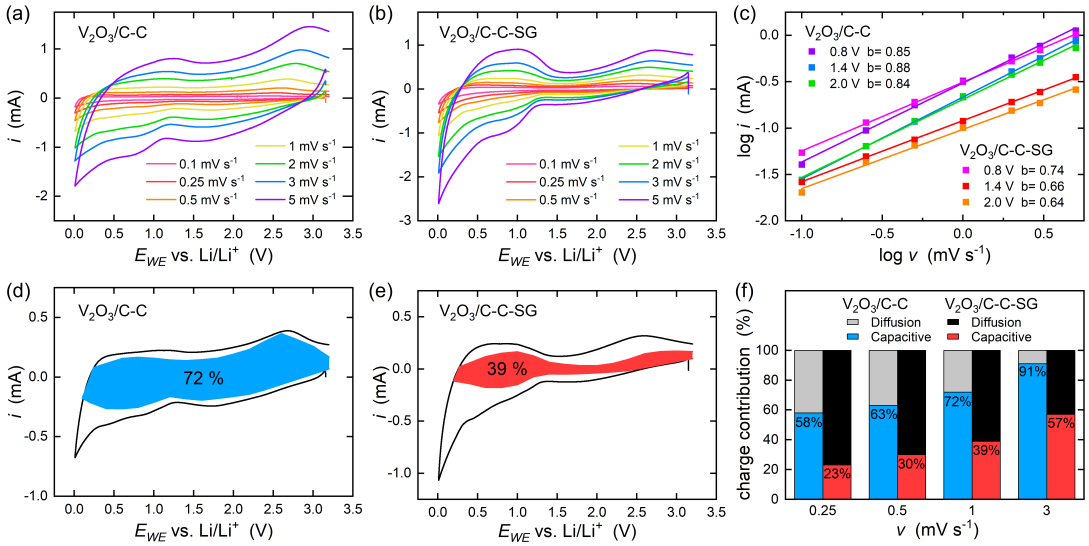

Fig. 7. Kinetic analysis: CV curves at different scan rates of (a) V_2O_3/C-C and (b) V_2O_3/C-C-SG. (c) Power law dependence of current response on scan rate at various potentials for reductive sweep. Capacitive contribution (shaded area) to the total current at a scan rate of 1 mV s^{-1} of (d) V_2O_3/C-C and (e) V_2O_3/C-C-SG. (f) Normalized contribution ratio of capacitive and diffusion-controlled charge storage at different scan rates.

Table 3
Comparison of the electrochemical performance of V_2O_3/C electrodes prepared via solvo- and hydrothermal synthesis as reported in the literature.

Material	Current density (mA•g^{-1})	1st charge capacity (mAh•g^{-1})	Specific capacity (mAh•g^{-1})/cycle no.	Refs.
Core-shell V_2O_3/C nanoplatelets	100	360[a]	260/100	[29]
Yolk-shell V_2O_3/C microspheres	100	470[a]	437.5/100	[33]
V_2O_3/C nanoparticles	200	380	525/200	[16]
Dandelion-like V_2O_3/C spheres	500	280[a]	474/400	[31]
Peapod-like V_2O_3/C nanowires	100	230	186/125	[54]
Core-shell V_2O_3/C microspheres	100	380	399/100	This work
Solid-structured V_2O_3/C microspheres	100	381	454/100	This work

[a] Values are estimated from the graphs.

from 0.01to 5 mV s^{-1} for one cycle each starting with the second cycle. The relationship of current (i) and scan rate (v) obeys the power law formula

$$i = av^b, \quad (4)$$

where both a and b are adjustable values [48,49]. A b value of 0.5 indicates a totally diffusion-controlled process, while for an ideal capacitive process the b value is 1 [49,50]. By plotting log(i) vs. log (v), the b value can be obtained from the slope. Fig. 7c shows the b values of V_2O_3/C-C and V_2O_3/C-C-SG at various potentials for reductive sweep. The higher b values calculated for V_2O_3/C-C compared to V_2O_3/C-C-SG suggest a higher capacitive contribution in the V_2O_3/C-C composite. Quantitatively, the capacity contribution of the current response can be determined by using the following equation [51,52]:

$$i(V) = k_1 v + k_2 v^{1/2}. \quad (5)$$

The current at a fixed potential V can be divided into two parts, one originating from the capacitive effects ($k_1 v$) and one from diffusion-controlled processes ($k_2\ v^{1/2}$). By plotting $i(V)/v^{1/2}$ vs. $v^{1/2}$, k_1 and k_2 at a certain potential can be determined by the slope and the y-axis intercept (Fig. S7). The kinetic analysis at 1 mV s^{-1} reveals that the Li^+ storage for V_2O_3/C-C is more determined by capacitive effects than for V_2O_3/C-C-SG. As shown in Fig. 7d, 72% of the total charge of V_2O_3/C-C results from capacitive processes (highlighted by the shaded area), while for V_2O_3/C-C-SG it is only 39% (Fig. 7e). A high fraction of capacitive charge storage is very advantageous since surface-induced processes are much faster than diffusion-controlled processes, and thus explains the excellent rate capability of V_2O_3/C-C. Furthermore, it causes smaller volume changes during de-/lithiation compared to diffusion-controlled processes resulting in an improved cycling stability [53]. We attributed these high capacitive contributions to the large surface area of V_2O_3/C-C spheres. As expected, with an increasing scan rate, increasing capacitive contributions were obtained (Fig. 7f). This can be explained by the slower Li^+ diffusion compared to the faster and less rate-depended contribution of the surface-induced capacitive processes.

The results of this study clearly indicate that the V_2O_3/C composites with sphere-like structure exhibit an enhanced electrochemical performance as compared to chunk-like V_2O_3/C. Moreover, as demonstrated by Table 3, the composite V_2O_3/C spheres also compete well with other V_2O_3/C materials prepared via solvo- or hydrothermal synthesis reported in literature. The excellent charge storage performance of the hierarchically structured V_2O_3/C microspheres can be attributed to their special architecture in several aspects. As above mentioned, the hierarchical assembly of nanoparticles may offer many advantages, including improved structural stability of the electrode material. Compared to V_2O_3/C chunks, the porous V_2O_3/C microspheres have a larger specific surface area, which shortens the diffusion path of Li-ions and increases the number of electrochemical active reaction sites. Moreover, it promotes surface-induced capacitive charge storage which, on one hand, provides a fast charge transfer improving the rate performance and causes less volume changes during de-/lithiation leading to an improved cycling stability on the other. Besides the above factors, also the carbon in V_2O_3/C has a beneficial impact on the electrochemical properties. It improves the electronic con-

ductivity and structural stability of the electrode material by providing a conductive backbone, which enhances the charge transfer, buffers the large volume changes during de-/lithiation, and hinders the self-aggregation of V_2O_3 nanostructures. This results in a high rate capacity and good cycling stability.

4. Conclusion

In summary, we demonstrate a facile hydrothermal thermolysis synthesis route to produce hierarchically structured porous V_2O_3/C microspheres. In this synthesis method, vanadyl hydroxide acts as precursor and different carboxylic acids as both the carbon source and reducing agents. The carbon content and specific surface area of the resulting V_2O_3/C nanocomposites can be controlled by varying the used carboxylic acid. In addition, the as-prepared products possess either core-shell or solid structure depending on the used carboxylic acid. Due to their special architecture, the V_2O_3/C composites exhibit very good electrochemical performance as anodes for LIBs, including high capacities and excellent cycling stabilities and rate capabilities. The high specific surface area facilitates a fast and less destructive capacitive charge storage contributing to superior electrochemical properties compared to chunk-like V_2O_3/C. Moreover, the carbon as conductive framework can effectively enhance the materials conductivity as well as the structural stability of the electrode material.

Declaration of Competing Interest

The authors declare that they have no known competing financial interests or personal relationships that could have appeared to influence the work reported in this paper.

Credit authorship contribution statement

E. Thauer: Conceptualization, Methodology, Investigation, Writing – original draft, Visualization. **G.S. Zakharova:** Conceptualization, Methodology, Investigation, Writing – original draft, Visualization. **L.F. Deeg:** Investigation. **Q. Zhu:** Investigation. **R. Klingeler:** Conceptualization, Writing – review & editing, Supervision.

Acknowledgments

This work was supported by the Deutsche Forschungsgemeinschaft through projects KL 1824/12–1 and KL 1824/14–1. G.Z. acknowledges support of the state order via the Ministry of Science and High Education of Russia (Theme no. AAAA-A19–119031890025–9). Partial support by the BMWi through project 03ET6095C (HiKoMat) is acknowledged. The authors thank I. Glass for experimental support.

Supplementary materials

Supplementary material associated with this article can be found, in the online version, at doi:10.1016/j.electacta.2021.138881.

References

[1] J.B. Goodenough, K.S. Park, The Li-ion rechargeable battery: a perspective, J. Am. Chem. Soc. 135 (2013) 1167–1176, doi:10.1021/ja3091438.
[2] B. Scrosati, J. Garche, Lithium batteries: status, prospects and future, J. Power Sources 195 (2010) 2419–2430, doi:10.1016/j.jpowsour.2009.11.048.
[3] F. Cheng, J. Liang, Z. Tao, J. Chen, Functional materials for rechargeable batteries, Adv. Mater. 23 (2011) 1695–1715, doi:10.1002/adma.201003587.
[4] G. Zubi, R. Dufo-López, M. Carvalho, G. Pasaoglu, The lithium-ion battery: state of the art and future perspectives, Renew. Sustain. Energy Rev. 89 (2018) 292–308, doi:10.1016/j.rser.2018.03.002.
[5] N. Nitta, F. Wu, J.T. Lee, G. Yushin, Li-ion battery materials: present and future, Mater. Today 18 (2015) 252–264, doi:10.1016/j.mattod.2014.10.040.
[6] S. Goriparti, E. Miele, F. de Angelis, E. Di Fabrizio, R. Proietti Zaccaria, C. Capiglia, Review on recent progress of nanostructured anode materials for Li-ion batteries, J. Power Sources 257 (2014) 421–443, doi:10.1016/j.jpowsour.2013.11.103.
[7] L. Ji, Z. Lin, M. Alcoutlabi, X. Zhang, Recent developments in nanostructured anode materials for rechargeable lithium-ion batteries, Energy Environ. Sci. 4 (2011) 2682, doi:10.1039/c0ee00699h.
[8] P. Poizot, S. Laruelle, S. Grugeon, L. Dupont, J.M. Tarascon, Nano-sized transition-metal oxides as negative-electrode materials for lithium-ion batteries, Nature 407 (2000) 496–499, doi:10.1038/35035045.
[9] S. Fang, D. Bresser, S. Passerini, Transition metal oxide anodes for electrochemical energy Storage in lithium- and sodium-ion batteries, Adv. Energy Mater. 10 (2020) 1902485, doi:10.1002/aenm.201902485.
[10] Q. Zhang, J. Wang, J. Dong, F. Ding, X. Li, B. Zhang, S. Yang, K. Zhang, Facile general strategy toward hierarchical mesoporous transition metal oxides arrays on three-dimensional macroporous foam with superior lithium storage properties, Nano Energy 13 (2015) 77–91, doi:10.1016/j.nanoen.2015.01.029.
[11] X. Yan, F. Jiang, X. Sun, R. Du, M. Zhang, L. Kang, Q. Han, W. Du, D. You, Y. Zhou, A simple, low-cost and scale-up synthesis strategy of spherical-graphite/Fe_2O_3 composites as high-performance anode materials for half/full lithium ion batteries, J. Alloys Compd. 822 (2020) 153719, doi:10.1016/j.jallcom.2020.153719.
[12] X. Gu, J. Yue, L. Li, H. Xue, J. Yang, X. Zhao, General synthesis of MnOx (MnO_2, Mn_2O_3, Mn_3O_4, MnO) hierarchical microspheres as lithium-ion battery anodes, Electrochim. Acta 184 (2015) 250–256, doi:10.1016/j.electacta.2015.10.037.
[13] E. Thauer, X. Shi, S. Zhang, X. Chen, L. Deeg, R. Klingeler, K. Wenelska, E. Mijowska, Mn_3O_4 encapsulated in hollow carbon spheres coated by graphene layer for enhanced magnetization and lithium-ion batteries performance, Energy 217 (2021) 119399, doi:10.1016/j.energy.2020.119399.
[14] Y. Dong, R. Ma, M. Hu, H. Cheng, J.-.M. Lee, Y.Y. Li, J.A. Zapien, Polymer-pyrolysis assisted synthesis of vanadium trioxide and carbon nanocomposites as high performance anode materials for lithium-ion batteries, J. Power Sources 261 (2014) 184–187, doi:10.1016/j.jpowsour.2014.03.020.
[15] Y. Shi, Z. Zhang, D. Wexler, S. Chou, J. Gao, H.D. Abruña, H. Li, H. Liu, Y. Wu, J. Wang, Facile synthesis of porous V_2O_3/C composites as lithium storage material with enhanced capacity and good rate capability, J. Power Sources 275 (2015) 392–398, doi:10.1016/j.jpowsour.2014.10.175.
[16] C. Huan, X. Zhao, X. Xiao, Y. Lu, S. Qi, Y. Zhan, L. Zhang, G. Xu, One-step solvothermal synthesis of V_2O_3@C nanoparticles as anode materials for lithium-ion battery, J. Alloys Compd. 776 (2019) 568–574, doi:10.1016/j.jallcom.2018.10.323.
[17] J. Leng, H. Mei, L. Zhan, Y. Wang, S. Yang, Y. Song, V_2O_3 nanoparticles anchored onto the reduced graphene oxide for superior lithium storage, Electrochim. Acta 231 (2017) 732–738, doi:10.1016/j.electacta.2017.01.133.
[18] D. Adler, J. Feinleib, Semiconductor-to-metal transition in V_2O_3, Phys. Rev. Lett. 12 (1964) 700–703, doi:10.1103/PhysRevLett.12.700.
[19] B. Qi, H.P. Gunnlaugsson, S. Ólafsson, H.P. Gislason, E.B. Thorsteinsson, U.B. Arnalds, R. Mantovan, I. Unzueta l, D.V. Zyabkin, K. Ram, K. Johnston, P.B. Krastev, T.E. Mølholt, H. Masenda, A. Martín-Luengo, D. Naidoo, J. Schell, Metal-insulator transition in crystalline V_2O_3 thin films probed at atomic-scale using emission Mössbauer spectroscopy, Thin Solid Films 714 (2020) 138389, doi:10.1016/j.tsf.2020.138389.
[20] C. Grygiel, A. Pautrat, P. Rodière, Galvanomagnetic properties and noise in a barely metallic film of V_2O_3, Phys. Rev. B 79 (2009), doi:10.1103/PhysRevB.79.235111.
[21] Y. Zhong, M. Yang, X. Zhou, Z. Zhou, Structural design for anodes of lithium-ion batteries: emerging horizons from materials to electrodes, Mater. Horiz. 2 (2015) 553–566, doi:10.1039/C5MH00136F.
[22] M. Zheng, H. Tang, L. Li, Q. Hu, L. Zhang, H. Xue, H. Pang, Hierarchically nanostructured transition metal oxides for lithium-ion batteries, Adv. Sci. 5 (2018) 1700592 (Weinheim, Baden-Wurttemberg, Germany), doi:10.1002/advs.201700592.
[23] H. Yue, Q. Wang, Z. Shi, C. Ma, Y. Ding, N. Huo, J. Zhang, S. Yang, Porous hierarchical nitrogen-doped carbon coated $ZnFe_2O_4$ composites as high performance anode materials for lithium ion batteries, Electrochim. Acta 180 (2015) 622–628, doi:10.1016/j.electacta.2015.08.139.
[24] L. Zhou, K. Zhang, Z. Hu, Z. Tao, L. Mai, Y.M. Kang, S.-.L. Chou, J. Chen, Recent developments on and prospects for electrode materials with hierarchical structures for lithium-ion batteries, Adv. Energy Mater. 8 (2018) 1701415, doi:10.1002/aenm.201701415.
[25] J. Liu, G. Cao, Z. Yang, D. Wang, D. Dubois, X. Zhou, G.L. Graff, L.R. Pederson, J.G. Zhang, Oriented nanostructures for energy conversion and storage, ChemSusChem 1 (2008) 676–697, doi:10.1002/cssc.200800087.
[26] Y. Wang, H. Li, P. He, E. Hosono, H. Zhou, Nano active materials for lithium-ion batteries, Nanoscale 2 (2010) 1294–1305, doi:10.1039/c0nr00068j.
[27] Y.G. Guo, J.S. Hu, L.J. Wan, Nanostructured materials for electrochemical energy conversion and storage devices, Adv. Mater. 20 (2008) 2878–2887, doi:10.1002/adma.200800627.
[28] B. Xiao, B. Zhang, L. Tang, C. An, Z. He, H. Tong, W. Yu, J. Zheng, V_2O_3/rGO composite as a potential anode material for lithium ion batteries, Ceram. Int. 44 (2018) 15044–15049, doi:10.1016/j.ceramint.2018.05.134.
[29] W. Cheng, G. Zeng, M. Niederberger, Design of vanadium oxide core–shell nanoplatelets for lithium ion storage, J. Mater. Chem. A 3 (2015) 2861–2868, doi:10.1039/C4TA05495D.
[30] X. Ren, D. Ai, C. Zhan, R. Lv, F. Kang, Z.H. Huang, NaCl-template-assisted freeze-drying synthesis of 3D porous carbon-encapsulated V_2O_3 for lithium-ion battery anode, Electrochim. Acta 318 (2019) 730–736, doi:10.1016/j.electacta.2019.06.138.

[31] L. Xun, S. Gao, Y. Xu, X. Cheng, X. Zhang, H. Zhao, L. Huo, Synthesis of dandelion-like V_2O_3/C composite with bicontinuous 3D hierarchical structures as an anode for high performance lithium ion batteries, Ceram. Int. 44 (2018) 14128–14135, doi:10.1016/j.ceramint.2018.05.012.
[32] P. Yu, X. Liu, L. Wang, C. Tian, H. Yu, H. Fu, Urchin-like V_2 O_3 /C hollow nanosphere hybrid for high-capacity and long-cycle-life lithium storage, ACS Sustain. Chem. Eng. 5 (2017) 11238–11245, doi:10.1021/acssuschemeng.7b01640.
[33] Le Jiang, Y. Qu, Z. Ren, P. Yu, D. Zhao, W. Zhou, L. Wang, H. Fu, *In situ* carbon-coated yolk-shell V_2O_3 microspheres for lithium-ion batteries, ACS Appl. Mater. Interfaces 7 (2015) 1595–1601, doi:10.1021/am5070393.
[34] P. Liu, K. Zhu, Y. Xu, K. Bian, J. Wang, G. Tai, Y. Gao, H. Luo, L. Lu, J. Liu, Hierarchical porous intercalation-type V_2 O_3 as high-performance anode materials for Li-ion batteries, J. Chem. 23 (2017) 7538–7544, doi:10.1002/chem.201700369.
[35] E. Thauer, G.S. Zakharova, S.A. Wegener, Q. Zhu, R. Klingeler, Sol-gel synthesis of Li_3VO_4/C composites as anode materials for lithium-ion batteries, J. Alloys Compd. 853 (2021) 157364, doi:10.1016/j.jallcom.2020.157364.
[36] C. Tenailleau, E. Suard, J. Rodriguez-Carvajal, M.P. Crosnier-Lopez, P. Lacorre, Effect of Mo doping on the room-temperature structure of vanadium sesquioxide, Chem. Mater. 14 (2002) 3569–3575, doi:10.1021/cm021127l.
[37] A.C. Ferrari, D.M. Basko, Raman spectroscopy as a versatile tool for studying the properties of graphene, Nat. Nanotechnol. 8 (2013) 235–246, doi:10.1038/NNANO.2013.46.
[38] N. Kuroda, H.Y. Fan, Raman scattering and phase transitions of V_2O_3, Phys. Rev. B 16 (1977) 5003–5008, doi:10.1103/PhysRevB.16.5003.
[39] Y. Ding, X. Xia, W. Chen, L. Hu, L. Mo, Y. Huang, S. Dai, Inside-out Ostwald ripening: a facile process towards synthesizing anatase TiO_2 microspheres for high-efficiency dye-sensitized solar cells, Nano Res. 9 (2016) 1891–1903, doi:10.1007/s12274-016-1081-2.
[40] L. Zhang, J. Yao, F. Xia, Y. Guo, C. Cao, Z. Chen, Y. Gao, H. Luo, VO_2 (D) hollow core–shell microspheres: synthesis, methylene blue dye adsorption and their transformation into C/VO x nanoparticles, Inorg. Chem. Front. 5 (2018) 550–558, doi:10.1039/C7QI00819H.
[41] J. Widoniak, S. Eiden-Assmann, G. Maret, Synthesis and characterisation of monodisperse zirconia particles, Eur. J. Inorg. Chem. 2005 (2005) 3149–3155, doi:10.1002/ejic.200401025.
[42] K.S.W. Sing, Reporting physisorption data for gas/solid systems with special reference to the determination of surface area and porosity (Recommendations 1984), Pure Appl. Chem. 57 (1985) 603–619, doi:10.1351/pac198557040603.
[43] A. Ottmann, M. Scholz, M. Haft, E. Thauer, P. Schneider, M. Gellesch, C. Nowka, S. Wurmehl, S. Hampel, R. Klingeler, Electrochemical magnetization switching and energy storage in manganese oxide filled carbon nanotubes, Sci. Rep. 7 (2017) 13625, doi:10.1038/s41598-017-14014-7.
[44] H. Li, P. Balaya, J. Maier, Li-storage via heterogeneous reaction in selected binary metal fluorides and oxides, J. Electrochem. Soc. 151 (2004) A1878, doi:10.1149/1.1801451.
[45] A. Tranchant, R. Messina, J. Perichon, Mechanism of electrochemical reduction of vanadium oxides, J. Electroanal. Chem. Interf. Electrochem. 113 (1980) 225–232, doi:10.1016/S0022-0728(80)80023-4.
[46] Y. Wang, H.J. Zhang, A.S. Admar, J. Luo, C.C. Wong, A. Borgna, J. Lin, Improved cyclability of lithium-ion battery anode using encapsulated V_2O_3 nanostructures in well-graphitized carbon fiber, RSC Adv. 2 (2012) 5748, doi:10.1039/c2ra20472j.
[47] G.S. Zakharova, E. Thauer, A.N. Enyashin, L.F. Deeg, Q. Zhu, R. Klingeler, V_2O_3/C composite fabricated by carboxylic acid-assisted sol–gel synthesis as anode material for lithium-ion batteries, J. SolGel Sci. Technol. 98 (2021) 549–558, doi:10.1007/s10971-021-05523-z.
[48] P. Simon, Y. Gogotsi, B. Dunn, Materials science. Where do batteries end and supercapacitors begin? Science 343 (2014) 1210–1211 (New York, N.Y.), doi:10.1126/science.1249625.
[49] T. Zhang, L. Zhang, L. Zhao, X. Huang, W. Li, T. Li, T. Shen, S. Sun, Y. Hou, Free-standing, foldable V_2O_3/multichannel carbon nanofibers electrode for flexible Li-ion batteries with ultralong lifespan, Small 16 (2020) e2005302 (Weinheim an der Bergstrasse, Germany), doi:10.1002/smll.202005302.
[50] C.S. Liu, X. Ye, B. Zhou, X.Q. Zeng, J. Xu, Q.C. Xu, J. Li, 2D mesoporous nanomesh from N-doped carbon-encapsulated V_2O_3 nanowires as an anode for lithium-ion batteries, J. Phys. Chem. C 124 (2020) 24073–24080, doi:10.1021/acs.jpcc.0c06899.
[51] L. Meng, R. Guo, F. Li, Y. Ma, J. Peng, T. Li, Y. Luo, Y. Li, X. Sun, Facile synthesis of flock-like V_2O_3 /C with improved electrochemical performance as an anode material for li-ion batteries, Energy Technol. 8 (2019) 1900986, doi:10.1002/ente.201900986.
[52] J. Liu, J. Liang, C. Wang, J. Ma, Electrospun CoSe@N-doped carbon nanofibers with highly capacitive Li storage, J. Energy Chem. 33 (2019) 160–166, doi:10.1016/j.jechem.2018.09.006.
[53] J. Yin, P. Sun, G. Qu, G. Xiang, P. Hou, X. Xu, A new CoO/Co_2B/rGO nanocomposite anode with large capacitive contribution for high-efficiency and durable lithium storage, Appl. Surf. Sci. 508 (2020) 144698, doi:10.1016/j.apsusc.2019.144698.
[54] X. Li, J. Fu, Z. Pan, J. Su, J. Xu, B. Gao, X. Peng, L. Wang, X. Zhang, P.K. Chu, Peapod-like V_2O_3 nanorods encapsulated into carbon as binder-free and flexible electrodes in lithium-ion batteries, J. Power Sources 331 (2016) 58–66, doi:10.1016/j.jpowsour.2016.09.031.

Supplementary Information

Hierarchically structured V_2O_3/C spheres: Synthesis, characterization, and their electrochemical properties

E. Thauer[1], G.S. Zakharova[2], L. F. Deeg,[1] Q. Zhu[3], R. Klingeler[1,4]

[1]*Kirchhoff Institute of Physics, Heidelberg University, Heidelberg, Germany*

[2]*Institute of Solid State Chemistry, Ural Division, Russian Academy of Sciences, Yekaterinburg, Russia*

[3]*School of Material Science and Engineering, Wuhan University of Technology, Wuhan, China*

[4]*Centre for Advanced Materials, Heidelberg University, Heidelberg, Germany*

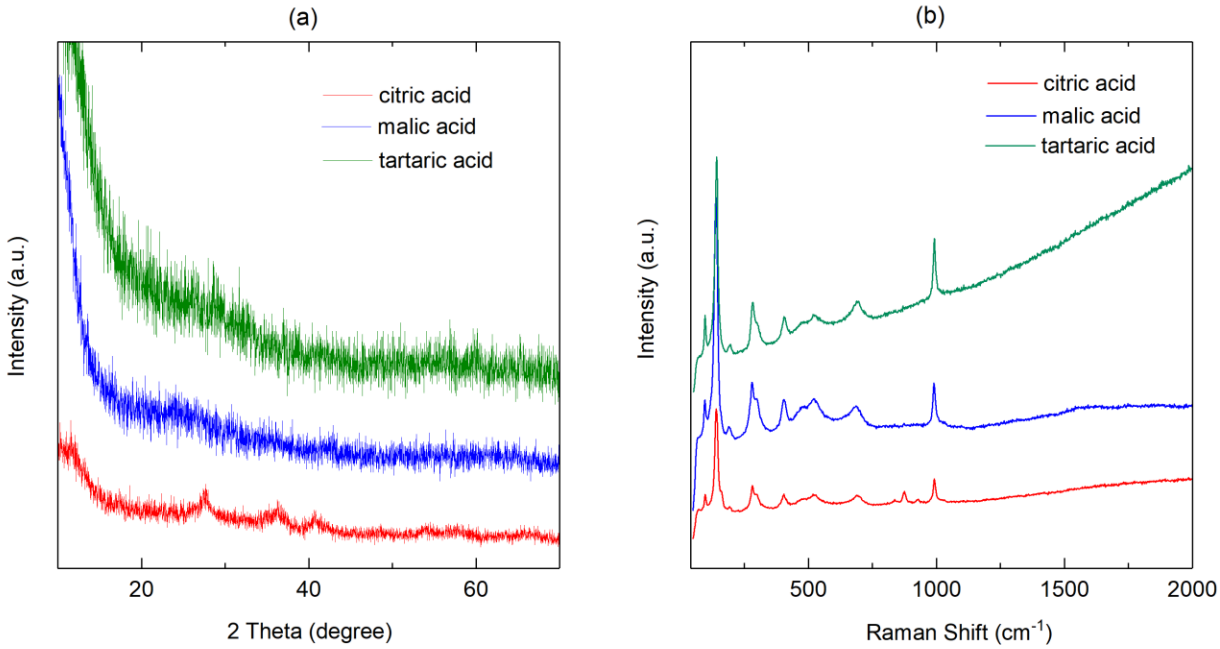

Fig. S1. (a) XRD patterns and (b) Raman spectra of the samples fabricated via the hydrothermal treatment but before annealing in inert atmosphere using citric acid, malic acid, and tartaric acid.

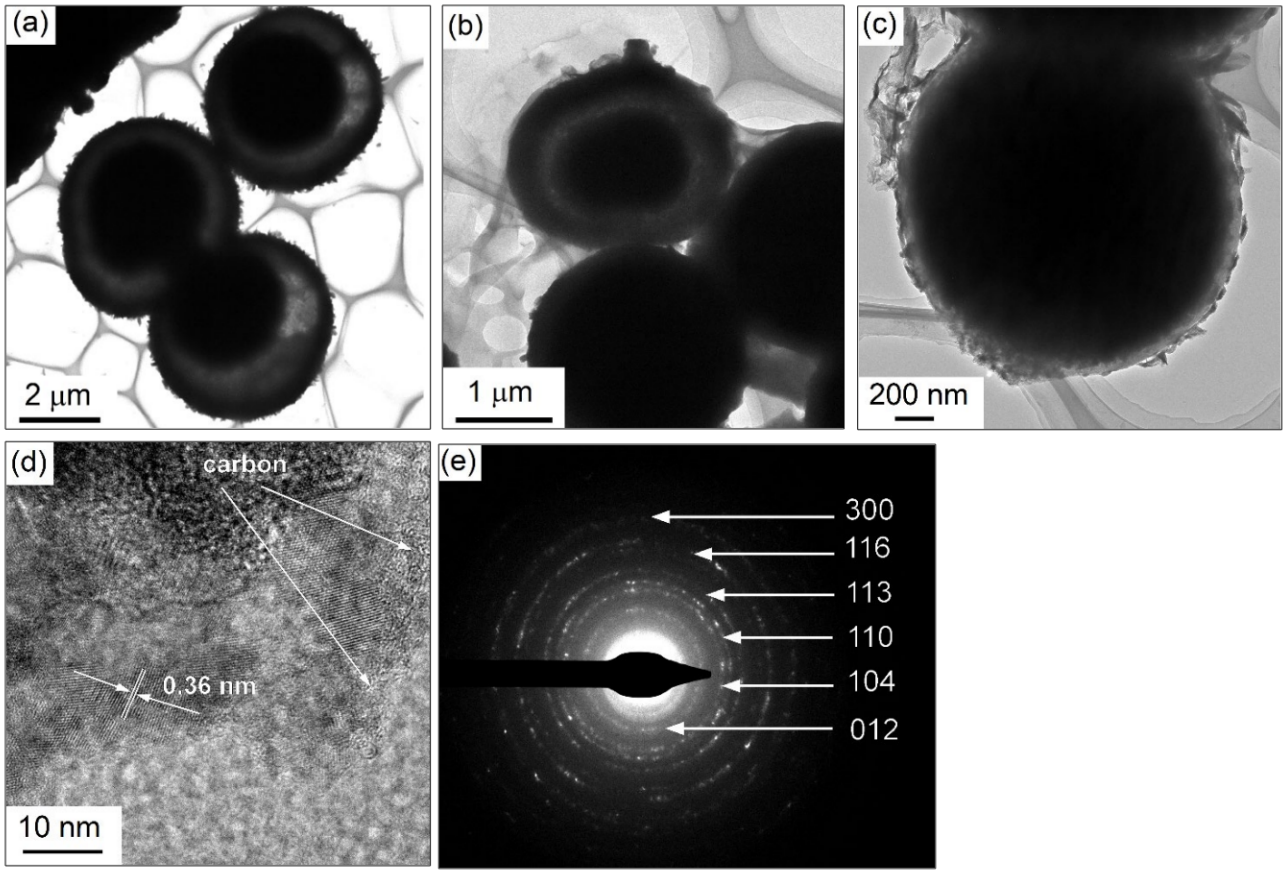

Fig. S2. TEM images of V_2O_3/C composites prepared using the different carboxylic acids: (a) citric acid, (b) malic acid, and (c) tartaric acid. (d) High resolution TEM image and (e) corresponding SAED pattern of V_2O_3/C composite synthesized using malic acid as carbon source.

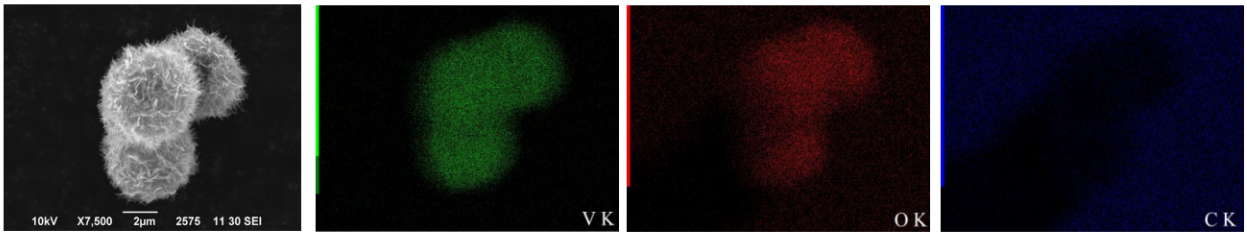

Fig. S3. SEM and corresponding elemental mapping images of V_2O_3/C-C composite.

3.4 Novel synthesis and electrochemical investigations of ZnO/C composites for lithium-ion batteries

Autoren:

E. Thauer, G.S. Zakharova, E.I. Andreikov, V. Adam, S.A. Wegener, J.-H. Nölke, L. Singer, A. Ottmann, A. Asyuda, M. Zharnikov, D.M. Kiselkov, Q. Zhu, I.S. Puzyrev, N.V. Podval'naya, R. Klingeler

veröffentlicht in Journal of Materials Science, 2021

abgedruckt mit freundlicher Genehmigung des Springer Nature Verlags

E. Thauer ist die Erst- und Korrespondenzautorin dieses Artikels. Das Manuskript wurde mit Ausnahme des experimentellen Teils zur Synthese und der Diskussion zu den TGA-, XPS, TEM- und BET-Messungen von E.Thauer konzipiert und verfasst. E. Thauer erstellte die Abb. 6 - 9 und Abb. S2 - S3 und übernahm die Gesamtkorrektur des Manuskripts. Die Charakterisierung mittels XRD, REM und alle elektochemischen Untersuchungen des reinen Materials erfolgte gemeinsam von E. Thauer mit dem Bachelorstudent S. Wegener unter ihrer Anleitung. Darüber hinaus führte E. Thauer teilweise gemeinsam mit dem Masterstudent V. Adam unter ihrer Anleitung die *ex-situ* XRD-Studien durch und übernahm die Rietveld-Analyse. Die Korrespondenz mit den Gutachtern sowie die Überarbeitung des Manuskripts wurde von E. Thauer gemeinsam mit G.S. Zakharovs und R. Klingeler übernommen.

G.S. Zakharova verfasste die Teile des Manuskripts zur Synthese sowie zu den TGA-, TEM- und BET-Messungen und erstellte die Abb. 1 und Abb. 3 - 5. Die Untersuchung mittels Raman-Spektroskopie und TGA erfolgte von G.S. Zakharova. E.I. Andreikov und I.S. Puzryrev führten die Synthese durch. L. Singer übernahm unter Anleitung von A. Asyuda und M. Zharnikov die XPS-Analyse (Abb. 2). Von N.V. Podval'naya bzw. Q. Zhu erfolgten die BET- und TEM-Messungen. A. Ottmann führte im Rahmen seiner Dissertation gemeinsam mit dem Bachelorstudent J.-H. Nölke die XRD, REM- und alle elektochemischen Untersuchungen der Komposite durch. R. Klingeler betreute das Projekt, stand beratend zur Seite und war an der Finalisierung des Manuskripts beteiligt. Alle Autoren haben das Manuskript korrekturgelesen.

J Mater Sci

Energy materials

Novel synthesis and electrochemical investigations of ZnO/C composites for lithium-ion batteries

E. Thauer[1,*], G. S. Zakharova[2,3], E. I. Andreikov[4], V. Adam[1], S. A. Wegener[1], J. -H. Nölke[1], L. Singer[1], A. Ottmann[1], A. Asyuda[5], M. Zharnikov[5], D. M. Kiselkov[6], Q. Zhu[7], I. S. Puzyrev[4], N. V. Podval'naya[2], and R. Klingeler[1,8]

[1] *Kirchhoff Institute of Physics, Heidelberg University, Heidelberg, Germany*
[2] *Institute of Solid State Chemistry, Ural Division, Russian Academy of Sciences, Yekaterinburg, Russia*
[3] *Ural Federal University, Yekaterinburg, Russia*
[4] *I.Ya. Postovskii Institute of Organic Synthesis, Ural Division, Russian Academy of Sciences, Yekaterinburg, Russia*
[5] *Applied Physical Chemistry, Heidelberg University, Heidelberg, Germany*
[6] *Institute of Technical Chemistry, Ural Division, Russian Academy of Sciences, Perm, Russia*
[7] *School of Material Science and Engineering, Wuhan University of Technology, Wuhan, China*
[8] *Centre for Advanced Materials, Heidelberg University, Heidelberg, Germany*

Received: 16 February 2021
Accepted: 21 April 2021

ABSTRACT

For the first time, ZnO/C composites were synthesized using zinc glycerolate as a precursor through one-step calcination under a nitrogen atmosphere. The effect of the heat treatment conditions on the structure, composition, morphology as well as on the electrochemical properties regarding application in lithium-ion batteries are investigated. The products obtained by calcination of the precursor in nitrogen at 400—800 °C consist of zinc oxide nanoparticles and amorphous carbon that is *in-situ* generated from organic components of the glycerolate precursor. When used as anode material for lithium-ion batteries, the as-prepared ZnO/C composite synthesized at a calcination temperature of 700 °C delivers initial discharge and charge capacities of 1061 and 671 mAh g^{-1} at a current rate of 100 mA g^{-1} and hence 1.5 times more than bare ZnO, which reaches only 749/439 mAh g^{-1}. The native carbon improves the conductivity, allowing efficient electronic conductivity and Li-ion diffusion. By means of *ex-situ* XRD studies a two-step storage mechanism is proven.

Handling Editor: Mark Bissett.

Address correspondence to E-mail: elisa.thauer@kip.uni-heidelberg.de

https://doi.org/10.1007/s10853-021-06125-4

Published online: 12 May 2021

Springer

Introduction

ZnO has attracted attention of a large community of researchers as an electrode material for lithium-ion batteries (LIBs) due to its low cost, environmental friendliness and high theoretical capacity in particular [1–4]. Assuming a two-step reaction mechanism that involves a conversion Eq. (1) and alloying process Eq. (2), as proposed by previous studies [5–7], up to 3 Li^+/f.u. can be reversibly stored corresponding to a theoretical capacity of 978 mAh/g:

$$ZnO + 2Li^+ + 2e^- \leftrightarrow Zn + Li_2O, \quad (1)$$

$$Zn + Li^+ + e^- \leftrightarrow LiZn. \quad (2)$$

However, there are some challenges to overcome. One issue is the large volume change of ZnO during the dis-/charge process resulting in pulverization of the electrode material [8]. Furthermore, the studies of Pelliccione et al. [6] and Park et al. [9] revealed the limited reversibility of the conversion reaction Eq. (1), which depends on the size of the electrochemically formed zinc particles, as additional reason behind the rapid capacity fading. Li_2O can only be partially decomposed due to its poor reactivity and low lithium ion conductivity [10]. Another factor that limits the practical application of ZnO for electrochemical energy storage is its poor electrical conductivity [11]. To overcome these difficulties and to enhance the electrochemical performance of ZnO-based anodes, hybridizing ZnO with varieties of conductive carbon materials is frequently employed. Carbonaceous materials can prevent the aggregation of ZnO nanoparticles and maintain the structural stability of the anode during charge/discharge processes. ZnO nanoparticles anchored on the surface of carbon nanotubes (CNT) have been shown to deliver a reversible capacity of 602 mAh g^{-1} at 100 mA g^{-1} for up to 50 cycles, i.e., superior cycling and rate performances [12]. Similarly, a ZnO/graphene anode exhibits an initial specific capacity of 850 mAh g^{-1} at 0.1 C and good cycling stability (capacity decay ~8% after 50 cycles) [13]. Also, films of ZnO nanosheets coated with 350 Å thick graphite layers showed specific capacity values of ~ 600 mAh g^{-1} at 1 A g^{-1} after 100 cycles [14].

Various synthesis methods and approaches have been used in the literature to fabricate ZnO/C composites. Yang et al. [15] reported the synthesis of porous carbon coated ZnO quantum dots by the carbonization of metal–organic frameworks. As-obtained composites exhibit a reversible capacity of 919 mAh g^{-1} over 100 cycles at 100 mA g^{-1}. The porous ZnO/C microboxes prepared by annealing of the analogous metal–organic framework carboxylate groups deliver an initial discharge capacity of 1290 mAh g^{-1} and reach a high reversible capacity of 716 mAh g^{-1} after 100 cycles at a current density of 100 mA g^{-1} [16]. Bai et al. [17] have synthesized ZnO/C nanospheres by a one-step co-pyrolysis method using Zn powder and acetylacetone as starting materials. As-prepared ZnO/C nanospheres show a reversible capacity of 440 mAh g^{-1} at a current density of 100 mA g^{-1} after 50 cycles. Electrospinning and subsequent thermal treatment by Zhao et al. yielded a ZnO/carbon nanofiber composite, which delivers a reversible capacity of 702 mAh g^{-1} at a current density of 200 mA g^{-1} [18]. Hydrothermally fabricated core–shell ZnO/C nanospheres by Liu et al. [19] obtained from Zn-resorcinol–formaldehyde polymer followed by carbonization at 650 °C under inert atmosphere show a capacity of 496 mAh g^{-1} after 200 cycles at a current density of 82.5 mA g^{-1}. Microwave-assisted solvothermal synthesis permitting to reduce the time of reaction was performed to produce ZnO/C composites using sucrose as carbon source [20]. However, these methods always need multi-step or strict experimental conditions which increase the costs and limit large-scale production.

There are, however, one-step methods as well, with calcination under a nitrogen atmosphere for the synthesis of ZnO/C composites being probably the most efficient, easily implementable, and low-cost approach. In this case, organometallic complexes suggested for thermal treatment such as zinc citrate dihydrate $(C_6H_5O_7)_2Zn_3{\cdot}2H_2O$ [21–24] and zinc tartrate $C_4H_4ZnO_6$ [25] can serve as precursors for both, ZnO and carbon.

Summarizing, although a significant progress has already been achieved, developing a facile route to synthesize carbon coated nanosized materials remains an important task to further improve the performance of ZnO-based anode materials. In the present paper, based on the results of our previous work [26], a synthetic route involving a thermal treatment of organometallic compounds was developed to prepare carbon-composited metal oxide. The formation of ZnO/C composites has been

successfully realized by heat treatment of zinc glycerolate (ZnGly) under inert atmosphere. The organic component of ZnGly partially transformed into carbon resulting in the formation of ZnO/C composites. Additionally, potential applications of the ZnO/C composites as anode materials for lithium-ion batteries were investigated.

Experimental

Materials preparation

Zinc acetate dihydrate $(CH_3COO)_2Zn{\cdot}2H_2O$ and freshly distilled glycerol (analytical grade) were used as the starting materials for the synthesis of zinc glycerolate $ZnC_3H_6O_3$. The ZnGly precursor was prepared via a polyol-mediated synthesis based on Dong's work [27]. Typically, 2.0 g $(CH_3COO)_2Zn{\cdot}2H_2O$ and 1 ml of distilled water were added to 50 mL of glycerol in a 100-mL round-bottom flask. This solution was heated to 160 °C and refluxed under Ar flow for 1 h. After cooling to room temperature, the resulting colorless precipitate, zinc glycerolate, was collected using centrifugation, washed with ethanol, and dried at 80 °C for 60 min. Finally, ZnO/C composites were prepared by annealing of the as-obtained ZnGly in a tube furnace at different temperatures between 400 and 800 °C for 2 h under N_2 flow at an initial heating rate of 5 °C min^{-1}. The carbonized products are termed as ZnO/C-X, where X is the annealing temperature. For the purpose of comparison, a bare ZnO sample was prepared by annealing of the ZnO/C-800 composite at 600 °C for 1 h in air.

Materials characterization

The synthesized ZnO/C-X composites were characterized by a variety of complementary experimental techniques, as described in detail below. X-ray diffraction (XRD) patterns were obtained with a Bruker AXS D8 Advance Eco diffractometer using Cu K_α radiation and a step size of $\Delta(2\theta) = 0.02°$ at the angular scan. The morphology of the samples was investigated using a ZEISS Leo 1530 scanning electron microscope (SEM) and a JEOL JEM 2100 transmission electron microscope (TEM). Raman spectra of the samples were recorded on a Bruker Senterra spectrometer equipped with Olympus BX-51 optical microscope using a 532 nm laser. To avoid damage to the samples, the emitted power was limited to 2 mW. All spectra were obtained at room temperature at a wavelength range from 100 to 4000 cm^{-1} using a 400 lines mm^{-1} grid and 25 × 1000 µm aperture. X-ray photoelectron (XP) spectra of the samples were measured with MAX200 (Leybold-Heraeus) spectrometer equipped with a non-monochromatized Mg Kα X-ray source (200 W) and a hemispherical analyzer. The powder materials were pressed into clean indium foil and thinned by a brush to suppress charging effects, following the established methodology [28]. Thermogravimetric analysis (TG/DTA) was performed on a Mettler Toledo TGA/DSC1 analyzer with a heating rate of 5 °C min^{-1} in air and Ar. The content of carbon was examined by elemental analysis using Vario MICRO Cubes (Elementar). Nitrogen sorption isotherms were determined on a Micromeritics Gemini VII 2390 Surface Area Analyzer. Prior to N_2 physisorption data collection, the samples were degassed at 150 °C under vacuum for 4 h. The specific surface area, pore size distribution, and pore volumes were obtained by means of the Brunauer–Emmett–Teller (BET) method and the Barrett-Joyner-Halenda model from the adsorption branches of the isotherms.

Electrochemical measurements

Electrochemical studies were performed in Swagelok-type two electrode cells at 25 °C by using a VMP3 potentiostat (Bio-Logic SAS) (see [26]). The preparation procedure of the working electrodes is as follows. A mixture of 80% ZnO/C, 15% carbon black (Super C65, Timcal), and 5% polyvinylidene fluoride binder (PVDF, Solvay Plastics) dissolved in N-methyl-2-pyrrolidone (NMP, Sigma-Aldrich) was stirred for at least 12 h. In order to obtain a spreadable slurry most of the NMP was evaporated in a vacuum oven (10 mbar, 65 °C). The resulting electrode slurry was applied on circular Cu meshes (diameter 10 mm) with a mass loading of about 2 mg cm^{-2}. Afterward, the electrodes were dried at 80 °C under vacuum, mechanically pressed at 10 MPa, and then dried again. The working electrode and the counter electrode, consisting of a lithium metal foil disk (Alfa Aesar) pressed on a nickel current collector, were separated by two layers of glass fiber separator (Whatman GF/D). As electrolyte 200 µL of a 1 M $LiPF_6$ salt solution in 1:1 ethylene

carbonate (EC) and dimethyl carbonate (DMC) (Merck Electrolyte LP30) was used. The cells were assembled in a glove box under argon atmosphere ($O_2/H_2O < 5$ ppm). For *ex-situ* XRD measurements the cells were galvanostatically cycled at 10 mA g^{-1} and disassembled at various dis-/charged states in the glove box. The electrodes were washed in DMC and dried under vacuum conditions overnight. The XRD measurement of the post-cycled electrode material was performed using an airtight sample carrier.

Results and discussion

The structure of the ZnO/C-X composites was analyzed by XRD (Fig. 1a). For comparison, the XRD pattern of ZnO obtained by annealing the ZnO/C-800 composite in air at 600 °C is also included. All diffraction peaks can be assigned to a hexagonal phase of wurtzite-type ZnO according to JCPDS # 36–1451, space group P63mc. Lattice parameters determined by means of full-profile analyses with the FullProf Suite (see Table 1) are in good agreement with the literature. The intensities of the characteristic peaks of ZnO increase with rising annealing temperatures. For ZnO/C composites prepared by heat treatment below 600 °C, the diffraction peaks are rather broad which is attributed to nanosized ZnO crystallites. The crystallite sizes of ZnO in the ZnO/C-X (X = 400, 500, 600) samples are calculated using the Scherrer equation:

$$D_{hkl} = K\lambda/\Delta(2\theta_{hkl})\cos\theta_{hkl}, \quad (3)$$

where D_{hkl} is the average grain size based on the particular reflecting crystal face (*hkl*) direction, K is a shape factor which can be approximated to 0.9, λ is the wavelength of the applied Cu Kα radiation, $\Delta(2\theta_{hkl})$ is the full width at half-maximum of the diffraction peak and θ_{hkl} is the Bragg angle. The analysis of the peaks below $2\theta_{hkl} = 65°$ yields the averaged crystallite size for the ZnO/C-X samples. Both, ZnO/C-400 and ZnO/C-500 composites, exhibit similar particle size of around 12 nm. By contrast, the ZnO/C-600 composite is characterized by a larger size of 19 ± 3 nm.

Raman spectra collected from the ZnO/C-X (X = 400 – 700) samples display two prominent peaks which are attributed to the carbon D- and G-bands (see Fig. 1b). The G-band corresponds to sp^2-bonded carbon atoms, while the D-band is associated with defects or disorders mainly due to sp^3 hybridization [29]. The D- and G-bands of the ZnO/C-400 composite are located at 1359 cm^{-1} and 1591 cm^{-1}, respectively. In comparison, the D-and G-peaks of the ZnO/C-700 sample are slightly red-shifted by 23 and 20 cm^{-1} toward 1314 and 1571 cm^{-1}, respectively. The same shift toward higher binding energy indicating the strong chemical interaction between the surface carbon and Zn atoms was observed by XPS on ZnO/C composite [23]. Similar shifts have been reported for TiO_2/C composites [30, 31]. These shifts are attributed to the stress induced by the chemical anchoring of ZnO atoms on the carbon surface. Obviously, such an interaction can change the Raman shifts describing the carbon bond energy. The ratio of the maximum intensities, I_D/I_G, was calculated as 0.73 and 0.91 for

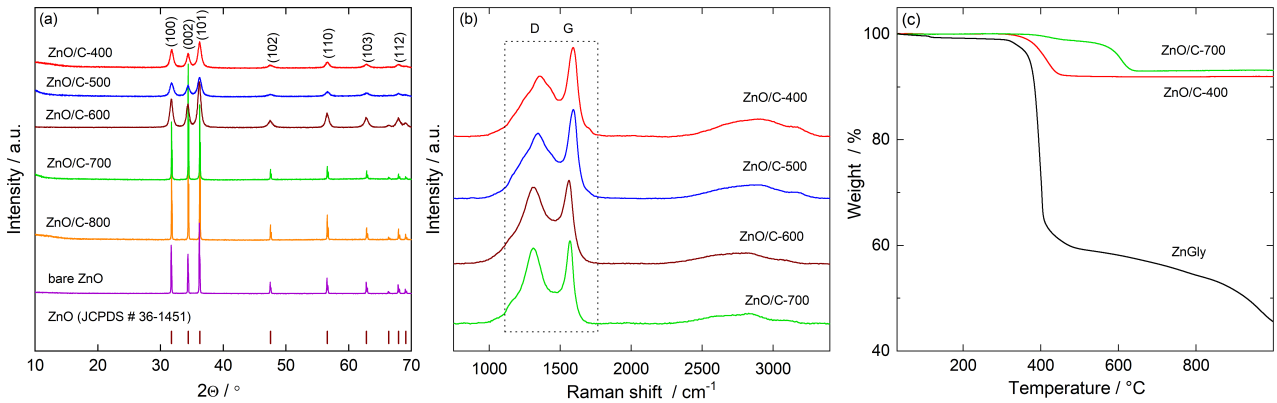

Figure 1 **a** XRD patterns and **b** Raman spectra of the ZnO/C-X composites and bare ZnO sample as well as (**c**) TG curves for the ZnGly precursor heated in an inert atmosphere and ZnO/C-400(700) composites heated in air.

Table 1 Lattice parameters obtained from Rietveld refinement, results of BET analysis, and carbon content for the ZnO/C-X composites and bare ZnO

Sample	Lattice parameters		S_{BET} (m g^{-1})	Total pore volume (cm^3 g^{-1})	Carbon content (wt%)	
	a (Å)	*c* (Å)			TG	Chemical analysis
ZnO/C-400	34.80	52.05	54.8	0.18	8.0	8.7(5)
ZnO/C-500	32.49	52.06	59.8	0.16	7.1	8.2(5)
ZnO/C-700	32.55	52.16	100.9	0.36	5.7	6.0(5)
ZnO/C-800	32.53	52.11	93.1	0.29	–	5.8(5)
ZnO	32.49	52.05	6.6	0.02	–	–

the ZnO/C-400 and ZnO/C-700 composite, respectively. According to the model proposed by Ferrari and Robertson, the ratio I_D/I_G is proportional to the crystallite size, when it is less than 2 nm for amorphous carbon [32]. The increasing intensity of the D-band with rising annealing temperature is characteristic of the carbonization process and implies less disorder and a lower number of defects in the carbon component due to a growing crystallite size [33, 34]. The peaks associated with ZnO were not observed by Raman spectroscopy using a laser wavelength of 532 nm.

TG/TGA analysis (Fig. 1c) of the ZnGly precursor illustrates its conversion into carbon containing zinc oxide upon annealing in a nitrogen atmosphere. A significant weight loss of ca. 40% at heating from 400 to 1000 °C can be explained by the total decomposition of the ZnGy precursor with simultaneous formation of zinc oxide, volatile products with low molecular weight and products of condensation of organic compounds, similar to titanium glycerolate [26]. Furthermore, the products of the condensation also undergo a disproportionation with the formation of volatile low molecular weight substances and the carbonaceous part of the ZnO composite. Therefore, 400 °C was selected as the start reaction temperature to calcine the ZnGly precursor under nitrogen environment to produce the ZnO/C composites. The carbon content in the as-prepared ZnO/C-X composites was determined by the TG/TGA measurements in air, performed in the temperature range up to 1000 °C to ensure the complete oxidation of carbon into carbon dioxide (cf. Table 1). As a result, the carbon contents in the ZnO/C-400 and ZnO/C-700 composites were estimated at 8.0 and 5.7 wt%, respectively. These values were additionally verified by the chemical analysis, with good agreement of the results (Table 1).

To confirm the formation of the ZnO/C composites and to exclude other oxidation states of Zn, XPS analyses were carried out on ZnO/C-400 and ZnO/C-700. The XPS survey spectrum and core level spectra of the Zn 2p, O 1 s and C 1 s peaks for both samples are shown in Fig. 2. The survey spectrum in Fig. 2a displays the presence of Zn, O, C without any detectable impurities. The Zn 2p spectra of both samples in Fig. 2b exhibit a single Zn $2p_{3/2,1/2}$ doublet, with the positions of the Zn $2p_{3/2}$ and Zn $2p_{1/2}$ components, 1021.6 eV and 1044.7 eV, respectively, corresponding to Zn^{2+} [11, 23]. This assignment is additionally supported by the kinetic energy position of the most intense Zn LMM Auger peak at 988 eV (Fig. S1), which corresponds to ZnO. The O 1 s spectrum, as shown in Fig. 2c, was resolved and the lower binding energy component at 530.7 for the ZnO/C-400 sample and 530.6 eV for the 700 sample can be attributed to the hexagonal close packing of O_2 in the wurtzite-ZnO structure. The peak at 532.3 eV for both samples is associated with surface hydroxyl groups (OH) and/or C=O. The peak at 533.9 and 534.2 eV corresponds to single bonds between oxygen and carbon (C-O) and/or absorbed water [35]. The C 1 s spectra, which are shown in Fig. 2d, can be fitted by four sub-peaks, the aliphatic C–C, the C–O, C=O, and O–C=O peak [35]. For ZnO/C-400 the positions of these peaks are at 284.8, 286.2, 287.9, and 289.9 eV and for ZnO/C-700 the peaks are located at 284.4, 286.6, 287.9, and 289.8 eV. The shift of the C–C peak from ZnO/C-400 to ZnO/C-700 towards lower binding energies indicates, in accordance with the Raman data, a more graphitic state for the carbon component of the ZnO/C-700 composite [36].

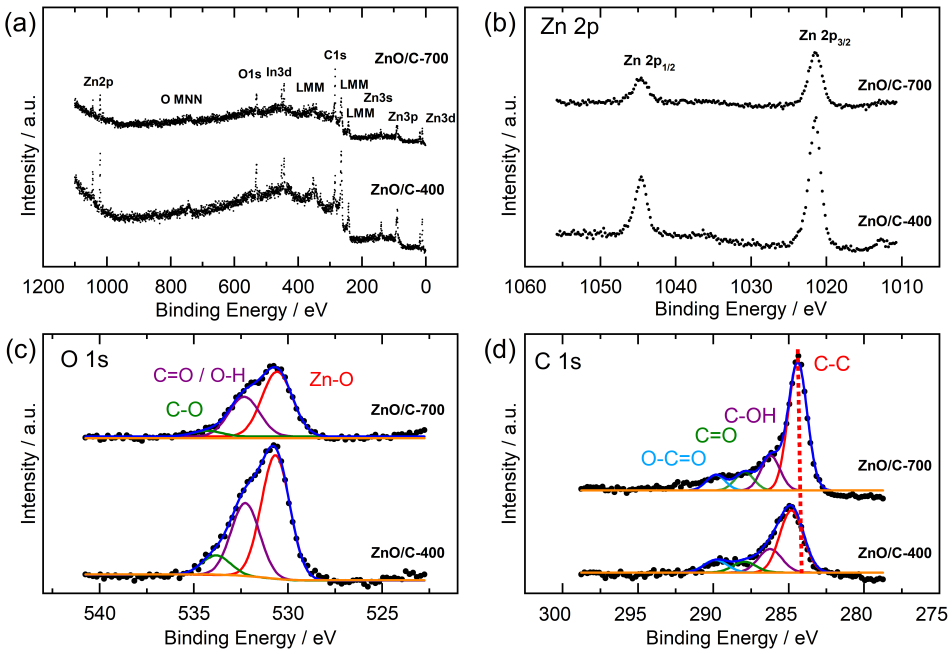

Figure 2 XPS spectra of ZnO/C-400 and ZnO/C-700: **a** survey spectrum, **b** Zn 2p, **c** O 1 s and **d** C 1 s.

SEM images of the ZnO/C-X composites in Fig. 3 show the drastic effect of the calcination temperature on the morphology of the samples. The pristine ZnGly precursor is mainly composed of irregularly shaped sheets with several micrometers in length (Fig. 3a). The ZnO/C composites fabricated via annealing of the precursor at a temperature below 500 °C consist of sheets with an average size of few micrometers, which are primarily composed of nanosized grains of ZnO (Fig. 3b, c). Probably, carbon acts as a cross-linking agent that holds the ZnO nanoparticles together. The cross-sectional SEM images of the sheets show that their thickness changes from 270 to 800 nm for ZnO/C-500 and ZnO/C-400 composites, respectively (Fig. 3b, c, insert). In contrast, the ZnO/C-700 and ZnO/C-800 composites consist of many thin sheets and several large particles of about 1 − 7 μm in diameters (Fig. 3d, e). As shown in Fig. 3f, the bare, carbon-free ZnO particles, obtained by the heat treatment of the ZnO/C-800 composite in air, represent hexagonal ZnO prisms with an average size of about 1–7 μm.

Further information on the morphology and structural features of the sheets in the ZnO/C-700 composite was obtained by TEM studies. The TEM images shown in Fig. 4a exhibit well crystallized ZnO nanoparticles which are dispersed in a carbon matrix. The corresponding high-resolution TEM (HRTEM) image in Fig. 4b exhibits lattice fringes with spacings of 0.26 and 0.28 nm, which correspond to the distances between the (002) and (100) planes of ZnO, respectively. Furthermore, the crystalline structure of the ZnO/C-700 composite is confirmed through the selected area electron diffraction (SAED) pattern as shown in Fig. 4c. Several clear diffraction rings from the SAED pattern can be assigned to the (100), (002), (101), (102), (110), (103), and (200) planes of hexagonal ZnO, suggesting a polycrystalline nature of the ZnO component in the composite.

The porous nature and the specific surface area of the as-prepared samples were investigated by nitrogen adsorption–desorption isotherms. Corresponding pore size distribution plots of the samples are shown in Fig. 5. The ZnO/C-X composites display isotherms of type IV, according to the IUPAC classification, with a H3 hysteresis loop (Fig. 5a) [37]. The isotherms of the bare ZnO powder are close to type II, which is typical for non-porous or macroporous materials. The BET specific surface area and the respective pore volumes of the samples are displayed in Table 1. The BET surface area of the ZnO/C-X composites is rather high which is attributed to the presence of mesopores, in contrast to the bare ZnO which displays a very low value of this parameter (6.7 $m^2 g^{-1}$). In the case of the ZnO/C-X hybrid materials, the annealing temperature of the ZnGly precursor affects the specific surface area significantly as this parameter increases with the increasing

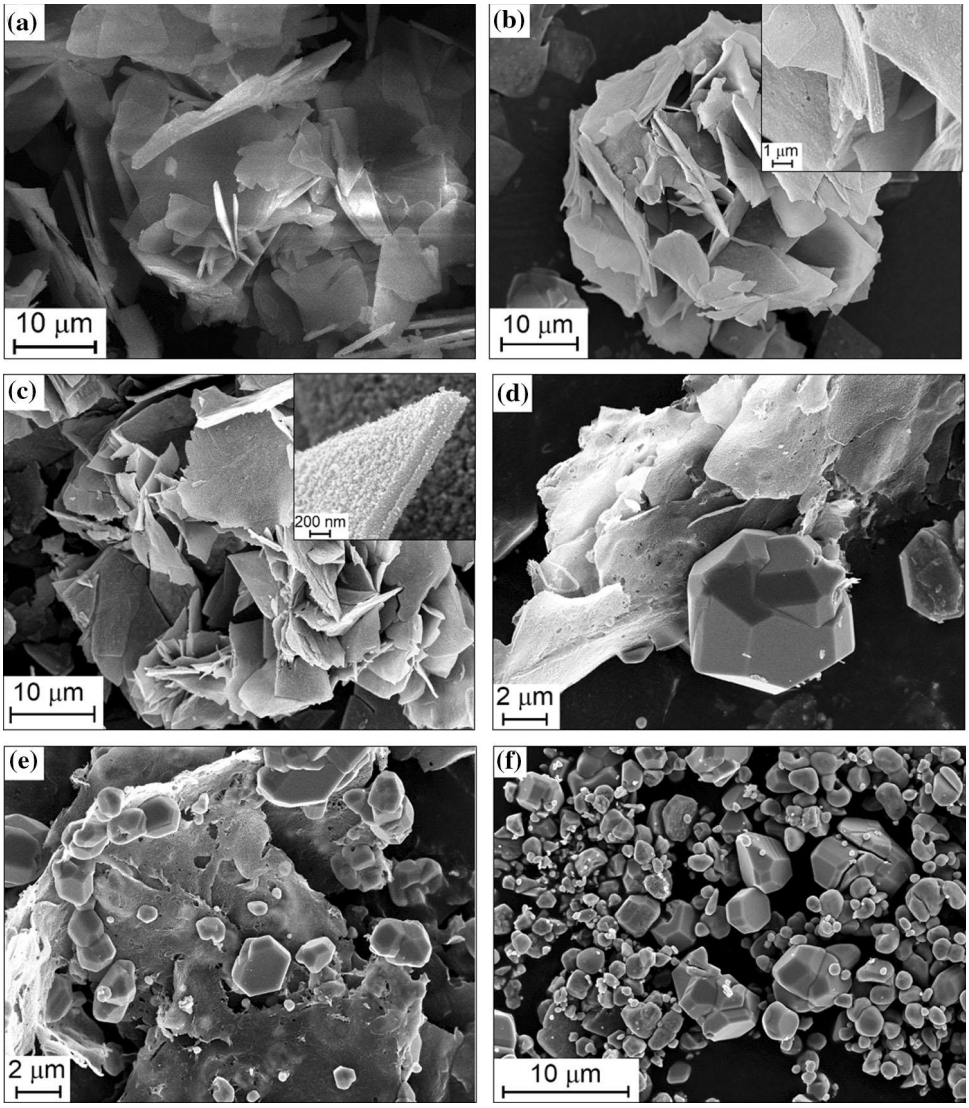

Figure 3 SEM images of (**a**) ZnGly precursor, **b** ZnO/C-400, **c** ZnO/C-500, **d** ZnO/C-700, **e** ZnO/C-800 composites, and **f** bare ZnO sample. Insets show high-magnification SEM images of cross sections of ZnO/C-400(500) composites.

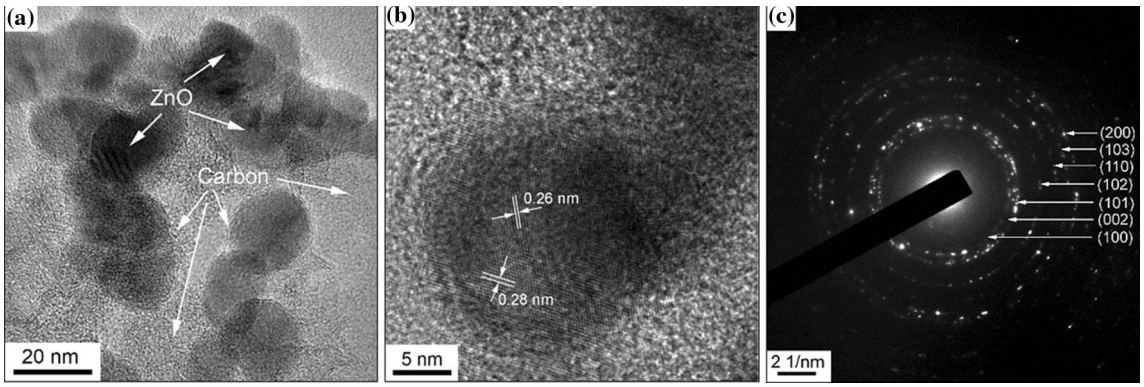

Figure 4 **a** TEM image, **b** HRTEM image, and **c** SAED pattern of ZnO/C-700 composite.

annealing temperature, from 400 to 700 °C. We attribute this behavior to the formation of defects in the composite structure during their annealing under N_2. The decrease in the specific surface area of the ZnO/C-800 composite compared to the ZnO/C-700 composite is attributed to the appearance of large

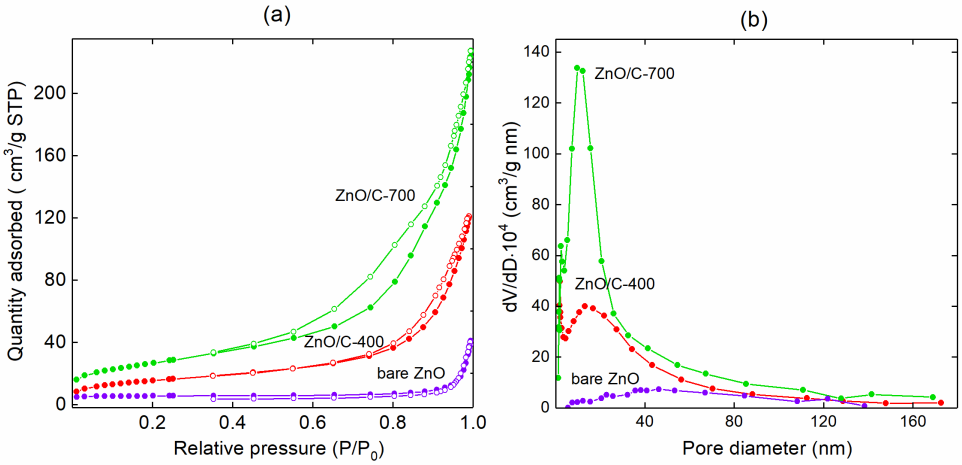

Figure 5 **a** N2 adsorption–desorption isotherms and **b** BJH pore size distribution curves of as-prepared ZnO/C composites and bare ZnO powder.

ZnO particles, as demonstrated by the SEM images (Fig. 3). Note, the ZnO/C-700 composite shows the highest BET surface of 100.9 $m^2\ g^{-1}$. From the pore size distribution plots (Fig. 5b), it is obvious that mesoporous structures are predominant in the fabricated ZnO/C-X composite materials.

The fabricated hybrid nanomaterials were studied with respect to their applicability as electrode materials in LIBs. Note, that the mesoporous nature of these materials is supposed to facilitate penetration of the electrolyte, thereby securing good electrical contact with the electrode and accelerating the diffusion kinetics. The electrochemical properties were investigated by cyclic voltammetry (CV) and galvanostatic cycling with potential limitation (GCPL). Figure 6a shows the first, second, third and tenth CV cycles for the ZnO/C-400 composite at a scan rate of 0.1 mV s^{-1} in a voltage range of 0.01–3.0 V. During the first reductive sweep the irreversible formation of the solid electrolyte interphase (SEI) occurs at around 0.6 V (R3). The peak R1 at the lower voltage limit of 0.01 V originates in part from the lithiation process related to carbon [38]. Since no corresponding oxidative peak is visible, we conclude that the delithiation process takes place over an extended voltage range. The reduction peak R2 and the oxidation peaks O1–O4 can be assigned to the Li^+ storage in ZnO [5, 6]. In the initial scan the reduction peak R2 at 0.3 V can be ascribed to both electrochemical reactions, the conversion and the alloying process [6]. After the second cycle R2 splits up in $R2_A$ (0.4 V) and $R2_C$ (0.7–0.8 V) which may be explained by a reduced overpotential of the conversion reaction at $R2_C$ due to structural changes during the initial cycle as compared to the conversion reaction at R2 while the alloying reaction at $R2_A$ is not significantly affected. Such a behavior is also observed for other conversion materials, such as Mn_3O_4 [38]. The oxidation peaks O1–O3 located between 0.3 and 0.7 V are assigned to the dealloying of LiZn alloy. The occurrence of several peaks suggests a multi-step process with various LiZn intermediate stages, such as Li_2Zn_3, $LiZn_2$ and Li_2Zn_5 [39, 40]. The peaks O1–O3 as well as $R2_A$ corresponding to the alloying process show good cycling stability. The oxidation feature O4 at around 1.3 V finally signals conversion to ZnO [6, 9]. Upon further cycling, the redox peak pair $R2_C$/O4 quickly decreases in intensity indicating an inactivation of the conversion reaction of ZnO Eq. (1). In contrast to the CV curve of the ZnO/C-400 composite, in case of the ZnO/C-700 composite (Fig. 6b) and bare ZnO (Fig. 6c) the oxidation peaks O1—O4 have lower intensity in the first cycle, while an additional oxidation peak at 2.6 V, labeled as O5, can be observed. The latter feature was also observed in several previous studies [3, 6, 7, 41, 42] but its origin still remains unclear. Huang et al. [3] and Pelliccione et al. [6] have speculatively assigned it to the back formation of ZnO Eq. (2) and the oxidation peak O4 to the dealloying process Eq. (1). In contrast, Mueller et al. [7] showed by means of *in-situ* XRD studies that the dealloying process is completed even before the oxidation process O4 starts and that ZnO is formed only afterwards, at O4. However, while these

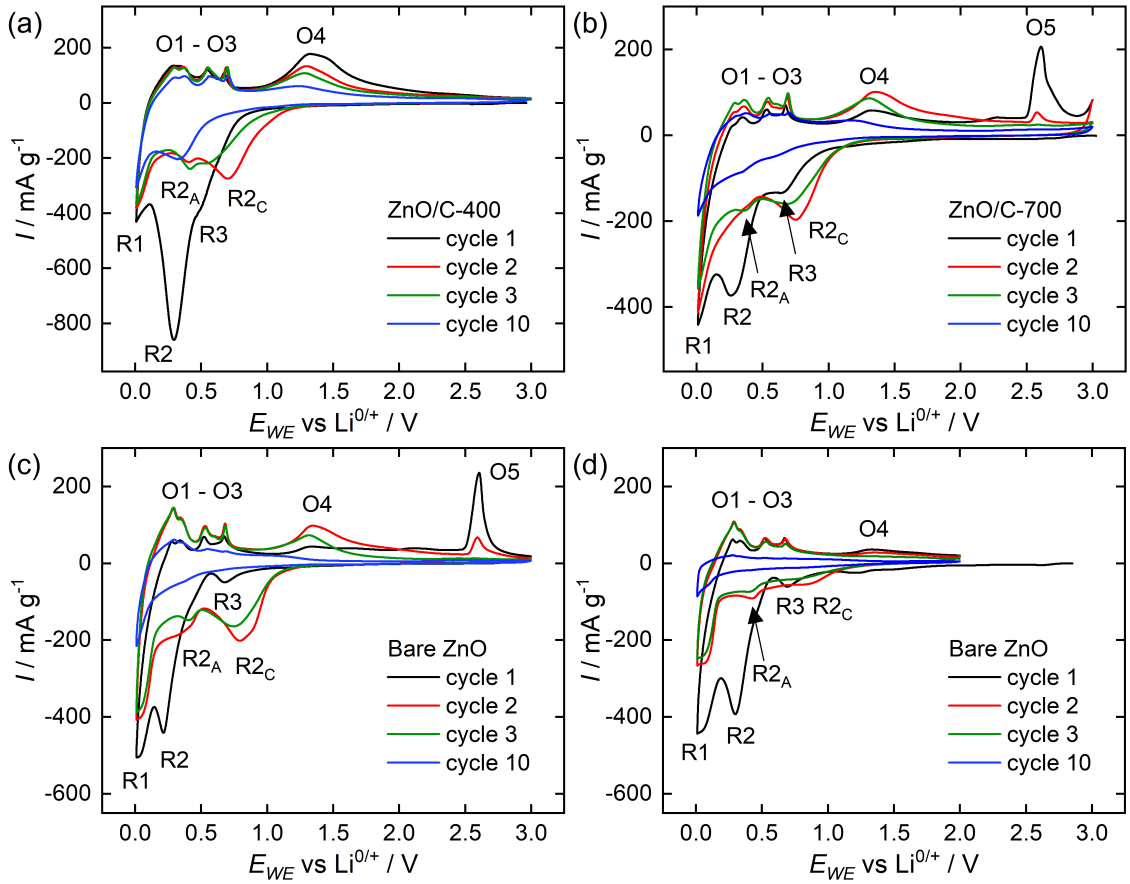

Figure 6 Cyclic voltammograms of (**a**) ZnO/C-400, **b** ZnO/C-700, and bare ZnO in the range of **c** 0.01–3 V and **d** 0.01–2 V at a scan rate of 0.1 mV s^{-1}. O1–O5 and R1–R4 label oxidation/reduction features as discussed in the text.

results exclude the above-mentioned assignment of O5, Mueller et al. make no further statements about this oxidation process. Hence, for understanding of the latter process we recorded a CV of the bare ZnO anode in a restricted potential range of 0.01–2.0 V (Fig. 6d), excluding O5. The comparison of this CV curve with the full range scans shows that the electrochemical activity steadily and strongly decreases in case of O5 exclusion, whereas otherwise, i.e., when the oxidation O5 takes place, the intensities of the subsequent features are significantly higher. Apparently, the oxidation process O5 plays a decisive role in the reversibility of Li^+ storage processes.

Ex-situ XRD measurements were performed in order to get insight into the structural changes of ZnO/C composites during electrochemical cycling. The XRD patterns of the ZnO/C-700 electrode at different dis-/charge states are shown in Fig. 7. In the initial state, the hexagonal ZnO phase (JCPDS #36–1451) is identified. The additional peaks at 44° and 51° originate from the Cu current collector. After discharging to 0.6 V the XRD pattern is similar to that of the as-prepared electrode. As expected, this implies that the electrode material does not undergo any structural transformation during the SEI formation. By further discharging to 0.3 V, the hexagonal ZnO phase completely transforms into a Zn phase (COD #9,008,522), which goes along with the conversion reaction according to Eq. (1). As can be seen from the expanded view of the 27–41° 2θ range in the inset of Fig. 7, a broad low intensity peak located at 33.7° indicates the presence of Li_2O (ICSD #54,368). It can be observed for all the following charge states as exemplarily shown by the XRD patterns of the fully charged and discharged state in the inset of Fig. 7. The XRD pattern of the completely discharged electrode (i.e., at 0.01 V) exhibits the characteristics of a single LiZn phase (COD #1,539,519), resulting from the alloying process described by Eq. (2). The observed structural changes upon cycling are in good

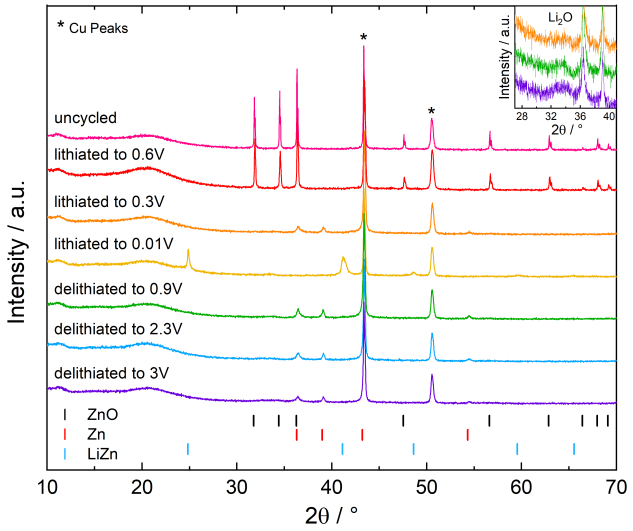

Figure 7 *Ex-situ* XRD patterns of a ZnO/C-700 electrode recorded at different stages of electrochemical Li^+ de-/insertion. The reflexes marked with * originate from the Cu current collector. In addition, the Bragg peak positions for ZnO (JCPDS # 36–1451), Zn (COD #9,008,522), and LiZn (COD #1,539,519) are shown. The inset shows the expanded view of XRD patterns of the samples lithiated up to 0.01 V (fully discharged), 0.9 V, and 3 V (fully charged) in the 27–41° 2θ range.

agreement with the reported results for a two-step mechanism for Li^+ storage in ZnO including a conversion and an alloying process [5, 40]. During the subsequent charging to 0.9 V, the peaks associated with LiZn vanish and the Zn phase reappears, confirming the reversibility of the alloying process. As charging proceeds to 3 V, the peaks associated with the Zn phase diminish in intensity, while no other crystalline phase shows up. Apparently, no structural changes are associated with the oxidation processes reflected by O4 and O5. Against expectation, there is no indication of crystalline ZnO in the completely charged electrode (i.e., at 3 V). This might be explained either by the amorphous structure or nanosize of the electrochemically formed ZnO or by the irreversibility of the conversion reaction Eq. (1). The lattice parameters of the Zn and LiZn phases appearing at various charging stages during the electrochemical cycling were determined by means of full-profile analyses with the FullProf Suite (Table S1). *Ex-situ* XRD studies on ZnO/C-400 show similar results (Fig. S2).

GCPL measurements at a current density of 100 mA g^{-1} in the range of 0.01–3.0 V enable assessing the cycling performance of the composite

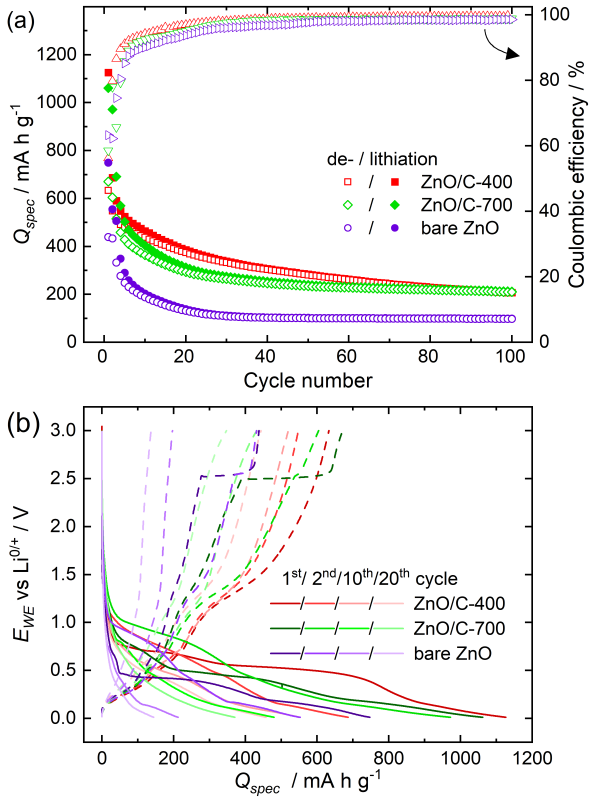

Figure 8 a Specific dis-/charge capacities and coulombic efficiencies of the ZnO/C-400 and ZnO/C-700 composites and of bare ZnO for galvanostatic cycling in the potential range between 0.01 and 3 V at 100 mA g^{-1} as well as (**b**) the respective potential profiles for the first, second, tenth and twentieth cycles.

nanomaterials under study. Figure 8a shows specific dis-/charge capacities and coulombic efficiencies for the first 100 cycles of the ZnO/C-400 and ZnO/C-700 composite as well as of the bare ZnO electrode. In the first cycle specific dis-/charge capacities of 1126/633 mAh g^{-1} (ZnO/C-400), 1061/671 mAh g^{-1} (ZnO/C-700) and 749/439 mAh g^{-1} (ZnO) were measured. One reason for the large capacity loss in the first cycle is the irreversible SEI formation during discharge. As can be seen from the potential profiles of the first lithiation (Fig. 8b), for bare ZnO the SEI contribution is quite small with less than 50 mAh g^{-1}, whereas for the composites it is larger due to the fact that the irreversible charge loss is roughly linearly proportional to the specific surface area of carbonaceous materials [43]. Cracking and fracture of the electrode material due to large volume changes can lead to an unstable SEI and irreversible capacity losses beyond

the first cycle [44], which also might explain the unexpected high second discharge capacity of ZnO/C-700 compared to the first charge capacity. Based on the reaction mechanism of ZnO Eqs. (1) and (2), a maximal theoretical specific capacity of 978 mAh g^{-1} can be reached. Considering the capacity from the SEI formation, it can be concluded that in the case of the composites the ZnO almost fully reacts with Li^+ according to the expected reaction mechanism, while this is not the case for the bare ZnO electrode. After 20 cycles 293 mAh g^{-1} can be charged from ZnO/C-700 and a slightly higher capacity of 374 mAh g^{-1} from ZnO/C-400, corresponding to a capacity fading of 44% and 41% relative to the first cycle. The poor coulombic efficiencies and rapid capacity fading during the first twenty cycles might be explained by the limited reversibility of the conversion reaction Eq. (1). This is supported by the results of *ex-situ* XRD studies. Under the assumption that the back formation to ZnO Eq. (1) is irreversible and the reversible lithiation reaction is a single alloying process Eq. (2) a maximal capacity of only 329 mAh g^{-1} can be expected. Obviously, the charge capacities exceed this value for about the first twenty cycles indicating that the reoxidation of Zn to ZnO is at least partly reversible as also observed by Pelliccione et al. [6] and Mueller et al. [7]. Interestingly, during further cycling the coulombic efficiencies are increasingly converging at 100% and simultaneously the cycling stabilities get much better. Exemplarily, the ZnO/C-700 composite delivers a discharge capacity of 212 mAh g^{-1} after 100 cycles exhibiting excellent cycle stability with an average capacity loss of only 0.04% per cycle over the last 80 cycles. The potential profiles of the first, second, tenth and twentieth cycle in Fig. 8b provide an insight into the origins of the capacity fading. Comparing the potential profiles, it is noticeable that the capacity loss can be mainly traced back to an inactivation of the conversion reaction Eq. (1), which can also be observed in the CV curves (Fig. 6). During the first cycles both processes, viz. the conversion and the alloying, take place but in the further course the alloying mainly contributes to the Li^+ storage, which might be due to the incomplete back formation of ZnO. In addition, the loss of electrical connectivity to the active material due to changes in the electrode structure, such as particle aggregation or pulverization, results in capacity losses. Comparing the two composites, indeed, the capacities of the ZnO/C-700 composite fade more rapidly in the first cycles with lower coulombic efficiency than for ZnO/C-400 but stabilize faster in the further course. It should be noted, that the evolution of the capacities of the ZnO/C-500 sample is similar to that of ZnO/C-400 while the evolution of the capacities of the ZnO/C-800 sample is similar to that of ZnO/C-700 (Fig. S3), who each have similar crystallographic and morphological properties, respectively. The worse cycling stability of the ZnO/C-700 composite in the first twenty cycles might be attributed to the presence of microscaled polyhedrons, whereas the ZnO/C-400 composite consists only of nanoscaled primary particles. For one thing, the reversibility of the conversion reaction depends on the crystallite size of the transition metal particles formed during electrochemical cycling [45]. Park et al. [9] have shown that the back formation of ZnO

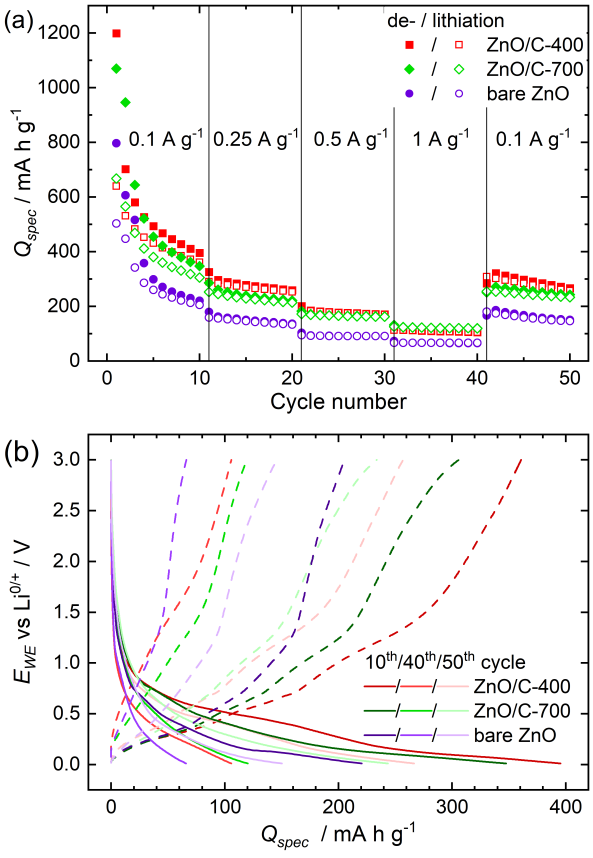

Figure 9 **a** Rate capability test of the ZnO/C-400 and ZnO/C-700 composites and of bare ZnO at current rates between 100 and 1000 mA g^{-1} as well as (**b**) the respective potential profiles of cycle 10 at 100 mA g^{-1}, cycle 40 at 1000 mA g^{-1} and cycle 50 again at 100 mA g^{-1}.

only occurs for extremely small Zn nanocrystallites. In addition, nanosized particles can better accommodate the strain caused by the volume changes during electrochemical cycling [46]. Looking at the comparison between the ZnO/C composites and the bare ZnO sample, it is remarkable that over the whole measurement the composites reach about twice the capacities of the bare sample. In cycle 20 and 100, the bare ZnO compound reaches specific capacities of 131 mAh g^{-1} and 97 mAh g^{-1}, respectively. The higher capacities of the composite materials can be probably traced back to the larger surface area offering more active sides as well as a better electronic connection of the ZnO particles due to the conductive network provided by the carbon. Furthermore, the stabilized coulombic efficiency and the cycling stability of the bare ZnO electrode is with a capacity loss of 70% in cycle 20 relative to the first cycle worse than for the composites. We conclude that degradation effects such as structural changes of the electrode material leading to the electrical disconnection of the active material as well as an unstable SEI can be at least partly prevented by the carbon. The carbon matrix can effectively suppress the nanoparticle aggregation and pulverization of the electrode material due to large volume changes maintaining the structural stability and, moreover, helping stabilize SEI formation [23, 47–49]. In addition, the electrochemical properties of bare ZnO and the ZnO/C-400 and ZnO/C-700 composites were also investigated by galvanostatic cycling with various current densities between 100 and 1000 mA g^{-1}. The specific dis-/charge capacities are shown in Fig. 9a along with the potential profiles of cycle 10 at 100 mA g^{-1}, cycle 40 at 1000 mA g^{-1} and cycle 50 again at 100 mA g^{-1} in Fig. 9b. The ZnO/C-400 composite reaches a charge capacity of 113 mAh g^{-1} at a high current rate of 1000 mA g^{-1} while for ZnO/C-700 a charge capacity of 125 mAh g^{-1} is measured and for bare ZnO 67 mAh g^{-1}. The inferior rate capability of the sample ZnO/C-400 compared to ZnO/C-700 is caused by a more severe polarization resistance due to kinetic effects. As can be seen from the potential profiles, at a high current rate of 1000 mA g-1, the potential gap between charge and discharge increases more for ZnO/C-400 than for ZnO/C-700. The reduced polarization resistance in case of ZnO/C-700 might be associated with better conductivity of the less disordered carbon as shown by Raman spectroscopy and the XPS analysis. When the current density is reset to 100 mA g^{-1} charge capacities of ca. 83%, 86% and even 88% relative to cycle 10 can be regained for the ZnO/C-400, ZnO/C-700 and bare ZnO samples, respectively.

Table 2 Comparison of the electrochemical performance of ZnO and ZnO/C electrodes prepared via different synthesis methods as reported in the literature

Sample	Method of synthesis	Current density (mA g^{-1})	Discharge capacity (mAh g^{-1})/cycle no	References
ZnO spheres	Hydrothermal	100	109/100	[2]
ZnO/C nanoparticles	Thermal decomposition of $Zn_3(C_6H_5O_7)_2$	100	850/200	[22]
ZnO/C spheres	Thermal decomposition of $Zn_3(C_6H_5O_7)_2$	100	520/150	[24]
ZnO/C nanoparticles	Thermal decomposition of $C_4H_4ZnO_6$	100	610/300	[25]
ZnO/C nanocages	Pyrolysis	100	750/100	[50]
ZnO/C spheres	Pyrolysis	100	750/100	[51]
ZnO/C nanoparticles	Ball milling	100	610/500	[52]
ZnO/C tetrahedron	Calcination	110.7	518/300	[53]
ZnO/C nanoparticles	Calcination	100	610/50	[54]
ZnO/C spheres	Coprecipitation	500	659/300	[55]
ZnO/C-400	Thermal decomposition of $ZnC_3H_6O_3$	100	208/100	This work
ZnO/C-700		100	212/100	
ZnO		100	98/100	

Interestingly, the comparison with the measurement consistently at 100 mA g^{-1} (Fig. 8) reveals that the capacity fading seems to be more serious for electrochemical cycling at lower rates accompanied with higher Li^+ storage capacity. For ZnO/C-400, ZnO/C-700 and bare ZnO which were continuously cycled at 100 mA g^{-1}, charge capacities of only 68%, 67% and 54% were obtained in cycle 41 relative to cycle 10. Higher degradation effects for a more comprehensive dis-/charge process might be explained as a result of more serious structural damages of the electrode material. For comparison purposes, Li storage performance of the as-prepared ZnO/C anodes and those of ZnO and ZnO/C materials reported in literature are summarized in Table 2. The results show that the cycling performance of ZnO/C composites compared with bare ZnO is much better owing to positive effects of carbon. The differences of the specific capacities of ZnO/C composites produced by various methods can be attributed to the morphology, crystal size, specific surface area as well as porosity which influence the electrochemical properties of the electrode materials. The lower electrochemical activity of the ZnO/C composites in this work compared to most of ZnO materials in literature can be explained by their morphological features and carbon content in the compounds. The as-prepared composites are composed of ZnO particles with relatively large dimensions. Small-sized particles have a large surface area, which provides more active sides resulting in high specific dis-/charge capacities. The good electrochemical performance of the electrodes prepared by the thermal decomposition of the different organometallic complexes [22, 24, 25] can be attributed to the distinctive carbon content in the products.

Conclusions

In conclusion, a facile method to synthesize ZnO/C composites, involving a thermal treatment of zinc glycerolate as a source of both carbon and zinc, was demonstrated. This one-pot method allows the synthesis of a variety of controllable ZnO/C composites with distinctive nano/microscaled arrays of ZnO particles. When used as anode material for lithium-ion batteries, the ZnO/C composite synthesized at a calcination temperature of 700 °C achieves high initial discharge and charge capacities of 1061 and 671 mAh g^{-1} at a current rate of 100 mA g^{-1}. As compared to the bare ZnO, the composites exhibit significantly better electrochemical properties, such as higher specific capacities and superior cycling stability. The carbon acts as a conductive network that runs through the material leading to the prevention of inactive areas and thus to a higher electrochemical activity. *Ex-situ* XRD studies confirm a two-step mechanism for lithiation of ZnO including a conversion and alloy process.

Acknowledgements

This work was supported by the Deutsche Forschungsgemeinschaft through projects KL1824/12-1 and KL 1824/14-1. G.Z. acknowledges support of the state order via the Ministry of Science and Higher Education of Russia (No AAAA-A19-119031890025-9). E.T. acknowledges support by the BMWi through project 03ET6095C (HiKoMat). The authors thank I. Glass for experimental support.

Funding

Open Access funding enabled and organized by Projekt DEAL.

Declarations

Conflict of interest The authors declare that they have no conflict of interest.

Supplementary Information: The online version contains supplementary material available at https://doi.org/10.1007/s10853-021-06125-4.

Supplementary Information: The online version contains supplementary material available at https://doi.org/10.1007/s10853-021-06125-4.

References

[1] Wang Y, Deng Q, Xue W, Jian Z, Zhao R, Wang J (2018) ZnO/rGO/C composites derived from metal–organic framework as advanced anode materials for Li-ion and Na-ion batteries. J Mater Sci. https://doi.org/10.1007/s10853-018-2003-3

[2] Wu G, Jia Z, Cheng Y, Zhang H, Zhou X, Wu H (2019) Easy synthesis of multi-shelled ZnO hollow spheres and their conversion into hedgehog-like ZnO hollow spheres with superior rate performance for lithium ion batteries. Appl Surf Sci. https://doi.org/10.1016/j.apsusc.2018.09.115

[3] Huang XH, Guo RQ, Wu JB, Zhang P (2014) Mesoporous ZnO nanosheets for lithium ion batteries. Mater Lett. https://doi.org/10.1016/j.matlet.2014.02.012

[4] Kundu S, Sain S, Yoshio M, Kar T, Gunawardhana N, Pradhan SK (2015) Structural interpretation of chemically synthesized ZnO nanorod and its application in lithium ion battery. Appl Surf Sci. https://doi.org/10.1016/j.apsusc.2014.12.152

[5] Fu Z-W, Huang F, Zhang Y, Chu Y, Qin Q-Z (2003) The electrochemical reaction of zinc oxide thin films with lithium. J Electrochem Soc. https://doi.org/10.1149/1.1570410

[6] Pelliccione CJ, Ding Y, Timofeeva EV, Segre CU (2015) In Situ XAFS study of the capacity fading mechanisms in ZnO anodes for lithium-ion batteries. J Electrochem Soc. https://doi.org/10.1149/2.1011509jes

[7] Mueller F, Geiger D, Kaiser U, Passerini S, Bresser D (2016) Elucidating the impact of cobalt doping on the lithium storage mechanism in conversion/alloying-type zinc oxide anodes. ChemElectroChem. https://doi.org/10.1002/celc.201600179

[8] Hao Y, Wang S, Zeng J, Li H, Yang P, Liu B, Zhang S, Xing Y (2018) A peapod-like ZnO@C design with internal void space to relieve its large-volume-change as lithium-ion battery anode. Ceram Int. https://doi.org/10.1016/j.ceramint.2017.08.088

[9] Park M-G, Sung G-K, Sung N-E, Kim J-H, Park C-M (2016) Partially reversible Li2O formation in ZnO: a critical finding supporting realization of highly reversible metal oxide electrodes. J Power Sources. https://doi.org/10.1016/j.jpowsour.2016.08.053

[10] Jamnik J, Maier J (2003) Nanocrystallinity effects in lithium battery materials. Phys Chem. https://doi.org/10.1039/b309130a

[11] Xiao L, Li E, Yi J, Meng W, Wang S, Deng B, Liu J (2018) Enhancing the performance of nanostructured ZnO as an anode material for lithium-ion batteries by polydopamine-derived carbon coating and confined crystallization. J Alloy Compd. https://doi.org/10.1016/j.jallcom.2018.06.081

[12] Abbas SM, Hussain ST, Ali S, Ahmad N, Ali N, Abbas S (2013) Structure and electrochemical performance of ZnO/CNT composite as anode material for lithium-ion batteries. J Mater Sci. https://doi.org/10.1007/s10853-013-7336-3

[13] Hsieh C-T, Lin C-Y, Chen Y-F, Lin J-S (2013) Synthesis of ZnO@Graphene composites as anode materials for lithium ion batteries. Electrochim Acta. https://doi.org/10.1016/j.electacta.2013.07.197

[14] Quartarone E, Dall'Asta V, Resmini A, Tealdi C, Tredici IG, Tamburini UA, Mustarelli P (2016) Graphite-coated ZnO nanosheets as high-capacity, highly stable, and binder-free anodes for lithium-ion batteries. J Power Sources. https://doi.org/10.1016/j.jpowsour.2016.04.107

[15] Yang T, Liu Y, Huang Z, Liu J, Bian P, Ling CD, Liu H, Wang G, Zheng R (2018) In situ growth of ZnO nanodots on carbon hierarchical hollow spheres as high-performance electrodes for lithium-ion batteries. J Alloy Compd. https://doi.org/10.1016/j.jallcom.2017.11.125

[16] Shen L, Wang C (2015) ZnO/C microboxes derived from coordination polymer particles for superior lithium ion battery anodes. RSC Adv. https://doi.org/10.1039/C5RA18254A

[17] Bai Z, Zhang Y, Fan N, Guo C, Tang B (2014) One-step synthesis of ZnO@C nanospheres and their enhanced performance for lithium-ion batteries. Mater Lett. https://doi.org/10.1016/j.matlet.2013.12.060

[18] Zhao Q, Xie H, Ning H, Liu J, Zhang H, Wang L, Wang X, Zhu Y, Li S, Wu M (2018) Intercalating petroleum asphalt into electrospun ZnO/Carbon nanofibers as enhanced free-standing anode for lithium-ion batteries. J Alloy Compd. https://doi.org/10.1016/j.jallcom.2017.12.091

[19] Liu Y, Li Y, Zhong M, Hu Y, Hu P, Zhu M, Li W, Li Y (2016) A facile synthesis of core-shell structured ZnO@C nanosphere and their high performance for lithium ion battery anode. Mater Lett. https://doi.org/10.1016/j.matlet.2016.02.112

[20] Rangel-Mendez JR, Matos J, Cházaro-Ruiz LF, González-Castillo AC, Barrios-Yáñez G (2018) Microwave-assisted synthesis of C-doped TiO_2 and ZnO hybrid nanostructured

materials as quantum-dots sensitized solar cells. Appl Surf Sci. https://doi.org/10.1016/j.apsusc.2017.10.236

[21] Xue J, Ma S, Zhou Y, Zhang Z (2015) Facile synthesis of ZnO-C nanocomposites with enhanced photocatalytic activity. Chem New J. https://doi.org/10.1039/C4NJ02004A

[22] Xiao C, Zhang S, Wang S, Xing Y, Lin R, Wei X, Wang W (2016) ZnO nanoparticles encapsulated in a 3D hierarchical carbon framework as anode for lithium ion battery. Electrochim Acta. https://doi.org/10.1016/j.electacta.2015.11.045

[23] Liu H, Shi L, Li D, Yu J, Zhang H-M, Ullah S, Yang B, Li C, Zhu C, Xu J (2018) Rational design of hierarchical ZnO@Carbon nanoflower for high performance lithium ion battery anodes. J Power Sources. https://doi.org/10.1016/j.jpowsour.2018.03.047

[24] Xie Q, Zhang X, Wu X, Wu H, Liu X, Yue G, Yang Y, Peng D-L (2014) Yolk-shell ZnO-C microspheres with enhanced electrochemical performance as anode material for lithium ion batteries. Electrochim Acta. https://doi.org/10.1016/j.electacta.2014.02.003

[25] Wei D, Xu Z, Wang J, Sun Y, Zeng S, Li W, Li X (2017) A one-pot thermal decomposition of C 4 H 4 ZnO 6 to ZnO@carbon composite for lithium storage. J Alloy Compd. https://doi.org/10.1016/j.jallcom.2017.04.214

[26] Zakharova GS, Ottmann A, Möller L, Andreikov EI, Fattakhova ZA, Puzyrev IS, Zhu Q, Thauer E, Klingeler R (2018) TiO2/C nanocomposites prepared by thermal annealing of titanium glycerolate as anode materials for lithium-ion batteries. J Mater Sci. https://doi.org/10.1007/s10853-018-2488-9

[27] Dong H, Feldmann C (2012) Porous ZnO platelets via controlled thermal decomposition of zinc glycerolate. J Alloy Compd. https://doi.org/10.1016/j.jallcom.2011.10.004

[28] Zubavichus Y, Shaporenko A, Grunze M, Zharnikov M (2005) Innershell absorption spectroscopy of amino acids at all relevant absorption edges. J Phys Chem. https://doi.org/10.1021/jp0535846

[29] Wang Y, Alsmeyer DC, McCreery RL (1990) Raman spectroscopy of carbon materials: structural basis of observed spectra. Mater Chem. https://doi.org/10.1021/cm00011a018

[30] Kumar R, Singh RK, Kumar Dubey P, Singh DP, Yadav RM, Tiwari RS (2015) Hydrothermal synthesis of a uniformly dispersed hybrid graphene–TiO_2 nanostructure for optical and enhanced electrochemical applications. RSC Adv. https://doi.org/10.1039/C4RA06852A

[31] Akhavan O, Abdolahad M, Esfandiar A, Mohatashamifar M (2010) Photodegradation of graphene oxide sheets by TiO_2 nanoparticles after a photocatalytic reduction. J Phys Chem C. https://doi.org/10.1021/jp103472c

[32] Ferrari AC, Robertson J (2000) Interpretation of Raman spectra of disordered and amorphous carbon. Rev B Phys. https://doi.org/10.1103/PhysRevB.61.14095

[33] Cho NH, Veirs DK, Ager JW, Rubin MD, Hopper CB, Bogy DB (1992) Effects of substrate temperature on chemical structure of amorphous carbon films. J Appl Phys. https://doi.org/10.1063/1.351122

[34] Deldicque D, Rouzaud J-N, Velde B (2016) A Raman–HRTEM study of the carbonization of wood: a new Raman-based paleothermometer dedicated to archaeometry. Carbon. https://doi.org/10.1016/j.carbon.2016.02.042

[35] Yan Y, Wang B, Yan C, Kang DJ (2019) Decorating ZnO nanoflakes on carbon cloth: free-standing, highly stable lithium-ion battery anodes. Ceram Int. https://doi.org/10.1016/j.ceramint.2019.05.097

[36] Chen X, Wang X, De Fang K (2020) A review on C1s XPS-spectra for some kinds of carbon materials. Fullerenes Nanotubes Carbon Nanostruct. https://doi.org/10.1080/1536383X.2020.1794851

[37] Rouquerol J, Avnir D, Fairbridge CW, Everett DH, Haynes JM, Pernicone N, Ramsay JDF, Sing KSW, Unger KK (1994) Recommendations for the characterization of porous solids (Technical Report). Pure Appl Chem. https://doi.org/10.1351/pac199466081739

[38] Ottmann A, Scholz M, Haft M, Thauer E, Schneider P, Gellesch M, Nowka C, Wurmehl S, Hampel S, Klingeler R (2017) Electrochemical magnetization switching and energy storage in manganese oxide filled carbon nanotubes. Sci Rep. https://doi.org/10.1038/s41598-017-14014-7

[39] Fujieda T, Takahashi S, Higuchi S (1992) Cycling behaviour of electrodeposited zinc alloy electrode for secondary lithium batteries. J Power Sources. https://doi.org/10.1016/0378-7753(92)80016-5

[40] Wang J, King P, Huggins R (1986) Investigations of binary lithium-zinc, lithium-cadmium and lithium-lead alloys as negative electrodes in organic solvent-based electrolyte. Solid State Ionics. https://doi.org/10.1016/0167-2738(86)90212-2

[41] Zhang CQ, Tu JP, Yuan YF, Huang XH, Chen XT, Mao F (2007) Electrochemical performances of Ni-coated ZnO as an anode material for lithium-ion batteries. J Electrochem Soc. https://doi.org/10.1149/1.2400609

[42] Xiao L, Mei D, Cao M, Qu D, Deng B (2015) Effects of structural patterns and degree of crystallinity on the performance of nanostructured ZnO as anode material for lithium-ion batteries. J Alloy Compd. https://doi.org/10.1016/j.jallcom.2014.11.195

[43] Winter M (1998) Graphites for lithium-ion cells: the correlation of the first-cycle charge loss with the Brunauer-

Emmett-Teller surface area. J Electrochem Soc. https://doi.org/10.1149/1.1838281

[44] Pender JP, Jha G, Youn DH, Ziegler JM, Andoni I, Choi EJ, Heller A, Dunn BS, Weiss PS, Penner RM, Mullins CB (2020) Electrode degradation in lithium-ion batteries. ACS Nano. https://doi.org/10.1021/acsnano.9b04365

[45] Poizot P, Laruelle S, Grugeon S, Dupont L, Tarascon JM (2000) Nano-sized transition-metal oxides as negative-electrode materials for lithium-ion batteries. Nature. https://doi.org/10.1038/35035045

[46] Guo Y-G, Hu J-S, Wan L-J (2008) Nanostructured materials for electrochemical energy conversion and storage devices. Mater Adv. https://doi.org/10.1002/adma.200800627

[47] Li H, Zhou H (2012) Enhancing the performances of Li-ion batteries by carbon-coating: present and future. Chem Commun 2:10. https://doi.org/10.1039/c1cc14764a

[48] Ge Y, Jiang H, Zhu J, Lu Y, Chen C, Hu Y, Qiu Y, Zhang X (2015) High cyclability of carbon-coated TiO_2 nanoparticles as anode for sodium-ion batteries. Electrochim Acta. https://doi.org/10.1016/j.electacta.2015.01.086

[49] Zhang W-M, Wu X-L, Hu J-S, Guo Y-G, Wan L-J (2008) Carbon coated Fe3O4 nanospindles as a superior anode material for lithium-ion batteries. Funct Mater Adv. https://doi.org/10.1002/adfm.200801386

[50] Song Y, Chen Y, Wu J, Fu Y, Zhou R, Chen S, Wang L (2017) Hollow metal organic frameworks-derived porous ZnO/C nanocages as anode materials for lithium-ion batteries. J Alloy Compd. https://doi.org/10.1016/j.jallcom.2016.10.110

[51] Fu Y, Zhong B, Chen Y, Song Y, Zhou R, Song Y, Chen S (2017) Porous ZnO@C core–shell nanocomposites as high performance electrode materials for rechargeable lithium-ion batteries. J Porous Mater. https://doi.org/10.1007/s10934-016-0297-6

[52] Yu M, Shao D, Lu F, Sun X, Sun H, Hu T, Wang G, Sawyer S, Qiu H, Lian J (2013) ZnO/graphene nanocomposite fabricated by high energy ball milling with greatly enhanced lithium storage capability. Electrochem Commun. https://doi.org/10.1016/j.elecom.2013.07.013

[53] Ren Z, Wang Z, Chen C, Wang J, Fu X, Fan C, Qian G (2014) Preparation of carbon-encapsulated ZnO tetrahedron as an anode material for ultralong cycle life performance lithium-ion batteries. Electrochim Acta. https://doi.org/10.1016/j.electacta.2014.09.038

[54] Li P, Liu Y, Liu J, Li Z, Wu G, Wu M (2015) Facile synthesis of ZnO/mesoporous carbon nanocomposites as high-performance anode for lithium-ion battery. Chem Eng J. https://doi.org/10.1016/j.cej.2015.02.077

[55] Fan H, Yu H, Zhang Y, Guo J, Wang Z, Wang H, Hao X, Zhao N, Geng H, Dai Z, Yan Q, Xu J (2017) From zinc-cyanide hybrid coordination polymers to hierarchical yolk-shell structures for high-performance and ultra-stable lithium-ion batteries. Nano Energy. https://doi.org/10.1016/j.nanoen.2017.01.043

Supplementary Materials

Table S1 Rietveld refinement data of Zn and LiZn appearing at various charging stages during electrochemical cycling.

Phase	Charging stage	Lattice parameters	
	(V)	*a* (Å)	*c* (Å)
Zn	0.3	2.66(1)	4.93(1)
LiZn	0.01	6.18(4)	6.18(4)
Zn	0.9	2.664(6)	4.934(8)
Zn	3.0	2.661(4)	4.94(1)

Figure S1: XPS Zn Auger spectra of ZnO/C-400 and ZnO/C-700

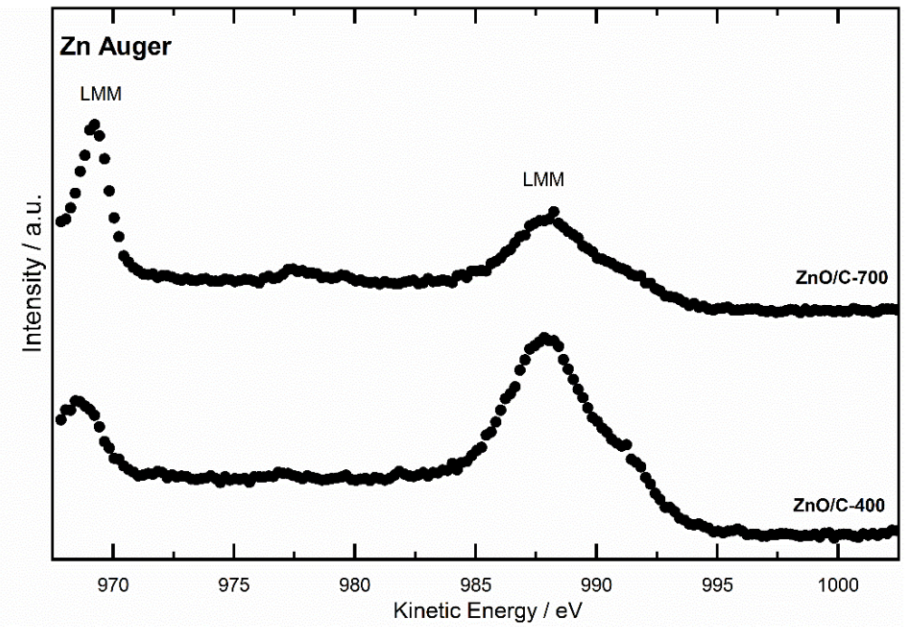

Figure S2 *Ex-situ* XRD patterns of an uncycled, fully discharged (0.01 V) and charged (3 V) ZnO/C-400 electrode. The reflexes marked with * originate from the Cu current collector. In addition, the Bragg peak positions for ZnO (JCPDS # 36-1451), Zn (COD #9008522), LiZn (COD #1539519) and Li2O (ICSD #54368) are shown.

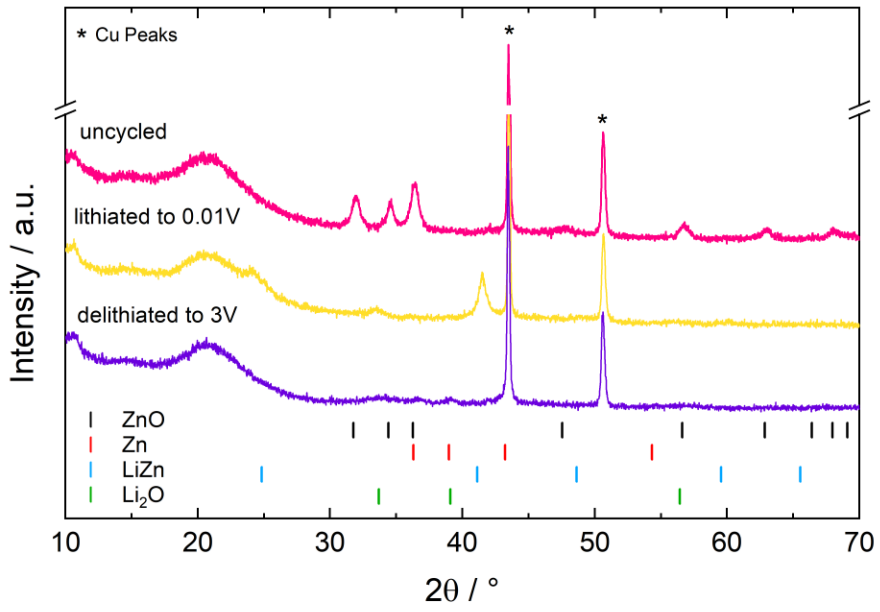

Figure S3 Specific dis-/charge capacities of the composites ZnO/C-X and of bare ZnO for galvanostatic cycling in the potential range between 0.01 and 3 V at 100 mA g^{-1}.

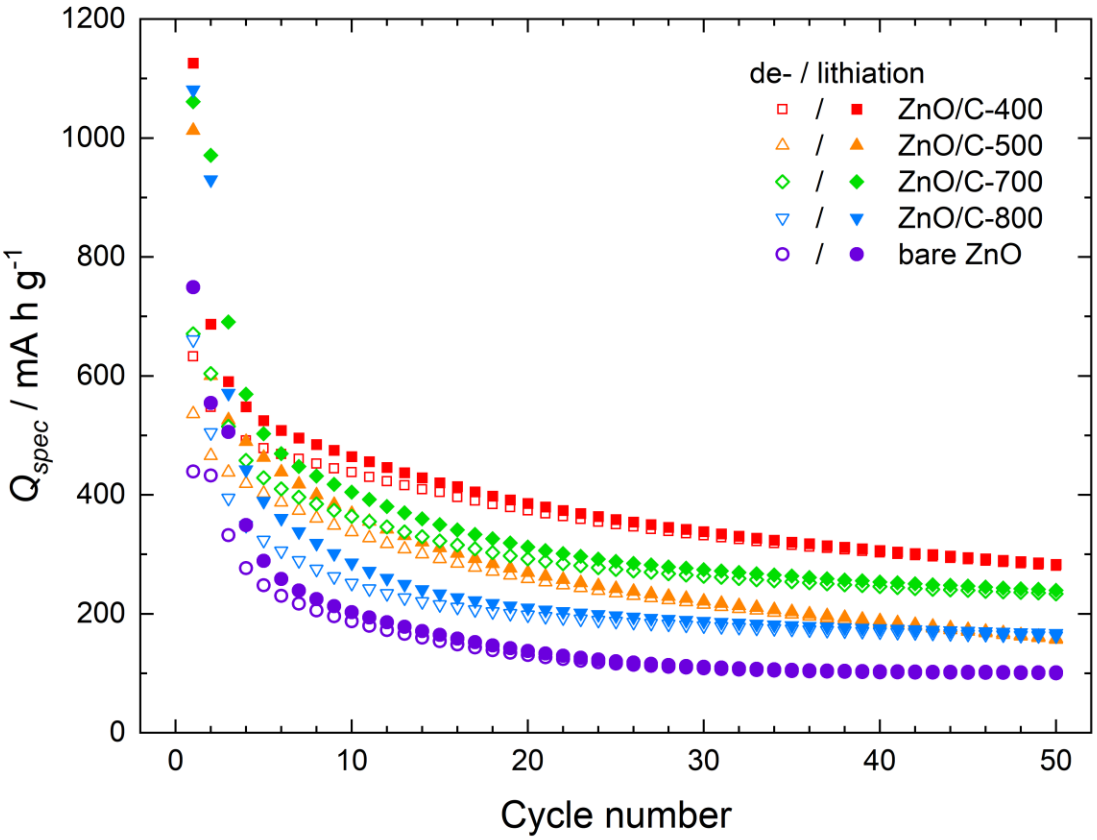

Kapitel 4

Funktionalisierung

mit

Kohlenstoffnanostrukturen

4.1 $CoFe_2O_4$-filled carbon nanotubes as anode material for lithium-ion batteries

Autoren:

L. Möller, E. Thauer, A. Ottmann, X. Chen, L. Deeg, R. Ghunaim, S. Hampel, R. Klingeler

veröffentlicht in Journal of Alloys and Compounds 834, 2020, 155018

E. Thauer ist die Korrespondenzautorin dieses Artikels. Die elektrochemische Untersuchung der reinen Probe erfolgte gemeinsam von E. Thauer und dem Masterstudent L. Deeg unter ihrer Anleitung. E. Thauer verfasste Teile des Manuskripts zu den eigenen Ergebnissen, erstellte die Abb. 4 a und 5 b und überarbeitete alle Abbildungen. Die Korrespondenz mit den Gutachtern sowie die Überarbeitung des Manuskripts wurde von E. Thauer zusammen mit R. Klingeler übernommen.

L. Möller ist der Erstautor dieses Artikels. A. Ottmann führte im Rahmen seiner Dissertation gemeinsam mit dem Bachelorstudent L. Möller die Magnetisierungs- (Abb. 3) und elektrochemischen Messungen (Abb. 4 b und 5 a) des Komposits unter seiner Anleitung durch. Die Synthese, die XRD, REM-, TEM- (Abb. 1) und TGA-Messungen sowie die Verfassung der entsprechenden Teile im Manuskript erfolgten von R. Ghunaim und S. Hampel. R. Klingeler ist Korrespondenzautor, betreute das Projekt und war an der Finalisierung des Manuskripts beteiligt. Alle Autoren haben das Manuskript korrekturgelesen.

Journal of Alloys and Compounds 834 (2020) 155018

Contents lists available at ScienceDirect

Journal of Alloys and Compounds

journal homepage: http://www.elsevier.com/locate/jalcom

$CoFe_2O_4$-filled carbon nanotubes as anode material for lithium-ion batteries

Lucas Möller [a], Elisa Thauer [a, *], Alexander Ottmann [a], Lukas Deeg [a], Rasha Ghunaim [b, c], Silke Hampel [b], Rüdiger Klingeler [a, d, **]

[a] Kirchhoff Institute of Physics, Heidelberg University, INF 227, 69120, Heidelberg, Germany
[b] Leibniz Institute for Solid State and Materials Research (IFW) Dresden, Helmholtzstraße 20, 01069, Dresden, Germany
[c] Department of Applied Chemistry, Palestine Polytechnic University, Hebron P.O. Box 198, Palestinian Territories, Germany
[d] Centre for Advanced Materials (CAM), Heidelberg University, INF 225, 69120, Heidelberg, Germany

ARTICLE INFO

Article history:
Received 30 January 2020
Received in revised form
31 March 2020
Accepted 1 April 2020
Available online 5 April 2020

Keywords:
Lithium-ion batteries
Carbon nanotubes
Cobalt ferrite
Anode material
Nanocomposite

ABSTRACT

Nanosized particles of cobalt ferrite $CoFe_2O_4$ incorporated into multi-walled carbon nanotubes (CNT) have been studied as anode material for Li-ion batteries. In order to evaluate the benefits of CNT shells, the results are compared to bare $CoFe_2O_4$ nanoparticles. Electrochemical measurements by means of cyclic voltammetry and galvanostatic cycling show typical redox activity associated with the ferrite conversion reaction which implies that the filled nanomaterial is electrochemically active. Galvanostatic cycling measurements reveal better cycling stability of the CNT-incorporated compared to the bare ferrite nanoparticles. The data imply that embedding nanoparticles inside the protective and conductive shells of CNTs opens a way to utilize high theoretical capacities of $CoFe_2O_4$ for electrochemical energy storage.

1. Introduction

First row transition metal oxides have been known to be promising materials for energy storage in lithium ion batteries (LIBs) [1,2]. This is due to their large theoretical specific capacities based on conversion mechanisms involving the reduction to their metallic constituents and Li_2O [3]. One of these promising conversion materials is the here studied spinel-structured cobalt ferrite $CoFe_2O_4$ which exhibits a theoretical capacity as large as 914 mA h g^{-1} if full conversion to Co and Fe is assumed, i.e., insertion of 8 Li^+/f.u. However, $CoFe_2O_4$ suffers from typical drawbacks of oxide conversion materials such as bad conductivity [4] and large volumetric changes upon the reaction with lithium [1,5]. This causes mechanical degradation of the materials including its electrical insulation and associated poor cycle life. The resulting capacity losses upon electrochemical cycling are the main reason that $CoFe_2O_4$ cannot be utilized as an electrode material in LIBs, yet. One approach to overcome the material's drawbacks has been the fabrication of nano-porous morphologies, thereby compensating for volumetric changes as well as improving the ionic conductivity [6,7]. The impact of porosity on the cycling stability has been demonstrated, e.g., by Fu et al. [8]. Highly improved reversible capacities have been reported for thin films [9], nanorods [10], and nanospheres [11], among others [12–14]. Another approach employs embedding of the ferrite material inside highly conductive carbon matrices in order to prevent $CoFe_2O_4$ from becoming electrically insulated. Successful attempts have been done by using $CoFe_2O_4$/C-fibers [15], coated graphene sheets [16], reduced graphene oxide composites [17] and coated carbon nanotubes [18,19]. For this work, a composite of $CoFe_2O_4$ and multi-walled carbon nanotubes (CNTs) is created by filling CNTs with iron and cobalt nitrite and subsequent conversion of the filling to $CoFe_2O_4$. Encapsulation of functional fillings into CNT for improving the stability is a known strategy to obtain improved materials properties. It is widely used and finds application in various fields such as electrocatalysis [20,21], magnetic data storage technologies [22,23], nanomedicine [24,25], and sensors for magnetic force microscopy [26]. Here, it is exploited to obtain a $CoFe_2O_4$ nanoparticle-based

* Corresponding author.
** Corresponding author. Kirchhoff Institute of Physics, Heidelberg University, INF 227, 69120, Heidelberg, Germany.
E-mail addresses: elisa.thauer@kip.uni-heidelberg.de (E. Thauer), klingeler@kip.uni-heidelberg.de (R. Klingeler).

https://doi.org/10.1016/j.jallcom.2020.155018
0925-8388/

material where the active nanomaterial is wrapped by the protective carbon-shells of CNT which form a conducting network [27–29]. The electrochemical performance of cobalt ferrite incorporated in CNTs ($CoFe_2O_4$@CNT) is investigated and compared to that of bare $CoFe_2O_4$ nanoparticles.

2. Experimental

2.1. Synthesis of filled CNTs

Multi-walled carbon nanotubes of the type PR-24-XT-HHT (Pyrograf products) have been used as template for filling them with cobalt ferrite. The filling procedure is an extension of a reported solution based filling approach for CNTs with $ZnFe_2O_4$ [30]. 1 M standard aqueous solutions of the following nitrates have been prepared: $Fe(NO_3)_3 \cdot 9H_2O$ (grade: ACS 99.0–100.2%) and $Co(NO_3)_2 \cdot 6H_2O$ (grade: ACS 98.0–102.0% metal basis) supplied by VWR Chemicals and Alfa Aesar GmbH & Co KG. The nitrate salts were used as provided and no further purifications have been performed. The nitrate solutions were combined in a stoichiometric ratio with respect to the metal ions (i.e., Fe:Co = 2:1), about 50 mg of CNTs were added, and the mixture was treated in an ultrasonication bath for 60 min at room temperature. The mixture was then vacuum-filtered and washed with about 20 ml washing agent of acetone and distilled water with a volumetric ratio of 1:1. Subsequently, the solid residue was dried for 24 h at a temperature of 108 °C and afterwards calcinated under argon flow atmosphere (100 sccm) at a temperature of 500 °C for 4 h to convert the nitrates into the corresponding cobalt ferrite according to the following equation:

$$Co(NO_3)_2(s) + 2Fe(NO_3)_3(s)\ CoFe_2O_4(s) + 8NO_2(g) + 2O_2(g)$$

Commercial $CoFe_2O_4$ nanopowder with a particle size of 30 nm have been obtained by Sigma Aldrich.

2.2. Characterization

The resulting $CoFe_2O_4$@CNT nanocomposite was investigated by scanning electron microscopy (SEM) with a Nova 200 NanoSEM (FEI Company, Hilsboro, Oregon, U.S.) operating at 15 kV, combined with an energy dispersive X-ray (EDX) analyzer (AMETEK, Berwyn, Pennsylvania, U.S.). The SEM sample was prepared by placing a tiny amount of powder sample on carbon tape. Crystal structure analyses were carried out by means of an X'Pert Pro MPD PW3040/60 X-ray diffractometer (XRD, PANalytical, Almelo, Niederlande) with Co Kα radiation ($\lambda = 1.79278$ Å) in reflection geometry at a scanning rate of 0.05° s^{-1} in the 2θ range of 10°–80°. Thermogravimetric analysis (TGA) was performed with an SDT-Q600 (TA instruments, Waters Corporation, Milford, Massachusetts, U.S.). In detail, approximately 5 mg of the material were heated to a temperature of 900 °C with a heating rate of 5 K min^{-1} followed by an isothermal dwelling for 15 min under air atmosphere with a flow rate of 100 ml min^{-1}. The magnetic field dependence of the magnetization at 5 K and 300 K in external magnetic fields up to ± 5T was measured by means of a superconducting quantum interference device (MPMS-XL5 SQUID) magnetometer by Quantum Design (San Diego CA, USA). Transmission electron microscopy (TEM) and high-resolution transmission electron microscopy (HRTEM) measurements were performed using a Tecnai F30 (FEI Company, Hilsboro, Oregon, U.S.) instrument operated at 300 kV. The TEM samples were prepared by adding a few drops of the sample suspension in acetone on a copper grid with a carbon coating on one side.

2.3. Electrochemical measurements

Electrochemical measurements were performed using Swagelok-type cells. Working electrodes were prepared from the active materials as follows [31]. The $CoFe_2O_4$@CNT composite was mixed with 10 wt% of polyvinylidene fluoride (PVDF) in *N*-methyl-2-pyrrolidinone (NMP) and stirred for 24 h before the resulting slurry was applied to copper net current collectors. The $CoFe_2O_4$ nanoparticles were mixed in a mortar with 5 wt% of PVDF and 10 wt % of carbon black in order to enhance electric conductivity, before adding NMP to fabricate the electrode slurry. The as-prepared electrodes were dried in a vacuum oven (80 °C, <10 mbar) over night, pressed at 10 MPa, and dried again. Subsequently, Swagelok-type cells were prepared in a glove box under dry argon with lithium counter electrodes pressed onto nickel plates. Two sheets of fiber glass separator were soaked with 200 µl of a 1 M $LiPF_6$ solution dissolved in a 1:1 mixture of ethylene carbonate and dimethyl carbonate acting as the electrolyte. Cyclic voltammetry (CV) at a scan rate of 0.1 mV s^{-1} and galvanostatic cycling (GCPL) at specific currents of 100 mA g^{-1}, both in the voltage range of 0.01–3.0 V vs. Li/Li^+, were carried out on a VMP3 potentiostat (BioLogic) at 25 °C.

3. Results and discussion

3.1. Morphology and structure

The morphology and geometry of the filling material and its location inside or outside the CNTs were examined by SEM and TEM, as illustrated by the images in Fig. 1. SEM overview images in secondary-electron (SE) mode (a) and back-scattered-electron (BSE) mode (b) for $CoFe_2O_4$@CNT show, that the filling material is distributed along the inner cavity of the hollow CNTs. Different morphologies of the filling particles (spherical, short rods, etc.) have been observed for the ferrites inside the CNTs. These observations also have also confirmed by TEM measurements as shown in Fig. 1(c–f). HRTEM confirms the crystallinity of the core material as highlighted by the appearance of the lattice fringes shown in Fig. 1 (f).

Elemental mapping reveals that Co and Fe are uniformly distributed within the particles/rods (Fig. S1). Line scans along and across the filling confirm the correlation between the Co and Fe concentration which is consistent with the oxide formation. The C and Co–Fe concentration profiles anti-correlate, indicating that the metal is located inside the tube cores. Quantitative analysis of the respective spectra reveals Fe and Co filling material with atomic percentages of 66(2) and 34(2) w%, respectively, thereby confirming the Fe/Co ratio of 2:1 (Table S1).

3.2. Structural characterization

The XRD pattern of the $CoFe_2O_4$@CNT nanocomposite presented in Fig. 2 confirms the presence of $CoFe_2O_4$. In addition to the characteristic peaks of pristine CNT, the pattern exhibits further reflections which agree with reference data for $CoFe_2O_4$ (cubic space group $Fd\bar{3}m$) from the Crystallography Open Database #1533163 [32]. Pronounced peak broadening indicates the presence of nanosized $CoFe_2O_4$ crystallites, whose grain size is estimated to be 20(5) nm by means of the Scherrer equation applied to the Bragg peak at 41.5°. Note, that other contributions to XRD peak broadening have been neglected for this estimate. TGA data of $CoFe_2O_4$@CNT (see the inset of Fig. 2) show a residual mass of 11(1) wt% after heating the compound to 900 °C in air. This mass content is ascribed to $CoFe_2O_4$ particles, which are the only crystalline constituent besides the CNTs, according to the XRD analysis.

The magnetization of $CoFe_2O_4$@CNT measured in external

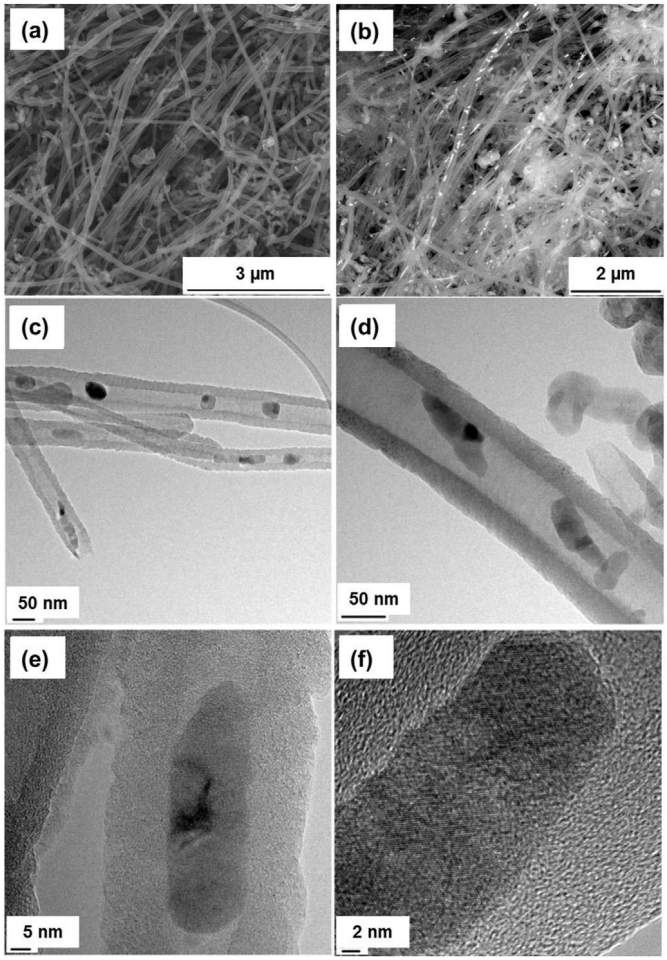

Fig. 1. Electron microscopy images of the $CoFe_2O_4$@CNT nanocomposite by means of (a) SE mode, (b) BSE mode, (c–d) TEM, and (e–f) HRTEM.

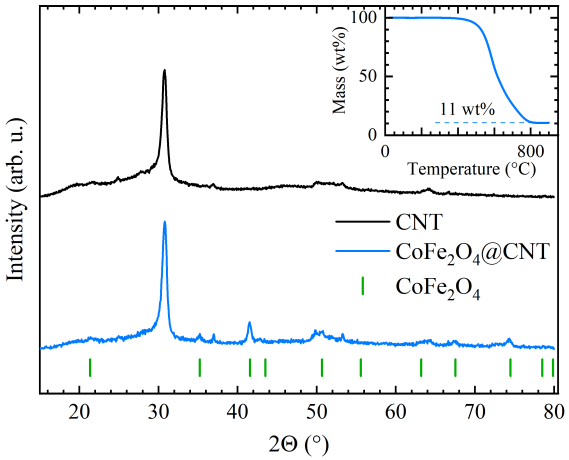

Fig. 2. Powder XRD patterns of $CoFe_2O_4$@CNT and of pristine CNT. Vertical ticks label Bragg positions of bulk $CoFe_2O_4$ (space group $Fd\bar{3}m$) [32]. Inset: TGA data of $CoFe_2O_4$@CNT.

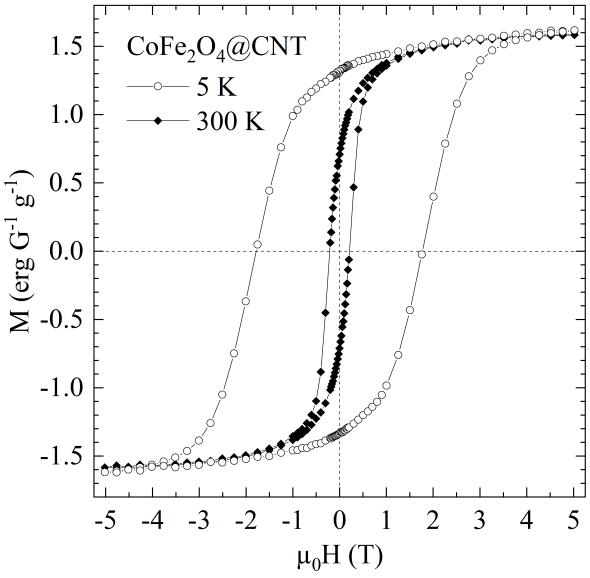

Fig. 3. Magnetization data of $CoFe_2O_4$@CNT, measured in external magnetic fields up to $\mu_0H = \pm 5$ T at constant temperatures of 5 K and 300 K, respectively.

magnetic fields up to $\mu_0H = \pm 5$ T is displayed in Fig. 3. Both at temperatures of T = 5 K and 300 K, hysteresis loops with a consistent average saturation magnetization of 1.6 erg G^{-1} g^{-1} are observed. This observation agrees with previous reports of the ferromagnetic behavior of $CoFe_2O_4$ nanoparticles [33,34], where the magnetic properties are found to be highly size-dependent [35–37]. Taking the mass fraction of the $CoFe_2O_4$ in the studied $CoFe_2O_4$@CNT nanocomposite of ~11 wt% into account, the detected saturation magnetization concurs with saturation values of $CoFe_2O_4$ nanoparticles reported in Ref. [37].

3.3. Electrochemical performance

The electrochemical performance of the $CoFe_2O_4$@CNT nanocomposite was studied in comparison to bare $CoFe_2O_4$ nanoparticles by means of CV and GCPL. Fig. 4 shows the 1st, 2nd and 10th cycles of CV measurements for both materials, initially starting with reductive scans at 0.1 mV s^{-1}. For the bare $CoFe_2O_4$ nanoparticles (Fig. 4(a)), in the initial half cycle reduction peaks occur at 1.5 V (R0), 1.1 V, and 0.55 V (R1/SEI) with a shoulder at 0.95 V, before ending in an active range at 0.01 V (R2). In all subsequent reductive half cycles the most pronounced reduction peak occurs at 0.85 V (R1*). While R0 completely vanishes after the first cycle, the intensities of all other reductive features gradually decrease until cycle 10. In all oxidative scans a broad oxidation double peak is observed between 1.5 V and 2.5 V with a maximum intensity around 1.65 V (O1), which also ceases until cycle 10.

The electrochemical lithium storage in $CoFe_2O_4$ of up to 8 Li^+/f.u. is supposed to follow a conversion mechanism according to Eq. (1), which can be preceded by initial intercalation of Li^+-ions into the original ferrite structure [38]. In the first CV cycle of the $CoFe_2O_4$ nanoparticles, the latter may be indicated by R0. The pronounced reduction peak R1 most likely signals both the conversion to Co and Fe, which leads to an irreversible decomposition of the ferrite starting compound [9,38], and the formation of a solid electrolyte interphase (SEI) [39]. The reductive activity R2 originates from the intercalation of Li^+-ions into the added carbon black [40]. After the reductive decomposition of $CoFe_2O_4$ in the initial half cycle, separate oxidation of Co and Fe to CoO and Fe_2O_3, respectively, at O1 is supposed to take place, followed by the corresponding conversion processes at R1* (Eq. (2)) [1,3,9,10,12,15,18].

$$CoFe_2O_4 + 8\ Li^+ + 8\ e^- \text{ -> } Co + 2\ Fe + 4\ Li_2O \quad (1)$$

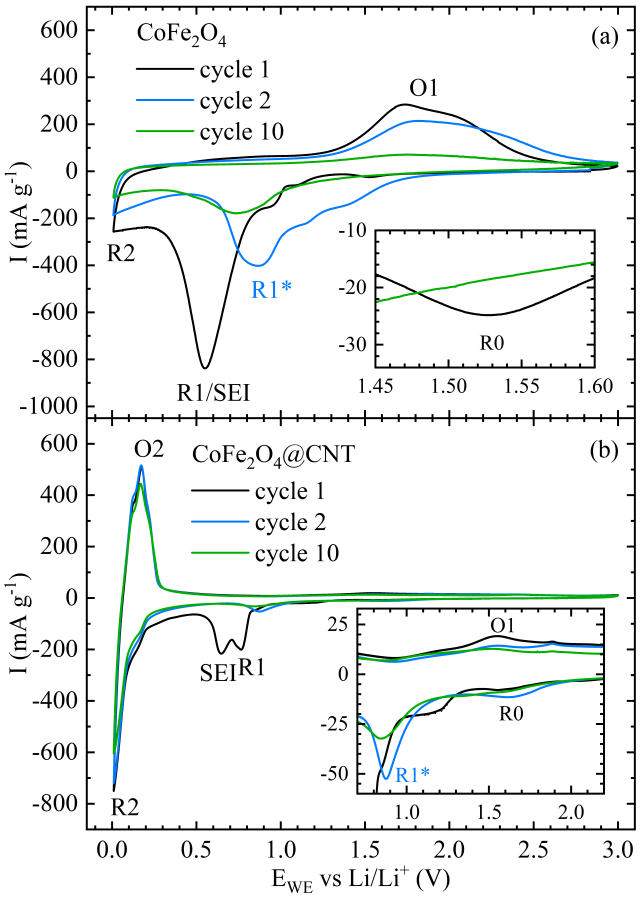

Fig. 4. Cyclic voltammograms of (a) $CoFe_2O_4$ nanoparticles, and (b) $CoFe_2O_4$@CNT obtained at a scan rate of 0.1 mV s^{-1}. R0 to R2 and O1 to O2 label reduction and oxidation features, respectively, as described in the text.

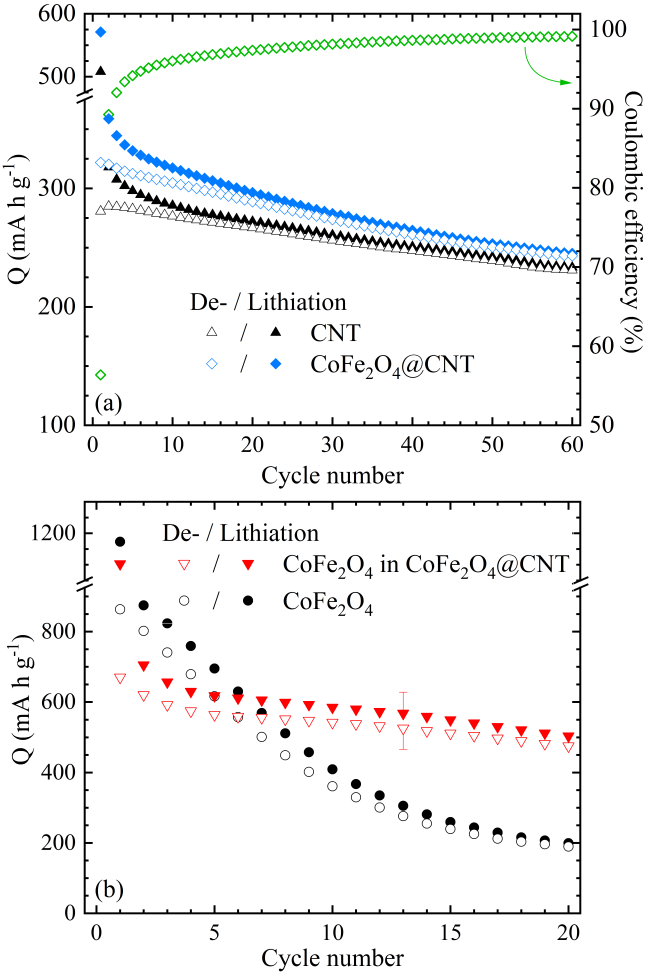

Fig. 5. (a) Dis-/charge capacities at 100 mA g^{-1} of CNTs and $CoFe_2O_4$@CNT as well as corresponding coulombic efficiencies. (b) Capacity contribution of only $CoFe_2O_4$ in $CoFe_2O_4$@CNT and capacities of bare $CoFe_2O_4$ nanoparticles.

$$Co + 2\ Fe + 4\ Li_2O <-> CoO + 2\ Fe_2O_3 + 8\ Li^+ + 8\ e^- \quad (2)$$

The $CoFe_2O_4$@CNT nanocomposite's CV in Fig. 4(b) can be understood considering both the electrochemical response of bare $CoFe_2O_4$ nanoparticles (see Fig. 4(a)) and of pristine CNTs [41–44]. In particular, the redox pair R2/O2 around 0.1 V indicates the intercalation/deintercalation of Li^+-ions between the graphitic layers of the CNTs [45,46]. It seems dominant due to the small mass content of $CoFe_2O_4$ of 11 wt% in the composite material. The reduction peaks attributed to $CoFe_2O_4$ are now observed at 1.6 V (R0), 1.2 V, and 0.7 V (SEI) with a distinct shoulder at 0.8 V (R1) in the initial half cycle, and subsequently at 1.6 V (R0) and 0.9 V (R1*). Reversible oxidation peaks again occur in the range between 1.5 V and 2.0 V reaching maximum intensity around 1.55 V (O1). Generally, compared with the bare $CoFe_2O_4$ nanoparticles, the corresponding reduction and oxidation peaks in $CoFe_2O_4$@CNT appear at slightly higher and lower potentials, respectively. This indicates smaller over potentials and thus improved energy efficiency in the compound. Furthermore, cycling stability is superior, yielding yet noticeable redox activity in the 10th cycle. Both improvements can be attributed to benefits of the CNTs in the $CoFe_2O_4$@CNT composite, i.e., to enhanced overall conductivity and better structural integrity.

Fig. 5(a) shows specific charge and discharge capacities of the $CoFe_2O_4$@CNT nanocomposite and of pristine CNTs, respectively, observed in GCPL measurements at 100 mA g^{-1}. Over the course of 60 dis-/charge cycles the $CoFe_2O_4$@CNT nanocomposite consistently retains higher capacities than the pristine CNTs. In both materials, a large initial discrepancy between charge and discharge capacity of 571/322 mA h g^{-1} and 508/281 mA h g^{-1}, respectively, is to a large extend attributed to SEI formation. However, irreversible capacity losses continuously occur during the first couple of cycles resulting in moderate coulombic efficiencies that in case of the $CoFe_2O_4$@CNT nanocomposite exceed 97% only after the 15th cycle. After 60 cycles 243 mA h g^{-1} can still be discharged from the nanocomposite which corresponds to an overall capacity retention of 76%. The specific contribution of the ferrite nanoparticles to the capacities of the $CoFe_2O_4$@CNT composite are evaluated by subtracting the measured capacities of pristine CNTs, weighted with the mass ratio of 89:11 (CNTs: $CoFe_2O_4$). The resulting capacities of the $CoFe_2O_4$ nanoparticles in $CoFe_2O_4$@CNT are depicted in Fig. 5(b) in comparison to those of bare $CoFe_2O_4$ nanoparticles. The initial charge capacities, 1173 mA h g^{-1} for the nanoparticles and 1103 mA h g^{-1} for the composite, are significantly higher than the theoretical expectation of 914 mA h g^{-1}. This can be attributed to SEI formation at the $CoFe_2O_4$/electrolyte interface. In both cases, there are significant capacity losses upon cycling, which are yet much more severe for the pure $CoFe_2O_4$ nanoparticles. After 20 cycles, the bare nanoparticles' discharge capacity has decreased to 190 mA h g^{-1}, corresponding to a loss of 78% of the initial discharge capacity. In the $CoFe_2O_4$@CNT electrode,

on the other hand, 475 mA h g^{-1}, i.e. 71% of the initial discharge capacity, are retained after 20 cycles, that corresponding to a loss of only 29%. This demonstrates that embedding nano sized $CoFe_2O_4$ in a conductive matrix of carbon by filling it into CNTs can partly compensate for the typical capacity fading associated with the conversion reactions upon electrochemical de-/lithiation known for ferrite materials.

4. Conclusions

$CoFe_2O_4$-filled multi-walled carbon nanotubes have been investigated by means of their lithium storage ability as an anode material for lithium ion batteries. The involved conversion mechanism known for nanosized $CoFe_2O_4$ was confirmed in cyclic voltammetry measurements. In comparison to bare $CoFe_2O_4$ nanoparticles, $CoFe_2O_4$@CNT nanocomposite shows smaller overpotentials and hence improved energy efficiency. We attribute this mainly to enhanced conductivity induced by the linked CNT network. Further, the ferrite's capacity retention over the first 20 dis-/charge cycles is improved from 22% in the pure nanoparticles to 71% in $CoFe_2O_4$@CNT. The data hence demonstrate that embedding nanoparticles inside the protective and conductive shells of CNTs opens a way to utilize high theoretical capacities of $CoFe_2O_4$ and other transition metal oxides for electrochemical energy storage.

Declaration of competing interest

The authors declare that they have no known competing financial interests or personal relationships that could have appeared to influence the work reported in this paper.

CRediT authorship contribution statement

Lucas Möller: Writing - original draft, Investigation, Visualization. **Elisa Thauer:** Writing - original draft, Writing - review & editing, Visualization. **Alexander Ottmann:** Conceptualization, Methodology. **Lukas Deeg:** Investigation. **Rasha Ghunaim:** Visualization. **Silke Hampel:** Conceptualization. **Rüdiger Klingeler:** Conceptualization, Writing - review & editing, Supervision.

Acknowledgements

The authors thank G. Kreutzer for performing the TEM and EDX studies. Financial support by the by Deutsche Forschungsgemeinschaft (DFG) via project KL1824/12 is gratefully acknowledged.

Appendix A. Supplementary data

Supplementary data to this article can be found online at https://doi.org/10.1016/j.jallcom.2020.155018.

References

[1] J. Cabana, L. Monconduit, D. Larcher, M.R. Palacín, Beyond intercalation-based Li-ion batteries: the state of the art and challenges of electrode materials reacting through conversion reactions, Adv. Energy Mater. 22 (2010) E170–E192.
[2] P. Poizot, S. Laruelle, S. Grugeon, L. Dupont, J.-M. Tarascon, S. Laruelle, J.-M. Tarascon, Searching for new anode materials for the Li-ion Searching for new anode materials for the Li-ion technology: time to deviate from the usual path, J. Power Sources 97–98 (2001) 235–239.
[3] P. Poizot, S. Laruelle, S. Grugeon, L. Dupont, J.M. Tarascon, Nano-sized transition-metal oxides as negative-electrode materials for lithium-ion batteries, Nature 407 (2000) 496–499.
[4] G.H. Jonker, Analysis of the semiconducting properties of cobalt ferrite, J. Phys. Chem. Solid. 9 (1959) 165–175.
[5] M. Fichtner, Konversionsmaterialien für die Energiespeicherung, Chem. Unserer Zeit 47 (2013) 230–238.
[6] P.G. Bruce, B. Scrosati, J.-M. Tarascon, Nanomaterials for rechargeable lithium batteries, Angew. Chem. Int. Ed. 47 (2008) 2930–2946.
[7] B. Scrosati, J. Garche, Lithium batteries: status, prospects and future, J. Power Sources 195 (2010) 2419–2430.
[8] X. Fu, D. Chen, M. Wang, Y. Yang, Q. Wu, J. Ma, X. Zhao, Synthesis of porous CoFe2O4 octahedral structures and studies on electrochemical Li storage behavior, Electrochim. Acta 116 (2014) 164–169.
[9] Y.-Q. Chu, Z.-W. Fu, Q.-Z. Qin, Cobalt ferrite thin films as anode material for lithium ion batteries, Electrochim. Acta 49 (2004) 4915–4921.
[10] N. Wang, H. Xu, L. Chen, X. Gu, J. Yang, Y. Qian, A general approach for MFe2O4 (M = Zn, Co, Ni) nanorods and their high performance as anode materials for lithium ion batteries, J. Power Sources 247 (2014) 163–169.
[11] S. Yoon, Facile microwave synthesis of CoFe2O4 spheres and their application as an anode for lithium-ion batteries, J. Appl. Electrochem. 44 (2014) 1069–1074.
[12] Y. Wang, D. Su, A. Ung, J.H. Ahn, G. Wang, Hollow CoFe2O4 nanospheres as a high capacity anode material for lithium ion batteries, Nanotechnology 23 (2012) 55402.
[13] D.H. Deng, H. Pang, J.M. Du, J.W. Deng, S.J. Li, J. Chen, J.S. Zhang, Fabrication of cobalt ferrite nanostructures and comparison of their electrochemical properties, Cryst. Res. Technol. 47 (2012) 1032–1038.
[14] Z.-J. Jiang, S. Cheng, H. Rong, Z. Jiang, J. Huang, General synthesis of MFe2O4/carbon (M = Zn, Mn, Co, Ni) spindles from mixed metal organic frameworks as high performance anodes for lithium ion batteries, J. Mater. Chem. A 5 (2017) 23641–23650.
[15] L. Wu, Q. Xiao, Z. Li, G. Lei, P. Zhang, L. Wang, CoFe2O4/C composite fibers as anode materials for lithium-ion batteries with stable and high electrochemical performance, Solid State Ionics 215 (2012) 24–28.
[16] L. Wang, L. Zhuo, C. Zhang, F. Zhao, Carbon dioxide-induced homogeneous deposition of nanometer-sized cobalt ferrite (CoFe2O4) on graphene as high-rate and cycle-stable anode materials for lithium-ion batteries, J. Power Sources 275 (2015) 650–659.
[17] P.R. Kumar, P. Kollu, C. Santhosh, K. Eswara Varaprasada Rao, D.K. Kim, A.N. Grace, Enhanced properties of porous CoFe2O4 –reduced graphene oxide composites with alginate binders for Li-ion battery applications, New J. Chem. 38 (2014) 3654–3661.
[18] L. Wang, L. Zhuo, H. Cheng, C. Zhang, F. Zhao, Porous carbon nanotubes decorated with nanosized cobalt ferrite as anode materials for high-performance lithium-ion batteries, J. Power Sources 283 (2015) 289–299.
[19] R. Jin, Q. Wang, Y. Cui, S. Zhang, MFe2O4 (M = Ni, Co) nanoparticles anchored on amorphous carbon coated multiwalled carbon nanotubes as anode materials for lithium-ion batteries, Carbon 123 (2017) 448–459.
[20] J. Wang, Z. Dong, J. Huang, J. Li, X. Jin, J. Niu, J. Sun, J. Jin, J. Ma, Filling carbon nanotubes with Ni–Fe alloys via methylbenzene-oriented constant current electrodeposition for hydrazine electrocatalysis, Appl. Surf. Sci. 270 (2013) 128–132.
[21] Y. Liu, H. Jiang, Y. Zhu, X. Yang, C. Li, Transition metals (Fe, Co, and Ni) encapsulated in nitrogen-doped carbon nanotubes as bi-functional catalysts for oxygen electrode reactions, J. Mater. Chem. A 4 (2016) 1694–1701.
[22] M.H. Xu, W. Zhong, X.S. Qi, C.T. Au, Y. Deng, Y.W. Du, Highly stable Fe–Ni alloy nanoparticles encapsulated in carbon nanotubes, J. Alloys Compd. 495 (2010) 200–204.
[23] R. Ghunaim, M. Scholz, C. Damm, B. Rellinghaus, R. Klingeler, B. Büchner, M. Mertig, S. Hampel, Single-crystalline FeCo nanoparticle-filled carbon nanotubes, Beilstein J. Nanotechnol. 9 (2018) 1024–1034.
[24] R. Klingeler, S. Hampel, B. Büchner, Carbon nanotube based biomedical agents for heating, temperature sensoring and drug delivery, Int. J. hyperther. 24 (2008) 496–505, the official journal of European Society for Hyperthermic Oncology, North American Hyperthermia Group.
[25] A. Vyalikh, A.U.B. Wolter, S. Hampel, D. Haase, M. Ritschel, A. Leonhardt, H.-J. Grafe, A. Taylor, K. Krämer, B. Büchner, R. Klingeler, A carbon-wrapped nanoscaled thermometer for temperature control in biological environments, Nanomedicine (London, England) 3 (2008) 321–327.
[26] A. Winkler, T. Mühl, S. Menzel, R. Kozhuharova-Koseva, S. Hampel, A. Leonhardt, B. Büchner, Magnetic force microscopy sensors using iron-filled carbon nanotubes, J. Appl. Phys. 99 (2006) 104905.
[27] Elisa Thauer, Alexander Ottmann, Philip Schneider, Lucas Möller, Lukas Deeg, Rouven Zeus, Florian Wilhelmi, Lucas Schlestein, Christoph Neef, Rasha Ghunaim, Markus Gellesch, Christian Nowka, Maik Scholz, Marcel Haft, Sabine Wurmehl, Karolina Wenelska, Ewa Mijowska, Aakanksha Kapoor, Ashna Bajpai, Silke Hampel, Rüdiger Klingeler, Filled carbon nanotubes as anode materials for Lithium-ion batteries, Molecules 25 (2020) 1064, https://doi.org/10.3390/molecules25051064.
[28] A. Ottmann, M. Scholz, M. Haft, E. Thauer, P. Schneider, M. Gellesch, C. Nowka, S. Wurmehl, S. Hampel, R. Klingeler, Electrochemical Magnetization Switching and Energy Storage in Manganese Oxide filled Carbon Nanotubes, Sci. Rep. 7 (2017), 13625, https://doi.org/10.1038/s41598-017-14014-7.
[29] Nan Yan, Xuhui Zhou, Yan Li, Fang Wang, Hao Zhong, Hui Wang, Qianwang Chen, Fe_2O_3 Nanoparticles Wrapped in Multi-walled Carbon Nanotubes With Enhanced Lithium Storage Capability, Sci. Rep. 3 (2013), 3392. https://doi.org/10.1038/srep03392.
[30] S. Al Khabouri, S. Al Harthi, T. Maekawa, Y. Nagaoka, M.E. Elzain, A. Al Hinai, A.D. Al-Rawas, A.M. Gismelseed, A.A. Yousif, Composition, electronic and

magnetic investigation of the encapsulated ZnFe2O4 nanoparticles in multi-wall carbon nanotubes containing Ni residuals, Nanoscale res.lett. 10 (2015) 262.
[31] A. Ottmann, G.S. Zakharova, B. Ehrstein, R. Klingeler, Electrochemical performance of single crystal belt-like NH4V3O8 as cathode material for lithium-ion batteries, Electrochim. Acta 174 (2015) 682–687.
[32] T.A.S. Ferreira, J.C. Waerenborgh, M.H.R.M. Mendonça, M.R. Nunes, F.M. Costa, Structural and morphological characterization of FeCo2O4 and CoFe2O4 spinels prepared by a coprecipitation method, Solid State Sci. 5 (2003) 383–392.
[33] S. Sun, H. Zeng, D.B. Robinson, S. Raoux, P.M. Rice, S.X. Wang, G. Li, Monodisperse MFe2O4 (M = Fe, Co, Mn) nanoparticles, J. Am. Chem. Soc. 126 (2004) 273–279.
[34] S. Ayyappan, S. Mahadevan, P. Chandramohan, M.P. Srinivasan, J. Philip, B. Raj, Influence of Co2+ ion concentration on the size, magnetic properties, and purity of CoFe2O4 spinel ferrite nanoparticles, J. Phys. Chem. C 114 (2010) 6334–6341.
[35] Sorensen Tang, Hadjipanayis Klabunde, Size-dependent Curie temperature in nanoscale MnFe2O4 particles, Phys. Rev. Lett. 67 (1991) 3602–3605.
[36] Q. Song, Z.J. Zhang, Shape control and associated magnetic properties of spinel cobalt ferrite nanocrystals, J. Am. Chem. Soc. 126 (2004) 6164–6168.
[37] M. Grigorova, H.J. Blythe, V. Blaskov, V. Rusanov, V. Petkov, V. Masheva, D. Nihtianova, L.M. Martinez, J.S. Muñoz, M. Mikhov, Magnetic properties and Mössbauer spectra of nanosized CoFe2O4 powders, J. Magn. Magn Mater. 183 (1998) 163–172.
[38] P. Lavela, G.F. Ortiz, J.L. Tirado, E. Zhecheva, R. Stoyanova, S. Ivanova, High-performance transition metal mixed oxides in conversion electrodes: a combined spectroscopic and electrochemical study, J. Phys. Chem. C 111 (2007) 14238–14246.
[39] P. Verma, P. Maire, P. Novák, A review of the features and analyses of the solid electrolyte interphase in Li-ion batteries, Electrochim. Acta 55 (2010) 6332–6341.
[40] R. Gnanamuthu, C.W. Lee, Electrochemical properties of Super P carbon black as an anode active material for lithium-ion batteries, Mater. Chem. Phys. 130 (2011) 831–834.
[41] B.J. Landi, M.J. Ganter, C.D. Cress, R.A. DiLeo, R.P. Raffaelle, Carbon nanotubes for lithium ion batteries, Energy Environ. Sci. 2 (2009) 638–654.
[42] de las Casas, W. Li Charles, A review of application of carbon nanotubes for lithium ion battery anode material, J. Power Sources 208 (2012) 74–85.
[43] A. Varzi, C. Täubert, M. Wohlfahrt-Mehrens, M. Kreis, W. Schütz, Study of multi-walled carbon nanotubes for lithium-ion battery electrodes, J. Power Sources 196 (2011) 3303–3309.
[44] A. Ottmann, M. Scholz, M. Haft, E. Thauer, P. Schneider, M. Gellesch, C. Nowka, S. Wurmehl, S. Hampel, R. Klingeler, Electrochemical magnetization switching and energy storage in manganese oxide filled carbon nanotubes, Sci. Rep. 7 (2017) 13625.
[45] S.Y. Chew, S.H. Ng, J. Wang, P. Novák, F. Krumeich, S.L. Chou, J. Chen, H.k. Liu, Flexible free-standing carbon nanotube films for model lithium-ion batteries, Carbon 47 (2009) 2976–2983.
[46] Z. Xiong, Y. Yun, H.-J. Jin, Applications of carbon nanotubes for lithium ion battery anodes, Materials 6 (2013) 1138–1158.

4.2 Mn_3O_4 encapsulated in hollow carbon spheres coated by graphene layer for enhanced magnetization and lithium-ion batteries performance

Autoren:

E. Thauer, X. Shi, S. Zhang, X. Chen, L. Deeg, R. Klingeler, K. Wenelska, E. Mijowska

veröffentlicht in Energy 217, 2021, 119399

abgedruckt mit freundlicher Genehmigung des Elsevier Verlags

E. Thauer ist die Erst- und Korrespondenzautorin dieses Artikels. E. Thauer führte die Charakterisierung der Materialien mittels XRD und Squid-Magnetometrie sowie die Messungen und Analyse der elektochemischen Eigenschaften gemeinsam mit dem Masterstudent L.F. Deeg unter ihrer Anleitung durch, verfasste die zugehörigen Teile im Manuskript und erstellte die Abb. 1 und Abb. 6 - 7. E. Thauer übernahm die Gesamtkorrektur des Manuskripts und war an der Finalisierung beteiligt. Die Korrespondenz mit den Gutachtern sowie die Überarbeitung des Manuskripts wurde von E. Thauer zusammen mit R. Klingeler und E. Mijowska übernommen.

X. Shi verfasste das Manuskript mit Ausnahme der Teile zur Charakterisierung mittels XRD und Squid-Magnetometrie sowie zu den elektrochemischen Untersuchungen und erstellte die Abb. 2 - 4. X. Shi führte die Synthese der Materialien (Scheme 1) und die TGA-Messungen unter der Betreuung von X. Chen durch. A. Zhang führte die Raman-Spektroskopie sowie die BET-Messungen durch und K. Wenelska die REM- und TEM-Untersuchungen. R. Klingeler und E. Mijowska betreuten das Projekt, standen beratend zur Seite und waren an der Finalisierung des Manuskripts beteiligt. Alle Autoren haben das Manuskript korrekturgelesen.

Energy 217 (2021) 119399

Contents lists available at ScienceDirect

Energy

journal homepage: www.elsevier.com/locate/energy

Mn_3O_4 encapsulated in hollow carbon spheres coated by graphene layer for enhanced magnetization and lithium-ion batteries performance

Elisa Thauer [a, *], Xiaoze Shi [b], Shuai Zhang [b], Xuecheng Chen [b, **], Lukas Deeg [a], Rüdiger Klingeler [a, c], Karolina Wenelska [b], Ewa Mijowska [b]

[a] Kirchhoff Institute for Physics, Heidelberg University, INF 227, D-69120, Heidelberg, Germany
[b] Nanomaterials Physicochemistry Department, Faculty of Chemical Technology and Engineering, West Pomeranian University of Technology, Szczecin, Piastów Ave. 42, 71-065, Szczecin, Poland
[c] Centre of Advanced Materials, Heidelberg University, INF 225, D-69120, Heidelberg, Germany

ARTICLE INFO

Article history:
Received 26 September 2020
Received in revised form
15 November 2020
Accepted 20 November 2020
Available online 23 November 2020

Keywords:
Hollow carbon spheres
Manganese oxide
Encapsulating method
Anode material
Lithium-ion batteries

ABSTRACT

We report a facile method to prepare graphene coated core-shell Mn_3O_4 nanoparticles encapsulated in hollow carbon sphere (HCS) (G–HCS–Mn_3O_4). HCSs were firstly prepared at high temperature based on a core-shell template, leading to good electrical conductivity of 21.6 S m^{-1}. The porous shells of HCSs provide passage for the manganese precursors and big cavities to store the inorganic particles. Furthermore, the Mn_3O_4 filling is proven by magnetization measurements showing characteristic ferrimagnetic ordering at 41 K. Electrochemical studies show that the Mn_3O_4 nanoparticles encapsulated in HCS are electrochemical active and there is full access to the theoretical capacity of Mn_3O_4. When used as anode material, G–HCS–Mn_3O_4 impresses by superior properties compared to pristine HCS. It can achieve a high specific charge capacity of 557 mAh g^{-1} at the current density of 100 mA g^{-1} and even 374 at 500 mA g^{-1}. The approach of exploiting HCS-based nanocomposites can be expanded to encapsulate a variety of inorganic materials with controllable size and amount, providing new choices for electrode materials and other potential applications.

1. Introduction

Lithium-ion batteries (LIBs), as the secondary batteries, have drawn tremendous attention for their great potential in portable electronics and hybrid vehicles due to the properties such as high energy density, good cycle performance and large power density [1–4]. However, the capacity of commercial graphite, an intercalation material, is limited to its theoretical capacity (372 mAh g^{-1}), which cannot meet the growing requirements of energy storage with the rapid development nowadays. Therefore, to enhance the performance of LIBs, advanced electrode materials with large capacity and energy density have been intensively investigated [5,6]. Transition metal oxides (TMOs) are good candidates as anode materials due to their high theoretical capacity, environmental benignity and abundant resource [7–19]. Among them, manganese oxide (Mn_3O_4) is widely explored for their high theoretical capacity (937 mAh g^{-1}), low lithiation potential, enhanced energy storage and low cost [20,21]. Moreover, Mn_3O_4 has been reported to show faster lithium ion insertion/desertion kinetics than other stable manganese oxides [22]. However, pure Mn_3O_4 suffers from poor electrical conductivity (10^{-7}–10^{-8} S cm^{-1}) and large volume changes during lithiation/delithiation (~75.4% [23,24]) resulting in a rapid capacity fading and short cycling life.

A potential solution to tackle these problems is to design an effective hybrid nanostructure of nano-Mn_3O_4 and carbonaceous materials. In such materials, nanosized Mn_3O_4 are incorporated into a carbon matrix combining advantageous of nanoscaling, i.e., short diffusion pathways for Li-ions and enhanced ability to endure large volume changes, with an electrically conducting matrix providing the integrity of a 3D material [25–32].

However, in most previous studies Mn_3O_4 particles are not completely surrounded by carbon but rather have partial contact,

* Corresponding author.
** Corresponding author.
E-mail addresses: elisa.thauer@kip.uni-heidelberg.de (E. Thauer), xuecheng.chen@zut.edu.pl (X. Chen).

https://doi.org/10.1016/j.energy.2020.119399
0360-5442/

which does not prevent the direct contact of Mn_3O_4 with electrolyte as well as the negative effects of a large volume expansion. It can be assumed that it is more favorable to encapsulate the Mn_3O_4 nanoparticles by carbon with void space between them allowing a certain volume expansion [33,34]. Herein, we choose HCSs as the carbon matrix for encapsulation of Mn_3O_4 nanoparticles. HCSs have drawn more and more attention in various applications due to their large specific surface area, low density, good porosity, high stability, and good surface permeability [35]. Since silica spheres with defined diameters as well as core-shell structures have been successfully fabricated [36,37], HCSs prepared from such templates can achieve controllable morphology, shell thickness and cavity diameter [38,39]. Different from the mostly reported methods, in which the nanoparticles are firstly synthesized before the deposition of carbon layers follows, we report a method where firstly HCS are prepared and then Mn_3O_4 nanoparticles are encapsulated. In traditional methods, in order to avoid the reduction of metal oxide by carbon under high temperature, low temperature is chosen to synthesize the carbon layer, leading to a relatively lower conductivity [40]. In this work, we use a core-shell template (SiO_2@m-SiO_2_CTAB) to fabricate HCSs under high temperature. The as-prepared HCSs with large surface area and good electrical conductivity have porous shells which provide passage for the manganese precursors and big cavities to store the inorganic precursors. The HCSs with manganese precursors were covered by a graphene layer to enhance the mechanical properties of the whole hybrid structure. After annealing, there are void spaces between Mn_3O_4 and carbon, allowing large volume expansion during the lithiation/delithiation process. The G—HCS—Mn_3O_4 nanocomposite exhibit enhanced electrochemical performance in LIBs as proven by the cyclic behavior upon electrochemical measurements. Furthermore, the manganese filling of the HCS is verified based on a magnetic phase transition associated to Mn_3O_4 due to SQUID-magnetometer measurements.

2. Experimental section

2.1. Synthesis of hollow carbon spheres (HCS)

HCSs were prepared via a chemical vapor deposition (CVD) method using a hard core-shell template (SiO_2@m-SiO_2_CTAB) according to our previous report [41]. It consists of synthesis of templates, deposition of carbon and removal of the templates. Firstly, silica spheres was synthesized by stirring the mixture solution of tetraethyl orthosilicate (TEOS) (1.5 mL), concentrated ammonia (28 wt%, 2.5 mL) and ethanol (50 mL) for 24 h. Secondly, the sacrificial core-shell SiO_2@m-SiO_2-CTAB was prepared by adding SiO_2 (100 mg) to the water/ethanol/ammonia (30/13/0.45 mL) solution with adding the surfactant cetyltrimethylammonium bromide (CTAB, 170 mg) and silica precursor TEOS (0.3 mL) every 6 h for twice. At last, the core-shell SiO_2@m-SiO_2-CTAB was placed in a tube furnace and a CVD process using C_2H_4 as the carbon source was undergoing for 3 h at 800 °C. HCS were obtained by etching the silica with HF.

2.2. Preparation of HCS-Mn_3O_4 and G—HCS—Mn_3O_4 nanocomposite

5 mL of the saturated $KMnO_4$ ethanol solution was added to 100 mg HCS at 80 °C dropwise. The mixture was washed, filtered, and then dried at 105 °C for 10 h. Graphene oxide (GO) was prepared via a modified Hummer's method according to our previous report [42]. 100 mg as-prepared composites were dispersed to 10 mL GO solution (0.3 mg/mL) and stirred for 4 h. The above solution was washing by centrifugation to remove the excess GO. The samples were heated to 300 °C for 2 h under 100 sccm Ar flow to obtain G—HCS—Mn_3O_4. HCS-Mn_3O_4 was prepared by heating the composites without GO coating to 300 °C for 2 h under 100 sccm Ar flow.

2.3. Characterization

Transmission electron microscopy (TEM) and high-resolution TEM (HRTEM) were performed on a Tecnai F30 transmission electron microscope (FEI Corporation, USA) at an acceleration voltage of 200 kV. The elemental mappings were performed on a scanning transmission electron microscope (STEM) unit with high-angle annular dark-field (HAADF) detector (FEI, Tecnai F30) operating at an acceleration voltage of 200 kV. Scanning electron microscopy (SEM, Hitachi SU8020) was carried out to measure the structural properties. X-ray diffraction (XRD) was carried out with a Bruker AXS D8 Advance Eco using Cu K_α radiation. The thermogravimetric analysis (TGA) was conducted on the DTA-Q600 SDT TA at a heating

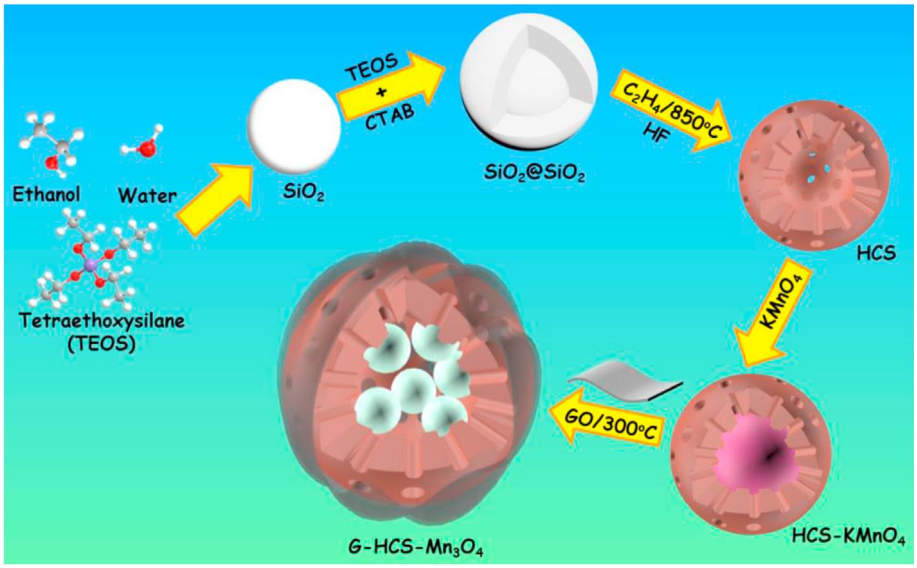

Scheme 1. Schematic illustration of preparation of graphene coated core-shell Mn_3O_4 nanoparticles confined in HCS.

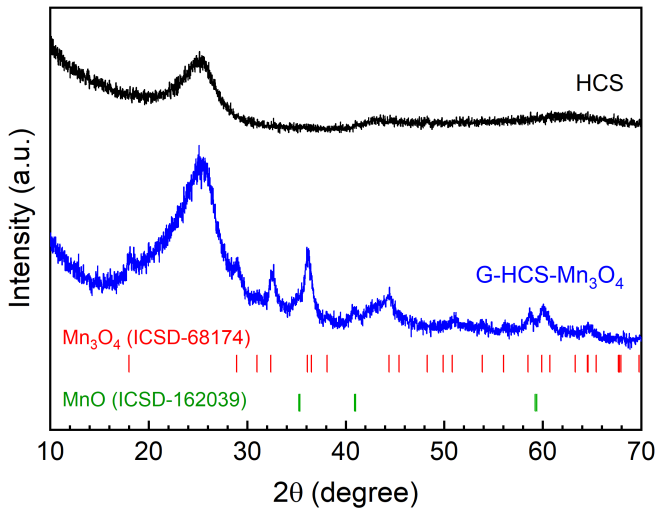

Fig. 1. XRD patterns of HCS and G–HCS–Mn_3O_4. The bars mark the reference Bragg positions of Mn_3O_4 [43] and MnO [44].

rate of 10 °C min^{-1} from room temperature to 900 °C under flowing air. The N_2 adsorption/desorption isotherms were obtained at liquid nitrogen temperature (77 K) using a Micromeritics ASAP 2010 M instrument. To examine the carbon content of the composite elemental analysis was performed using a Vario MICRO Cubes (Elementar). The Brunauer-Emmett-Teller (BET) and density functional theory (DFT) methods were adopted to calculate the specific surface area and pore size distribution. Raman spectra were collected with a Renishaw micro Raman spectrometer ($\lambda = 785$ nm). To further investigate incorporated Mn_3O_4, magnetic measurements were performed on G–HCS–Mn_3O_4 powder samples using a MPMS-XL5 SQUID magnetometer (Quantum Design). The magnetization was measured by varying the temperature between 2 and 300 K applying zero-field-cooled (ZFC) and field-cooled (FC) procedures at B = 1 T. In addition, hysteresis loops, i.e., magnetization vs. external magnetic field, were obtained at 2 K and 300 K in magnetic fields up to ±5 T.

2.4. Electrochemical measurements

The working electrodes were prepared by mixing the active material with carbon black (C-NERGY™ SUPER C65, Timcal) and polyvinylidene difluoride (PVDF, Solvay Plastics) at a mass ratio of 8:1:1 in 1-Methyl-2-pyrrolidone (NMP, Sigma Aldrich) by magnetic stirring for at least 12 h. Afterwards most of the NMP was evaporated in a vacuum oven at 65 °C to obtain a spreadable slurry, which was applied on Cu meshes. The as-prepared working electrodes with a mass loading of about 2 mg cm^{-2} were dried at 65 °C in a vacuum oven, mechanically pressed at 10 MPa and dried again. The Swagelok-type cells [14] were assembled in an Ar-filled glove box ($O_2/H_2O < 1$ ppm) using a lithium foil (Sigma Aldrich) pressed on a nickel plate as the counter electrode and two layers of glass microfibre separator (Whatman GF/D) soaked with 200 µl of a1 M solution of $LiPF_6$ in ethylene carbonate (EC)/dimethyl carbonate (DMC) (1:1 by volume) (LP30, Merck). The electrochemical properties were investigated by means of galvanostatic cycling with potential limitation (GCPL) and cyclic voltammetry in the voltage range 0.01–3 V, that were performed on a VMP3 potentiostat (BioLogic) at 25 °C. The calculation of the specific capacity is based on the total mass weight of G–HCS–Mn_3O_4 composite.

3. Results and discussion

The preparation of G–HCS–Mn_3O_4 nanocomposite is illustrated in Scheme 1. The solid SiO_2 nanospheres were prepared by a

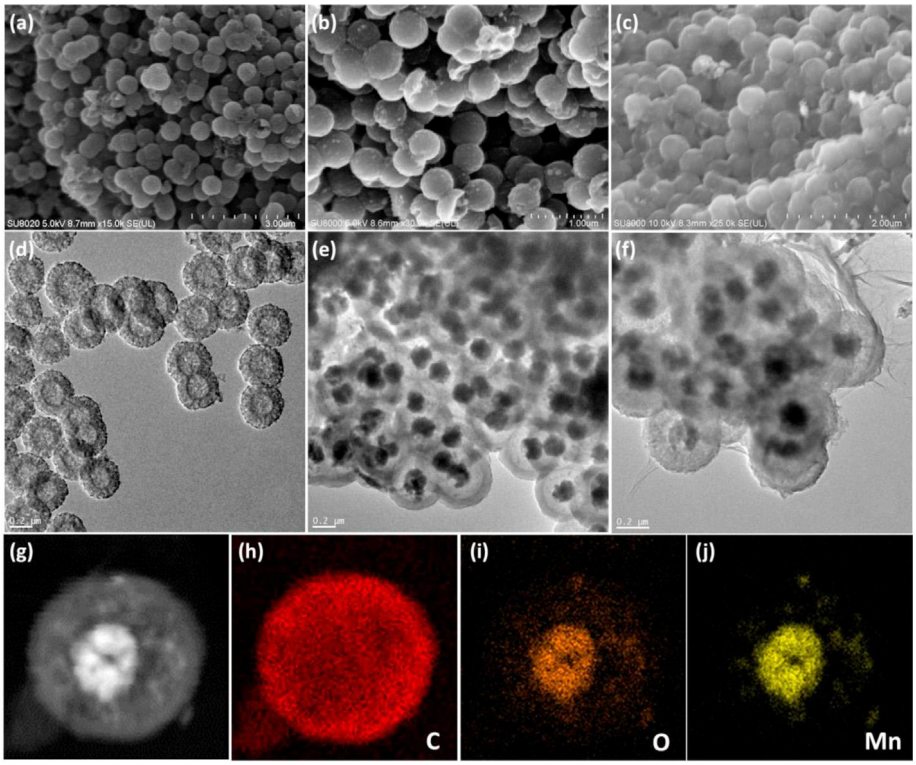

Fig. 2. SEM (a–c) and TEM (d–f) images of HCS (a,d), HCS-Mn_3O_4 (b,e) and G–HCS–Mn_3O_4 (c,f). STEM image (g) and C (h), O (i), and Mn (j) elemental mapping of G–HCS–Mn_3O_4.

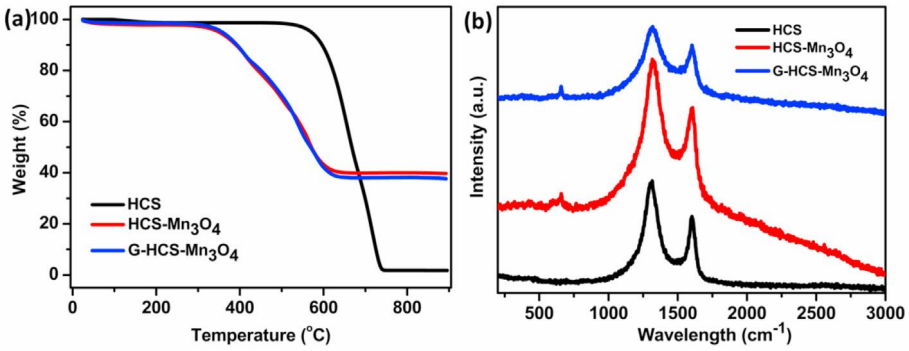

Fig. 3. TGA curves (a) and Raman spectra (b) of HCS, HCS-Mn_3O_4 and G—HCS—Mn_3O_4.

modified Stöber sol-gel process [36]. Then the core-shell SiO_2@m-SiO_2-CTAB was fabricated based on the solid silica core by coating a mesoporous SiO_2 (m-SiO_2) shell with the surfactant CTAB. The m-SiO_2 shells allow carbon deposition in the pores and cylindrical channels formed after the decomposition of CTAB under high temperature, while the solid silica core cannot allow the deposition of carbon into the core structure, forming a core-shell SiO_2@m-SiO_2-C. Since the carbon is formed only in the shells, HCSs can be obtained after removal of SiO_2 and m-SiO_2 in the shells. The porous shells of HCS can provide passage for the diffusion of small molecules. $KMnO_4$ dissolved in ethanol was added to HCSs by incipient wetness. The salts can diffuse into the cavity of HCSs via the porous shells. Finally, the impregnated HCSs were covered by graphene layers and annealed under 300 °C to convert the salt precursors to Mn_3O_4 nanoparticles. In most reported methods, nanoparticles are firstly synthesized followed by the formation of carbon layers. Here, HCS were prepared at high temperature, leading to a high graphitization as shown in the XRD pattern (Fig. 1) and good electrical conductivity (21.6 S m^{-1}). The XRD pattern of G—HCS—Mn_3O_4 confirms the existence of tetragonal Mn_3O_4 (ICSD-68174 [43]) and of some MnO (ICSD-1514120 [44]). The rough estimate of the average size of the Mn_3O_4 crystallites by Scherrer analysis provides grain sizes of about 20(10) nm. The higher intensity of the diffraction peak at 2θ of 26.57° can be attributed to the graphene.

The morphologies of HCS, HCS-Mn_3O_4 and G—HCS—Mn_3O_4 were examined by SEM (Fig. 2a—c) and TEM (Fig. 2d and e). SEM images indicated the maintaining of the spherical structure for all the samples. A small amount of nanoparticles can be observed in Fig. 2b and c, suggesting the existence of Mn_3O_4. Different from the rough surface of HCS and HCS-Mn_3O_4, the surface of G—HCS—Mn_3O_4 becomes smooth after coating with graphene. TEM image of HCS (Fig. 2d) shows a big contrast between the pale centers and dark edges with regular cylindrical channels indicating that HCS has a hollow cavity and mesoporous shell. As a control sample, HCS-Mn_3O_4 has a solid core of aggregated Mn_3O_4 nanoparticles in the center cavity of HCS (Fig. 2e). Thin graphene layers can be easily found in the G—HCS—Mn_3O_4 composites (Fig. 2f). Due to the shrinkage of metal oxide after annealing, void space can be observed between Mn_3O_4 nanoparticles and the shells of the HCS, providing space for volume expansion during lithiation. Energy-dispersive X-ray spectroscopy (EDS) was further conducted to evaluate the elemental distribution. Fig. 2g—j reveals that the Mn and O are mostly present in the cavity of HCS.

TGA is applied to measure the concentration of the carbon and metal oxide in the composites. The samples were heated in air to 900 °C so that carbon and Mn_3O_4 will be oxidized to CO_2 and Mn_2O_3, leaving Mn_2O_3 in the residual. The small variant in the blue and red curves from 400 to 500 °C derived from the synergistic effect of weight loss caused by combustion of carbon and weight gain resulting from oxidation of Mn_3O_4. HCS shows negligible remaining weight, suggesting a pure carbon composition. About 39.7 wt% of the sample weight was left in HCS-Mn_3O_4 representing the mass concentration of Mn_3O_4 nanoparticles. Graphene contributes a small increase in the weight loss for sample G—HCS—Mn_3O_4, what results in 37.6 wt% of the Mn_3O_4 concentration in the final product (Fig. 3a). The elemental analysis provides a carbon content of 56.3(5) wt % for the composite G—HCS—Mn_3O_4. As shown in the Raman spectra (Fig. 3b), for pristine HCS, two peaks at 1307 cm^{-1} (D band) and 1607 cm^{-1} (G band) are observed. A new peak at about 655 cm^{-1} attributed to the stretching vibration of Mn—O appears in both HCS-Mn_3O_4 and G—HCS—Mn_3O_4, indicating the presence of Mn_3O_4. In addition, the intensity ratios I_D/I_G for HCS, HCS-Mn_3O_4 and G—HCS—Mn_3O_4 were 1.37, 1.22 and 1.07, respectively, suggesting the decrease in defects

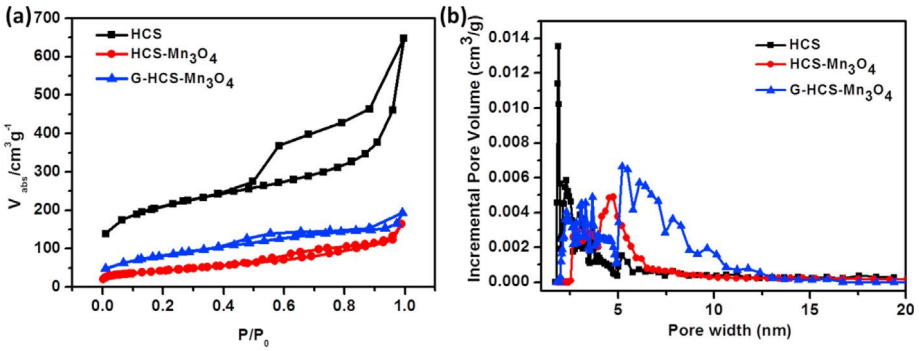

Fig. 4. (a) Nitrogen adsorption/desorption isotherms and (b) pore size distributions of HCS, HCS-Mn_3O_4 and G—HCS—Mn_3O_4.

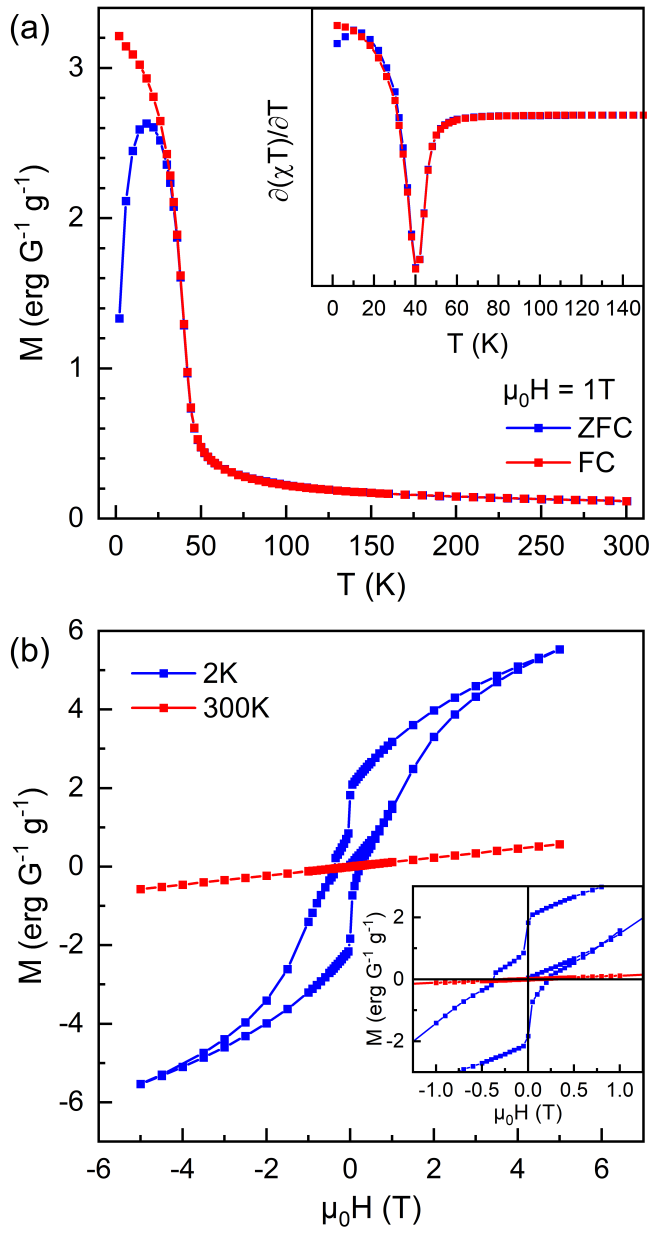

Fig. 5. Magnetization of G–HCS–Mn_3O_4 (a) vs. temperature at B = 1 T (inset: Fisher's specific heat ∂(χT)/∂T) and (b) vs. external magnetic field, at T = 2 K and 300 K.

and disorder of carbon in the composite samples.

The porous structure of G–HCS–Mn_3O_4 composite was further investigated by nitrogen adsorption/desorption isotherms. The isotherms exhibit typical type-IV behavior [45]. In the relative pressure (P/P_0) range from 0.4 to 1.0, a significant hysteresis loop appears in all isotherms, indicating the existence of mesopores (Fig. 4a). The BET surface area of HCS, HCS-Mn_3O_4 and G–HCS–Mn_3O_4 is calculated as 749, 174 and 278 $m^2\ g^{-1}$, respectively. The larger BET surface area of G–HCS–Mn_3O_4 with respect to HCS-Mn_3O_4 is due to the presence of graphene. The pore size distribution based on the adsorption data is shown in Fig. 4b. A mesopores distribution from 2 to 6 nm is attributed to the porous shells of HCS, while a wider mesopores distribution from 5 to 10 nm for G–HCS–Mn_3O_4 may be related to the addition of graphene. The large specific surface area and abundant porosity can facilitate the

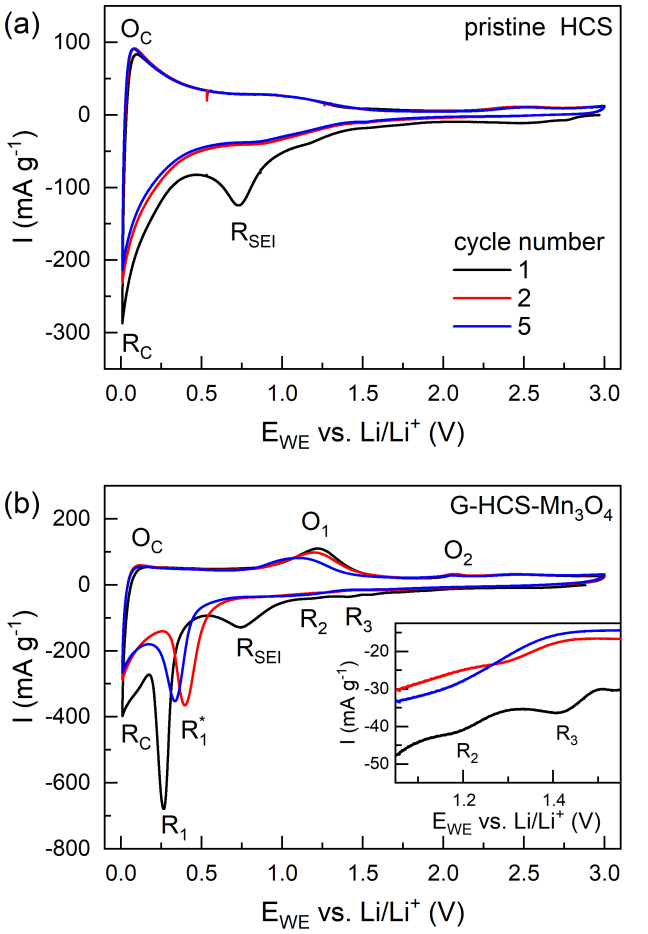

Fig. 6. Cyclic voltammogram of (a) pristine HCS and (b) G–HCS–Mn_3O_4 at 0.05 mV s^{-1}. R_i and O_i label various redox features associated with SEI formation, carbon (C), and Mn_3O_4 (i = 1–3) (see the text).

electrolyte accessibility and diffusion during the dis-/charging process.

Furthermore, temperature and magnetic field dependent magnetization studies were performed on G–HCS–Mn_3O_4 to investigate the encapsulated oxide. The magnetic response of carbon can be neglected as it is very weakly diamagnetic. Fig. 5a shows the evolution of a finite ferromagnetic moment at low temperatures. The corresponding derivative ∂(χT)/∂T (Fisher's specific heat) shows a clear peak which is associated with evolution of ferrimagnetic ordering in Mn_3O_4 [46,47]. We note the absence of further anomalies up to 300 K. In particular, there is no anomaly at around 130 K (and 92 K) which would indicate the presence of significant amounts of MnO (or MnO_2) [48]. The λ-shaped magnetic specific heat anomaly implies a continuous phase transition and indicates the magnetic ordering temperature of $T_C = 41.0(5)$ K.[1] This value is slightly smaller than the bulk value which is explained by the nanosized nature of the oxide incorporate and would agree to particles of less than 15 nm in diameter [46,47]. The paramagnetic (or antiferromagnetic) nature of magnetism at 300 K is demonstrated by a linear field dependence of M (Fig. 5b). The ferrimagnetic phase is signaled by a pronounced hysteresis in M vs B, at

[1] Note the finite external field of B = 1 T.

T = 2 K. T, which features a remanent magnetization (M_r) of 2.05(5) ergG^{-1}g^{-1} while M(5 T, 2 K) = 5.56(5) ergG^{-1}g^{-1}. Considering the filling rate, this implies M_r ~5.5 ergG^{-1}g$^{-1}_{Mn3O4}$ which is much smaller than the bulk value of 38 ergG^{-1}g$^{-1}_{Mn3O4}$. And again, agrees to the nanoscale nature of encapsulate. Notably, there is a sharp drop around zero field which has been also observed in the literature [49]. This feature might be attributed to differently sized Mn_3O_4 particles with diameters both above and below the superparamagnetic limit causing variation of magnetic anisotropy and hence superposition of a ferrimagnetic and superparamagnetic response. In addition, the hysteresis loop is not fully centered, but the coercive fields differ as −0.37 T and 0.23 T. This indicates an exchange bias effect, which suggests the presence of an antiferromagnetic phase such as MnO, which presence is also implied by the XRD results in Fig. 1.

The electrochemical properties of the G—HCS—Mn_3O_4 composite are investigated by cyclic voltammetry (CV) and galvanostatic cycling (GCPL). In order to assess the effects of the carbon matrix, respective measurements were performed also for pristine HCS under the same conditions. Fig. 6a and b shows the first, second and fifth cycle of the cyclic voltammograms of HCS and G—HCS—Mn_3O_4 at a scan rate of 0.05 mVs^{-1}. All peaks occurring in the CV curves of pristine HCS are also observed for the composite. The irreversible reduction peak R_{SEI} at 0.7 V can be mainly assigned to the formation of the solid electrolyte interface (SEI) [50] and the redox peak pair R_C/O_C at the lower measurement limit 0.01 V to lithiation and delithiation of carbon. All remaining peaks in Fig. 6b can be attributed to incorporated Mn_3O_4 which is known to perform the following electrochemical reaction processes, among which only the last step is fully reversible [51,52]:

$$Mn_3O_4 + Li^+ + e^- \rightarrow LiMn_3O_4 \quad (1)$$

$$LiMn_3O_4 + Li^+ + e^- \rightarrow 3MnO + Li_2O \quad (2)$$

$$MnO + 2Li^+ + 2e^- \leftrightarrow Mn + Li_2O \quad (3)$$

In the initial cathodic scan, the reduction process R_3 about 1.5 V indicates the intercalation of Li^+ into Mn_3O_4 (A) and R_2, which partly overlaps with the SEI formation R_{SEI}, the reduction to MnO (B). The peak pair R_1/O_1 at 0.3 V/1.2 V can be assigned to the conversion of MnO to metallic Mn (C) and the belonging back reaction. The weak oxidation peak O_2 at 2.1 V may be attributed to minor back formation to Mn_3O_4 [28,53]. In the subsequent cycles, R_1 is shifted to 0.4 V (R_1*) which reflects structural changes caused by the conversion reaction (C) [54].

Fig. 7a shows the dis-/charge capacities of pristine HCS and G—HCS—Mn_3O_4 upon galvanostatic cycling at 100 mA g^{-1}. The large differences of the initial dis-/charge capacities of 697/399 mAh g^{-1} (HCS) and 972/557 mAh g^{-1} (G—HCS—Mn_3O_4) are explained by SEI formation. As seen in the potential profiles (Fig. 7b), for pristine HCS the formation of the SEI contributes more than 200 mAh g^{-1} to the discharge capacity. In case of the composite, in addition, the mainly irreversible reduction processes of Mn_3O_4 to MnO (Eq. (2)

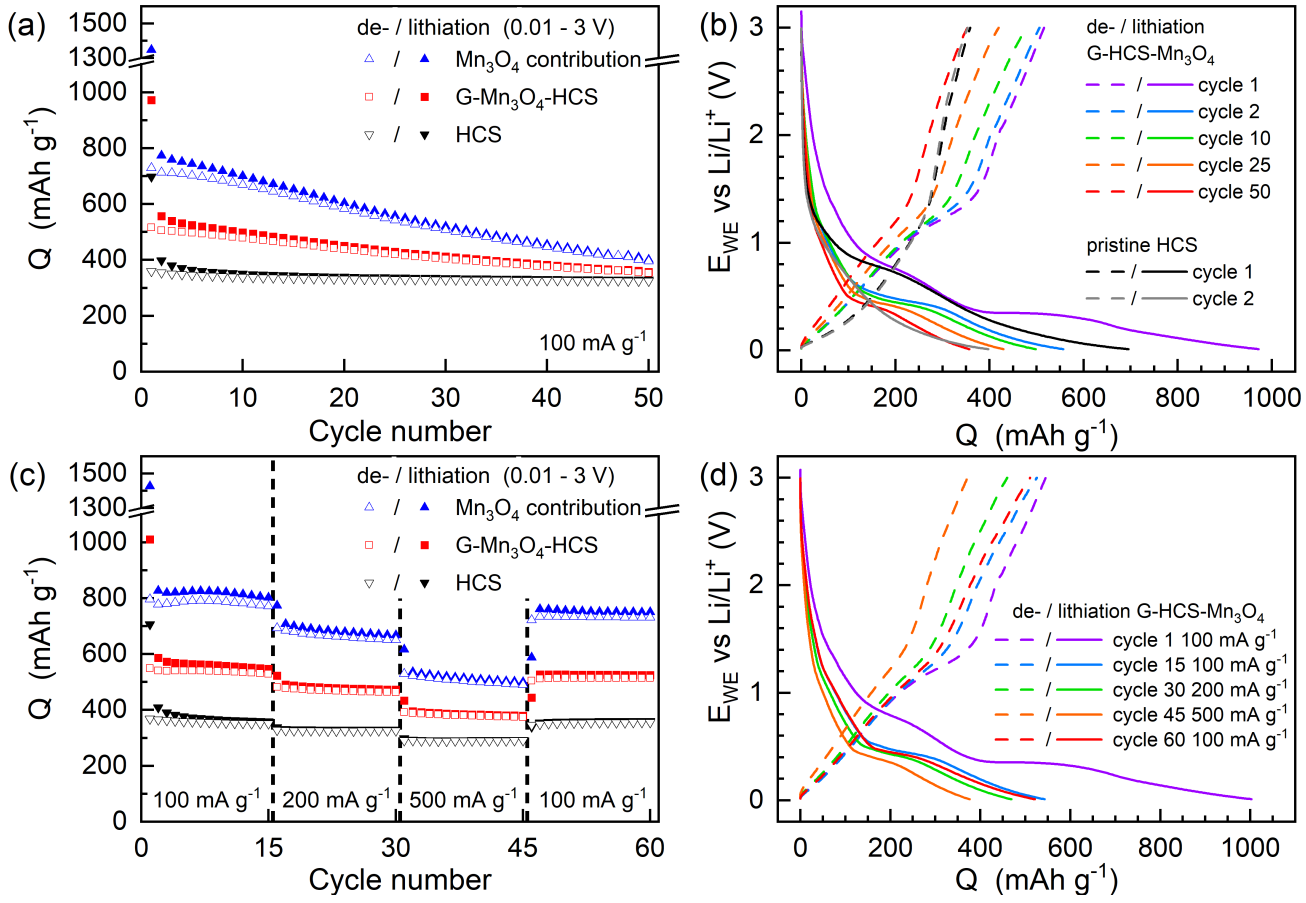

Fig. 7. Specific dis-/charge capacities of pristine HCS and G—HCS—Mn_3O_4 as well as the calculated contribution of the incorporated Mn_3O_4 at 100 mA g^{-1} (a) and varying current densities (c). The corresponding potential profiles obtained by GCPL, at 100 mA g^{-1} (b), and rate capability test with specific charge/discharge currents from 100 to 500 mA g^{-1} (d).

and (3)) contribute to the initial capacity losses. For all cycles under study, the results show higher capacity of the composite material as compared to the pristine one, especially in the first 25 cycles. However, in comparison to excellent cycle stability of pristine HCS with charge capacity retention of 91% after 50 cycles, the composite displays more pronounced relative capacity fading as the charge capacity steadily decreases to 353 mAh g^{-1}, corresponding to capacity retention of 63%. Both the analysis in Fig. 7a and the potential profiles of G–HCS–Mn_3O_4 (Fig. 7b) show that mainly the capacity related to Mn_3O_4 fades upon cycling which is attributed to degradation processes due to volume and structural changes of the conversion reaction of Mn_3O_4.

Superior performance of the G–HCS–Mn_3O_4 –based electrodes as compared to pristine HCS is confirmed by rate capability test (Fig. 7c) with varying current densities 100 mA g^{-1}, 200 mA g^{-1}, 500 mA g^{-1} and 100 mA g^{-1}, each applied for 15 cycles. After each 15 cycles, G–HCS–Mn_3O_4 reaches charge capacities of 529 mAh g^{-1}, 463 mAh g^{-1} and 374 mAh g^{-1} at 100 mA g^{-1}, 200 mA g^{-1} and 500 mA g^{-1} and thus 50%, 43% and 30% more than pristine HCS. As seen in the potential profiles (Fig. 7d), by increasing the current rate up to 500 mA g^{-1} the shape of the potential profiles is not significantly affected. While all feature remains present, the plateaus however become less pronounced and more sloping.

Thus, the data clearly show strongly enhanced specific capacity due to incorporation of Mn_3O_4. In order to separately assess electrochemical activity of the incorporated oxide, the data have been corrected for the contribution of pristine HCS and normalized accordingly (Fig. 7a and c) (cf [47]). In the first cycles, the contribution of the oxide to the discharge capacity amounts to about 750 mAh g^{-1}, thereby even exceeding the full theoretical specific capacity of 703 mAh g^{-1} associated with the reversible conversion reaction (C). These high values may be assigned to the partial back reaction of (B) and (A) as indicated by the oxidation feature O_2 (Fig. 6b) [28,29]. In general, excessive capacity beyond the theory values is often observed in transition metal oxide/carbon nanomaterials and has been discussed in terms of formation of a polymer/gel-like film on the nanoparticles [55] and interface charging effects by lithium accommodation at the metal/Li_2O interface [56].

4. Conclusions

A novel composite nanomaterial involving graphene coated core-shell Mn_3O_4 nanoparticles encapsulated in HCS was designed and synthesized successfully. G–HCS–Mn_3O_4 has a large specific surface area and mesoporous structure, providing high accessible areas and promises sufficient passages for the electrolyte when applied in LIBs. When used as anode material, G–HCS–Mn_3O_4 can deliver a high specific charge capacity of 557 mAh g^{-1} at 100 mA g^{-1}. The electrochemical studies demonstrate the full access to the theoretical capacity of Mn_3O_4. We attribute high electrochemical activity of Mn_3O_4 to the good electrical connection provided by the conductive HCS network and the nanoscale dimensions permitting fast reaction kinetics. Our results show that incorporation of Mn_3O_4 strongly enhances the specific capacity compared to pristine HCS. This facile method can be extended for other TMOs@HCS composites with controllable carbon shell thickness and cavity size, as well as the loading mass of TMOs.

Credit author statement

Elisa Thauer: Conceptualization, Methodology, Investigation, Writing- Original draft, Visualization. Xiaoze Shi: Investigation, Writing- Original draft, Visualization. Shuai Zhang: Investigation. Xuecheng Chen: Conceptualization, Funding acquisition. Lukas Deeg: Investigation, Writing- Original draft. Rüdiger Klingeler: Conceptualization, Writing- Review and Editing, Funding acquisition, Supervision. Karolina Wenelska: Investigation, Resources. Ewa Mijowska: Writing- Review and Editing, Supervision.

Declaration of competing interest

The authors declare that they have no known competing financial interests or personal relationships that could have appeared to influence the work reported in this paper.

Acknowledgments

Work was supported by National Science Centre, Poland Beethoven UMO-2016/23/G/ST5/04200 and Deutsche Forschungsgemeinschaft DFG via KL 1824/12–1. E.T. and R.K. acknowledge support by the BMWi through project 03 ET6095C (HiKoMat). The authors thank I. Glass for experimental support.

References

[1] Etacheri V, Marom R, Elazari R, Salitra G, Aurbach D. Challenges in the development of advanced Li-ion batteries: a review. Energy Environ Sci 2011;4:3243–62.
[2] Dunn B, Kamath H, Tarascon JM. Electrical energy storage for the grid: a battery of choices,. Science 2011;334:928–35.
[3] Goodenough JB, Kim Y. Challenges for rechargeable Li batteries. Chem Mater 2010;22:587–603.
[4] Li Z, Khajepour A, Song J. A comprehensive review of the key technologies for pure electric vehicles,. Energy 2019;182:824–39.
[5] Liu C, Li F, Ma LP, Cheng HM. Advanced materials for energy storage. Adv Mater 2010;22. E28-+.
[6] Kang B, Ceder G. Battery materials for ultrafast charging and discharging. Nature 2009;458:190–3.
[7] Wu HB, Chen JS, Hng HH, Lou XW. Nanostructured metal oxide-based materials as advanced anodes for lithium-ion batteries. Nanoscale 2012;4:2526–42.
[8] Poizot P, Laruelle S, Grugeon S, Dupont L, Tarascon JM. Nano-sized transition-metaloxides as negative-electrode materials for lithium-ion batteries. Nature 2000;407:496–9.
[9] Cho JS, Park J-S, Jeon KM, Chan Kang Y. 1-D nanostructure comprising porous Fe2O3/Se composite nanorods with numerous nanovoids, and their electrochemical properties for use in lithium-ion batteries. J Mater Chem 2017;5:10632–9.
[10] Chen X, Huang Y, Zhang K. Cobalt nanofibers coated with layered nickel silicate coaxial core-shell composites as excellent anode materials for lithium ion batteries. J Colloid Interface Sci 2018;513:788–96.
[11] Chen X, Huang Y, Zhang K, Feng X, Wang M. Porous TiO2 nanobelts coated with mixed transition-metal oxides Sn3O4 nanosheets core-shell composites as high-performance anode materials of lithium ion batteries. Electrochim Acta 2018;259:131–42.
[12] Liu XL, Chen YX, Liu HB, Liu ZQ. SiO2@C hollow sphere anodes for lithium-ion batteries. J Mater Sci Technol 2017;33:239–45.
[13] Zhong KF, Xia X, Zhang B, Li H, Wang ZX, Chen LQ. MnO powder as anode active materials for lithium ion batteries. J Power Sources 2010;195:3300–8.
[14] Zakharova GS, Thauer E, Wegener SA, Nölke JH, Zhu Q, Klingeler R. Hydrothermal microwave-assisted synthesis of Li3VO4 as an anode for lithium-ion battery. J Solid State Electrochem 2019;23:2205–12.
[15] Zakharova GS, Jähne C, Popa A, Täschner C, Gemming T, Leonhardt A, Büchner B, Klingeler R. Anatase nanotubes as an electrode material for lithium-ion batteries. J Phys Chem C 2012;116:8714–20.
[16] Möller L, Thauer E, Ottmann A, Deeg L, Ghunaim R, Hampel S, Klingeler R. CoFe2O4-filled carbon nanotubes as anode material for lithium-ion batteries. J Alloys Compd 2020:155018.
[17] Wenelska K, Ottmann A, Schneider P, Thauer E, Klingeler R, Mijowska E. Hollow carbon sphere/metal oxide nanocomposites anodes for lithium-ion batteries. Energy 2016;103:100–6.
[18] Pang H, Yang Z, Lv J, Yan W, Guo T. Novel MnOx@ Carbon hybrid nanowires with core/shell architecture as highly reversible anode materials for lithium ion batteries. Energy 2014;69:392–8.
[19] Cauda V, Pugliese D, Garino N, Sacco A, Bianco S, Bella F, Lamberti A, Gerbaldi C. Multi-functional energy conversion and storage electrodes using flower-like Zinc oxide nanostructures. Energy 2014;65:639–46.
[20] Yu D-w, Hou Y-l, Han X, Zheng X-j, Yu S-j, Chen Y-m, Wang X-l. Enhanced lithium-ion storage performance from high aspect ratio Mn3O4 nanowires. Mater Lett 2015;159:182–4.
[21] Yue J, Gu X, Chen L, Wang N, Jiang X, Xu H, Yang J, Qian Y. General synthesis of hollow MnO2, Mn3O4 and MnO nanospheres as superior anode materials for

lithium ion batteries. J Mater Chem 2014;2:17421–6.
[22] Xiao W, Chen JS, Lou XW. Synthesis of octahedral Mn3O4 crystals and their derived Mn3O4–MnO2 heterostructures via oriented growth. CrystEngComm 2011;13:5685–7.
[23] Ma X, Zhai Y, Wang N, Yang J, Qian Y. Mn3O4@C core–shell composites as an improved anode for advanced lithium ion batteries. RSC Adv 2015;5:46829–33.
[24] Ponrouch A, Taberna P-L, Simon P, Palacín MR. On the origin of the extra capacity at low potential in materials for Li batteries reacting through conversion reaction. Electrochim Acta 2012;61:13–8.
[25] Zhang R, Wang D, Qin L-C, Wen G, Pan H, Zhang Y, Tian N, Zhou Y, Huang X. MnCO3/Mn3O4/reduced graphene oxide ternary anode materials for lithium-ion batteries: facile green synthesis and enhanced electrochemical performance. J Mater Chem 2017;5:17001–11.
[26] Nam I, Kim ND, Kim G-P, Park J, Yi J. One step preparation of Mn3O4/graphene composites for use as an anode in Li ion batteries, J. Power Sources 2013;244:56–62.
[27] Jiang Y, Yue J-L, Guo Q, Xia Q, Zhou C, Feng T, Xu J, Xia H. Highly porous Mn3O4 micro/nanocuboids with in situ coated carbon as advanced anode material for lithium-ion batteries. Small 2018;14:1704296.
[28] Bai Z, Zhang X, Zhang Y, Guo C, Tang B. Facile synthesis of mesoporous Mn3O4 nanorods as a promising anode material for high performance lithium-ion batteries. J Mater Chem A 2014;2:16755–60.
[29] Li L, Guo Z, Du A, Liu H. Rapid microwave-assisted synthesis of Mn3O4–-graphene nanocomposite and its lithium storage properties. J Mater Chem 2012;22.
[30] Luo S, Wu H, Wu Y, Jiang K, Wang J, Fan S. Mn3O4 nanoparticles anchored on continuous carbon nanotube network as superior anodes for lithium ion batteries. J Power Sources 2014;249:463–9.
[31] Thauer E, Ottmann A, Schneider P, Moller L, Deeg L, Zeus R, Wilhelmi F, Schlestein L, Neef C, Ghunaim R, Gellesch M, Nowka C, Scholz M, Haft M, Wurmehl S, Wenelska K, Mijowska E, Kapoor A, Bajpai A, Hampel S, Klingeler R. Filled carbon nanotubes as anode materials for lithium-ion batteries. Molecules 2020;25.
[32] Park S-K, Seong C-Y, Yoo S, Piao Y. Porous Mn3O4 nanorod/reduced graphene oxide hybrid paper as a flexible and binder-free anode material for lithium ion battery. Energy 2016;99:266–73.
[33] Liu Y, Han J, Fan L, Li Y, Guo R. Pomegranate-like multicore-shell Mn3O4 encapsulated mesoporous N-doped carbon with internal void space for high-performance lithium-ion batteries. Chem Commun 2019.
[34] Wang B, Li F, Wang X, Wang G, Wang H, Bai J. Mn3O4 nanotubes encapsulated by porous graphene sheets with enhanced electrochemical properties for lithium/sodium-ion batteries. Chem Eng J 2019;364:57–69.
[35] Chen X, Kierzek K, Cendrowski K, Pelech I, Zhao X, Feng J, Kalenczuk RJ, Tang T, Mijowska E. CVD generated mesoporous hollow carbon spheres as supercapacitors. Colloid Surface Physicochem Eng Aspect 2012;396:246–50.
[36] Stober W, Fink A, Bohn E. Controlled growth of monodisperse silica spheres in micron size range. J Colloid Interface Sci 1968;26:62.
[37] Tang K, Fu LJ, White RJ, Yu LH, Titirici MM, Antonietti M, Maier J. Hollow carbon nanospheres with superior rate capability for sodium-based batteries. Adv. Energy Mater. 2012;2:873–7.
[38] Chen XC, Kierzek K, Jiang ZW, Chen HM, Tang T, Wojtoniszak M, Kalenczuk RJ, Chu PK, Borowiak-Palen E. Synthesis, growth mechanism, and electrochemical properties of hollow mesoporous carbon spheres with controlled diameter. J Phys Chem C 2011;115:17717–24.
[39] Li S, Pasc A, Fierro V, Celzard A. Hollow carbon spheres, synthesis and applications – a review. J Mater Chem 2016;4:12686–713.
[40] Shi X, Zhang S, Chen X, Chu PK, Tang T, Mijowska E. Formation of ultra-small Mn3O4 nanoparticles trapped in nanochannels of hollow carbon spheres by nanoconfinement with excellent supercapacitor performance. Int J Hydrogen Energy 2019;44:13675–83.
[41] Shi X, Zhang S, Chen X, Tang T, Mijowska E. Effect of iron oxide impregnated in hollow carbon sphere as symmetric supercapacitors. J Alloys Compd 2017;726:466–73.
[42] Yang K, Zhang S, Zhang G, Sun X, Lee S-T, Liu Z. Graphene in mice: ultrahigh in vivo tumor uptake and efficient photothermal therapy. Nano Lett 2010;10:3318–23.
[43] Jarosch D. Crystal structure refinement and reflectance measurements of hausmannite, Mn3O4. Mineral Petrol 1987;37:15–23.
[44] Trukhanov SV, Troyanchuk IO, Bobrikov IA, Simkin VG, Balagurov AM. Crystal structure phase separation in anion-deficient La0.70Sr0.30MnO3 – δ manganite system, Journal of Surface Investigation. X-ray. Synchrotron and Neutron Techniques 2007;1:705–10.
[45] Ambroz F, Macdonald TJ, Martis V, Parkin IP. Evaluation of the BET theory for the characterization of meso and microporous MOFs. Small Methods 2018;2.
[46] Seo WS, Jo HH, Lee K, Kim B, Oh SJ, Park JT. Size-dependent magnetic properties of colloidal Mn3O4 and MnO nanoparticles. Angew Chem Int Ed Engl 2004;43:1115–7.
[47] Ottmann A, Scholz M, Haft M, Thauer E, Schneider P, Gellesch M, Nowka C, Wurmehl S, Hampel S, Klingeler R. Electrochemical magnetization switching and energy storage in manganese oxide filled carbon nanotubes. Sci Rep 2017;7:13625.
[48] Djerdj I, Arčon D, Jagličić Z, Niederberger M. Nonaqueous synthesis of manganese oxide nanoparticles, structural characterization, and magnetic properties. J Phys Chem C 2007;111:3614–23.
[49] Du J, Gao Y, Chai L, Zou G, Li Y, Qian Y. Hausmannite Mn3O4 nanorods: synthesis, characterization and magnetic properties. Nanotechnology 2006;17:4923–8.
[50] Novák P, Joho F, Lanz M, Rykart B, Panitz J-C, Alliata D, Kötz R, Haas O. The complex electrochemistry of graphite electrodes in lithium-ion batteries,. J Power Sources 2001;97–98:39–46.
[51] Fang X, Lu X, Guo X, Mao Y, Hu Y-S, Wang J, Wang Z, Wu F, Liu H, Chen L. Electrode reactions of manganese oxides for secondary lithium batteries. Electrochem Commun 2010;12:1520–3.
[52] Lowe MA, Gao J, Abruña HD. In operando X-ray studies of the conversion reaction in Mn3O4lithium battery anodes. J Mater Chem A 2013;1:2094–103.
[53] Kim S-W, Lee H-W, Muralidharan P, Seo D-H, Yoon W-S, Kim DK, Kang K. Electrochemical performance and ex situ analysis of ZnMn2O4 nanowires as anode materials for lithium rechargeable batteries. Nano Research 2011;4:505–10.
[54] Zhong K, Zhang B, Luo S, Wen W, Li H, Huang X, Chen L. Investigation on porous MnO microsphere anode for lithium ion batteries. J Power Sources 2011;196:6802–8.
[55] Laruelle S, Grugeon S, Poizot P, Dollé M, Dupont L, Tarascon JM. On the origin of the extra electrochemical capacity displayed by MO/Li cells at low potential. J Electrochem Soc 2002;149.
[56] Jamnik J, Maier J. Nanocrystallinity effects in lithium battery materials. Phys Chem Chem Phys 2003;5.

Kapitel 5 Abschliessende Diskussion

Der erste Abschnitt dieses Kapitels enthält zu jedem der in dieser Arbeit enthaltenen Unterkapitel eine Zusammenfassung, in der die wichtigsten Ergebnisse und Schlussfolgerungen hervorgehoben werden. Für detaillierte Beschreibungen der verwendeten Methoden wird der Leser auf die entsprechenden Kapitel und auf die Originalartikel verwiesen. Im zweiten Abschnitt werden die Resultate der einzelnen Unterkapitel einander gegenübergestellt und in einem größeren Kontext diskutiert.

5.1 Zusammenfassung

In der vorliegenden Arbeit wurden potentielle Anodenmaterialien für Lithium-Ionen-Batterien hinsichtlich ihrer physikalischen und elektrochemischen Eigenschaften untersucht. Dabei war es insbesondere das Ziel, den Zusammenhang zwischen Partikelgröße, Morphologie, Funktionalisierung und elektrochemischen Eigenschaften näher zu untersuchen.

Die Struktur, Morphologie und Partikelgröße der pulverförmigen Materialien wurden anhand von Röntgendiffraktometrie und Rasterelektronenmikroskopie untersucht. Energiedispersive Röntgenspektroskopie und CHN-Analysen gaben Aufschluss über die chemische Zusammensetzung, SQUID-Magnetometrie über die magnetischen Eigenschaften. Als elektrochemische Charakterisierungsmethoden kamen zyklische Voltammetrie und galvanostatische Zyklierung zum Einsatz. Darüber hinaus war es über Kooperationen möglich die Materialien mittels Transmissionselektronenmikroskopie, BET-Messungen, thermischen Analysen sowie Raman- und Röntgenphotoelektronenspektroskopie zu untersuchen.

Am Beispiel des Lithiumorthovanadats Li_3VO_4 wurde der Einfluss der morphologischen Beschaffenheit und Kompositbildung mit Kohlenstoff auf die elektrochemischen Eigenschaften an einem Interkalationsmaterial untersucht (Kapitel 2).

Die Synthese der reinen Li_3VO_4-Proben unterschiedlicher Morphologie erfolgte über eine Hydrothermalsynthese, bei der durch die Wahl des Lösungsmittels die Primärpartikelgröße

und der Agglomerationsgrad beeinflusst werden kann. Zum Aufbrechen der Agglomerate wurde auf eine nachträgliche mechanische Vermahlung mittels Mörser zurückgegriffen. Die Nanoskalierung der Partikel resultiert in höhere spezifische Kapazitäten und eine bessere Hochstromfähigkeit. So weisen die Nanopartikel mit einer Größe um 60(10) nm bei der ersten Delithiierung mit 163 mA h g^{-1}, entsprechend 41 % der theoretischen Kapazität, den höchsten Wert auf, während bei einer Partikelgröße um 2,5(1,0) µm lediglich 39 mA h g^{-1}erreicht werden. Der Vergleich der Materialien zeigt, dass einerseits eine größere Oberfläche zwar mit einer höheren elektrochemischen Aktivität verbunden ist, andererseits aber auch mit stärkeren Degradationseffekten. Die hierarchische Anordnung der Nanopartikel zu mikrometergroßen Sekundärpartikel erweist sich als erfolgreiche Strategie gegen die hohen Kapazitätsverluste in Höhe von 36 % nach 100 Zyklen, unter denen die Nanopartikel leiden. Mit einem Kapazitätsverlust von nur 2 % nach 100 Zyklen besitzen diese eine hervorragende Zyklenstabilität.

Zur Untersuchung der elektrochemischen Eigenschaften von Li_3VO_4 im Verbund in Kohlenstoffkompositen wurden über ein Sol-Gel-Verfahren verschiedene Li_3VO_4/C-Komposite hergestellt. Abhängig von der verwendeten Kohlenstoffquelle unterscheiden sich die Komposite in ihrer Morphologie sowie dem Anteil an Kohlenstoff. Eine reine Li_3VO_4-Probe, die mittels thermischer Behandlung aus einem der Komposite gewonnen wurde, dient als Referenzmaterial. Die Herstellung von Kohlenstoffkompositen erweist sich als wirksame Strategie zur Steigerung der elektrochemischen Aktivität von Li_3VO_4. Im Gegensatz zum reinen Li_3VO_4 mit einer Kapazität von 57 mA h g^{-1} ist bei den Kompositen, die mit Carbonsäuren als Kohlenstoffquelle hergestellt wurden, nahezu die volle theoretische Kapazität von 397 mA h g^{-1} zugänglich. Die /textitex-situ XRD-Studien zeigen, dass beim reinen Li_3VO_4-Material ein großer Teil des Aktivmaterials inaktiv ist, wohingegen für die Komposite die vollständige Amorphisierung der Struktur beobachtet wird. Insgesamt die beste elektrochemische Performance liefert das Komposit, das mit Glukose hergestellt wurde. Obwohl es im ersten Delithiierungzyklus mit 289 mA h g^{-1} die niedrigste Kapazität unter den Kompositen erreicht, übertrifft es die anderen Materialien im Langzeittest aufgrund seiner hervorragenden Zyklenstabilität. Der Kapazitätsverlust nach 100 Zyklen beträgt lediglich 4 %. Die Unterschiede der elektrochemischen Eigenschaften der Komposite sind auf ihre unterschiedliche Morphologie und Kohlenstoffanteil zurückzuführen. Die größere Oberfläche der mit Carbonsäuren hergestellten Komposite erklärt deren höhere elektrochemische Aktivität und die stärkeren Degradationseffekte. Im Vergleich dazu führt die kleinere spezifische Oberfläche und der höhere Anteil an Kohlenstoff des Komposits, das mit Glukose hergestellt wurde, zu einer niedrigeren, aber stabilen spezifischen Kapazität.

In Kapitel 3 wurde der Einfluss von Morphologie und Funktionalisierung mit amorphen Kohlenstoff auf die elektrochemischen Eigenschaften verschiedener Konversionsmaterialien untersucht.

Der erste Teil beinhaltet die Ergebnisse zu den Untersuchungen am Konversionsmaterials Molybdändioxid MoO_2. Die Synthese der MoO_2/C-Komposite erfolgte über ein Sol-Gel-Verfahren. Während die verwendete Kohlenstoffquelle maßgeblich den Kohlenstoffanteil der Komposite bestimmt, zeigt sich kein Einfluss auf die morphologischen Eigenschaften. Die Größenreduktion der resultierenden Agglomerate wurde mit einer nachträglichen Kolloidvermahlung realisiert. Die Ergebnisse der elektrochemischen Untersuchungen zeigen einen deutlichen Einfluss der Sekundärpartikelgröße und des Kohlenstoffanteils auf die elektrochemischen Eigenschaften von MoO_2. Die Reduktion der Sekundärpartikelgröße resultiert in einer höheren spezifischen Kapazität und in einer besseren Zyklenstabilität. So weisen die Agglomerate mit der kleinsten Größe um 550(450) nm bei der ersten Delithiierung mit $660\,\mathrm{mA\,h\,g^{-1}}$, entsprechend 78 % der theoretischen spezifischen Kapazität, den höchsten Wert auf. Der Kapazitätsverlust nach 15 Zyklen beträgt lediglich 6 %. Im Gegensatz dazu erreicht das Komposit mit einer Partikelgröße um 3(1) µm weniger als die Hälfte und unterliegt mit einem Verlust von 69 % nach 15 Zyklen starken Degradationseffekten. Hier sei anzumerken, dass die Komposite den gleichen Kohlenstoffanteil besitzen und sie sich nur in der Sekundärpartikelgröße unterscheiden. Aufgrund der guten metallartigen elektronischen Leitfähigkeit von MoO_2, die ausreicht, um den Elektronentransport im Elektrodenmaterial zu gewährleistet, zeigt die Höhe des Kohlenstoffanteils keine Auswirkungen auf die spezifische Kapazität. Selbst wenn der Beitrag des Kohlenstoffs bei der theoretischen Kapazität berücksichtigt wird, zeigen sich nur marginale Unterschiede. Im Vergleich zum Komposit mit einem Kohlenstoffanteil von 2,4 wt%, das 37 % der theoretischen Kapazität erreicht, ist für das Komposit mit 23,7 % Kohlenstoff mit 42 wt% der theoretischen Kapazität leidiglich eine minimal höhere Aktivität zu verzeichnen. Anders verhält es sich hinsichtlich der Zyklenstabilität, auf die sich ein hoher Kohlenstoffanteil deutlich positiv auswirkt. So erleidet das Komposit mit niedrigem Kohlenstoffanteil nach 15 Zyklen einen Kapazitätsverlust von 69 %, wohingegen es bei einem zehnfach höheren Kohlenstoffanteil nur 38 wt% sind. Auch hier sei anzumerken, dass die Untersuchungen zu den Effekten verschiedener Kohlenstoffanteile an Kompositen mit ähnlicher Morphologie erfolgten.

Als weiteres Konversionsmaterial wurde Vanadiumdioxid V_2O_3 in Kompositen mit amorphen Kohlenstoff untersucht. Die Synthese der V_2O_3/C-Komposite erfolgte zum einen über ein Sol-Gel-Verfahren als auch mittels Hydrothermalsynthese, wobei die Morphologie der Materialien maßgeblich durch die Synthesemethode bestimmt wird. Alle aus dem Sol-Gel-Verfahren resultierenden Komposite bestehen unabhängig von der verwendeten

Kohlenstoffquelle aus kantigen mikrometergroßen Sekundärpartikel, die aus Nanopartikel aufgebaut sind. Insgesamt weisen sie recht ähnliche elektrochemische Eigenschaften auf. Sie zeichnen sich durch eine gute Zyklenstabilität aus, wenngleich mit spezifischen Kapazitäten um lediglich 30 % des theoretischen Werts ein hohes Optimiertungspotential im Hinblick auf die elektrochemische Aktivität besteht. Die höchsten spezifischen Kapazitäten liefert das Komposit, das mit Apfelsäure hergestellt wurde, so z.B. 337 mA h g^{-1} bei 100 mA g^{-1} und 183 mA h g^{-1} bei 500 mA g^{-1} nach jeweils 15 Zyklen, was einer Kapazitätserhalt von 54 % bei einem fünffach höheren Strom entspricht. Im Unterschied zu den Kompositen, die über ein Sol-Gel-Verfahren hergestellt wurden, besitzen die hydrothermal synthetisierten Komposite eine sphärische Morphologie. Die Materialien bestehen aus hierarchisch strukturierten Mikrosphären, die abhängig von der Kohlenstoffquelle eine Kern-Schale- oder massive Struktur besitzen. Des Weiteren beeinflusst die Kohlenstoffquelle die Größe der nanometergroßen Primärpartikel und somit die Topografie der Sekundärpartikel. Entgegen den Erwartungen lässt sich kein direkter Zusammenhang zwischen spezifischer Oberfläche und elektrochemischer Aktivität feststellen. Obwohl die Oberfläche des Komposits, das mit Weinsäure hergestellt wurde, dreimal so groß ist wie die des mit Apfelsäure hergestellten Komposits mit vergleichbaren Kohlenstoffanteil zeigen sich keine großen Unterschiede bei den erreichten Kapazitäten. Dies ist möglicherweise auf die fehlende Kern-Schale-Struktur des mit Weinsäure hergestellten Komposits zurückzuführen, von der angenommen wird, dass sie die elektrochemische Aktivität positiv beeinflusst. REM-Aufnahmen nach 200 Zyklen bestätigen die strukturelle Stabilität der hierarchisch strukturierten Sphären, was deren hervorragende Zyklenstabilität erklärt. Das Komposit, das mit Apfelsäure hergestellt wurde, liefert die höchsten Kapazitäten, so z.B. 351 mA h g^{-1} bei 100 mA g^{-1} und 236 mA h g^{-1} bei 500 mA g^{-1} nach jeweils 15 Zyklen. Dies entspricht einem Kapazitätserhalt von 75 % bei einem fünffach höheren Strom und ist somit deutlich höher als bei den V_2O_3/C-Kompositen, die über ein Sol-Gel-Verfahren synthetisiert wurden. Die kinetische Analyse zeigt, dass die überlegene Hochstromfähigkeit der V_2O_3/C-Mikrossphären auf den höheren Anteil an pseudo-kapazitiver Ladungsspeicherung zurückzuführen ist, der durch deren größere Oberfläche begünstigt wird. Als oberflächeninduzierter Prozess ist dieser deutlich schneller als diffusionsgesteuerte Prozesse.

Als Vertreter der Klasse der legierungsbildenden Materialien wurde Zinkoxid ZnO untersucht. Der bei der Speicherung von Li^+-Ionen vorliegende zweistufige Prozess, bestehend aus einer Konversion und Legierungsbildung, konnte anhand von *ex-situ* XRD-Studien bestätigt werden. Die Synthese der Komposite erfolgte durch das Tempern des Alkoxides Zinkglycerol, bei dem durch die Wahl der Temperatur Einfluss auf die Morphologie sowie auf den Anteil und die Struktur des Kohlenstoffs genommen werden kann. Die Materialien bestehen aus

Nanopartikel die zu flachen Überstrukturen agglomeriert sind. Im Gegensatz zu den Niedertemperaturkompositen treten bei den Hochtemperaturkomposite zusätzlich mikrometergroße ZnO-Polyeder auf. Eine reine ZnO-Probe, die mittels thermischer Nachbehandlung aus einem der Komposite gewonnen wurde, dient als Referenzmaterial zur Untersuchung des Effekts der Kompositbildung mit Kohlenstoff. Der Verbund mit Kohlenstoff führt insbesondere zu einer Verbesserung der Kapazität und Hochstromfähigkeit von ZnO. Die höchste Kapazität im ersten Delithiierungszyklus erreicht das Komposit ZnO/C-700 mit $670\,\mathrm{mA\,h\,g^{-1}}$, was 69 % der theoretischen Kapazität entspricht. Trotz der doppelt so großen Oberfläche der Hochtemperaturkomposite, erreichen diese entgegen der Erwartung eine nur marginal höhere spezifische Kapazität bei der ersten Delithiierung. Mögliche Ursachen, die sich negativ auf die elektrochemische Aktivität auswirken könnten, sind das Auftreten der mikrometergroßen ZnO-Polyeder oder der geringere Kohlenstoffanteil der Hochtemperaturkomposite. Letzteres wird jedoch aufgrund der nur geringen Unterschiede im Kohlenstoffgehalt als eher unwahrscheinlich angesehen. Alle ZnO-Materialien erleiden in den ersten 20 Zyklen große Kapazitätsverluste, für die die nur teilweise reversibel ablaufende Konversionsreaktion als Hauptursache identifiziert wurde. Als weitere Ursache sind die großen Volumenänderungen zu nennen, die während der Li^+-Speicherung auftretenden, und zur Zerstörung der Elektrodenstruktur führen. Stärkere Degradationseffekte zeigen sich bei den Hochtemperaturkompositen, was auf die mikrometergroßen ZnO-Polyeder zurückgeführt werden kann. Die Raman- und XPS-Untersuchungen zeigen, dass der Kohlenstoff bei höherer Synthesetemperatur erwartungsgemäß eine höher geordnete Struktur aufweist. Dies äußert sich in einer besseren Hochstromfähigkeit bedingt durch einen kleineren Polarisationswiderstand.

Der Effekt der Funktionalisierung von konversionbasierten Übergangsmetalloxiden mit Kohlenstoffnanostrukturen wurde in Kapitel 4 untersucht.

Im ersten Teil wurde am Beipiel des Ferrits $CoFe_2O_4$ der Verbund mit Kohlenstoffnanoröhren untersucht. Das Komposit $CoFe_2O_4$@CNTbesteht zu 11(1) wt% aus $CoFe_2O_4$, das einerseits in Form von Nanopartikeln im Inneren der CNTs und andererseits als unregelmäßig geformte Partikel mit Abmessungen von einigen 100 nm außerhalb der CNTs vorliegt. Durch die Gegenüberstellung der elektrochemischen Eigenschaften des Komposits mit denen von ungefüllten CNTs sowie unmodifizierten $CoFe_2O_4$-Nanopartikel wird der Effekt der Funktionalisierung demonstriert. Im Vergleich zu den leeren CNTs liefert das Komposit $CoFe_2O_4$@CNT mit $322\,\mathrm{mA\,h\,g^{-1}}$ bei $100\,\mathrm{mA\,g^{-1}}$ im ersten Delithiierungszyklus eine um 13 % höhere spezifische Kapazität. Dabei entspricht der $CoFe_2O_4$-Beitrag zur Kompositkapazität mit $630\,\mathrm{mA\,h\,g^{-1}}$ 73 % der theoretischen Kapazität. Der Vergleich mit unmodifizierten $CoFe_2O_4$-Nanopartikel zeigt, dass durch den Verbund mit Kohlenstoffnanoröhren die Zyklenstabilität von $CoFe_2O_4$

deutlich verbessert wird, so bleiben nach 20 Zyklen noch 71 % des Beitrags von $CoFe_2O_4$ zur Kompositkapazität der ersten Delithiierung erhalten. Im Gegensatz dazu erreichen die unmodifizierten $CoFe_2O_4$-Nanopartikel nur 22 % der initialen delithiierungskapazität. Zusammengefasst zeigen die Ergebnisse, dass die Einkapselung von $CoFe_2O_4$ in CNTs einerseits eine erfolgreiche Strategie ist, um eine höhere spezifische Kapazität verglichen mit leeren CNTs zu erzielen, und zum anderen um die Zyklenstabilität von $CoFe_2O_4$ zu erhöhen, was auch für andere konversionsbasierte Übergangsmetalle als vielversprechend angesehen wird.

Im zweiten Teil wurde der Verbund mit Kohlenstoffhohlkugeln an dem Manganoxid Mn_3O_4 untersucht. Das Komposit G-HCS-Mn_3O_4 besteht aus graphenbeschichteten HCS mit einem Innendurchmesser von 200 nm in deren Inneren Mn_3O_4 mit einem Massenanteil von 37,6 wt% eingekapselt ist. Die Ergebnisse der elektrochemischen Untersuchungen weisen die für Mn_3O_4 typischen Redoxmerkmale auf, was die elektrochemische Aktivität der eingekapselten Mn_3O_4-Partikel bestätigt. Darüber hinaus zeigen sie, dass die Konversionsreaktion von Mn_3O_4 vollständig und reversibel umgesetzt werden kann. Das Komposit liefert im ersten Delithiierungszyklus eine spezifische Kapazität von $557\,\mathrm{mA\,h\,g^{-1}}$ was einer Steigerung von 40 % im Vergleich zu der ungefüllter HCS entspricht. Sie zeigen zudem eine bessere Performance bei hohen Stromraten. Damit erweist sich die Einlagerung von Mn_3O_4 in HCS als erfolgreiche Strategie zur Steigerung der spezifischen Kapazität verglichen mit leeren HCS.

5.2 Diskussion der Ergebnisse

Der Fokus der vorliegenden Arbeit liegt auf dem Einfluss der Morphologie und Funktionalisierung mit Kohlenstoff auf die elektrochemischen Eigenschaften verschiedener Anodenmaterialien. Im Folgenden werden die Ergebnisse der Untersuchungen hinsichtlich der spezifischen Kapazität sowie der Zyklenstabilität als relevante Eigenschaften für die Funktionalität als Anodenmaterial gegenübergestellt.

Neben dem Interkalationsmaterial Li_3VO_4 wurden die Konversionmaterialien MoO_2 und V_2O_3 sowie ZnO als Vertreter der legierungsbildenden Materialien in Kompositen mit amorphen Kohlenstoff untersucht. In Abb. 5.1 a und b sind die spezifische Kapazität des ersten Delithiierungzyklus, normiert auf die theoretische Kapazität und der Kapazitätsverlust nach 95 Zyklen in Abhängigkeit der spezifischen Oberfläche für alle untersuchten Materialien zusammengetragen. Aus den Daten wird ersichtlich, dass keine allgemeingültige Aussage für die verschiedenen Materialien getroffen werden kann. Gleiches gilt für den Zusammenhang zwischen Kapazität bzw. Kapazitätsverlust und Kohlenstoffanteil in Abb. 5.2 a und b.

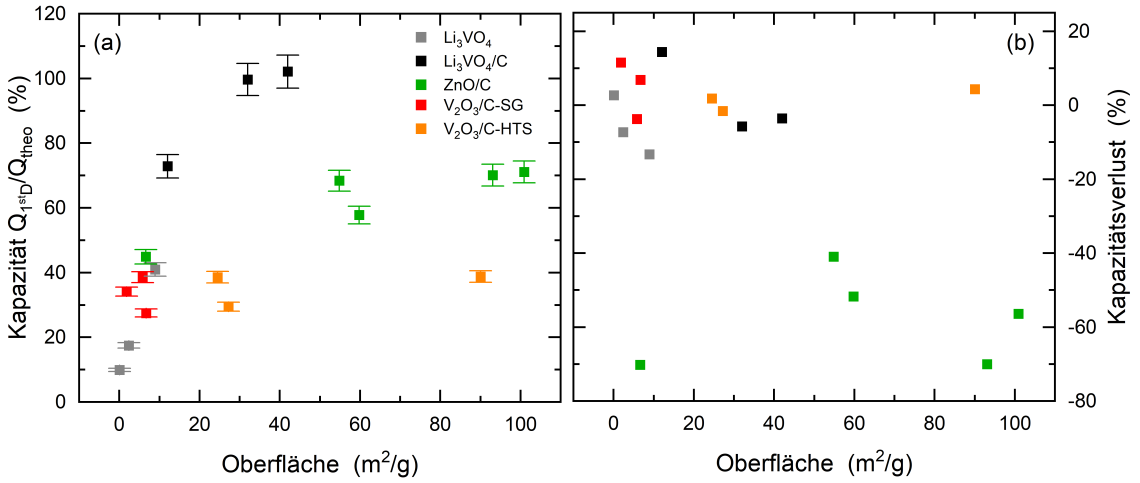

Abbildung 5.1: Spezifische Kapazität des ersten Delithiierungzyklus, normiert auf die theoretische Kapazität (a), und der Kapazitätsverlust nach 20 Zyklen (b) bei galvanostatischer Zyklierung mit 100 mA g^{-1} in Abhängigkeit der spezifischen Oberfläche aller untersuchter Li_3VO_4-, ZnO- und V_2O_3-Materialien.

Die Daten bestätigen, dass eine Vielzahl an Effekten die Eignung eines Materials für den Einsatz in LIBs beeinflusst, die jeweils im Detail untersucht werden müssen, wie an den vorangegangenen Kapiteln gezeigt.

Insbesondere sind die spezifische Oberfläche und der Kohlenstoffanteil als alleinige Parameter für eine umfassende Analyse/Beurteilung nur bedingt ausreichend. Es müssen darüber hinaus, wie die Untersuchungen an ZnO und V_2O_3 zeigen, zum Beispiel auch die genauen morphologischen Eigenschaften sowie die Kohlenstoffverteilung im Komposit zusätzlich miteinbezogen werden

Des Weiteren demonstriert die folgende übergreifende Analyse der Ergebnisse aller Li_3VO_4-Proben repräsentativ für alle Materialien, dass die spezifische Oberfläche und der Kohlenstoffanteil nicht separat voneinander betrachtet werden können. Sie stehen in einer komplexen, wechselseitigen Beziehung mit den elektrochemischen Eigenschaften. Die Untersuchungen an Li_3VO_4-Materialien, die einen vergleichbaren Kohlenstoffanteil besitzen sich aber in ihre Oberfläche unterscheiden und vice versa, lassen folgenden Schluss hinsichtlich der spezifischen Kapazität zu. Sowohl eine größere Oberfläche als auch der Verbund mit Kohlenstoff führen zu einer höheren elektrochemischen Aktivität. Auf Basis der Daten der Li_3VO_4/C-Komposite lässt sich darüber hinaus folgern, dass bei einem Kohlenstoffanteil über 10 wt% die spezifische Oberfläche der maßgebliche Faktor ist, der die Kapazität beeinflusst. Während die Komposite mit einem Kohlenstoffanteil um 10 wt% bereits nahezu die volle theoretische Kapazität liefern, erreicht das Komposit mit doppelt so hohem Kohlenstoffanteil, aber einer um zwei Drittel kleineren Oberfläche lediglich 70 % der theoretischen Kapazität. In Bezug

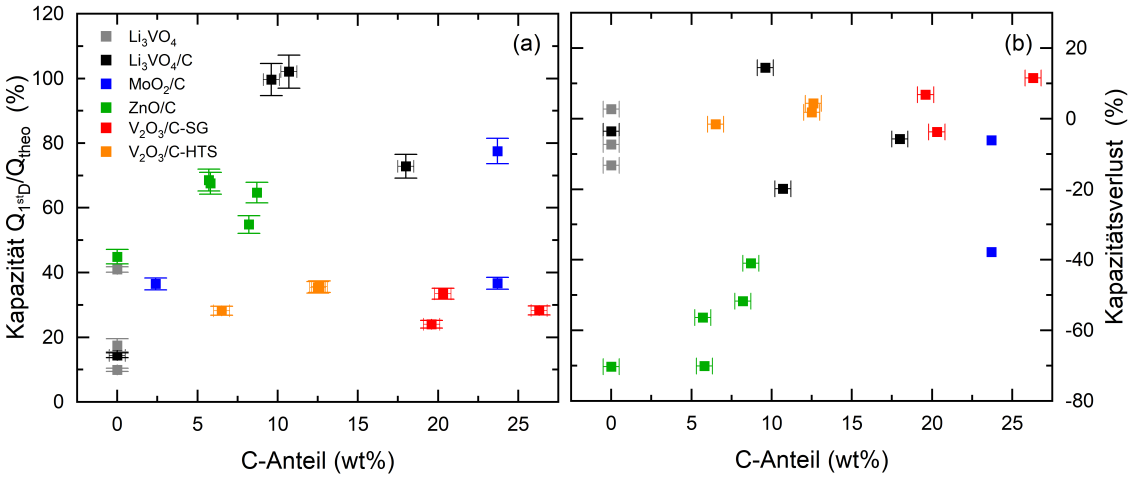

Abbildung 5.2: Spezifische Kapazität des ersten Delithiierungzyklus, normiert auf die theoretische Kapazität (a), und der Kapazitätsverlust nach 20 Zyklen (b) bei galvanostatischer Zyklierung mit 100 mA g^{-1} in Abhängigkeit des Kohlenstoffanteils aller untersuchter Li_3VO_4-, Mn_3O_4-, ZnO- und V_2O_3-Materialien.

auf die Zyklenstabilität lassen sich aus dem Vergleich der Ergebnisse der Li_3VO_4-Materialien, die einen vergleichbaren Kohlenstoffanteil besitzen sich aber in ihre Oberfläche unterscheiden und umgekehrt folgende Aussagen ableiten. Einerseits ist eine größere Oberfläche mit stärkeren Degradationseffekten verbunden, andererseits kann diesen durch den Verbund mit Kohlenstoff entgegengewirkt werden. Unter Einbeziehung dieser Beobachtungen können die Ergebnisse zu den Li_3VO_4/C-Kompositen wie folgt eingeordnet werden. Im Fall der mit Carbonsäuren hergestellten Komposite scheint ein Kohlenstoffanteil von lediglich 10 wt% nicht auszureichen, um die aufgrund deren größeren Oberfläche beschleunigten Degradationsprozess zu verhindern. Demgegenüber treten beim Komposit, das mit Glukose hergestellt wurde und eine kleinere Oberfläche sowie einen höheren Kohlenstoffanteil von 23 wt% besitzt, selbst nach über 100 Zyklen keine Kapazitätsverluste auf. Offen bleibt die Frage, in welchem Maße dabei die kleinere Oberfläche bzw. der höhere Kohlenstoffanteil eine Rolle spielen.

Nichtsdestotrotz können auf Basis der Ergebnisse der vorliegenden Arbeit in Bezug auf die verschiedenen Strategien zur Optimierung der elektrochemischen Eigenschaften folgende Schlüsse gezogen werden.

Insbesondere die Untersuchungen am Interkalationsmaterials Li_3VO_4 als auch am Konversionsmaterial MoO_2 demonstrieren, dass die Reduktion der Partikelgröße und damit verbundene größere Oberfläche sich positiv auf die elektrochemische Aktivität der Materialien auswirkt. Dieser Effekt beruht auf dem besseren Massentransport bedingt durch die größere Oberfläche. Zum einen ist die Diffusionslänge im Aktivmaterial verkürzt und die

größere Kontaktfläche mit dem leitfähigen Additiv verbessert die elektronische Leitfähigkeit des Elektrodenmaterials. Des Weiteren begünstigt eine größere Kontaktfläche von Elektrode und Elektrolyt den schnellen Li^+-Ionen Transfer im Elektrolyten. Somit ist dieser Effekt abhängig von den Transporteigenschaften des Materials, nicht aber vom vorliegenden Speichermechanismus. Betrachtet man die Kristallstruktur von MoO_2finden sich in Richtung der kristallographischen a-Achse Tunnel, von denen angenommen wird, dass sie die Diffusion der Li^+-Ionen begünstigen. Somit stellt die gezielte Reduktion der Partikeldimension in Richtung der kristallographischen a-Achse ein vielversprechender Ansatz dar, um die spezifische Kapazität und Hochstromfähigkeit weiter zu optimieren. In der Literatur wurde diese Strategie unter anderem bereits bei Anatas-Nanosheets erfolgreich angewendet [185].

Hinsichtlich der Auswirkung einer kleineren Partikelgröße auf die Zyklenstabilität unterscheiden sich die Ergebnisse je nach vorliegendem Speichermechanismus, Interkalation, Konversion oder Legierungsbildung. Im Fall des Interkalationsmaterial Li_3VO_4 führt die Nanoskalierung der Partikel zu stärkeren Degradationseffekten, da aufgrund der großen Oberfläche und hohen Oberflächenenergie Li_3VO_4-Nanopartikel dazu neigen zu agglomerieren und zum anderen begünstigt eine große Elektrode/Elektrolyt-Kontaktfläche Nebenreaktionen, die die Degradation des Elektrodenmaterials zur Folge haben. Außerdem führt bei Li_3VO_4 eine große Ladetiefe anders als bei den typischen Interkalationsmaterialen, die bis zu $1\,Li^+$/f.u. speichern, zu strukturellen Schäden aufgrund großer Volumenänderungen oder Gitterverzerrungen. Dementgegen resultiert bei dem Konversionsmaterial MoO_2 die Reduktion der Sekundärpartikel in einer höheren Zyklenstabilität. Für den vorliegenden Fall von Sekundärpartikel kann eine eindeutige Erklärung in der Literatur nicht gefunden werden, jedoch ist dieser Effekt für Primärpartikel bekannt. Zu den Hauptdegradationsursachen bei Konversionsmaterialien zählen die großen Volumenänderungen, die während der Speicherung der Li^+-Ionen auftreten. Kleinere Partikel erleiden geringere strukturelle Schäden, da diese aufgrund der kleineren absoluten Volumenänderungen, einer geringeren mechanischen Belastung unterliegen. Eine weitere Ursache für Kapazitätsverluste ist die Irreversibilität der Konversion, die abhängig ist von der Größe der Übergangsmetallpartikel, die während der elektrochemischen Zyklierung gebildet werden. Die negativen Auswirkungen großer Partikel auf die Zyklenstabilität zeigen sich auch bei den Untersuchungen zum Konversions- und legierungsbildenden Material ZnO, wobei die gleichen Ursachen zu nennen sind.

Ein weiterer interessanter Aspekt, der mit einer größeren Oberfläche einhergeht, zeigt sich anhand der Untersuchungen an V_2O_3/C. Eine hohe spezifische Oberfläche begünstigt die pseudo-kapazitive Ladungsspeicherung, die weniger destruktiv und deutlich schneller ist als die diffusionslimitierte Speicherung im Inneren des Elektrodenmaterials.

Der Verbund von Anodenmaterialien in Kohlenstoffkompositen ist ein weit verbreiteter

Ansatz zur Optimierung der elektrochemischen Eigenschaften. Wie es die Ergebnisse zu den Untersuchungen zu Li_3VO_4 und ZnO demonstrieren, bildet der Kohlenstoff im Elektrodenmaterial ein Netz aus leitfähigen Pfaden und verhindert damit die Bildung inaktiver Bereiche, was zu höheren spezifischen Kapazitäten führt. Dieser Effekt ist wiederum von den Transporteigenschaften, nicht vom vorliegenden Speichermechanismus abhängig. So hat im Fall von MoO_2 aufgrund dessen gute metallartige elektronische Leitfähigkeit ein höherer Anteil an Kohlenstoff nahezu keine Auswirkung auf die spezifische Kapazität. Die Ergebnisse zu den Untersuchungen an Li_3VO_4, MoO_2 und ZnO zeigen, dass der Verbund in einem Kohlenstoff unabhängig vom vorliegenden Speichermechanismus einen positiven Effekt auf die Zyklenstabilität hat, wobei teils unterschiedliche Ursachen zugrunde liegen. Zum einen verbessert die Kohlenstoffmatrix im Elektrodenmaterial deren strukturelle Stabilität, indem sie als Puffer der Volumenänderungen dient, die beim Zyklieren auftreten, und verhindert, dass das Elektrodenmaterial pulverisiert und aggregiert was den elektrischen Kontaktverlust und die Bildung inaktiver Bereiche im Material zur Folge hätte. Bei Konversions- und legierungsbildenden Materialien ist die Pufferfunktion des Kohlenstoffs aufgrund der größeren Volumenänderungen von höherer Bedeutung als bei Interkalationsmaterialien. Im Fall von Li_3VO_4 schützt er zusätzlich die Oberfläche der Partikel vor Nebenreaktionen mit dem Elektrolyten.

Die Untersuchungen an den Kompositen G-HCS-Mn_3O_4 und $CoFe_2O_4$@CNT mit Kohlenstoffnanostrukturen zeigen, dass sowohl die Funktionalisierung mit Kohlenstoffnanoröhrchen als auch mit -hohlkugeln sich als erfolgreiche Strategien erweisen zur Optimierung der elektrochemischen Performance konversionsbasierter Übergangsmetalloxide. Sie vereint die beiden Lösungsansätze, Nanoskalierung und den Verbund mit Kohlenstoff. Die Kohlenstoffmodifikationen fungieren als leitfähiges Netzwerk, das in Kombination mit den nanoskaligen Abmessungen zu einer verbesserten Reaktionskinetik führen und eine hohe elektrochemische Aktivität der Übergangsmetalloxide sichert. Außerdem kann die Problematik einer schlechten Zyklenstabilität, die Konversionsmaterialien üblicherweise aufweisen, entgegengewirkt werden. Die nanoskaligen Partikel im Inneren der Kohlenstoffmodifikationen nehmen aufgrund der geringeren absoluten Effekte weniger Schaden von starken Volumenänderungen. Außerdem bietet das Kohlenstoffnetzwerk eine höhere strukturelle Stabilität und gewährleistet auch bei Schäden weiterhin die leitfähige Anbindung der Partikel.

Im Folgenden werden die Ergebnisse der Komposite G-HCS-Mn_3O_4 und $CoFe_2O_4$@CNT denen des früher untersuchten Komposits Mn_3O_4@CNT ([59], Anhang) vergleichend gegenübergestellt. In Abb. 5.3 sind die Beiträge der Übergangsmetalloxide zu den Kompositkapazitäten jeweils normiert auf deren theoretische Kapazität aufgetragen. Sowohl die CNTs als auch

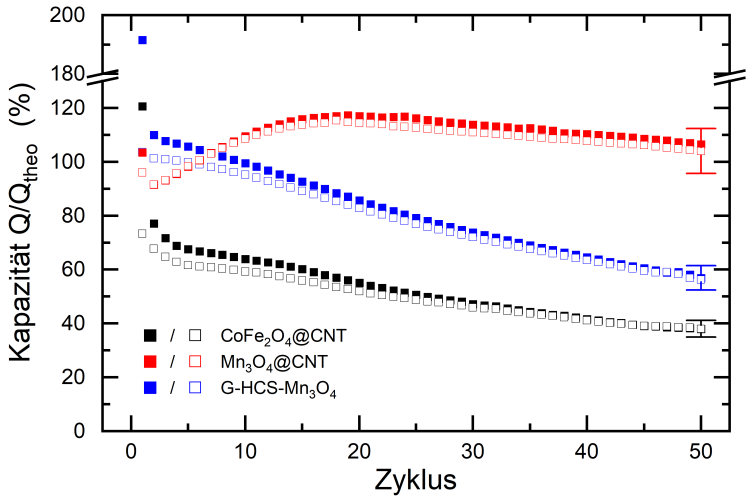

Abbildung 5.3: Vergleich der Beiträge der Übergangsmetalloxide zu den Kompositkapazitäten von $CoFe_2O_4$@CNT, Mn_3O_4 und G-HCS-Mn_3O_4 jeweils normiert auf deren theoretische Kapazität.

die HCS können gewährleisten, dass die Konversionsreaktion von Mn_3O_4 vollständig und reversibel umgesetzt wird. Im Vergleich zu den HCS scheinen die CNTs jedoch eine stabilere Umgebung für das Manganoxid zu bieten. Die Zyklenstabilität des Manganoxids, das in den CNTs eingekapselt ist, ist deutlich höher, was vermutlich auf die kleinere Partikelgröße zurückzuführen ist. Die Größe der Mn_3O_4-Partikel im Inneren der CNTs (Innendurchmesser: 35 nm) beträgt nur 15 ± 7 nm, wohingegen die Größe der Partikel im Innern der HCS (Innendurchmesser: 200 nm) um 100 ± 10 nm liegt. Ein Lösungsansatz, um die Zyklenstabilität des Komposits G-HCS-Mn_3O_4weiter zu optimieren, ist die Verwendung von HCS mit kleinerem Innendurchmesser. Bei der Synthese von HCS mittels Siliziumkugelmatrizen lässt sich der Innendurchmesser und die Schalendicke leicht kontrollieren. Im Vergleich der beiden Komposite mit CNTs schneidet Mn_3O_4@CNT sowohl in Bezug auf die elektrochemische Aktivität als auch die Zyklenstabilität des eingekapselten Übergangmetalloxids deutlich besser ab. Beides ist vermutlich darauf zurückzuführen, dass anders als bei Mn_3O_4@CNT im Komposit $CoFe_2O_4$@CNT $CoFe_2O_4$-Partikel auch außerhalb der CNTs vorliegen, die zudem nicht nanoskalig sind. Aufgrund dessen unterliegen sie den negativen Auswirkungen, die mit den großen Volumenänderungen bei der Konversion verbunden sind, wie die Zerstörung der Elektrodenstruktur und der Ablösung vom leitfähigen Kohlenstoffnetzwerk. Durch eine Optimierung des Füllprozesses könnte dies verhindert werden.

Insgesamt zeigen die Ergebnisse der vorgestellten Untersuchungen, dass die elektrochemischen Eigenschaften von interkalations- und konversionsbasierten Übergangsmetalloxide durch morphologische Modifikation und den Verbund mit Kohlenstoff signifikant verbessert

werden können. Durch die gezielte Kontrolle der Partikelgröße und Morphologie kann sowohl der ionische als auch elektronische Transport im Elektrodenmaterial optimiert werden kann. Darüber hinaus können dadurch auch alternative Speichermechanismen induziert werden. So begünstigt eine große spezifische Oberfläche die schnelle und weniger destruktive pseudo-kapazitive Ladungsspeicherung wie die Untersuchungen an V_2O_3/C zeigen. In Bezug auf die strukturelle Stabilität profitieren insbesondere Konversions- und legierungsbildende Materialien von kleineren Partikelgrößen und den Verbund mit Kohlenstoff. Des Weiteren kann bei elektronisch schlecht leitenden Anodenmaterialien durch den Verbund mit Kohlenstoff die Reaktionskinetik und die elektrochemische Aktivität der Materialien verbessert werden. Entscheidend für den Erfolg bei der Entwicklung neuer Anodenmaterialien für hochleistungsfähige Lithium-Ionen-Batterien ist die gezielte Anpassung des Materialdesigns an die jeweiligen intrinsischen Eigenschaften der Materialien, wie der vorliegende Speichermechanismus und die elektronische und ionische Leitfähigkeit.

Anhang

molecules

MDPI

Review

Filled Carbon Nanotubes as Anode Materials for Lithium-Ion Batteries

Elisa Thauer [1], Alexander Ottmann [1], Philip Schneider [1], Lucas Möller [1], Lukas Deeg [1], Rouven Zeus [1], Florian Wilhelmi [1], Lucas Schlestein [1], Christoph Neef [1], Rasha Ghunaim [2,3], Markus Gellesch [2], Christian Nowka [2], Maik Scholz [2], Marcel Haft [2], Sabine Wurmehl [2,4], Karolina Wenelska [5], Ewa Mijowska [5], Aakanksha Kapoor [6], Ashna Bajpai [6], Silke Hampel [2] and Rüdiger Klingeler [1,7,*]

[1] Kirchhoff Institute for Physics, Heidelberg University, INF 227, 69120 Heidelberg, Germany; elisa.thauer@kip.uni-heidelberg.de (E.T.); alex.ottmann@posteo.de (A.O.); schneider_philip@web.de (P.S.); lucas.moeller@me.com (L.M.); lukas-deeg@gmx.de (L.D.); rouven.zeus@gmx.net (R.Z.); florianwilhelmi@gmx.de (F.W.); lucasschlestein@gmx.de (L.S.); Christoph.Neef@isi.fraunhofer.de (C.N.)

[2] Leibniz Institute for Solid State and Materials Research (IFW) Dresden, 01069 Dresden, Germany; rgonaim@ppu.edu (R.G.); M.Gellesch@bham.ac.uk (M.G.); c.nowka@ifw-dresden.de (C.N.); maik.scholz@ifw-dresden.de (M.S.); m.haft@ifw-dresden.de (M.H.); s.wurmehl@ifw-dresden.de (S.W.); s.hampel@ifw-dresden.de (S.H.)

[3] Department of Applied Chemistry, Palestine Polytechnic University, Hebron P.O. Box 198, Palestine

[4] Institute for Physics of Solids, Technical University of Dresden, 01062 Dresden, Germany

[5] Nanomaterials Physicochemistry Department, Faculty of Chemical Technology and Engineering, West Pomeranian University of Technology, 71-065 Szczecin, Poland; Karolina.Wenelska@zut.edu.pl (K.W.); emijowska@zut.edu.pl (E.M.)

[6] Indian Institute of Science Education and Research, Pune 411 008, India; aakanksha.kapoor@students.iiserpune.ac.in (A.K.); ashna@iiserpune.ac.in (A.B.)

[7] Centre for Advanced Materials (CAM), Heidelberg University, INF 225, 69120 Heidelberg, Germany

* Correspondence: klingeler@kip.uni-heidelberg.de

Received: 3 February 2020; Accepted: 23 February 2020; Published: 27 February 2020

Abstract: Downsizing well-established materials to the nanoscale is a key route to novel functionalities, in particular if different functionalities are merged in hybrid nanomaterials. Hybrid carbon-based hierarchical nanostructures are particularly promising for electrochemical energy storage since they combine benefits of nanosize effects, enhanced electrical conductivity and integrity of bulk materials. We show that endohedral multiwalled carbon nanotubes (CNT) encapsulating high-capacity (here: conversion and alloying) electrode materials have a high potential for use in anode materials for lithium-ion batteries (LIB). There are two essential characteristics of filled CNT relevant for application in electrochemical energy storage: (1) rigid hollow cavities of the CNT provide upper limits for nanoparticles in their inner cavities which are both separated from the fillings of other CNT and protected against degradation. In particular, the CNT shells resist strong volume changes of encapsulates in response to electrochemical cycling, which in conventional conversion and alloying materials hinders application in energy storage devices. (2) Carbon mantles ensure electrical contact to the active material as they are unaffected by potential cracks of the encapsulate and form a stable conductive network in the electrode compound. Our studies confirm that encapsulates are electrochemically active and can achieve full theoretical reversible capacity. The results imply that encapsulating nanostructures inside CNT can provide a route to new high-performance nanocomposite anode materials for LIB.

Keywords: filled carbon nanotubes; lithium-ion batteries; hybrid nanomaterials; anode material

1. Introduction

Lithium-ion batteries (LIB) offer high gravimetric and volumetric energy densities which renders them particularly suitable for mobile applications. In order to optimize their performance, in particular with larger energy density, there is a continuous search for novel electrode materials. Electrode materials based on conversion and alloying mechanisms promise extremely enhanced electrochemical capacities in lithium-ion batteries as compared to conventional materials [1–3]. However, severe fading of the electrochemical capacity due to fractionation, resulting from pronounced volume changes upon electrochemical cycling, is one of the major drawbacks with respect to application. In addition to volume changes associated with the conversion reaction, low electric conductivity of many conversion materials seriously hinders their applicability in secondary batteries [4]. Nanosizing promises enhanced capability to accommodate strain induced by electrochemical cycling and may reduce kinetic limitations of the macroscopic counterparts of electrode materials [5–7] since downsizing particles yields shorter diffusion lengths and hence enhances rate performances of electrode materials. However, low density limiting volumetric energy densities of actual electrodes as well as high surface areas are relevant issues to be considered in nanomaterials as well. High reactivity associated with high surface area typically promotes irreversible processes and associated electrolyte consumption. In this respect, due to carbon's restricted voltage regime of electrochemical activity, carbon (nano) coating is a valuable tool to protect active nanomaterials, thereby avoiding enhanced electrolyte degradation and associated (and potentially dangerous) gas production [8]. Downscaling materials towards carbon-shielded hybrid nanomaterials hence offers a route to obtain electrode materials for LIB with enhanced performance.

Rational design of electrode materials has to tackle the abovementioned issues of low electronic conductivity limiting many promising electrode materials as well as of large volume changes during electrochemical cycling, with the latter particularly causing electrode structure and particles distortions and hence strong performance fading. Hierarchical nanocomposite carbon/active material structures offer an effective way to solve these issues as such materials exploit size effects of the nanoscaled building blocks [9–14]. Mechanical strain arising from volume changes is additionally buffered by the hierarchical structures. In this way, such materials optimally maintain the integrity of the bulk material while offering improved electrical conductivity owing to a carbon-based backbone structure [15–28]. Moreover, a strong backbone structure improves the stability of the composite with respect to mechanical strain arising from volume changes during electrochemical cycling.

We report CNT-based composite nanomaterials with enhanced electrochemical performance realized by filling material into CNT (for a schematics see Figure 1) which is electrochemically active when nanoscaled [30]. CNT display excellent conductivity as well as mechanical and chemical stability which renders them an excellent carbon source in hybrid nanomaterials [31]. However, in conventional approaches using exohedrally functionalized CNT, synthesis of uniformly sized and shape-controlled nanoparticles is challenging. In addition, while the interconnected network of carbon nanotubes provides an electrically conducting backbone structure, decorated nanoparticles onto the outer CNT-walls tend to lose electrical contact upon cycling-induced disintegration and particular methods have to be developed to improve connection to CNT [32–35]. Our results demonstrate successful synthesis of hybrid nanomaterial of CNT filled with Mn_3O_4, $CoFe_2O_4$, Fe_xO_y, Sn, and CoSn and show the electrochemical activity of encapsulated materials. Encapsulates are either conversion or alloying electrode materials which perform the following general reactions upon electrochemical cycling, respectively [2,36,37]:

$$\text{Conversion:} \quad M_aO_b + 2bLi^+ + 2be^- \leftrightarrow aM^0 + bLi_2O \qquad (1)$$

$$\text{Alloying:} \quad M + x\ Li^+ + x\ e^- \leftrightarrow Li_xM\ (x < 4.25) \qquad (2)$$

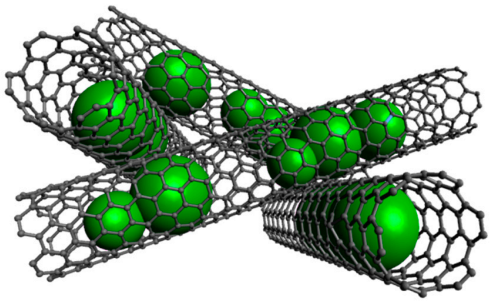

Figure 1. Schematics of nanocomposite material formed by interconnected carbon nanotubes (CNT) filled with high-capacity electrode materials. Essential characteristics are (1) size-controlled nanoparticles in the inner cavities of CNT which are separated from encapsulates in other CNT, (2) electrical contact of the incorporated material to a stable conductive network of CNT, (3) limitation of direct electrolyte/active material contact yielding and hence improved chemical stability. Created with Avogadro [29].

In this work, we demonstrate that in the case of conversion materials filled inside CNT, the encapsulated material completely participates in electrochemical cycling, i.e., the theoretical capacity is fully accessible. The backbone network of CNT is indeed unaffected by cracks of encapsulate which usually inhibit long-term stability. Our data hence imply that endohedrally functionalized CNT offer a promising route to new nanohybrid anode materials for LIB.

2. Synthesis and Characterization of Filled CNT

We report studies on hybrid nanomaterial of multiwalled carbon nanotubes (CNT) filled with Mn_3O_4, $CoFe_2O_4$, Fe_xO_y, Sn, and CoSn which have been fabricated by a variety of methods. Mostly, CNT of type PR-24-XT-HHT (Pyrograf Products, Inc., Cedarville OH, USA) have been used as templates. For introducing materials into the inner cavity of the CNT, mainly extensions of solution-based approaches reported in [38–43] have been applied [44,45]. This is illustrated by the example of Mn_3O_4@CNT which has been obtained by filling CNT with a manganese salt solution and a subsequent reducing step yielding homogeneously MnO-filled CNT (MnO@CNT) [4]. Subsequent heat treatment of MnO@CNT yields the complete conversion into Mn_3O_4@CNT, as confirmed by the XRD pattern in Figure 2. In case of filling with Co-Fe spinels, nitrate solutions of $Fe(NO_3)_3{\cdot}9H_2O$ (grade: ACS 99.0%–100.2%) and $Co(NO_3)_2{\cdot}6H_2O$ (grade: ACS 98.0%–102.0% metal basis) were used in stoichiometric ratios with respect to the metal ions (i.e., Fe:Co = 2:1). After adding CNT and treating the mixture in an ultrasonic bath with appropriate washing steps, the solid residue was dried and afterwards calcinated under argon flow atmosphere (100 sccm) at a temperature of 500 °C for 4 h to convert the nitrates into the corresponding cobalt ferrite. This is confirmed by XRD data in Figure 2 which indicate the presence of $CoFe_2O_4$. Pronounced peak broadening indicates the presence of nano-sized $CoFe_2O_4$ crystallites, with an estimated grain size of 20(5) nm by means of the Scherrer equation applied to the Bragg peak at 41.5°.

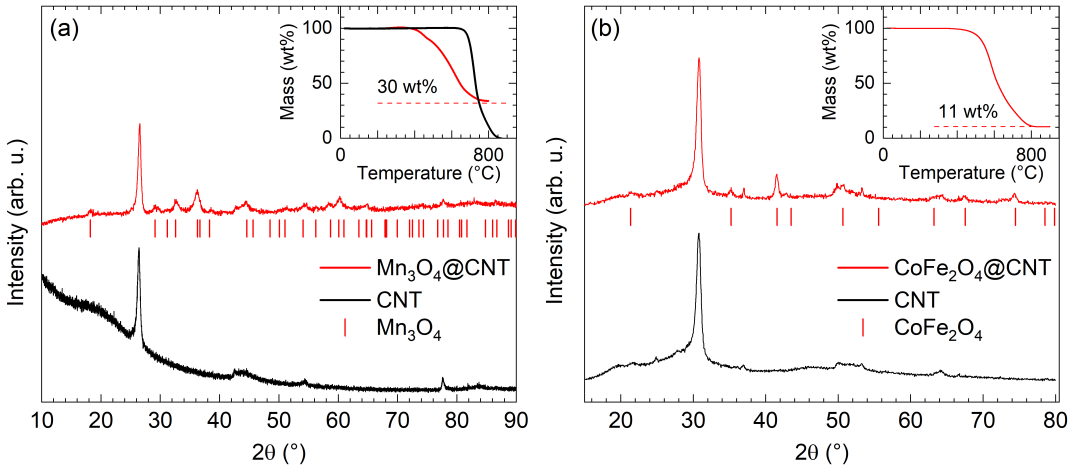

Figure 2. Left (**a**): PXRD patterns of Mn_3O_4@CNT and pure CNT. Vertical lines show the Bragg positions of Mn_3O_4 (space group $I4_1/amd$) [46]. Inset: Thermogravimetric analysis (TGA) data of Mn_3O_4@CNT and pure CNT. Right (**b**): PXRD patterns of $CoFe_2O_4$@CNT and of pristine CNT. Vertical ticks label Bragg positions of bulk $CoFe_2O_4$ (space group $Fd\bar{3}m$) [47]. Inset: TGA of $CoFe_2O_4$@CNT.

XRD patterns show relatively broad Bragg reflections which indicate small primary particle size of the noncarbon materials of the composite as expected for nanoparticles fitting inside the interior of CNT. This is confirmed by exemplary SEM and TEM studies presented in Figure 3. The images clearly show that the metal oxide nanoparticles are rather spherical and are located inside the CNT. Note the exception of possible nanowire formation in the case of metal-filled Sn@CNT as discussed in Section 3.4 (see Figure 15). The filling rate of Mn_3O_4@CNT is about 30(1) wt% and that of $CoFe_2O_4$@CNT (see the inset of Figure 2) is about 11(1) wt% as determined by thermogravimetric measurements (TGA).

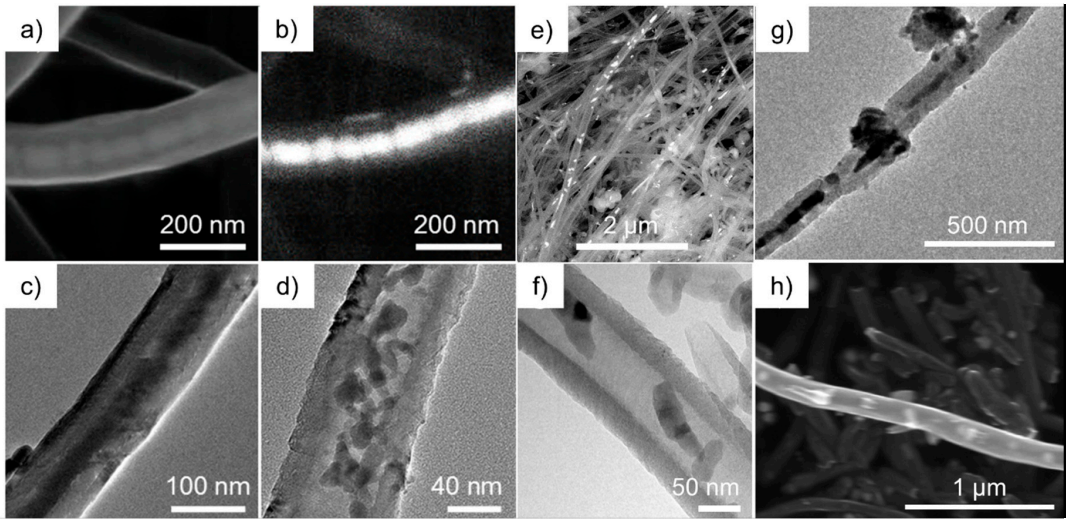

Figure 3. (**a**) SEM image of an individual Mn_3O_4@CNT (SE mode); (**b**) corresponding BSE mode image; (**c**,**d**) TEM images of different individual Mn_3O_4@CNT. Taken from [45]. (**e**) Overview SEM image of $CoFe_2O_4$@CNT (BSE mode); (**f**) TEM image of an individual $CoFe_2O_4$@CNT. (**g**) TEM image of an individual Fe_xO_y@CNT [48]. (**h**) SEM image of CoSn@CNT [49].

Electron microscopy confirms that the filling materials are located mainly inside the CNT. Exemplary SEM and TEM images are shown in Figure 3 (see also Figure 15 for Sn-filled CNT). In Mn_3O_4@CNT, the encapsulated particles are rather spherical with the average diameter of 15 ± 7 nm obtained by TEM analysis. Note, that this is smaller than the size-limiting inner diameter of the utilized CNT (~35 nm). The SEM overview image (Figure 3e) on $CoFe_2O_4$@CNT also confirms that the filling material is distributed along the inner cavity of the hollow CNT. TEM indicates spherical encapsulates as well as short rods inside CNT (Figure 3 e,f). Fe_xO_y@CNT (synthesis reported in [48]) appears to be mainly filled with α-Fe_2O_3 but also exhibits Fe_3O_4 as shown, e.g., by associated features in the magnetic susceptibility (see Section 3.3). Figure 3g also shows the presence of Fe_xO_y nanoparticles outside CNT. In addition to separated spherical nanoparticles, encapsulates in CoSn@CNT and Sn@CNT form also nanowires up to 1 μm length (see Figure 3h and Figure 15). In either case, the encapsulates fill the complete inner diameter of the CNT, which is about 50 nm [44]. In summary, the results show that our synthesis approaches result in CNT filled with nanoparticles whose diameters are limited by the inner diameter of the CNT.

3. Electrochemical Studies

3.1. Mn_3O_4@CNT [30,45]

Cyclic voltammetry studies on Mn_3O_4@CNT and on pristine CNT, performed in the voltage range of 0.01–3.0 V vs. $Li^{0/+}$ and recorded at a scan rate of 0.1 mV s^{-1}, confirm electrochemical activity of encapsulates (Figure 4). During the initial cycle, starting with the cathodic scan, five distinct reduction peaks (R1–R5) and three oxidation peaks (O1–O3) are observed. The redox pair R1/O1 around 0.1 V and the irreversible reduction peak R3 at 0.7 V can be attributed to processes related to multiwalled CNT (Figure 4a). The irreversible reaction peak R3 signals formation of the solid electrolyte interphase (SEI) expected for carbon-based (here: CNT) systems [50]. The pronounced redox pair R1/O1 demonstrates that the bare CNT subsystem in the hybrid material is electrochemically active as it signals (de)lithiation of Li^+ ions between the layers of CNT [51,52]. Slight splitting of oxidation peak O1 indicates a staging phenomenon reported for graphite electrodes [37], and very similar behavior upon cycling is found in bare CNT [45]. All other features observed in Figure 4b are ascribed to the electrochemical reaction mechanism which has been reported for Mn_3O_4 as follows [53,54] (for further details see [45]):

(A) $Mn_3(\frac{1}{3}\cdot II,\frac{2}{3}\cdot III)O_4 + Li^+ + e^- \rightarrow LiMn_3(\frac{2}{3}\cdot II,\frac{1}{3}\cdot III)O_4$

(B) $LiMn_3O_4 + Li^+ + e^- \rightarrow Li_2O + 3\cdot Mn(II)O$

(C) $Mn(II)O + 2\cdot Li^+ + 2\cdot e^- \leftrightarrow Li_2O + Mn(0)$

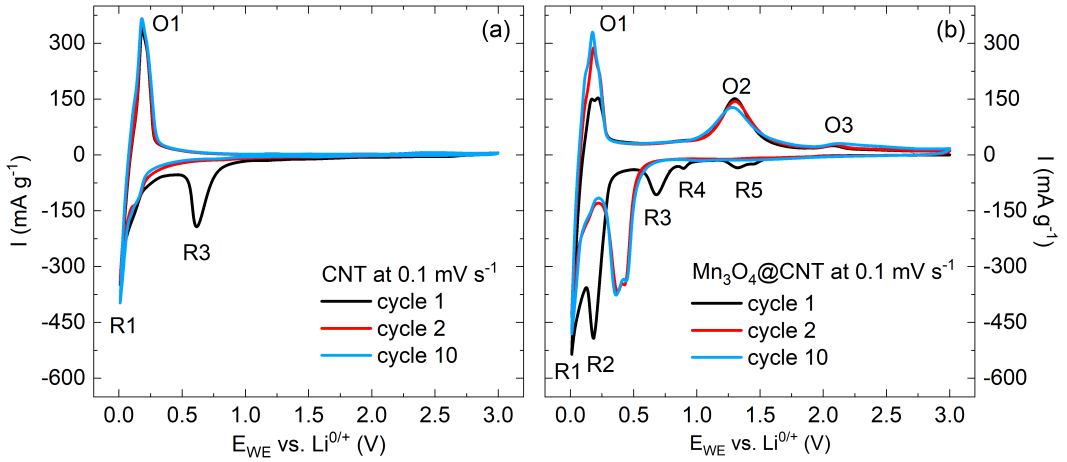

Figure 4. Cyclic voltammograms of (**a**) pristine CNT and (**b**) Mn_3O_4@CNT at 0.1 mV s^{-1} [30].

The cyclic voltammograms (CVs) confirm electrochemical activity of encapsulated Mn_3O_4. Absence of significant changes between cycles 2 and 10 indicate good cycling stability which will be investigated in more detail below. Since the materials associated with the mechanism detailed in Equations (A) to (C) exhibit strong differences in magnetic properties, magnetic studies are suitable to follow the redox reaction. In particular, there are strong changes of magnetic properties upon electrochemical cycling from ferrimagnetic Mn_3O_4 to antiferromagnetic MnO (Figure 5; for further magnetization data see [45]). Pristine Mn_3O_4@CNT shows ferrimagnetic order below T_C = 42 K as indicated by the magnetization data. In contrast, materials extracted after step (B) of the abovementioned redox reactions, i.e., after galvanostatic reduction at 5 mA g^{-1} down to 0.5 V and passing the reduction peaks R5, R4, and R3 labelled in Figure 4b, displays nearly no traces of ferrimagnetic material. Quantitatively, the magnetization data indicate about 1% remainder of ferrimagnetic Mn_3O_4 after the first half cycle. Meanwhile, antiferromagnetic order is found below a temperature of ~120 K, which is expected for MnO [55] and is in agreement with Equation (B). Hence, our magnetometry data confirm electrochemical reactions as postulated in Equations (A–C) by tracking down individual magnetic species.

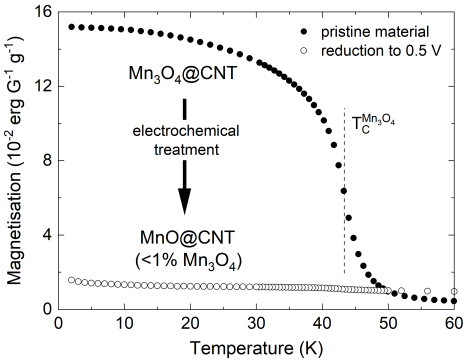

Figure 5. Magnetization of pristine and electrochemically cycled Mn_3O_4@CNT measured at B = 0.1 T (FC). The vertical line indicates the ferrimagnetic ordering temperature in Mn_3O_4.

Charge and discharge studies at specific current rates (Figure 6) display plateau-like regions in the voltage profiles signaling the redox features discussed above by means of Figure 4. In the initial cycle performed at 50 mA g^{-1}, specific charge and discharge capacities of 677 and 455 mAh g^{-1}, respectively, are achieved. Increasing the charge/discharge current to 100 and 250 mA g^{-1},

respectively, does not significantly affect the shape of the curves but yields smaller discharge capacities, e.g., 331 mAh g^{-1} after 30 cycles. For higher currents, the plateaus corresponding to delithiation and lithiation of CNT vanish, while the conversion reaction (Equation (C)) is still visible in the data. The rate capability studies presented in Figure 6 display pronounced capacity losses when increasing charge/discharge currents. Specifically, maximum discharge capacities of 468, 439, 349, 245, and 148 mAh g^{-1} are reached at 50, 100, 250, 500 and 1000 mA g^{-1}, respectively.

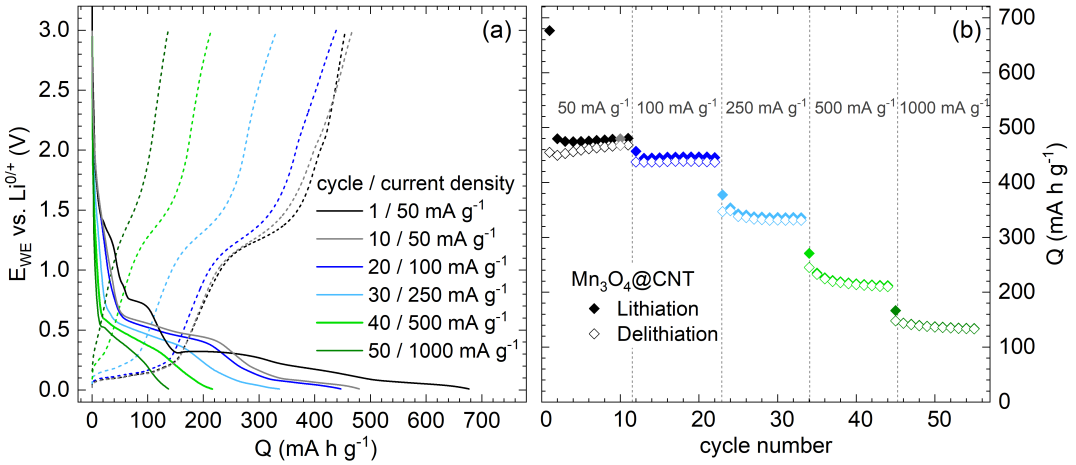

Figure 6. Rate capability studies of Mn3O4@CNT at 50, 100, 250, 500, and 1000 mA g^{-1}. (**a**) Potential profiles of specific lithiation (solid lines) and delithiation cycles (dashed lines). (**b**) Specific charge/discharge capacities upon cycling [30].

In order to assess the electrochemical performance of the composite with particular emphasis on the encapsulate, evolution of capacities at 100 mA g^{-1} (galvanostatic cycling with potential limitation) upon cycling of Mn_3O_4@CNT and pristine CNT is shown in Figure 7. While the initial half cycle is strongly affected by irreversible processes associated with solid electrolyte interface (SEI) formation, the Mn_3O_4@CNT nanocomposite exhibits increasing capacities for approximately 15 cycles in contrast to decreasing values of pristine CNT. The nanocomposite reveals a maximum discharge capacity of 463 mA h g^{-1} in cycle 18, of which 93% is maintained after 50 cycles (429 mA h g^{-1}). Thus, incorporation of Mn_3O_4 into CNT leads to more than 40% enhanced specific capacities on average as compared to unfilled CNT. The data, i.e., on filled and unfilled CNT, enable calculating the specific capacity of incorporated Mn_3O_4 (29.5 wt%). The encapsulate's initial capacity of about 700 mAh g^{-1} increases significantly to 829 and 820 mAh g^{-1} (cycle 18) and declines thereafter, with capacity retention of around 90% after 50 cycles. The Mn_3O_4 capacity even exceeds the theoretical expectations of the conversion reaction (C) from cycle 6 on (dashed line in Figure 7). This might be associated with a capacity contribution due to oxidative feature O3 (Figure 4b), which supposedly indicates the back-formation of Mn_3O_4 and corresponding reduction processes [56,57]. Note, however, the error bars of 5% due to mass determination of encapsulate and subtraction of data on pristine CNT. Initial capacity increase was also observed in previous studies on Mn_3O_4/CNT composites [58,59].

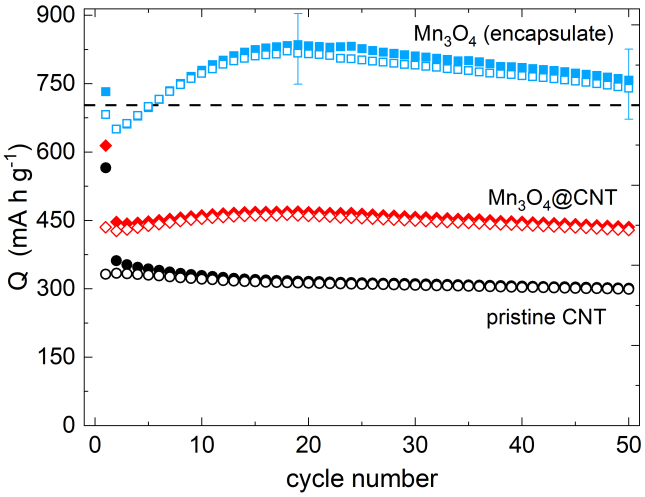

Figure 7. Specific charge/discharge capacities at 100 mA g^{-1} of pristine CNT, Mn_3O_4@CNT, and calculated capacity of the encapsulate. The dashed line shows the theoretical capacity of the reversible conversion reaction (C) [30].

Our analysis shows that full conversion between MnO and metallic Mn can be achieved reversibly and the maximum of the contributed capacity by the Mn_3O_4 encapsulate is accessible (Figure 7). In particular, the nanoparticles inside CNT are completely involved in the electrochemical processes. This finding is supported by the fact that the active material inside CNT experiences distinct structural changes, as evidenced by TEM studies (Figure 8). Figure 8 b,c presents materials after 13 galvanostatic cycles, at 100 mA g^{-1}, taken after delithiation and lithiation. No clear differences are observed between the lithiated and the subsequently delithiated material. In both cycled materials, the encapsulate which initially exhibits well-defined, rather spherical nanoparticles has developed extended patches. The TEM image also shows lower contrast of the encapsulate to the CNT environment which is indicative of lower density of the encapsulate. Equations (A) and (B) indeed suggest rather larger volume expansion of Mn_3O_4 during initial lithiation and concomitant agglomeration as well as amorphization of the filling which is in agreement with the TEM results. Notably, despite the strong changes of encapsulate, CNT mantles still display the characteristic graphitic layers of multiwalled carbon nanotubes (see Figure 8d). Hence, electrochemical cycling does not severely damage the structure of the CNT. Furthermore, an amorphous layer of ~5 nm thickness can be observed on top of the graphitic CNT layers, which can be attributed to the SEI. The TEM analysis hence shows that the CNT indeed offer a stable environment for the manganese oxides which is able to accommodate the strain due to volume expansion during electrochemical cycling and guarantees a consistent electrical contact to the active material.

Figure 8. TEM images of (**a**) uncycled, (**b**) galvanostatically lithiated, and (**c**) delithiated Mn_3O_4@CNT.

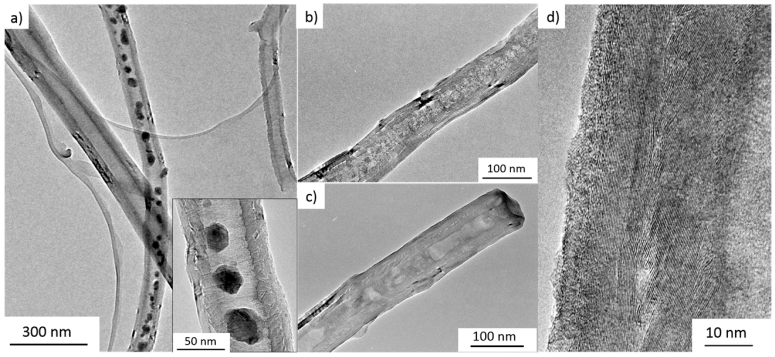

(**d**) High-resolution TEM image of a CNT shell of delithiated material after 13 cycles. Taken from [45].

3.2. $CoFe_2O_4$@CNT

As shown in Figure 3 f,g, nanosized particles of cobalt ferrite $CoFe_2O_4$ are incorporated into CNT by a similar procedure as applied in the case of Mn_3O_4@CNT. The mass content of $CoFe_2O_4$ in the composite materials however amounts to only 11 wt%, leading to smaller effects of the encapsulate. In order to evaluate the benefits of CNT shells, the electrochemical performance of the nanocomposite $CoFe_2O_4$@CNT is compared to that of bare $CoFe_2O_4$ nanoparticles (Figure 9). In general, electrochemical lithium storage of up to 8 Li^+/f.u. in $CoFe_2O_4$ follows a conversion mechanism (Equation (D)), which may be preceded by initial intercalation of Li^+ ions into the original ferrite structure [60]:

(D) $CoFe_2O_4 + 8\ Li^+ + 8\ e^- \rightarrow Co + 2\ Fe + 4\ Li_2O$

(E) $Co + 2\ Fe + 4\ Li_2O \leftrightarrow CoO + Fe_2O_3 + 8\ Li^+ + 8\ e^-$

Both processes show up as redox features in the CVs in Figure 9 which for $CoFe_2O_4$@CNT also show features present in pristine CNT (Figure 4a) [45,51,61,62].

In bare $CoFe_2O_4$ nanoparticles (Figure 9a), the initial half cycle reduction peaks indicate, at 1.5 V, initial intercalation into the spinel structure (R0), and at 1.1 and 0.55 V indicate R1/SEI formation. In addition, there is a shoulder at 0.95 V and a peak at 0.01 V (R2). In all subsequent reductive half cycles, the most pronounced reduction peak occurs at 0.85 V (R1*). Expectedly, R0 vanishes after the first cycle. The oxidative scans display a broad oxidation double peak between 1.5 V and 2.5 V with a maximum intensity around 1.65 V (O1). R1 most likely indicates both conversion of the spinel to Co and Fe [60,63] and SEI formation [64], while R2 signals intercalation of Li^+ ions into added carbon black [64,65]. Upon further cycling, Co and Fe oxidize to CoO and Fe_2O_3, respectively (O1), followed by the corresponding conversion processes at R1* (Equation (D)) [36,63,66–69].

CVs on $CoFe_2O_4$@CNT in Figure 9b show features associated with $CoFe_2O_4$ superimposed by redox peaks related to CNT. In the initial cycle, features attributed to $CoFe_2O_4$ appear at 1.6 (R0), 1.2, and 0.7 V (SEI) with a shoulder at 0.8 V (R1). Upon further cycling, they are shifted to 1.6 (R0) and 0.9 V (R1*). Reversible oxidation peaks appear at similar voltages as compared to bare $CoFe_2O_4$ nanoparticles, i.e., between 1.5 and 2.0 V with a maximum at 1.55 V (O1). The results imply smaller overpotentials in $CoFe_2O_4$@CNT as compared to the bare $CoFe_2O_4$ nanoparticles, indicating improved energy efficiency. Furthermore, cycling stability is superior, yielding noticeable redox activity of the $CoFe_2O_4$ encapsulate in the 10th cycle. Both improvements can be attributed to benefits of the $CoFe_2O_4$@CNT composite material, i.e., to enhanced overall conductivity and better structural integrity.

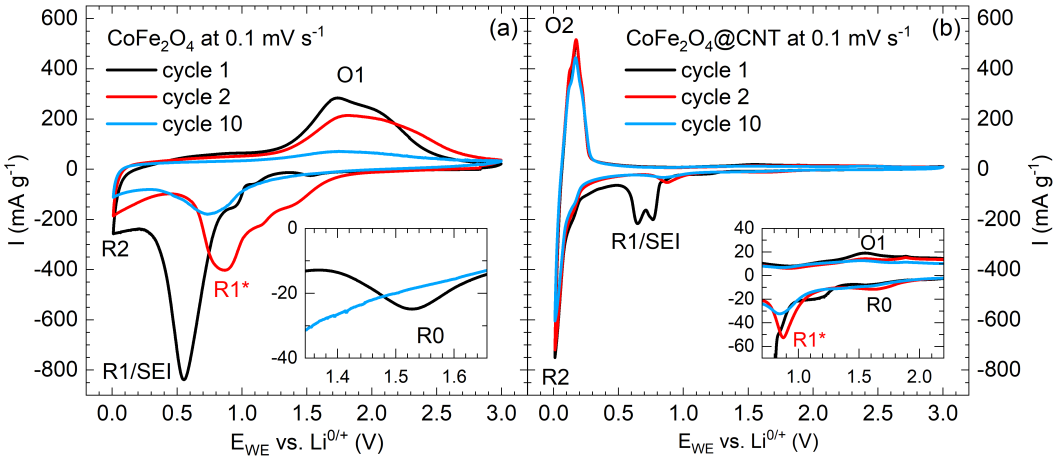

Figure 9. Cyclic voltammograms of (**a**) pristine $CoFe_2O_4$ and (**b**) $CoFe_2O_4$@CNT, at 0.1 mV s^{-1} [30].

These conclusions are corroborated by galvanostatic cycling with potential limitation (GCPL) data (Figure 10). Firstly, higher capacities of $CoFe_2O_4$@CNT as compared to pristine CNT imply electrochemical activity of encapsulates for 60 cycles under study. In addition to irreversible effects associated with SEI formation, there are capacity losses, in particular in initial cycles, so that the electrode demonstrates only 97% of Coulombic efficiency after 15 cycles. Capacity retention of $CoFe_2O_4$@CNT amounts to a fair value of 76% after 60 cycles (243 mAh g^{-1}). Analogously to Section 3.1, the specific contribution of $CoFe_2O_4$ is evaluated by subtracting the measured capacities of pristine CNT, weighted with the mass ratio of 89:11 (CNT:$CoFe_2O_4$). The analysis shows (Figure 10b) that both for pristine and CNT-encapsulated $CoFe_2O_4$ there are pronounced capacity losses upon cycling while the initial capacities exceed the theoretical maximum value of 914 mAh g^{-1} due to SEI formation. CNT-encapsulated active material clearly outperforms bare $CoFe_2O_4$ nanoparticles. To be specific, after 20 cycles, 475 mAh g^{-1} (71%) is retained in $CoFe_2O_4$@CNT while the bare particles show 190 mAh g^{-1} (22%). This result again demonstrates that embedding nanosized $CoFe_2O_4$ inside CNT partly compensates for the typical capacity fading associated with the conversion reactions upon electrochemical delithiation or lithiation known for spinel materials.

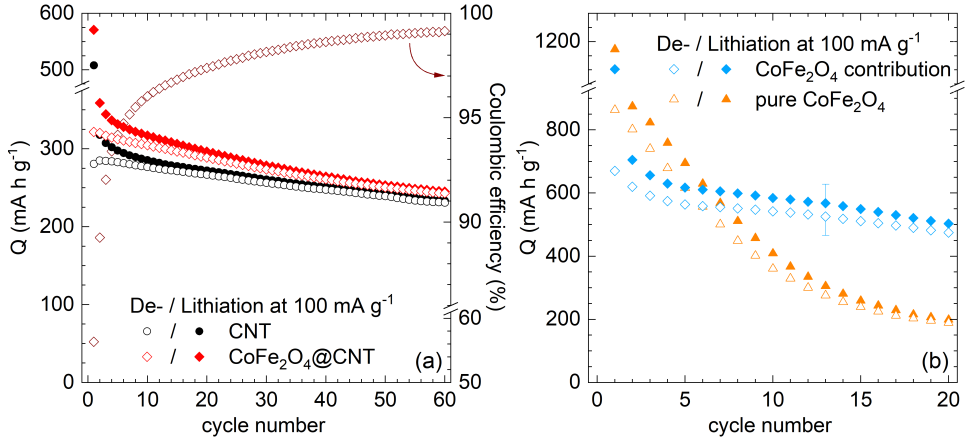

Figure 10. (**a**) Specific charge/discharge capacities, at 100 mA g^{-1}, of pristine CNT and $CoFe_2O_4$@CNT as well as the Coulombic efficiencies of the latter. (**b**) Capacity contribution of the encapsulated $CoFe_2O_4$ in comparison to pristine $CoFe_2O_4$ [29].

While encapsulated $CoFe_2O_4$@CNT demonstrates electrochemical activity, it is illustrative to compare the results with alternative carbon/$CoFe_2O_4$ hybrid nanomaterials. Direct comparison is often hindered by the fact that the carbon-related capacity is not always subtracted as done here. For many carbon/$CoFe_2O_4$ hybrid materials, much higher values than maximum theoretical capacity of $CoFe_2O_4$ are reported. A value of 1046 mAh g^{-1} is reported for mesoporous $CoFe_2O_4$ nanospheres cross-linked by carbon nanotubes [70]. Porous carbon nanotubes decorated with nanosized cobalt ferrite show 1077 mAh g^{-1}, after 100 cycles [69]. More than 700 mAh g^{-1} of total capacity of the composite was obtained when $CoFe_2O_4$ is encapsulated into carbon nanofibers with 36% carbon content [71]. A list of recently achieved record values may be found in [72]. We note that excessive capacity beyond the theory values in transition metal oxide/carbon nanomaterials have been associated, e.g., to decomposition of electrolyte and formation of a polymer/gel-like film on the nanoparticles [73]. Another hypothesis refers to interface charging effects by lithium accommodation at the metal/Li_2O interface [74]. Our data indeed suggest that surface effects might be relevant as CNT-encapsulation of active material evidently suppresses this phenomenon.

3.3. Fe_xO_y@CNT and CNT@Co_3O_4

Fe_xO_y@CNT has been synthesized as described in [48]. XRD and magnetic characterization studies [30] imply the presence of several iron oxides (i.e., of α-Fe_2O_3 as well as of γ-Fe_2O_3 or/and Fe_3O_4) in the materials. While the main phase appears as α-Fe_2O_3, magnetic studies show both the Morin and Verwey transitions which enable to unambiguously identify α-Fe_2O_3 and Fe_3O_4, respectively. Note, that the presence of antiferromagnetic γ-Fe_2O_3 can neither be confirmed nor excluded by our magnetic studies. Analyzing the magnetization data indicates the presence of ferromagnetic iron oxide (i.e., γ-Fe_2O_3 and/or Fe_3O_4) of about 30(8) wt%.

The CVs shown in Figure 11a display two reductions (R1, R2) and two oxidations (O1, O2) which are observed in all cycles. We attribute R1/O1 to electrochemical activity of CNT. Except for typical initial irreversible effects at R2/SEI, all features are well explained by electrochemical processes known in iron oxides. Mechanisms in α-Fe_2O_3 as identified by Larcher et al. [75,76] involve Li-intercalation in nanoparticles, followed by conversion to metallic Fe and Li_2O via intermediately formed cubic $Li_2Fe_2O_3$. This process is partly reversible as it includes formation of FeO [77] and γ-Fe_2O_3 [78,79]. For Fe_3O_4, after initial intercalation, $Li_2Fe_3O_4$ is formed which is subsequently reduced to Fe and Li_2O [80,81]. In all iron oxides present in Fe_xO_y@CNT, including γ-Fe_2O_3, electrochemical processes display similar features which are not well distinguishable [82,83]. The inset of Figure 11a presents a weak reduction peak R3 which we attribute to abovementioned Li-intercalation into iron oxides. Note, that the second peak in the inset is due to an intrinsic cell setup effect. Conversion reactions appear at around 0.6 V and are signaled by feature R2. The shoulder at 0.8 V indicates the successive nature of the lithiation processes. Upon cycling, R2 shifts to 0.9–1.2 V, thereby indicating significant structural changes due to the initial conversion process. The large width of O2 might indicate several oxidation processes upon delithiation. The evolution of the oxidation features upon cycling implies severe fading effects.

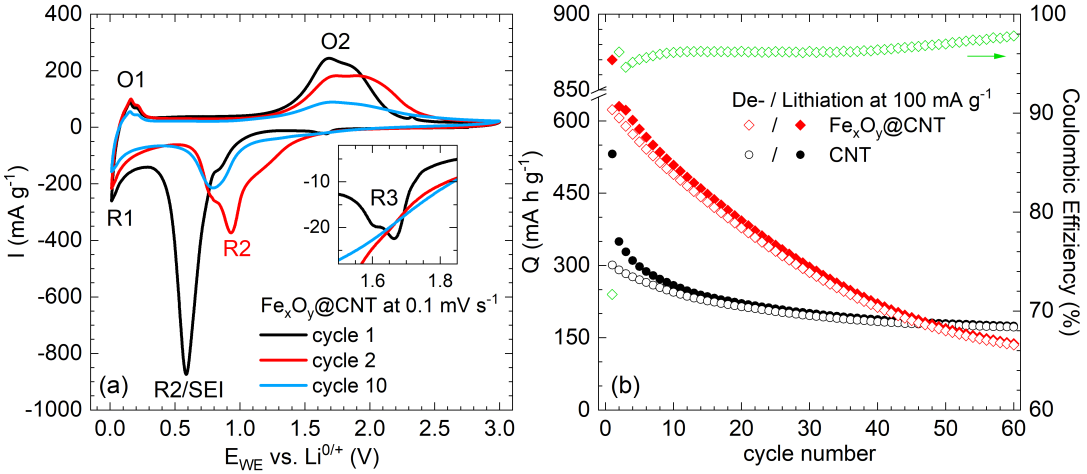

Figure 11. (**a**) Cyclic voltammogram of Fe_xO_y@CNT at 0.1 mV s^{-1}. (**b**) Specific charge/discharge capacities, at 100 mA g^{-1}, of pristine CNT (Pyrograf Products, type PR-24-XT-HHT) and Fe_xO_y@CNT, as well as the Coulombic efficiencies of the latter [30].

This is confirmed by the data in Figure 11b which presents specific charge/discharge capacities of Fe_xO_y@CNT obtained at 100 mA g^{-1}. Respective data on bare CNT (Pyrograf Products, type PR-24-XT-HHT) are shown for comparison. The initial capacities of the composite amount to 870 and 624 mAh g^{-1}, which reflects initial irreversible processes. There is a strong decay in capacity which yields only 78% (489 mAh g^{-1}) in cycle 10 and 26% (165 mAh g^{-1}) in cycle 50 of the initial discharge capacity. The results clearly show that envisaged improvement of cycling stability due to encapsulation into CNT is not achieved. Presumably, iron oxide content outside CNT is rather large so that a significant part of functionalization is exohedral. In such case, we assume that volume changes upon cycling leads to detachment of these particles from the CNT network which results in diminished electrochemical activity. In contrast, [84] reports α-Fe_2O_3-filled CNT which show 90% capacity retention in cycle 50.

Inferior stability of exohedrally functionalized CNT upon electrochemical cycling is further confirmed, e.g., for CNT decorated by mesoporous cobalt oxide (CNT@Co_3O_4). The material was synthesized as reported in [34]. The composite exhibits 41 wt% of mesoporous Co_3O_4 spheres with mean diameters between 100 and 250 nm decorated to the CNT network. The electrochemical behavior of CNT@Co_3O_4 (Figure 12a) during the initial cycle shows SEI formation and the initial reduction process of Co_3O_4 to metallic cobalt and formation of amorphous Li_2O during the initial cycle. Double peaks appearing in cycle 2 correspond to a multistep redox reaction caused by the Co^{2+}/Co^0 and Co^{3+}/Co^{2+} couples [85,86]. The integrated specific capacities calculated from the CVs (Figure 12b) display significant capacity fading upon continued cycling. For comparison, a blend of separately fabricated CNT and Co_3O_4 nanoparticles were mechanically mixed postsynthesis in the same ratio of 59% CNT and 41% Co_3O_4 which, according to TGA, is realized in the decorated CNT@Co_3O_4 nanocomposite. The blend's CV shows similar peak positions as found in CNT@Co_3O_4, and a similarly high reductive capacity is measured for the postsynthesis blend in the first cycle. However, the associated reversible capacity is much lower as compared to the CNT@Co_3O_4 hybrid nanomaterial and the irreversible loss between charge and discharge capacity is higher. After a few cycles, both the blend and CNT@Co_3O_4 show similarly low performance, which indicates that the benefit of attaching mesoporous Co_3O_4 to the surface of CNT has completely faded, presumably due to detachment of the mesoporous Co_3O_4 nanospheres [34].

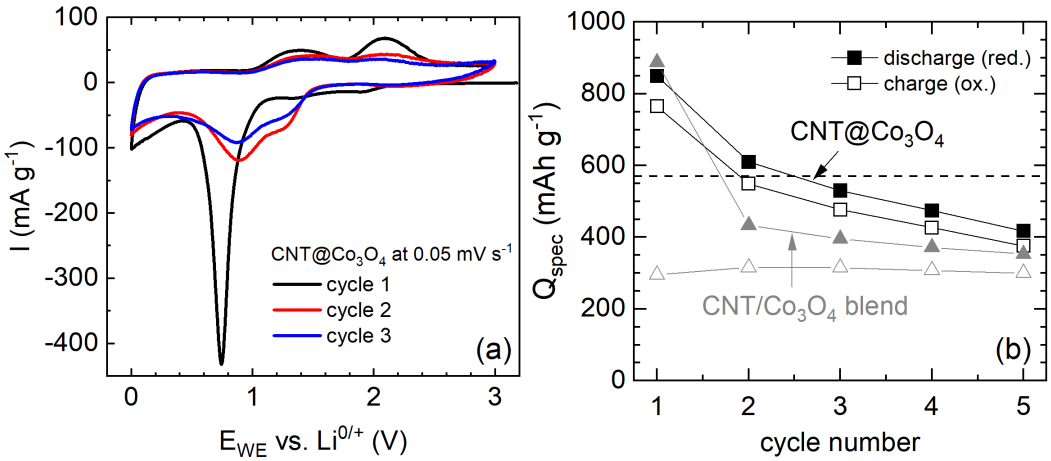

Figure 12. (**a**) CV curves of CNT@Co_3O_4, at 0.05 mV s^{-1} in the voltage range of 0.01–3.00 V. Integrated charge and discharge capacities for five cycles as deduced from CV [32].

3.4. Sn@CNT and CoSn@CNT

The alloying process described by Equation (2) implies feasibility of (semi)metallic electrode materials for electrochemical energy storage. Using M = Ge, Sn, the alloy Li_xM is formed with x up to 4.25 Li^+/f.u. [87,88]. While Ge exhibits lower molecular weight and good Li^+-diffusivity, Sn is much cheaper and exhibits higher electrical conductivity [89]. For Sn, the most Li-rich alloy is $Li_{17}Sn_4$ (= $Li_{4.25}Sn$) which implies a theoretical capacity of 960 mAh g^{-1} [90]. Upon lithiation, several stable alloys such as LiSn and Li_7Sn_2 are formed, resulting in complex (de)alloying processes of several stages which are associated with large volume changes [91]. In CoSn@CNT, Co is electrochemically inactive and is supposed to buffer the volume changes as similarly done in a commercial Sn-Co-C composite by Sony [87,92,93].

Synthesis of Sn@CNT has been published in [44]. While the encapsulate in Sn@CNT is β-Sn with a filling ratio of 20 wt%, encapsulate in CoSn@CNT is a mixture of β-Sn, CoSn, and mainly $CoSn_2$ with in total 17 wt% of Sn and 5 wt% of Co. In addition to encapsulated separated spherical nanoparticles, encapsulates in Sn@CNT also form nanowires up to 1 μm in length. Both spheres and wires fill the complete inner diameter of the CNT, which is about 50 nm [44].

The CVs of Sn@CNT- and CoSn@CNT-based electrode materials shown in Figure 13 are similar to each other and confirm the multistage processes expected from reports on non-CNT materials. In both cases, in addition to the SEI formation, the peaks R1/O1 signal electrochemical activity of CNT. The reduction peak R3 at 0.6 V and the pair R2/O2 at 0.3 V as well as several features at 0.35–0.85 V, are all attributed to multi-stage (de)alloying processes.

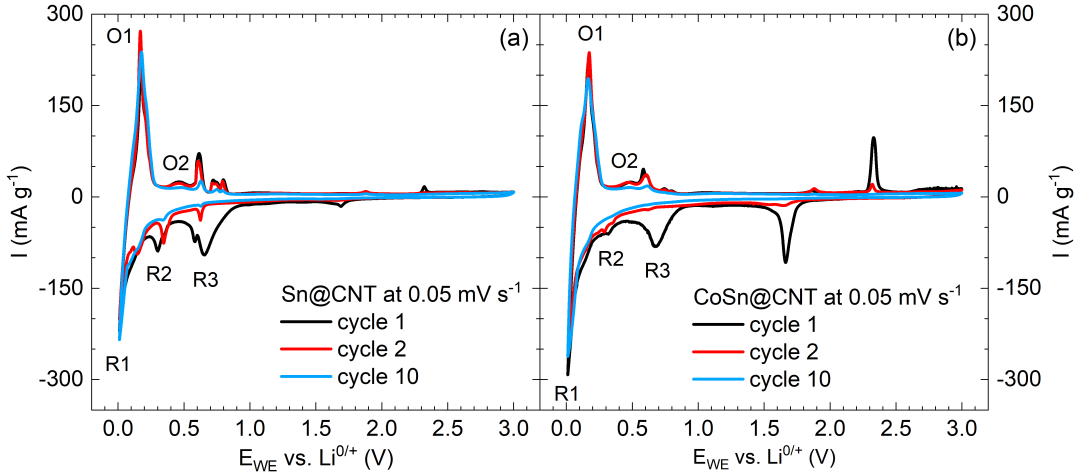

Figure 13. CVs of Sn@CNT (**a**) and CoSn@CNT (**b**) in the regime 0.01–3.0V vs. Li/Li+ at a scan rate 0.05 mV/s. Note that the oxidation peaks at 1.9 and 2.3 V and the reduction peak at 1.7 V appearing in the first two cycles are due to the experimental cell setup [30].

Galvanostatic cycling of Sn@CNT and CoSn@CNT as compared to pristine CNT (Pyrograf Products, Typ PR-24-XT-HHT) quantifies the contribution of encapsulates to the materials' capacities (Figure 14a). Sn@CNT displays clearly improved values. Quantitatively, the data imply an initial reversible capacity of 322 mAh g^{-1} in cycle 2, of which 281 mAh g^{-1}, i.e., 87%, is retained in cycle 50. In contrast, fading is much more severe in CoSn@CNT, which shows only 66% retained of the initial capacity 317 mAh g^{-1}, i.e., its performance in cycle 50 falls below that of pristine CNT. As will be discussed below, these data show that there is no positive (buffering) effect of alloyed Co. Rate capacities shown in Figure 14b at cycling rates 100–2000 mA g^{-1} illustrate the strong effect of fast cycling on both materials, thereby confirming limiting kinetics of the underlying electrochemical alloying processes.

Figure 14a also presents the specific capacity of the Sn encapsulate which is derived by correcting the data by the effect of pristine CNT. Note error bars of Sn-capacity of up to 20% resulting in particular from errors in determining the filling ratio. In the first cycle, the reversible capacity amounts to 589 mAh g^{-1} which suggests deintercalation of x = 2.6 Li^+/f.u. Capacity fading is about 15% between cycle 5 (495 mAh g^{-1}) and cycle 50 (422 mAh g^{-1}). Even the initial capacities are much smaller than the theoretical one of 960 mAh g^{-1} that would be achieved for x = 4.25.

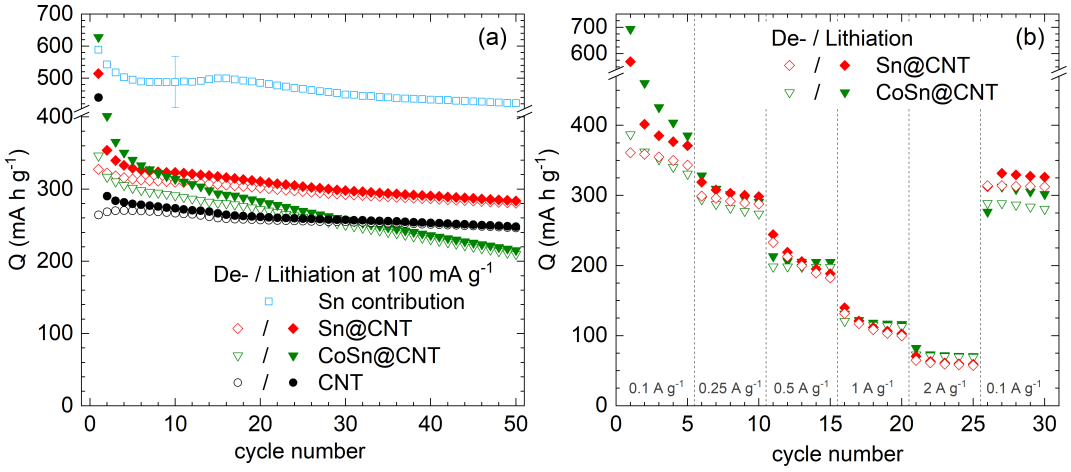

Figure 14. Specific capacities of Sn@CNT-, CoSn@CNT-, and pristine CNT-based electrodes. (**a**) Galvanostatic cycling with potential limitation (GCPL) at 100 mA g^{-1}. Blue data markers show the specific capacity of the Sn encapsulate after correcting the contribution of CNT. (**b**) GCPL at different rates of 0.1–2.0 A g^{-1} [30].

In-situ XRD studies on Li_xSn_y have shown that intermediate phases Li_2Sn_5 and LiSn are expected [94]. In agreement with these studies, the presence of (at least) two reduction peaks in the CVs of both materials (see Figure 13) suggests at least a two-stage process in the materials at hand. However, comparison to the literature does not allow to attribute these peaks to a specific process. This also holds for the observed (at least) four oxidation peaks which indicate step-wise delithiation of the Li_xSn_y-alloy. For CoSn@CNT where the encapsulate mainly consists of $CoSn_2$, Mössbauer studies have shown the formation of Li_xSn with $x \approx 3.5$ in the first cycle [95]. Such a process is not visible in the CV (Figure 13b) but the respective feature might be masked by the SEI-peak. It is argued in [95] that, upon delithiation, $Li_{\sim 3.5}Sn$ forms an amorphous $Li_xCo_ySn_2$-matrix which is crucial for the expected buffering associated with Co-alloying. We conclude that, in CoSn@CNT, this $Li_xCo_ySn_2$-matrix is not realized but Co just deteriorates the electrochemical performance. This conclusion is supported by the fact that the CVs in Figure 13 display the same number of peaks at similar potentials in both Sn@CNT and CoSn@CNT, which indicates identical processes. We assume separation of Co and Sn instead of $Li_xCo_ySn_2$-formation yielding electrochemically inactive regions.

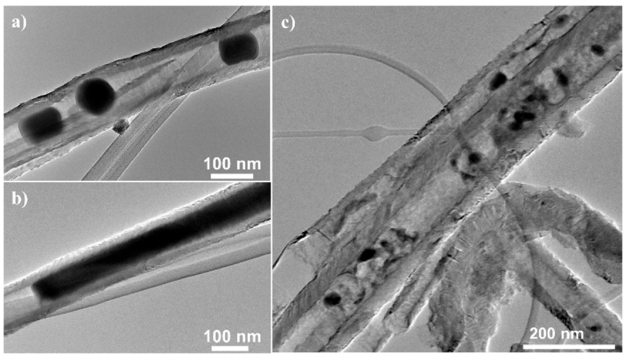

Figure 15. TEM images of pristine (**a**,**b**) and galvanostatically cycled (10 cycles) Sn@CNT (**c**).

The effect of galvanostatic cycling, at 50 mA g^{-1}, on Sn@CNT is demonstrated by TEM images in Figure 15. In the cycled materials, well separated homogenous encapsulates (Figure 15a,b) in the pristine material convert to rather completely but inhomogeneously filled CNT whose filling is indicated by different TEM contrast, i.e., different densities of encapsulate. These finding agrees with expected volume changes, in particular to large expansion upon lithiation, and phase separation of encapsulated material. One may speculate that the dark regions visible after cycling indicate electrochemically-inactive domains of Sn. The presence of inactive regions would be in agreement to the GCPL data (Figure 14) which show that only a maximum of 60% of the full Sn-capacity is achieved. Finally we note that previous studies on Sn-filled CNT have demonstrated better performance as compared to the material at hand. Wang et al. have reported Sn@CNT with filling ratios of 38 wt% and 87 wt% [96]. The former, i.e., less filled, CNT have demonstrated superior performance with capacities of 500 mAh g^{-1} for 80 cycles at 100 mA g^{-1}. The relevant parameter seems to be the size of Sn particles, which was 6–10 nm in [96]. Larger encapsulates filling the complete inner diameter of the CNT of about 50 nm as realized in the materials at hand seem to be detrimental and may cause electrochemically inactive regions. Addition of Co as a potential buffer does not improve the performance of such rather large nanoparticles inside CNT but even causes additional capacity fading.

4. Experimental Methods

4.1. Material Characterization

Materials were characterized by X-ray diffraction (XRD) with either Stadi P (Stoe, Darmstadt, Germany) using Cu Kα1 radiation (λ = 1.5406 Å) or X'Pert Pro MPD PW3040/60 (PANanalytical, Almelo, Niederlande) using Co Kα radiation (λ = 1.79278 Å). Thermogravimetric analysis (TGA) was carried out with SDT Q600 (TA Instruments, Waters Corporation, Milford, MA, U.S.). The morphology was investigated by means of scanning electron microscopy (SEM, Nova NanoSEM 200 (FEI company, Hilsboro, Oregon, U.S.)) and transmission electron microscopy (TEM, JEM-2010F (JEOL, Akishima, Japan), Tecnai (FEI company, Hilsboro, Oregon, U.S.)). A MPMS-XL5 (Quantum Design, San Diego, Californis, U.S.) superconducting quantum interference device (SQUID) magnetometer was used to perform magnetic measurements.

4.2. Electrochemical measurements

Electrochemical properties were studied by cyclic voltammetry (CV) and galvanostatic cycling with potential limitation (GCPL) in Swagelok-type cells [97]. The measurements were performed on a VMP3 potentiostat (BioLogic) at a temperature of 25 °C. For the preparation of the working electrode, the active material was optionally mixed with carbon black (Super C65, Ymeris Graphite and Carbon, Bironico, Switzerland) and stirred in a solution of polyvinylidene fluoride (PVDF, Solvay, Brussels, Belgium) in N-methyl-2-pyrrolidone (NMP) for at least 12 h. After evaporat,ing most of the NMP in a vacuum oven (80 °C, <10 mbar) the spreadable slurry was applied on copper mesh current collectors (Ø 10 mm). The as-prepared electrodes were dried at 80 °C in a vacuum oven (<10 mbar), mechanically pressed at 10 MPa, and afterwards dried again. The assembly of cells was done in a glovebox under argon atmosphere (O_2/H_2O < 5 ppm) using a lithium metal foil disk (Alfa Aesar, Haverhill, MA, U.S.) pressed on a nickel current collector as counter electrode. The electrodes were separated by two layers of glass microfibre (Whatman GF/D) soaked with 200 µL of a 1 M $LiPF_6$ salt solution in 1:1 ethylene carbonate and dimethyl carbonate (Merck ElectrolyteLP30). For post cycling studies, working electrodes were washed three times in dimethyl carbonate and afterwards dried under vacuum.

5. Conclusions

Endohedral functionalization of multiwalled carbon nanotubes by means of high-capacity electrode materials is studied with respect to application for electrochemical energy storage. Encapsulation indeed yields size-controlled nanoparticles inside CNT. The presented data imply that the filled materials are electrochemically active and can achieve full theoretical reversible capacity. While conversion and alloying processes yield cracks and amorphization of the encapsulate, the CNT mantles are found to be only very little affected by electrochemical cycling. The backbone network of CNT hence maintains its integrity and improved performance with respect to unshielded or exohedrally-attached nanomaterials. For appropriately tailored materials, CNT-based nanocomposites show smaller overpotentials and hence improved energy efficiency as well as improved cycling stability. The results imply that encapsulating nanostructures inside CNT provides a successful route to new high-performance nanocomposite anode materials for LIB.

Author Contributions: Conceptualization, E.T., A.O. and R.K.; methodology, E.T., A.O., S.H., A.B., E.M. and R.K.; data analysis, E.T., A.O. and R.K.; synthesis and material characterization, R.G., M.G., C.N. (Christian Nowka), M.S., M.H., S.W., S.H., A.K., A.B., K.W. and E.M.; electrochemical investigations, E.T., A.O., P.S., L.M., L.D., R.Z., F.W., L.S. and C.N. (Christoph Neef); writing—original draft preparation, E.T., A.O., and R.K.; writing—review, E.T., A.B., E.M., C.N., A.O, S.H., S.W. and R.K. All authors have read and agreed to the published version of the manuscript.

Funding: Work was partly supported by Deutsche Forschungsgemeinschaft DFG via KL 1824/12-1 and the CleanTech-Initiative of the Baden-Württemberg-Stiftung (Project CT3: Nanostorage). KW and EM acknowledge financial support from the National Science Center Poland (UMO-2016/23/G/ST5/04200).

Acknowledgments: The authors thank G. Kreutzer for technical support.

Conflicts of Interest: The authors declare no conflict of interest.

References

1. Palacín, M.R. Recent advances in rechargeable battery materials: A chemist's perspective. *Chem. Soc. Rev.* **2009**, *38*, 2565–2575, doi:10.1039/b820555h.
2. Aravindan, V.; Lee, Y.-S.; Madhavi, S. Research Progress on Negative Electrodes for Practical Li-Ion Batteries: Beyond Carbonaceous Anodes. *Adv. Energy Mater.* **2015**, *5*, 1402225, doi:10.1002/aenm.201402225.
3. Mahmood, N.; Tang, T.; Hou, Y. Nanostructured Anode Materials for Lithium Ion Batteries: Progress, Challenge and Perspective. *Adv. Energy Mater.* **2016**, *6*, 1600374, doi:10.1002/aenm.201600374.
4. Deng, Y.; Wan, L.; Xie, Y.; Qin, X.; Chen, G. Recent advances in Mn-based oxides as anode materials for lithium ion batteries. *RSC Adv.* **2014**, *4*, 23914–23935, doi:10.1039/C4RA02686A.
5. Arico, A.S.; Bruce, P.; Scrosati, B.; Tarascon, J.-M.; van Schalkwijk, W. Nanostructured materials for advanced energy conversion and storage devices. *Nat. Mater.* **2005**, *4*, 366–377, doi:10.1038/nmat1368.
6. Nazar, L.F.; Goward, G.; Leroux, F.; Duncan, M.; Huang, H.; Kerr, T.; Gaubicher, J. Nanostructured materials for energy storage. *Int. J. Inorg. Mater.* **2001**, *3*, 191–200, doi:10.1016/S1466-6049(01)00026-5.
7. Armand, M.; Tarascon, J.-M. Building better batteries. *Nature* **2008**, *451*, 652–657.
8. Goriparti, S.; Miele, E.; de Angelis, F.; Di Fabrizio, E.; Proietti Zaccaria, R.; Capiglia, C. Review on recent progress of nanostructured anode materials for Li-ion batteries. *J. Power Sources* **2014**, *257*, 421–443, doi:10.1016/j.jpowsour.2013.11.103.
9. Ji, L.; Lin, Z.; Alcoutlabi, M.; Zhang, X. Recent developments in nanostructured anode materials for rechargeable lithium-ion batteries. *Energy Environ. Sci.* **2011**, *4*, 2682–2699, doi:10.1039/c0ee00699h.
10. Huang, X.; Cui, S.; Chang, J.; Hallac, P.B.; Fell, C.R.; Luo, Y.; Metz, B.; Jiang, J.; Hurley, P.T.; Chen, J. A hierarchical tin/carbon composite as an anode for lithium-ion batteries with a long cycle life. *Angew. Chem. Int. Ed. Engl.* **2015**, *54*, 1490–1493, doi:10.1002/anie.201409530.
11. Gao, G.; Le, Y.; Wu, H.B.; Lou, X.W.D. Hierarchical tubular structures constructed by carbon-coated α-Fe_2O_3 nanorods for highly reversible lithium storage. *Small* **2014**, *10*, 1741–1745, doi:10.1002/smll.201303818.
12. Wang, P.-P.; Sun, H.; Ji, Y.; Li, W.; Wang, X. Three-dimensional assembly of single-layered MoS(2). *Adv. Mater.* **2014**, *26*, 964–969, doi:10.1002/adma.201304120.
13. Li, Z.; Ottmann, A.; Zhang, T.; Sun, Q.; Meyer, H.-P.; Vaynzof, Y.; Xiang, J.; Klingeler, R. Preparation of hierarchical C@MoS2@C sandwiched hollow spheres for lithium ion batteries. *J. Mater. Chem. A* **2017**, *5*, 3987–3994, doi:10.1039/C6TA10439H.
14. Li, Z.; Ottmann, A.; Sun, Q.; Kast, A.K.; Wang, K.; Zhang, T.; Meyer, H.-P.; Backes, C.; Kübel, C.; Schröder, R.R.; et al. Hierarchical MoS 2 –carbon porous nanorods towards atomic interfacial engineering for high-performance lithium storage. *J. Mater. Chem. A* **2019**, *7*, 7553–7564, doi:10.1039/C8TA12293H.
15. Lou, X.W.; Chen, J.S.; Chen, P.; Archer, L.A. One-Pot Synthesis of Carbon-Coated SnO2 Nanocolloids with Improved Reversible Lithium Storage Properties. *Chem. Mater.* **2009**, *21*, 2868–2874, doi:10.1021/cm900613d.
16. Kang, T.-W.; Lim, H.-S.; Park, S.-J.; Sun, Y.-K.; Suh, K.-D. Fabrication of flower-like tin/carbon composite microspheres as long-lasting anode materials for lithium ion batteries. *Mater. Chem. Phys.* **2017**, *185*, 6–13, doi:10.1016/j.matchemphys.2016.09.017.
17. Chen, X.; Xiao, T.; Wang, S.; Li, J.; Xiang, P.; Jiang, L.; Tan, X. Superior Li-ion storage performance of graphene decorated NiO nanowalls on Ni as anode for lithium ion batteries. *Mater. Chem. Phys.* **2019**, *222*, 31–36, doi:10.1016/j.matchemphys.2018.09.061.
18. Sun, H.; Sun, X.; Hu, T.; Yu, M.; Lu, F.; Lian, J. Graphene-Wrapped Mesoporous Cobalt Oxide Hollow Spheres Anode for High-Rate and Long-Life Lithium Ion Batteries. *J. Phys. Chem. C* **2014**, *118*, 2263–2272, doi:10.1021/jp408021m.
19. Choi, S.H.; Ko, Y.N.; Jung, K.Y.; Kang, Y.C. Macroporous Fe3O4/carbon composite microspheres with a short Li+ diffusion pathway for the fast charge/discharge of lithium ion batteries. *Chemistry* **2014**, *20*, 11078–11083, doi:10.1002/chem.201402359.

20. Lei, C.; Han, F.; Sun, Q.; Li, W.-C.; Lu, A.-H. Confined nanospace pyrolysis for the fabrication of coaxial Fe3O4@C hollow particles with a penetrated mesochannel as a superior anode for Li-ion batteries. *Chemistry* **2014**, *20*, 139–145, doi:10.1002/chem.201303175.
21. Wu, C.; Li, X.; Li, W.; Li, B.; Wang, Y.; Wang, Y.; Xu, M.; Xing, L. Fe2O3 nanorods/carbon nanofibers composite: Preparation and performance as anode of high rate lithium ion battery. *J. Power Sources* **2014**, *251*, 85–91, doi:10.1016/j.jpowsour.2013.11.030.
22. Zhang, S.; Zhu, L.; Song, H.; Chen, X.; Zhou, J. Enhanced electrochemical performance of MnO nanowire/graphene composite during cycling as the anode material for lithium-ion batteries. *Nano Energy* **2014**, *10*, 172–180, doi:10.1016/j.nanoen.2014.09.012.
23. Shi, X.; Zhang, S.; Chen, X.; Tang, T.; Klingeler, R.; Mijowska, E. Ultrathin NiO confined within hollow carbon sphere for efficient electrochemical energy storage. *J. Alloys Compd.* **2019**, *797*, 702–709, doi:10.1016/j.jallcom.2019.05.147.
24. Kan, J.; Wang, Y. Large and fast reversible Li-ion storages in Fe2O3-graphene sheet-on-sheet sandwich-like nanocomposites. *Sci. Rep.* **2013**, *3*, 3502, doi:10.1038/srep03502.
25. Park, S.-K.; Jin, A.; Yu, S.-H.; Ha, J.; Jang, B.; Bong, S.; Woo, S.; Sung, Y.-E.; Piao, Y. In Situ Hydrothermal Synthesis of Mn3O4 Nanoparticles on Nitrogen-doped Graphene as High-Performance Anode materials for Lithium Ion Batteries. *Electrochim. Acta* **2014**, *120*, 452–459, doi:10.1016/j.electacta.2013.12.018.
26. Zakharova, G.S.; Ottmann, A.; Möller, L.; Andreikov, E.I.; Fattakhova, Z.A.; Puzyrev, I.S.; Zhu, Q.; Thauer, E.; Klingeler, R. TiO2/C nanocomposites prepared by thermal annealing of titanium glycerolate as anode materials for lithium-ion batteries. *J. Mater. Sci.* **2018**, *53*, doi:10.1007/s10853-018-2488-9.
27. Wenelska, K.; Ottmann, A.; Schneider, P.; Thauer, E.; Klingeler, R.; Mijowska, E. Hollow carbon sphere/metal oxide nanocomposites anodes for lithium-ion batteries. *Energy* **2016**, *103*, 100–106, doi:10.1016/j.energy.2016.02.063.
28. Guan, X.; Nai, J.; Zhang, Y.; Wang, P.; Yang, J.; Zheng, L.; Zhang, J.; Guo, L. CoO Hollow Cube/Reduced Graphene Oxide Composites with Enhanced Lithium Storage Capability. *Chem. Mater.* **2014**, *26*, 5958–5964, doi:10.1021/cm502690u.
29. Avogadro: An Open-Source Molecular Builder and Visualization Tool, 2.0. Available online: http://avogadro.cc/ (accessed on 18 January 2019).
30. Ottmann, A. Nanostrukturierte Kohlenstoff-Komposite und Ammoniumvanadate als Elektrodenmaterialien für Lithium-Ionen-Batterien. Ph.D. Thesis, Ruprecht-Karls-Universität, Heidelberg, Germany, 2018.
31. Dai, H. Carbon nanotubes: Opportunities and challenges. *Surf. Sci.* **2002**, *500*, 218–241, doi:10.1016/S0039-6028(01)01558-8.
32. Wenelska, K.; Neef, C.; Schlestein, L.; Klingeler, R.; Kalenczuk, R.J.; Mijowska, E. Carbon nanotubes decorated by mesoporous cobalt oxide as electrode material for lithium-ion batteries. *Chem. Phys. Lett.* **2015**, *635*, 185–189, doi:10.1016/j.cplett.2015.06.072.
33. Zhang, X.; Zhou, Y.; Mao, Y.; Wei, M.; Chu, W.; Huang, K. Rapid synthesis of ultrafine NiCo2O4 nanoparticles loaded carbon nanotubes for lithium ion battery anode materials. *Chem. Phys. Lett.* **2019**, *715*, 278–283, doi:10.1016/j.cplett.2018.11.053.
34. Wen, Z.; Ci, S.; Mao, S.; Cui, S.; He, Z.; Chen, J. CNT@TiO2 nanohybrids for high-performance anode of lithium-ion batteries. *Nanoscale Res. Lett.* **2013**, *8*, 499, doi:10.1186/1556-276X-8-499.
35. Bhaskar, A.; Deepa, M.; Narasinga Rao, T. MoO2/multiwalled carbon nanotubes (MWCNT) hybrid for use as a Li-ion battery anode. *ACS Appl. Mater. Interfaces* **2013**, *5*, 2555–2566, doi:10.1021/am3031536.
36. Poizot, P.; Laruelle, S.; Grugeon, S.; Dupont, L.; Tarascon, J.M. Nano-sized transition-metal oxides as negative-electrode materials for lithium-ion batteries. *Nature* **2000**, *407*, 496–499, doi:10.1038/35035045.
37. Winter, M.; Besenhard, J.O.; Spahr, M.E.; Novák, P. Insertion Electrode Materials for Rechargeable Lithium Batteries. *Adv. Mater.* **1998**, *10*, 725–763, doi:10.1002/(SICI)1521-4095(199807)10:10<725:AID-ADMA725>3.0.CO;2-Z.
38. Tsang, S.C.; Chen, Y.K.; Harris, P.J.F.; Green, M.L.H. A simple chemical method of opening and filling carbon nanotubes. *Nature* **1994**, 159–162, doi:10.1038/372159a0.
39. Gellesch, M.; Dimitrakopoulou, M.; Scholz, M.; Blum, C.G.F.; Schulze, M.; van den Brink, J.; Hampel, S.; Wurmehl, S.; Büchner, B. Facile Nanotube-Assisted Synthesis of Ternary Intermetallic Nanocrystals of the Ferromagnetic Heusler Phase Co2FeGa: Supporting Information. *Cryst. Growth Des.* **2013**, *13*, 2707–2710, doi:10.1021/cg400405k.

40. Al Khabouri, S.; Al Harthi, S.; Maekawa, T.; Nagaoka, Y.; Elzain, M.E.; Al Hinai, A.; Al-Rawas, A.D.; Gismelseed, A.M.; Yousif, A.A. Composition, Electronic and Magnetic Investigation of the Encapsulated ZnFe2O4 Nanoparticles in Multiwall Carbon Nanotubes Containing Ni Residuals. *Nanoscale Res. Lett.* **2015**, *10*, 262, doi:10.1186/s11671-015-0971-7.
41. Ghunaim, R.; Damm, C.; Wolf, D.; Lubk, A.; Büchner, B.; Mertig, M.; Hampel, S. Fe1-xNix Alloy Nanoparticles Encapsulated Inside Carbon Nanotubes: Controlled Synthesis, Structure and Magnetic Properties. *Nanomaterials* **2018**, *8*, doi:10.3390/nano8080576.
42. Ghunaim, R.; Eckert, V.; Scholz, M.; Gellesch, M.; Wurmehl, S.; Damm, C.; Büchner, B.; Mertig, M.; Hampel, S. Carbon nanotube-assisted synthesis of ferromagnetic Heusler nanoparticles of Fe 3 Ga (Nano-Galfenol). *J. Mater. Chem. C* **2018**, *6*, 1255–1263, doi:10.1039/C7TC04618A.
43. Ghunaim, R.; Scholz, M.; Damm, C.; Rellinghaus, B.; Klingeler, R.; Büchner, B.; Mertig, M.; Hampel, S. Single-crystalline FeCo nanoparticle-filled carbon nanotubes: Synthesis, structural characterization and magnetic properties. *Beilstein J. Nanotechnol.* **2018**, *9*, 1024–1034, doi:10.3762/bjnano.9.95.
44. Haft, M.; Grönke, M.; Gellesch, M.; Wurmehl, S.; Büchner, B.; Mertig, M.; Hampel, S. Tailored nanoparticles and wires of Sn, Ge and Pb inside carbon nanotubes. *Carbon* **2016**, *101*, 352–360, doi:10.1016/j.carbon.2016.01.098.
45. Ottmann, A.; Scholz, M.; Haft, M.; Thauer, E.; Schneider, P.; Gellesch, M.; Nowka, C.; Wurmehl, S.; Hampel, S.; Klingeler, R. Electrochemical Magnetization Switching and Energy Storage in Manganese Oxide filled Carbon Nanotubes. *Sci. Rep.* **2017**, *7*, 13625, doi:10.1038/s41598-017-14014-7.
46. Jarosch, D. Crystal structure refinement and reflectance measurements of hausmannite, Mn3O4. *Mineral. Petrol.* **1987**, *37*, 15–23, doi:10.1007/BF01163155.
47. Ferreira, T.A.S.; Waerenborgh, J.C.; Mendonça, M.H.R.M.; Nunes, M.R.; Costa, F.M. Structural and morphological characterization of FeCo2O4 and CoFe2O4 spinels prepared by a coprecipitation method. *Solid State Sci.* **2003**, *5*, 383–392, doi:10.1016/S1293-2558(03)00011-6.
48. Kapoor, A.; Singh, N.; Dey, A.B.; Nigam, A.K.; Bajpai, A. 3d transition metals and oxides within carbon nanotubes by co-pyrolysis of metallocene & camphor: High filling efficiency and self-organized structures. *Carbon* **2018**, *132*, 733–745, doi:10.1016/j.carbon.2018.02.092.
49. Heider, R. Nanoskalige Sn-Co-Verbindungen Durch Füllen von CNT. Master Thesis, BTU Cottbus-Senftenberg, Cottbus, Germany, 2015.
50. Frackowiak, E.; Béguin, F. Electrochemical storage of energy in carbon nanotubes and nanostructured carbons. *Carbon* **2002**, *40*, 1775–1787, doi:10.1016/S0008-6223(02)00045-3.
51. Chew, S.Y.; Ng, S.H.; Wang, J.; Novák, P.; Krumeich, F.; Chou, S.L.; Chen, J.; Liu, H.K. Flexible free-standing carbon nanotube films for model lithium-ion batteries. *Carbon* **2009**, *47*, 2976–2983, doi:10.1016/j.carbon.2009.06.045.
52. Xiong, Z.; Yun, Y.; Jin, H.-J. Applications of Carbon Nanotubes for Lithium Ion Battery Anodes. *Materials* **2013**, *6*, 1138–1158, doi:10.3390/ma6031138.
53. Fang, X.; Lu, X.; Guo, X.; Mao, Y.; Hu, Y.-S.; Wang, J.; Wang, Z.; Wu, F.; Liu, H.; Chen, L. Electrode reactions of manganese oxides for secondary lithium batteries. *Electrochem. Commun.* **2010**, *12*, 1520–1523, doi:10.1016/j.elecom.2010.08.023.
54. Zhong, K.; Xia, X.; Zhang, B.; Li, H.; Wang, Z.; Chen, L. MnO powder as anode active materials for lithium ion batteries. *J. Power Sources* **2010**, *195*, 3300–3308, doi:10.1016/j.jpowsour.2009.11.133.
55. Tyler, R.W. The Magnetic Susceptibility of MnO as a Function of the Temperature. *Phys. Rev.* **1933**, *44*, 776–777, doi:10.1103/PhysRev.44.776.
56. Bai, Z.; Zhang, X.; Zhang, Y.; Guo, C.; Tang, B. Facile synthesis of mesoporous Mn3O4 nanorods as a promising anode material for high performance lithium-ion batteries. *J. Mater. Chem. A* **2014**, *2*, 16755–16760, doi:10.1039/c4ta03532a.
57. Li, L.; Guo, Z.; Du, A.; Liu, H. Rapid microwave-assisted synthesis of Mn3O4–graphene nanocomposite and its lithium storage properties. *J. Mater. Chem.* **2012**, *22*, 3600–3605, doi:10.1039/c2jm15075a.
58. Wang, Z.-H.; Yuan, L.-X.; Shao, Q.-G.; Huang, F.; Huang, Y.-H. Mn3O4 nanocrystals anchored on multi-walled carbon nanotubes as high-performance anode materials for lithium-ion batteries. *Mater. Lett.* **2012**, *80*, 110–113, doi:10.1016/j.matlet.2012.04.056.
59. Luo, S.; Wu, H.; Wu, Y.; Jiang, K.; Wang, J.; Fan, S. Mn3O4 nanoparticles anchored on continuous carbon nanotube network as superior anodes for lithium ion batteries. *J. Power Sources* **2014**, *249*, 463–469, doi:10.1016/j.jpowsour.2013.10.133.

60. Lavela, P.; Ortiz, G.F.; Tirado, J.L.; Zhecheva, E.; Stoyanova, R.; Ivanova, S. High-Performance Transition Metal Mixed Oxides in Conversion Electrodes: A Combined Spectroscopic and Electrochemical Study. *J. Phys. Chem. C* **2007**, *111*, 14238–14246, doi:10.1021/jp074142s.
61. de las Casas, C.; Li, W. A review of application of carbon nanotubes for lithium ion battery anode material. *J. Power Sources* **2012**, *208*, 74–85, doi:10.1016/j.jpowsour.2012.02.013.
62. Varzi, A.; Täubert, C.; Wohlfahrt-Mehrens, M.; Kreis, M.; Schütz, W. Study of multi-walled carbon nanotubes for lithium-ion battery electrodes. *J. Power Sources* **2011**, *196*, 3303–3309, doi:10.1016/j.jpowsour.2010.11.101.
63. Chu, Y.-Q.; Fu, Z.-W.; Qin, Q.-Z. Cobalt ferrite thin films as anode material for lithium ion batteries. *Electrochim. Acta* **2004**, *49*, 4915–4921, doi:10.1016/j.electacta.2004.06.012.
64. Verma, P.; Maire, P.; Novák, P. A review of the features and analyses of the solid electrolyte interphase in Li-ion batteries. *Electrochim. Acta* **2010**, *55*, 6332–6341, doi:10.1016/j.electacta.2010.05.072.
65. Gnanamuthu, R.; Lee, C.W. Electrochemical properties of Super P carbon black as an anode active material for lithium-ion batteries. *Mater. Chem. Phys.* **2011**, *130*, 831–834, doi:10.1016/j.matchemphys.2011.08.060.
66. Cabana, J.; Monconduit, L.; Larcher, D.; Palacín, M.R. Beyond intercalation-based Li-ion batteries: The state of the art and challenges of electrode materials reacting through conversion reactions. *Adv. Mater.* **2010**, *22*, E170–E192, doi:10.1002/adma.201000717.
67. Wang, Y.; Su, D.; Ung, A.; Ahn, J.H.; Wang, G. Hollow $CoFe_2O_4$ nanospheres as a high capacity anode material for lithium ion batteries. *Nanotechnology* **2012**, *23*, 55402, doi:10.1088/0957-4484/23/5/055402.
68. Wu, L.; Xiao, Q.; Li, Z.; Lei, G.; Zhang, P.; Wang, L. CoFe2O4/C composite fibers as anode materials for lithium-ion batteries with stable and high electrochemical performance. *Solid State Ion.* **2012**, *215*, 24–28, doi:10.1016/j.ssi.2012.03.044.
69. Wang, L.; Zhuo, L.; Cheng, H.; Zhang, C.; Zhao, F. Porous carbon nanotubes decorated with nanosized cobalt ferrite as anode materials for high-performance lithium-ion batteries. *J. Power Sources* **2015**, *283*, 289–299, doi:10.1016/j.jpowsour.2015.02.138.
70. Zhang, Z.; Wang, Y.; Zhang, M.; Tan, Q.; Lv, X.; Zhong, Z.; Su, F. Mesoporous CoFe2O4 nanospheres cross-linked by carbon nanotubes as high-performance anodes for lithium-ion batteries. *J. Mater. Chem. A* **2013**, *1*, 7444–7450, doi:10.1039/c3ta10762k.
71. Ren, S.; Zhao, X.; Chen, R.; Fichtner, M. A facile synthesis of encapsulated CoFe2O4 into carbon nanofibres and its application as conversion anodes for lithium ion batteries. *J. Power Sources* **2014**, *260*, 205–210, doi:10.1016/j.jpowsour.2014.03.012.
72. Zhang, L.; Wei, T.; Jiang, Z.; Liu, C.; Jiang, H.; Chang, J.; Sheng, L.; Zhou, Q.; Yuan, L.; Fan, Z. Electrostatic interaction in electrospun nanofibers: Double-layer carbon protection of CoFe2O4 nanosheets enabling ultralong-life and ultrahigh-rate lithium ion storage. *Nano Energy* **2018**, *48*, 238–247, doi:10.1016/j.nanoen.2018.03.053.
73. Laruelle, S.; Grugeon, S.; Poizot, P.; Dollé, M.; Dupont, L.; Tarascon, J.-M. On the Origin of the Extra Electrochemical Capacity Displayed by MO/Li Cells at Low Potential. *J. Electrochem. Soc.* **2002**, *149*, A627–A634, doi:10.1149/1.1467947.
74. Jamnik, J.; Maier, J. Nanocrystallinity effects in lithium battery materials. *Phys. Chem. Chem. Phys.* **2003**, *5*, 5215, doi:10.1039/B309130A.
75. Larcher, D.; Bonnin, D.; Cortes, R.; Rivals, I.; Personnaz, L.; Tarascon, J.-M. Combined XRD, EXAFS, and Mössbauer Studies of the Reduction by Lithium of α-Fe2O3 with Various Particle Sizes. *J. Electrochem. Soc.* **2003**, *150*, A1643–A1650, doi:10.1149/1.1622959.
76. Larcher, D.; Masquelier, C.; Bonnin, D.; Chabre, Y.; Masson, V.; Leriche, J.-B.; Tarascon, J.-M. Effect of Particle Size on Lithium Intercalation into α-Fe2O3. *J. Electrochem. Soc.* **2003**, *150*, A133–A139, doi:10.1149/1.1528941.
77. Morales, J.; Sánchez, L.; Martín, F.; Berry, F.; Ren, X. Synthesis and Characterization of Nanometric Iron and Iron-Titanium Oxides by Mechanical Milling. *J. Electrochem. Soc.* **2005**, *152*, A1748–A1754, doi:10.1149/1.1972812.
78. Cherian, C.T.; Sundaramurthy, J.; Kalaivani, M.; Ragupathy, P.; Kumar, P.S.; Thavasi, V.; Reddy, M.V.; Sow, C.H.; Mhaisalkar, S.G.; Ramakrishna, S.; et al. Electrospun α-Fe2O3 nanorods as a stable, high capacity anode material for Li-ion batteries. *J. Mater. Chem.* **2012**, *22*, 12198–12204, doi:10.1039/c2jm31053h.
79. Hariharan, S.; Saravanan, K.; Balaya, P. Lithium Storage Using Conversion Reaction in Maghemite and Hematite. *Electrochem. Solid State Lett.* **2010**, *13*, A132–A134, doi:10.1149/1.3458648.

80. Thackeray, M.M. Spinel Electrodes for Lithium Batteries. *J. Am. Ceram. Soc.* **1999**, *82*, 3347–3354, doi:10.1111/j.1151-2916.1999.tb02250.x.
81. Thackeray, M.M.; David, W.I.F.; Goodenough, J.B. Structural characterization of the lithiated iron oxides LixFe3O4 and LixFe2O3 (0<x<2). *Mater. Res. Bull.* **1982**, *17*, 785–793, doi:10.1016/0025-5408(82)90029-0.
82. Xu, J.-S.; Zhu, Y.-J. Monodisperse Fe3O4 and γ-Fe2O3 magnetic mesoporous microspheres as anode materials for lithium-ion batteries. *ACS Appl. Mater. Interfaces* **2012**, *4*, 4752–4757, doi:10.1021/am301123f.
83. Yuan, S.; Zhou, Z.; Li, G. Structural evolution from mesoporous α-Fe2O3 to Fe3O4@C and γ-Fe2O3 nanospheres and their lithium storage performances. *CrystEngComm* **2011**, *13*, 4709–4713, doi:10.1039/c0ce00902d.
84. Yan, N.; Zhou, X.; Li, Y.; Wang, F.; Zhong, H.; Wang, H.; Chen, Q. Fe2O3 Nanoparticles Wrapped in Multi-walled Carbon Nanotubes With Enhanced Lithium Storage Capability. *Sci. Rep.* **2013**, *3*, 3392, doi:10.1038/srep03392.
85. Zhuo, L.; Wu, Y.; Ming, J.; Wang, L.; Yu, Y.; Zhang, X.; Zhao, F. Facile synthesis of a Co 3 O 4 –carbon nanotube composite and its superior performance as an anode material for Li-ion batteries. *J. Mater. Chem. A* **2013**, *1*, 1141–1147, doi:10.1039/C2TA00284A.
86. Xu, M.; Wang, F.; Zhang, Y.; Yang, S.; Zhao, M.; Song, X. Co3O4-carbon nanotube heterostructures with bead-on-string architecture for enhanced lithium storage performance. *Nanoscale* **2013**, *5*, 8067–8072, doi:10.1039/c3nr02538a.
87. Obrovac, M.N.; Chevrier, V.L. Alloy negative electrodes for Li-ion batteries. *Chem. Rev.* **2014**, *114*, 11444–11502, doi:10.1021/cr500207g.
88. Wu, S.; Han, C.; Iocozzia, J.; Lu, M.; Ge, R.; Xu, R.; Lin, Z. Germanium-Based Nanomaterials for Rechargeable Batteries. *Angew. Chem. Int. Ed.* **2016**, *55*, 7898–7922, doi:10.1002/anie.201509651.
89. Srajer, G.; Lewis, L.H.; Bader, S.D.; Epstein, A.J.; Fadley, C.S.; Fullerton, E.E.; Hoffmann, A.; Kortright, J.B.; Krishnan, K.M.; Majetich, S.A.; et al. Advances in nanomagnetism via X-ray techniques. *J. Magn. Magn. Mater.* **2006**, *307*, 1–31, doi:10.1016/j.jmmm.2006.06.033.
90. Goward, G.R.; Taylor, N.J.; Souza, D.C.S.; Nazar, L.F. The true crystal structure of Li17M4 (M=Ge, Sn, Pb) – revised from Li22M5. *J. Alloys Compd.* **2001**, *329*, 82–91, doi:10.1016/S0925-8388(01)01567-5.
91. Yin, F.; Su, X.; Li, Z.; Wang, J. Thermodynamic assessment of the Li–Sn (Lithium–Tin) system. *J. Alloys Compd.* **2005**, *393*, 105–108, doi:10.1016/j.jallcom.2004.09.047.
92. Todd, A.D.W.; Mar, R.E.; Dahn, J.R. Combinatorial Study of Tin-Transition Metal Alloys as Negative Electrodes for Lithium-Ion Batteries. *J. Electrochem. Soc.* **2006**, *153*, A1998–A2005, doi:10.1149/1.2257985.
93. Zhang, J.-j.; Xia, Y.-y. Co-Sn Alloys as Negative Electrode Materials for Rechargeable Lithium Batteries. *J. Electrochem. Soc.* **2006**, *153*, A1466–A1471, doi:10.1149/1.2204871.
94. Courtney, I.A.; Dahn, J.R. Electrochemical and In Situ X-Ray Diffraction Studies of the Reaction of Lithium with Tin Oxide Composites. *J. Electrochem. Soc.* **1997**, *144*, 2045–2052, doi:10.1149/1.1837740.
95. Ionica-Bousquet, C.M.; Lippens, P.E.; Aldon, L.; Olivier-Fourcade, J.; Jumas, J.C. In situ 119Sn Mössbauer Effect Study of Li−CoSn2 Electrochemical System. *Chem. Mater.* **2006**, *18*, 6442–6447, doi:10.1021/cm062132i.
96. Wang, Y.; Wu, M.; Jiao, Z.; Lee, J.Y. Sn@CNT and Sn@C@CNT nanostructures for superior reversible lithium ion storage. *Chem. Mater.* **2009**, *21*, 3210–3215, doi:10.1021/cm900702d.
97. Zakharova, G.S.; Thauer, E.; Wegener, S.A.; Nölke, J.-H.; Zhu, Q.; Klingeler, R. Hydrothermal microwave-assisted synthesis of Li3VO4 as an anode for lithium-ion battery. *J. Solid State Electrochem.* **2019**, *23*, 2205–2212, doi:10.1007/s10008-019-04315-4.

Publikationsliste

An den folgenden nach dem Peer-Review-Verfahren veröffentlichten Artikeln hat die Autorin der vorliegenden Arbeit maßgeblich mitgearbeitet und wurden in der vorliegenden Arbeit verwendet :

G.S. Zakharova, **E. Thauer**, S.A. Wegener, J.-H. Nölke, Q. Zhu, R. Klingeler, „Hydrothermal microwave-assisted synthesis of Li_3VO_4 as an anode for lithium-ion battery“, *J Solid State Electrochem* 23 (2019) 2205–2212.https://doi.org/10.1007/s10008-019-04315-4.

E. Thauer, G.S. Zakharova, S.A. Wegener, Q. Zhu, R. Klingeler, „Sol-gel synthesis of Li_3VO_4/C composites as anode materials for lithium-ion batteries“, *Journal of Alloys and Compdounds* 853 (2021) 157364. https://doi.org/10.1016/j.jallcom.2020.157364.

G.S. Zakharova, L. Singer, Z.A. Fattakhova, S. Wegener, **E. Thauer**, Q. Zhu, E.V. Shalaeva, R. Klingeler, „MoO_2/C composites prepared by tartaric acid and glucose-assisted sol-gel processes as anode materials for lithium-ion batteries“, *Journal of Alloys and Compounds* 863 (2021) 158353. https://doi.org/10.1016/j.jallcom.2020.158353.

G.S. Zakharova, **E. Thauer**, A.N. Enyashin, L.F. Deeg, Q. Zhu, R. Klingeler, „V_2O_3/C composite fabricated by carboxylic acid-assisted sol–gel synthesis as anode material for lithium-ion batteries“, *Journal of Sol-Gel Science and Technology* 98 (2021) 549–558. https://doi.org/10.1007/s10971-021-05523-z.

E. Thauer, G.S. Zakharova, L.F. Deeg, Q. Zhu, R. Klingeler, „Hierarchically structured V_2O_3/C microspheres: Synthesis, characterization, and their electrochemical properties“, *Electrochimica Acta* 390 (2021) 138881. https://doi.org/10.1016/j.electacta.2021.138881.

E. Thauer, G.S. Zakharova, E.I. Andreikov, V. Adam, S.A. Wegener, J.-H. Nölke, L. Singer, A. Ottmann, A. Asyuda, M. Zharnikov, D.M. Kiselkov, Q. Zhu, I.S. Puzyrev, N.V. Podval'naya, R. Klingeler, „Novel synthesis and electrochemical investigations of ZnO/C composites for lithium-ion batteries“, *Journal of Material Science* 56 (2021) 13227–13242. https://doi.org/10.1007/s10853-021-06125-4.

L. Möller, **E. Thauer**, A. Ottmann, L. Deeg, R. Ghunaim, S. Hampel, R. Klingeler, „$CoFe_2O_4$-filled carbon nanotubes as anode material for lithium-ion batteries“, *Journal of Alloys and Compounds* 834 (2020) 155018. https://doi.org/10.1016/j.jallcom.2020.155018.

E. Thauer, X. Shi, S. Zhang, X. Chen, L. Deeg, R. Klingeler, K. Wenelska, E. Mijowska, „Mn_3O_4 encapsulated in hollow carbon spheres coated by graphene layer for enhanced magnetization and lithium-ion batteries performance“, *Energy* 217 (2021) 119399. https://doi.org/10.1016/j.energy.2020.119399

E. Thauer, A. Ottmann, P. Schneider, L. Möller, L. Deeg, R. Zeus, F. Wilhelmi, L. Schlestein, C. Neef, R. Ghunaim, M. Gellesch, C. Nowka, M. Scholz, M. Haft, S. Wurmehl, K. Wenelska, E. Mijowska, A. Kapoor, A. Bajpai, S. Hampel, R. Klingeler, „Filled Carbon Nanotubes as Anode Materials for Lithium-Ion Batteries“, *Molecules* 25 (2020). https://doi.org/10.3390/molecules25051064

Weitere Veröffentlichungen in Peer-Review-Journalen mit Beiträgen der Autorin, die als Doktorantin angefertigt, aber nicht für die vorliegende Arbeit verwendet wurden:

W. Hergett, C. Neef, H. Wadepohl, H.-P. Meyer, M.M. Abdel-Hafiez, C. Ritter, **E. Thauer**, R. Klingeler, „High-pressure optical floating-zone growth of Li_2FeSiO_4 single crystals“, *Journal of Crystal Growth* 515 (2019) 37–43. https://doi.org/10.1016/j.jcrysgro.2019.03.010.

C. Neef, A. Reiser, **E. Thauer**, R. Klingeler, „Anisotropic ionic conductivity of $LiMn_{1-x}Fe$ PO4 ($0 \leq x \leq 1$) single crystals“, *Solid State Ionics* 346 (2020) 115197. https://doi.org/10.1016/j.ssi.2019.115197.

Literatur

[1] Vereinte Nationen, *Rahmenübereinkommen der Vereinten Nationen über Klimaänderungen*, 1994.

[2] Deutscher Bundestag, *Entwurf eines Ersten Gesetzes zur Änderung des Bundes-Klimaschutzgesetzes*, 2021.

[3] C. M. Hayner, X. Zhao und H. H. Kung, "Materials for rechargeable lithium-ion batteries", *Annual Review of Chemical and Biomolecular Engineering*, Jg. 3, Nr. 1, S. 445–471, 2012, ISSN: 1947-5438. DOI: 10.1146/annurev-chembioeng-062011-081024.

[4] B. J. Landi, M. J. Ganter, C. D. Cress, R. A. DiLeo und R. P. Raffaelle, "Carbon nanotubes for lithium ion batteries", *Energy & Environmental Science*, Jg. 2, Nr. 6, S. 638, 2009, ISSN: 1754-5692. DOI: 10.1039/b904116h.

[5] Y. Miao, P. Hynan, A. von Jouanne und A. Yokochi, "Current Li-Ion Battery Technologies in Electric Vehicles and Opportunities for Advancements", *Energies*, Jg. 12, Nr. 6, S. 1074, 2019. DOI: 10.3390/en12061074.

[6] J. M. Tarascon und M. Armand, "Issues and challenges facing rechargeable lithium batteries", *Nature*, Jg. 414, Nr. 6861, S. 359–367, 2001, ISSN: 0028-0836. DOI: 10.1038/35104644.

[7] X.-B. Cheng, R. Zhang, C.-Z. Zhao und Q. Zhang, "Toward Safe Lithium Metal Anode in Rechargeable Batteries: A Review", *Chemical Reviews*, Jg. 117, Nr. 15, S. 10 403–10 473, 2017, ISSN: 0009-2665. DOI: 10.1021/acs.chemrev.7b00115.

[8] T. Nagaura und K. Tozawa, "Lithium Ion Rechargeable Battery", *Progress in Batteries & Solar Cells*, Jg. 9, S. 209, 1990. Adresse: https://ci.nii.ac.jp/naid/10002997721/.

[9] N. Nitta, F. Wu, J. T. Lee und G. Yushin, "Li-ion battery materials: present and future", *Mater. Today*, Jg. 18, Nr. 5, S. 252–264, 2015. DOI: 10.1016/j.mattod.2014.10.040.

[10] J. Lu, Z. Chen, F. Pan, Y. Cui und K. Amine, "High-Performance Anode Materials for Rechargeable Lithium-Ion Batteries", *Electrochemical Energy Reviews*, Jg. 1, Nr. 1, S. 35–53, 2018, ISSN: 2520-8489. DOI: 10.1007/s41918-018-0001-4.

[11] Hong Li, Lihong Shi, Qing Wang, Liquan Chen, Xuejie Huang, "Nano-alloy anode for lithium ion batteries", *Solid State Ionics*, Jg. 148, Nr. 3-4, S. 247–258, 2002, ISSN: 0167-2738. DOI: 10.1016/S0167-2738(02)00061-9.

[12] J. Cabana, L. Monconduit, D. Larcher und M. R. Palacín, "Beyond intercalation-based Li-ion batteries: the state of the art and challenges of electrode materials reacting through conversion reactions", *Advanced materials (Deerfield Beach, Fla.)*, Jg. 22, Nr. 35, E170–92, 2010. DOI: 10.1002/adma.201000717.

[13] P. Poizot, S. Laruelle, S. Grugeon, L. Dupont und J. M. Tarascon, "Nano-sized transition-metal oxides as negative-electrode materials for lithium-ion batteries", *Nature*, Jg. 407, Nr. 6803, S. 496–499, 2000, ISSN: 0028-0836. DOI: 10.1038/35035045.

[14] A. Kraytsberg und Y. Ein-Eli, "A critical review-promises and barriers of conversion electrodes for Li-ion batteries", *Journal of Solid State Electrochemistry*, Jg. 21, Nr. 7, S. 1907–1923, 2017, ISSN: 1432-8488. DOI: 10.1007/s10008-017-3580-9.

[15] J. Wang, Y.-c. K. Chen-Wiegart und J. Wang, "In situ three-dimensional synchrotron X-Ray nanotomography of the (de)lithiation processes in tin anodes", *Angewandte Chemie (International ed. in English)*, Jg. 53, Nr. 17, S. 4460–4464, 2014, ISSN: 1433-7851. DOI: 10.1002/anie.201310402.

[16] S.-K. Jung, I. Hwang, D. Chang, K.-Y. Park, S. J. Kim, W. M. Seong, D. Eum, J. Park, B. Kim, J. Kim, J. H. Heo und K. Kang, "Nanoscale Phenomena in Lithium-Ion Batteries", *Chemical Reviews*, Jg. 120, Nr. 14, S. 6684–6737, 2020, ISSN: 0009-2665. DOI: 10.1021/acs.chemrev.9b00405.

[17] S. W. Lee, M. T. McDowell, J. W. Choi und Y. Cui, "Anomalous shape changes of silicon nanopillars by electrochemical lithiation", *Nano Letters*, Jg. 11, Nr. 7, S. 3034–3039, 2011, ISSN: 1530-6984. DOI: 10.1021/nl201787r.

[18] F. Wu, J. Maier und Y. Yu, "Guidelines and trends for next-generation rechargeable lithium and lithium-ion batteries", *Chemical Society Reviews*, Jg. 49, Nr. 5, S. 1569–1614, 2020, ISSN: 0306-0012. DOI: 10.1039/C7CS00863E.

[19] A. K. Padhi, K. S. Nanjundaswamy und J. B. Goodenough, "Phosphoolivines as Positive Electrode Materials for Rechargeable Lithium Batteries", *Journal of The Electrochemical Society*, Jg. 144, Nr. 4, S. 1188–1194, 1997, ISSN: 0013-4651. DOI: 10.1149/1.1837571.

[20] C. Wang und J. Hong, "Ionic/Electronic Conducting Characteristics of $LiFePO_4$ Cathode Materials", *Electrochemical and Solid-State Letters*, Jg. 10, Nr. 3, A65, 2007, ISSN: 10990062. DOI: 10.1149/1.2409768.

[21] K. Zaghib, A. Mauger und C. M. Julien, "Overview of olivines in lithium batteries for green transportation and energy storage", *Journal of Solid State Electrochemistry*, Jg. 16, Nr. 3, S. 835–845, 2012, ISSN: 1432-8488. DOI: 10.1007/s10008-011-1629-8.

[22] K. T. Lee und J. Cho, "Roles of nanosize in lithium reactive nanomaterials for lithium ion batteries", *Nano Today*, Jg. 6, Nr. 1, S. 28–41, 2011, ISSN: 17480132. DOI: 10.1016/j.nantod.2010.11.002.

[23] H. Li und H. Zhou, "Enhancing the performances of Li-ion batteries by carbon-coating: Present and future", *Chemical communications (Cambridge, England)*, Jg. 48, Nr. 9, S. 1201–1217, 2012. DOI: 10.1039/c1cc14764a.

[24] A. J. Bard und L. R. Faulkner, *Electrochemical Methods: Fundamentals and Applications*, 2nd edition. Jon Wiley & Sons, 2001.

[25] C. Hamann und W. Vielstrich, *Elektrochemie*, 4. WILEY-VCH, 2005.

[26] C. Brett, *Electrochemistry Principles, Methods and Applications*. Oxford Science Publications, 1993.

[27] A. Einstein, "Über die von der molekularkinetischen Theorie der Wärme geforderte Bewegung von in ruhenden Flüssigkeiten suspendierten Teilchen [AdP 17, 549 (1905)]", *Annalen der Physik*, Jg. 14, S. 182–193, S1 2005. DOI: 10.1002/andp.200590005.

[28] M. Richter, "Bau und Konstruktion einer neuen elektrochemischen In-Situ Zelle für ein MPMS SQUID Magnetometer", Masterarbeit, Universität Heidelberg, 2017.

[29] J. Asenbauer, T. Eisenmann, M. Kuenzel, A. Kazzazi, Z. Chen und D. Bresser, "The success story of graphite as a lithium-ion anode material – fundamentals, remaining challenges, and recent developments including silicon (oxide) composites", *Sustainable Energy & Fuels*, Jg. 4, Nr. 11, S. 5387–5416, 2020. DOI: 10.1039/D0SE00175A.

[30] C. de las Casas und W. Li, "A review of application of carbon nanotubes for lithium ion battery anode material", *Journal of Power Sources*, Jg. 208, S. 74–85, 2012, ISSN: 0378-7753. DOI: 10.1016/j.jpowsour.2012.02.013.

[31] S. S. Zhang, "The effect of the charging protocol on the cycle life of a Li-ion battery", *Journal of Power Sources*, Jg. 161, Nr. 2, S. 1385–1391, 2006, ISSN: 0378-7753. DOI: 10.1016/j.jpowsour.2006.06.040.

[32] W. Lu, C. M. López, N. Liu, J. T. Vaughey, A. Jansen und D. Dennis W., "Overcharge effect on morphology and structure of carbon electrodes for lithium-Ion batteries", *Journal of The Electrochemical Society*, Jg. 159, Nr. 5, A566–A570, 2012, ISSN: 0013-4651. DOI: 10.1149/2.jes035205.

[33] J. H. Park, H. Yoon, Y. Cho und C.-Y. Yoo, "Investigation of Lithium Ion Diffusion of Graphite Anode by the Galvanostatic Intermittent Titration Technique", *Materials (Basel, Switzerland)*, Jg. 14, Nr. 16, S. 4683, 2021, ISSN: 1996-1944. DOI: 10.3390/ma14164683.

[34] H. Zhang, Y. Yang, H. Xu, L. Wang, X. Lu und X. He, "$Li_4Ti_5O_12$ spinel anode: Fundamentals and advances in rechargeable batteries", *InfoMat*, 2021, ISSN: 2567-3165. DOI: 10.1002/inf2.12228.

[35] A. Eftekhari, "Low voltage anode materials for lithium-ion batteries", *Energy Storage Materials*, Jg. 7, S. 157–180, 2017, ISSN: 24058297. DOI: 10.1016/j.ensm.2017.01.009.

[36] S. Iijima, "Helical microtubules of graphitic carbon", *Nature*, Jg. 354, Nr. 6348, S. 56–58, 1991, ISSN: 0028-0836. DOI: 10.1038/354056a0.

[37] M. M. Shulaker, G. Hills, N. Patil, H. Wei, H.-Y. Chen, H.-S. P. Wong und S. Mitra, "Carbon nanotube computer", *Nature*, Jg. 501, Nr. 7468, S. 526–530, 2013, ISSN: 0028-0836. DOI: 10.1038/nature12502.

[38] P. Avouris, J. Appenzeller, R. Martel und S. J. Wind, "Carbon nanotube electronics", *Proceedings of the IEEE*, Jg. 9, Nr. 11, S. 1772–1784, 2003, ISSN: 0018-9219. DOI: 10.1109/JPROC.2003.818338.

[39] K. Koziol, J. Vilatela, A. Moisala, M. Motta, P. Cunniff, M. Sennett und A. Windle, "High-performance carbon nanotube fiber", *Science (New York, N.Y.)*, Jg. 318, Nr. 5858, S. 1892–1895, 2007. DOI: 10.1126/science.1147635.

[40] A. Srivastava, O. N. Srivastava, S. Talapatra, R. Vajtai und P. M. Ajayan, "Carbon nanotube filters", *Nature Materials*, Jg. 3, Nr. 9, S. 610–614, 2004, ISSN: 1476-1122. DOI: 10.1038/nmat1192.

[41] Y. Che, H. Chen, H. Gui, J. Liu, B. Liu und C. Zhou, "Review of carbon nanotube nanoelectronics and macroelectronics", *Semiconductor Science and Technology*, Jg. 29, Nr. 7, S. 073 001, 2014, ISSN: 0268-1242. DOI: 10.1088/0268-1242/29/7/073001.

[42] L. Bokobza, "Multiwall carbon nanotube elastomeric composites: A review", *Polymer*, Jg. 48, Nr. 17, S. 4907–4920, 2007, ISSN: 00323861. DOI: 10.1016/j.polymer.2007.06.046.

[43] B. Mahar, C. Laslau, R. Yip und Y. Sun, "Development of Carbon Nanotube-Based Sensors–A Review", *IEEE Sensors Journal*, Jg. 7, Nr. 2, S. 266–284, 2007, ISSN: 1530-437X. DOI: 10.1109/JSEN.2006.886863.

[44] D. Qian, G. J. Wagner, W. K. Liu, M.-F. Yu und R. S. Ruoff, "Mechanics of carbon nanotubes", *Applied Mechanics Reviews*, Jg. 55, Nr. 6, S. 495–533, 2002, ISSN: 0003-6900. DOI: 10.1115/1.1490129.

[45] F. Leroux, K. Méténier, S. Gautier, E. Frackowiak, S. Bonnamy und F. Béguin, "Electrochemical insertion of lithium in catalytic multi-walled carbon nanotubes", *Journal of Power Sources*, Jg. 81-82, S. 317–322, 1999, ISSN: 0378-7753. DOI: 10.1016/S0378-7753(99)00130-5.

[46] B. Gao, A. Kleinhammes, X. P. Tang, C. Bower, L. Fleming, Y. Wu und O. Zhou, "Electrochemical intercalation of single-walled carbon nanotubes with lithium", *Chemical Physics Letters*, Jg. 307, Nr. 3-4, S. 153–157, 1999, ISSN: 00092614. DOI: 10.1016/S0009-2614(99)00486-8.

[47] C. Kang, M. Patel, B. Rangasamy, K.-N. Jung, C. Xia, S. Shi und W. Choi, "Three-dimensional carbon nanotubes for high capacity lithium-ion batteries", *Journal of Power Sources*, Jg. 299, S. 465–471, 2015, ISSN: 0378-7753. DOI: 10.1016/j.jpowsour.2015.08.103.

[48] S. Yang, J. Huo, H. Song und X. Chen, "A comparative study of electrochemical properties of two kinds of carbon nanotubes as anode materials for lithium ion batteries", *Electrochimica Acta*, Jg. 53, Nr. 5, S. 2238–2244, 2008, ISSN: 00134686. DOI: 10.1016/j.electacta.2007.09.040.

[49] S. Y. Chew, S. H. Ng, J. Wang, P. Novák, F. Krumeich, S. L. Chou, J. Chen und H. K. Liu, "Flexible free-standing carbon nanotube films for model lithium-ion batteries", *Carbon*, Jg. 47, Nr. 13, S. 2976–2983, 2009, ISSN: 00086223. DOI: 10.1016/j.carbon.2009.06.045.

[50] C. H. Mi, G. S. Cao und X. B. Zhao, "A non-GIC mechanism of lithium storage in chemical etched MWNTs", *Journal of Electroanalytical Chemistry*, Jg. 562, Nr. 2, S. 217–221, 2004, ISSN: 1572-6657. DOI: 10.1016/j.jelechem.2003.09.004.

[51] B. Gao, C. Bower, J. D. Lorentzen, L. Fleming, A. Kleinhammes, X. P. Tang, L. E. McNeil, Y. Wu und O. Zhou, "Enhanced saturation lithium composition in ball-milled single-walled carbon nanotubes", *Chemical Physics Letters*, Jg. 327, Nr. 1-2, S. 69–75, 2000, ISSN: 00092614. DOI: 10.1016/s0009-2614(00)00851-4.

[52] D. S. Su und R. Schlögl, "Nanostructured carbon and carbon nanocomposites for electrochemical energy storage applications", *ChemSusChem*, Jg. 3, Nr. 2, S. 136–168, 2010, ISSN: 1864-5631. DOI: 10.1002/cssc.200900182. Adresse: https://chemistry-europe.onlinelibrary.wiley.com/doi/10.1002/cssc.200900182.

[53] V. Meunier, J. Kephart, C. Roland und J. Bernholc, "Ab initio investigations of lithium diffusion in carbon nanotube systems", *Physical Review Letters*, Jg. 88, Nr. 7, S. 075 506, 2002, ISSN: 0031-9007. DOI: 10.1103/PhysRevLett.88.075506.

[54] J. Zhao, A. Buldum, J. Han und J. Ping Lu, "First-principles study of Li-intercalated carbon nanotube ropes", *Physical Review Letters*, Jg. 85, Nr. 8, S. 1706–1709, 2000, ISSN: 0031-9007. DOI: 10.1103/PhysRevLett.85.1706.

[55] A. L. M. Reddy, M. M. Shaijumon, S. R. Gowda und P. M. Ajayan, "Coaxial MnO_2/carbon nanotube array electrodes for high-performance lithium batteries", *Nano Letters*, Jg. 9, Nr. 3, S. 1002–1006, 2009, ISSN: 1530-6984. DOI: 10.1021/nl803081j.

[56] H.-X. Zhang, C. Feng, Y.-C. Zhai, K.-L. Jiang, Q.-Q. Li und S.-S. Fan, "Cross-Stacked Carbon Nanotube Sheets Uniformly Loaded with SnO_2 Nanoparticles: A Novel Binder-Free and High-Capacity Anode Material for Lithium-Ion Batteries", *Advanced Materials*, Jg. 21, Nr. 22, S. 2299–2304, 2009, ISSN: 09359648. DOI: 10.1002/adma.200802290.

[57] T. H. Yoon und Y. J. Park, "Electrochemical properties of CNTs/Co_3O_4 blended-anode for rechargeable lithium batteries", *Solid State Ionics*, Jg. 225, S. 498–501, 2012, ISSN: 0167-2738. DOI: 10.1016/j.ssi.2012.02.041.

[58] Y. Xu, Y. Qiu, C. Zhang, C. Gan, L. Huang, X. Tang und X. Luo, "Yolk-Shell Structured C/Mn_3O_4 Microspheres Derived from Metal–Organic Frameworks with Enhanced Lithium Storage Performance", *Energy Technology*, Jg. 8, Nr. 9, S. 2 000 376, 2020, ISSN: 2194-4288. DOI: 10.1002/ente.202000376.

[59] A. Ottmann, M. Scholz, M. Haft, E. Thauer, P. Schneider, M. Gellesch, C. Nowka, S. Wurmehl, S. Hampel und R. Klingeler, "Electrochemical Magnetization Switching and Energy Storage in Manganese Oxide filled Carbon Nanotubes", *Sci. Rep.*, Jg. 7, Nr. 1, S. 13 625, 2017. DOI: 10.1038/s41598-017-14014-7.

[60] J. Zang, J. Ye, X. Fang, X. Zhang, M. Zheng und Q. Dong, "Hollow-in-Hollow Carbon Spheres for Lithium-ion Batteries with Superior Capacity and Cyclic Performance", *Electrochimica Acta*, Jg. 186, S. 436–441, 2015, ISSN: 00134686. DOI: 10.1016/j.electacta.2015.11.002.

[61] K. Tang, R. J. White, X. Mu, M.-M. Titirici, P. A. van Aken und J. Maier, "Hollow carbon nanospheres with a high rate capability for lithium-based batteries", *ChemSusChem*, Jg. 5, Nr. 2, S. 400–403, 2012, ISSN: 1864-5631. DOI: 10.1002/cssc.201100609.

[62] Y. Wang, F. Su, J. Y. Lee und X. S. Zhao, "Crystalline Carbon Hollow Spheres, Crystalline Carbon−SnO_2 Hollow Spheres, and Crystalline SnO 2 Hollow Spheres: Synthesis and Performance in Reversible Li-Ion Storage", *Chemistry of Materials*, Jg. 18, Nr. 5, S. 1347–1353, 2006, ISSN: 1520-5002. DOI: 10.1021/cm052219o.

[63] F. Su, X. S. Zhao, Y. Wang, L. Wang und J. Y. Lee, "Hollow carbon spheres with a controllable shell structure", *Journal of Materials Chemistry*, Jg. 16, Nr. 45, S. 4413, 2006, ISSN: 0959-9428. DOI: 10.1039/b609971h.

[64] T. Jaumann, M. Gerwig, J. Balach, S. Oswald, E. Brendler, R. Hauser, B. Kieback, J. Eckert, L. Giebeler und E. Kroke, "Dichlorosilane-derived nano-silicon inside hollow carbon spheres as a high-performance anode for Li-ion batteries", *J. Mater. Chem. A*, Jg. 5, Nr. 19, S. 9262–9271, 2017, ISSN: 2050-7488. DOI: 10.1039/C7TA00188F. Adresse: https://pubs.rsc.org/en/content/articlehtml/2010/ta/c7ta00188f.

[65] D. Li, C. Feng, H. K. Liu und Z. Guo, "Hollow carbon spheres with encapsulated germanium as an anode material for lithium ion batteries", *J. Mater. Chem. A*, Jg. 3, Nr. 3, S. 978–981, 2015, ISSN: 2050-7488. DOI: 10.1039/C4TA05982D. Adresse: https://pubs.rsc.org/en/content/articlehtml/2014/ta/c4ta05982d.

[66] Y. J. Hong und Y. C. Kang, "General formation of tin nanoparticles encapsulated in hollow carbon spheres for enhanced lithium storage capability", *Small*, Jg. 11, Nr. 18, S. 2157–2163, 2015, ISSN: 1613-6810. DOI: 10.1002/smll.201402994.

[67] W.-M. Zhang, J.-S. Hu, Y.-G. Guo, S.-F. Zheng, L.-S. Zhong, W.-G. Song und L.-J. Wan, "Tin-Nanoparticles Encapsulated in Elastic Hollow Carbon Spheres for High-Performance Anode Material in Lithium-Ion Batteries", *Advanced Materials*, Jg. 20, Nr. 6, S. 1160–1165, 2008, ISSN: 1521-4095. DOI: 10.1002/adma.200701364.

[68] F. Zheng, M. He, Y. Yang und Q. Chen, "Nano electrochemical reactors of Fe_2O_3 nanoparticles embedded in shells of nitrogen-doped hollow carbon spheres as high-performance anodes for lithium-ion batteries", *Nanoscale*, Jg. 7, Nr. 8, S. 3410–3417, 2015. DOI: 10.1039/C4NR06321J. Adresse: https://pubs.rsc.org/en/content/articlehtml/2015/nr/c4nr06321j.

[69] F. Li, Q.-Q. Zou und Y.-Y. Xia, "CoO-loaded graphitable carbon hollow spheres as anode materials for lithium-ion battery", *Journal of Power Sources*, Jg. 177, Nr. 2, S. 546–552, 2008, ISSN: 0378-7753. DOI: 10.1016/j.jpowsour.2007.10.097.

[70] L. Zhan, Y. Wang, W. Qiao, L. Ling und S. Yang, "Hollow carbon spheres with encapsulation of Co_3O_4 nanoparticles as anode material for lithium ion batteries", *Electrochimica Acta*, Jg. 78, S. 440–445, 2012, ISSN: 00134686. DOI: 10.1016/j.electacta.2012.06.017.

[71] S. Sakata, W. Itoyama, I. Fujii und K. Iishi, "Preparation of low-temperature Li_3VO_4 single crystal by floating zone technique", *Journal of Crystal Growth*, Jg. 135, Nr. 3-4, S. 555–560, 1994, ISSN: 00220248. DOI: 10.1016/0022-0248(94)90147-3.

[72] Z. Chen, Z. Zhang, X. Dong, Y. Shi, Y. Liu und Q. Jing, "Li_3VO_4 : A Promising Mid-Infrared Nonlinear Optical Material with Large Laser Damage Threshold", *Crystal Growth & Design*, Jg. 17, Nr. 5, S. 2792–2800, 2017, ISSN: 1528-7483. DOI: 10.1021/acs.cgd.7b00250.

[73] J. Liu, P.-J. Lu, S. Liang, W. Wang, M. Lei, S. Tang und Q. Yang, "Ultrathin Li_3VO_4 nanoribbon/graphene sandwich-like nanostructures with ultrahigh lithium ion storage properties", *Nano Energy*, Jg. 12, S. 709–724, 2015, ISSN: 22112855. DOI: 10.1016/j.nanoen.2014.12.019.

[74] H. Li, X. Liu, T. Zhai, D. Li und H. Zhou, "Li_3VO_4: A Promising Insertion Anode Material for Lithium-Ion Batteries", *Advanced Energy Materials*, Jg. 3, Nr. 4, S. 428–432, 2013, ISSN: 16146832. DOI: 10.1002/aenm.201200833. Adresse: https://onlinelibrary.wiley.com/doi/10.1002/aenm.201200833.

[75] A. R. West und F. P. Glasser, “Preparation and crystal chemistry of some tetrahedral Li_3PO_4-type compounds”, *Journal of Solid State Chemistry*, Jg. 4, Nr. 1, S. 20–28, 1972, ISSN: 00224596. DOI: 10.1016/0022-4596(72)90127-2. Adresse: https://www.sciencedirect.com/science/article/pii/0022459672901272.

[76] R. D. Shannon und C. Calvo, “Refinement of the crystal structure of low temperature Li_3VO_4 and analysis of mean bond lengths in phosphates, arsenates, and vanadates”, *Journal of Solid State Chemistry*, Jg. 6, Nr. 4, S. 538–549, 1973, ISSN: 00224596. DOI: 10.1016/S0022-4596(73)80012-X.

[77] W.-T. Kim, Y. U. Jeong, Y. J. Lee, Y. J. Kim und J. H. Song, “Synthesis and lithium intercalation properties of Li_3VO_4 as a new anode material for secondary lithium batteries”, *Journal of Power Sources*, Jg. 244, S. 557–560, 2013, ISSN: 0378-7753. DOI: 10.1016/j.jpowsour.2013.01.163.

[78] C. Q. Du, J. W. Wu, J. Liu, M. Yang, Q. Xu, Z. Y. Tang und X. H. Zhang, “Synthesis of Lithium vanadium tetroxide anode material via a fast sol-gel method based on spontaneous chemical reactions”, *Electrochimica Acta*, Jg. 152, S. 473–479, 2015, ISSN: 00134686. DOI: 10.1016/j.electacta.2014.11.121.

[79] G. Shao, L. Gan, Y. Ma, H. Li und T. Zhai, “Enhancing the performance of Li_3VO_4 by combining nanotechnology and surface carbon coating for lithium ion batteries”, *Journal of Materials Chemistry A*, Jg. 3, Nr. 21, S. 11 253–11 260, 2015, ISSN: 2050-7488. DOI: 10.1039/C5TA02094H.

[80] D. Zhao und M. Cao, “Constructing Highly Graphitized Carbon-Wrapped Li_3VO_4 Nanoparticles with Hierarchically Porous Structure as a Long Life and High Capacity Anode for Lithium-Ion Batteries”, *ACS Applied Materials & Interfaces*, Jg. 7, Nr. 45, S. 25 084–25 093, 2015, ISSN: 1944-8244. DOI: 10.1021/acsami.5b05269.

[81] C. Liao, Q. Zhang, T. Zhai, H. Li und H. Zhou, “Development and perspective of the insertion anode Li_3VO_4 for lithium-ion batteries”, *Energy Storage Materials*, Jg. 7, S. 17–31, 2017, ISSN: 24058297. DOI: 10.1016/j.ensm.2016.11.009.

[82] Z. Liang, Z. Lin, Y. Zhao, Y. Dong, Q. Kuang, X. Lin, X. Liu und D. Yan, “New understanding of Li_3VO_4/C as potential anode for Li-ion batteries: Preparation, structure characterization and lithium insertion mechanism”, *Journal of Power Sources*, Jg. 274, S. 345–354, 2015. DOI: 10.1016/j.jpowsour.2014.10.024.

[83] S. Ni, J. Zhang, J. Ma, X. Yang, L. Zhang, X. Li und H. Zeng, “Approaching the Theoretical Capacity of Li_3VO_4 via Electrochemical Reconstruction”, *Advanced Materials Interfaces*, Jg. 3, Nr. 1, S. 1 500 340, 2016, ISSN: 21967350. DOI: 10.1002/admi.201500340.

[84] M. E. Arroyo-de Dompablo, P. Tartaj, J. M. Amarilla und U. Amador, “Computational Investigation of Li Insertion in F”, *Chemistry of Materials*, Jg. 28, Nr. 16, S. 5643–5651, 2016, ISSN: 1520-5002. DOI: 10.1021/acs.chemmater.6b01519.

[85] Q. Li, Q. Wei, J. Sheng, M. Yan, L. Zhou, W. Luo, R. Sun und L. Mai, “Mesoporous Li_3VO_4/C Submicron-Ellipsoids Supported on Reduced Graphene Oxide as Practical Anode for High-Power Lithium-Ion Batteries”, *Advanced science (Weinheim, Baden-Wurttemberg, Germany)*, Jg. 2, Nr. 12, S. 1 500 284, 2015, ISSN: 2198-3844. DOI: 10.1002/advs.201500284.

[86] S. Ni, X. Lv, J. Ma, X. Yang und L. Zhang, "Electrochemical characteristics of lithium vanadate, Li_3VO_4 as a new sort of anode material for Li-ion batteries", *Journal of Power Sources*, Jg. 248, S. 122–129, 2014. DOI: 10.1016/j.jpowsour.2013.09.050.

[87] Y. Shi, J. Gao, H. D. Abruña, H.-J. Li, H.-K. Liu, D. Wexler, J.-Z. Wang und Y. Wu, "The mechanism of the one-step synthesis of hollow-structured Li_3VO_4 as an anode for lithium-ion batteries", *Chemistry (Weinheim an der Bergstrasse, Germany)*, Jg. 20, Nr. 19, S. 5608–5612, 2014. DOI: 10.1002/chem.201400118.

[88] W.-T. Kim, B.-K. Min, H. C. Choi, Y. J. Lee und Y. U. Jeong, "Lithium intercalation and crystal chemistry of Li_3VO_4 synthesized by ultrasonic nebulization as a new anode material for secondary lithium batteries", *Journal of The Electrochemical Society*, Jg. 161, Nr. 9, A1302–A1305, 2014, ISSN: 0013-4651. DOI: 10.1149/2.0651409jes.

[89] G. Yang, B. Zhang, J. Feng, Y. Lu, Z. Wang, V. Aravindan, M. Aravind, J. Liu, M. Srinivasan, Z. Shen und Y. Huang, "Morphology controlled lithium storage in Li_3VO_4 anodes", *Journal of Materials Chemistry A*, Jg. 6, Nr. 2, S. 456–463, 2018, ISSN: 2050-7488. DOI: 10.1039/C7TA09023D.

[90] C. Zhang, C. Liu, X. Nan, H. Song, Y. Liu, C. Zhang und G. Cao, "Hollow-Cuboid Li_3VO_4/C as High-Performance Anodes for Lithium-Ion Batteries", *ACS Applied Materials & Interfaces*, Jg. 8, Nr. 1, S. 680–688, 2016, ISSN: 1944-8244. DOI: 10.1021/acsami.5b09810.

[91] Z. Liang, Y. Zhao, Y. Dong, Q. Kuang, X. Lin, X. Liu und D. Yan, "The low and high temperature electrochemical performance of Li_3VO_4/C anode material for Li-ion batteries", *Journal of Electroanalytical Chemistry*, Jg. 745, S. 1–7, 2015, ISSN: 1572-6657. DOI: 10.1016/j.jelechem.2015.03.013.

[92] Z. Jian, M. Zheng, Y. Liang, X. Zhang, S. Gheytani, Y. Lan, Y. Shi und Y. Yao, "Li_3VO_4 anchored graphene nanosheets for long-life and high-rate lithium-ion batteries", *Chemical communications (Cambridge, England)*, Jg. 51, Nr. 1, S. 229–231, 2015. DOI: 10.1039/C4CC07444K. Adresse: https://pubs.rsc.org/en/content/articlehtml/2014/cc/c4cc07444k.

[93] S. Ni, X. Lv, J. Zhang, J. Ma, X. Yang und L. Zhang, "The electrochemical performance of lithium vanadate/natural graphite composite material as anode for lithium ion batteries", *Electrochimica Acta*, Jg. 145, S. 327–334, 2014, ISSN: 00134686. DOI: 10.1016/j.electacta.2014.09.018.

[94] Q. Li, J. Sheng, Q. Wei, Q. An, X. Wei, P. Zhang und L. Mai, "A unique hollow Li_3VO_4/carbon nanotube composite anode for high rate long-life lithium-ion batteries", *Nanoscale*, Jg. 6, Nr. 19, S. 11 072–11 077, 2014. DOI: 10.1039/C4NR03119A. Adresse: https://pubs.rsc.org/en/content/articlehtml/2014/nr/c4nr03119a.

[95] Y. Yang, J. Li, D. Chen und J. Zhao, "Spray Drying-Assisted Synthesis of Li_3VO_4/C/CNTs Composites for High-Performance Lithium Ion Battery Anodes", *Journal of The Electrochemical Society*, Jg. 164, Nr. 1, A6001–A6006, 2017, ISSN: 0013-4651. DOI: 10.1149/2.0031701jes. Adresse: https://iopscience.iop.org/article/10.1149/2.0031701jes/meta.

[96] Y. Han, G. Huang und S. Xu, "Structural Reorganization-Based Nanomaterials as Anodes for Lithium-Ion Batteries: Design, Preparation, and Performance", *Small*, Jg. 16, Nr. 15, e1902841, 2020, ISSN: 1613-6810. DOI: 10.1002/smll.201902841.

[97] K. Cao, T. Jin, L. Yang und L. Jiao, "Recent progress in conversion reaction metal oxide anodes for Li-ion batteries", *Materials Chemistry Frontiers*, Jg. 1, Nr. 11, S. 2213–2242, 2017. DOI: 10.1039/C7QM00175D.

[98] S. Lany, "Band-structure calculations for the 3 d transition metal oxides in GW", *Physical Review B*, Jg. 87, Nr. 8, 2013, ISSN: 0163-1829. DOI: 10.1103/PhysRevB.87.085112.

[99] S.-C. Lim, M. S. Chae, J. W. Heo und S.-T. Hong, "Electrochemical lithium intercalation chemistry of condensed molybdenum metal cluster oxide: $LiMo_4O_6$", *Journal of Solid State Chemistry*, Jg. 254, S. 90–95, 2017, ISSN: 00224596. DOI: 10.1016/j.jssc.2017.07.004.

[100] J. J. Auborn und Y. L. Barberio, "Lithium Intercalation Cells Without Metallic Lithium: and", *Journal of The Electrochemical Society*, Jg. 134, Nr. 3, S. 638–641, 1987, ISSN: 0013-4651. DOI: 10.1149/1.2100521.

[101] J. R. Dahn und W. R. McKinnon, "Structure and electrochemistry of Li_xMoO_2", *Solid State Ionics*, Jg. 23, Nr. 1-2, S. 1–7, 1987, ISSN: 0167-2738. DOI: 10.1016/0167-2738(87)90074-9.

[102] U. K. Sen, A. Shaligram und S. Mitra, "Intercalation anode material for lithium ion battery based on molybdenum dioxide", *ACS Applied Materials & Interfaces*, Jg. 6, Nr. 16, S. 14 311–14 319, 2014, ISSN: 1944-8244. DOI: 10.1021/am503605u.

[103] A. Kim, E. Park, H. Lee und H. Kim, "Highly reversible insertion of lithium into MoO_2 as an anode material for lithium ion battery", *Journal of Alloys and Compounds*, Jg. 681, S. 301–306, 2016, ISSN: 09258388. DOI: 10.1016/j.jallcom.2016.04.188.

[104] X. Liu, J. Yang, W. Hou, J. Wang und Y. Nuli, "Highly Reversible Lithium-ions Storage of Molybdenum Dioxide Nanoplates for High Power Lithium-ion Batteries", *ChemSusChem*, Jg. 8, Nr. 16, S. 2621–2624, 2015, ISSN: 1864-5631. DOI: 10.1002/cssc.201500574.

[105] D.-Y. Park, Y.-K. Sun und S.-T. Myung, "Carbothermal synthesis of molybdenum(IV) oxide as a high rate anode for rechargeable lithium batteries", *Journal of Power Sources*, Jg. 280, S. 1–4, 2015, ISSN: 0378-7753. DOI: 10.1016/j.jpowsour.2015.01.042.

[106] L. C. Yang, Q. S. Gao, Y. H. Zhang, Y. Tang und Y. P. Wu, "Tremella-like molybdenum dioxide consisting of nanosheets as an anode material for lithium ion battery", *Electrochemistry Communications*, Jg. 10, Nr. 1, S. 118–122, 2008, ISSN: 13882481. DOI: 10.1016/j.elecom.2007.11.009.

[107] X. Ji, P. S. Herle, Y. Rho und L. F. Nazar, "Carbon/MoO_2 Composite Based on Porous Semi-Graphitized Nanorod Assemblies from In Situ Reaction of Tri-Block Polymers", *Chemistry of Materials*, Jg. 19, Nr. 3, S. 374–383, 2007, ISSN: 1520-5002. DOI: 10.1021/cm060961y.

[108] J. H. Ku, Y. S. Jung, K. T. Lee, C. H. Kim und S. M. Oh, "Thermoelectrochemically Activated MoO_2 Powder Electrode for Lithium Secondary Batteries", *Journal of The Electrochemical Society*, Jg. 156, Nr. 8, A688, 2009, ISSN: 0013-4651. DOI: 10.1149/1.3141670.

[109] B. Guo, X. Fang, B. Li, Y. Shi, C. Ouyang, Y.-S. Hu, Z. Wang, G. D. Stucky und L. Chen, "Synthesis and Lithium Storage Mechanism of Ultrafine MoO_2 Nanorods", *Chemistry of Materials*, Jg. 24, Nr. 3, S. 457–463, 2012, ISSN: 1520-5002. DOI: 10.1021/cm202459r.

[110] Y. Sun, X. Hu, J. C. Yu, Q. Li, W. Luo, L. Yuan, W. Zhang und Y. Huang, "Morphosynthesis of a hierarchical MoO_2 nanoarchitecture as a binder-free anode for lithium-ion batteries", *Energy & Environmental Science*, Jg. 4, Nr. 8, S. 2870, 2011, ISSN: 1754-5692. DOI: 10.1039/c1ee01189h.

[111] Y. Shi, B. Guo, S. A. Corr, Q. Shi, Y.-S. Hu, K. R. Heier, L. Chen, R. Seshadri und G. D. Stucky, "Ordered mesoporous metallic MoO_2 materials with highly reversible lithium storage capacity", *Nano Letters*, Jg. 9, Nr. 12, S. 4215–4220, 2009, ISSN: 1530-6984. DOI: 10.1021/nl902423a.

[112] K. H. Seng, G. D. Du, L. Li, Z. X. Chen, H. K. Liu und Z. P. Guo, "Facile synthesis of graphene-molybdenum dioxide and its lithium storage properties", *Journal of Materials Chemistry*, Jg. 22, Nr. 31, S. 16 072, 2012, ISSN: 0959-9428. DOI: 10.1039/c2jm32822d.

[113] D. Han, S. Hwang, S.-M. Bak und K.-W. Nam, "Controlling MoO_2 and MoO_3 phases in MoO_x/CNTs nanocomposites and their application to anode materials for lithium-ion batteries and capacitors", *Electrochimica Acta*, Jg. 388, S. 138 635, 2021, ISSN: 00134686. DOI: 10.1016/j.electacta.2021.138635.

[114] W. Cho, J. H. Song, J.-H. Kim, G. Jeong, E. Y. Lee und Y.-J. Kim, "Electrochemical characteristics of nano-sized MoO_2/C composite anode materials for lithium-ion batteries", *Journal of Applied Electrochemistry*, Jg. 42, Nr. 11, S. 909–915, 2012, ISSN: 0021-891X. DOI: 10.1007/s10800-012-0470-9.

[115] Y. Sun, X. Hu, W. Luo und Y. Huang, "Ultrafine MoO_2 nanoparticles embedded in a carbon matrix as a high-capacity and long-life anode for lithium-ion batteries", *Journal of Materials Chemistry*, Jg. 22, Nr. 2, S. 425–431, 2012, ISSN: 0959-9428. DOI: 10.1039/C1JM14701C.

[116] J. K. Shon, H. S. Lee, G. O. Park, J. Yoon, E. Park, G. S. Park, S. S. Kong, M. Jin, J.-M. Choi, H. Chang, S. Doo, J. M. Kim, W.-S. Yoon, C. Pak, H. Kim und G. D. Stucky, "Discovery of abnormal lithium-storage sites in molybdenum dioxide electrodes", *Nature communications*, Jg. 7, Nr. 1, S. 11 049, 2016. DOI: 10.1038/ncomms11049.

[117] L. Dillemans, T. Smets, R. R. Lieten, M. Menghini, C.-Y. Su und J.-P. Locquet, "Evidence of the metal-insulator transition in ultrathin unstrained V_2O_3 thin films", *Applied Physics Letters*, Jg. 104, Nr. 7, S. 071 902, 2014, ISSN: 0003-6951. DOI: 10.1063/1.4866004.

[118] M. M. Qazilbash, A. A. Schafgans, K. S. Burch, S. J. Yun, B. G. Chae, B. J. Kim, H. T. Kim und D. N. Basov, "Electrodynamics of the vanadium oxides VO_2 and V_2O_3", *Physical Review B*, Jg. 77, Nr. 11, 2008, ISSN: 0163-1829. DOI: 10.1103/PhysRevB.77.115121.

[119] Y. Jin, C. P. Yang, X. H. Rui, T. Cheng und C. H. Chen, "V2O3 modified $LiFePO_4$/C composite with improved electrochemical performance", *Journal of Power Sources*, Jg. 196, Nr. 13, S. 5623–5630, 2011, ISSN: 0378-7753. DOI: 10.1016/j.jpowsour.2011.02.059.

[120] A. Tranchant, R. Messina und J. Perichon, "Mechanism of electrochemical reduction of vanadium oxides", *J. Electroanal. Chem. Interf. Electrochem.*, Jg. 113, Nr. 2, S. 225–232, 1980. DOI: 10.1016/S0022-0728(80)80023-4.

[121] H. Li, P. Balaya und J. Maier, "Li-Storage via Heterogeneous Reaction in Selected Binary Metal Fluorides and Oxides", *Journal of The Electrochemical Society*, Jg. 151, Nr. 11, A1878, 2004, ISSN: 0013-4651. DOI: 10.1149/1.1801451.

[122] X. Xu, F. Xiong, J. Meng, X. Wang, C. Niu, Q. An und L. Mai, "Vanadium-Based Nanomaterials: A Promising Family for Emerging Metal–Ion Batteries", *Advanced Functional Materials*, Jg. 30, Nr. 10, S. 1 904 398, 2020, ISSN: 1616-3028. DOI: 10.1002/adfm.201904398.

[123] L. Jiang, Y. Qu, Z. Ren, P. Yu, D. Zhao, W. Zhou, L. Wang und H. Fu, "In situ carbon-coated yolk-shell V_2O_3 microspheres for lithium-ion batteries", *ACS Appl. Mater. Interfaces*, Jg. 7, Nr. 3, S. 1595–1601, 2015. DOI: 10.1021/am5070393.

[124] Y. Dong, R. Ma, M. Hu, H. Cheng, J.-M. Lee, Y. Y. Li und J. A. Zapien, "Polymer-pyrolysis assisted synthesis of vanadium trioxide and carbon nanocomposites as high performance anode materials for lithium-ion batteries", *Journal of Power Sources*, Jg. 261, S. 184–187, 2014. DOI: 10.1016/j.jpowsour.2014.03.020.

[125] H. Jiang, G. Jia, Y. Hu, Q. Cheng, Y. Fu und C. Li, "Ultrafine V_2O_3 Nanowire Embedded in Carbon Hybrids with Enhanced Lithium Storage Capability", *Industrial & Engineering Chemistry Research*, Jg. 54, Nr. 11, S. 2960–2965, 2015, ISSN: 0888-5885. DOI: 10.1021/acs.iecr.5b00132.

[126] Y. Bai, Y. Tang, L. Liu, X. Li und Y. Gao, "Peapod-like CNT@V_2O_3 with Superior Electrochemical Performance as an Anode for Lithium-Ion Batteries", *ACS Sustainable Chemistry & Engineering*, Jg. 6, Nr. 11, S. 14 614–14 620, 2018, ISSN: 2168-0485. DOI: 10.1021/acssuschemeng.8b03218.

[127] B. Xiao, B. Zhang, L.-b. Tang, C.-s. An, Z.-j. He, H. Tong, W.-j. Yu und J.-c. Zheng, "V_2O_3/rGO composite as a potential anode material for lithium ion batteries", *Ceram. Int.*, Jg. 44, Nr. 13, S. 15 044–15 049, 2018. DOI: 10.1016/j.ceramint.2018.05.134.

[128] Y. Zhang, A. Pan, S. Liang, T. Chen, Y. Tang und X. Tan, "Reduced graphene oxide modified V_2O_3 with enhanced performance for lithium-ion battery", *Materials Letters*, Jg. 137, S. 174–177, 2014, ISSN: 0167-577X. DOI: 10.1016/j.matlet.2014.09.013.

[129] S.-C. Weng, S. Brahma, P.-C. Huang, Y.-C. Huang, Y.-H. Lee, C.-C. Chang und J.-L. Huang, "Enhanced capacity and significant rate capability of Mn_3O_4/reduced graphene oxide nanocomposite as high performance anode material in lithium-ion batteries", *Applied Surface Science*, Jg. 505, S. 144 629, 2020, ISSN: 0169-4332. DOI: 10.1016/j.apsusc.2019.144629.

[130] X. Fang, X. Lu, X. Guo, Y. Mao, Y.-S. Hu, J. Wang, Z. Wang, F. Wu, H. Liu und L. Chen, "Electrode reactions of manganese oxides for secondary lithium batteries", *Electrochemistry Communications*, Jg. 12, Nr. 11, S. 1520–1523, 2010, ISSN: 13882481. DOI: 10.1016/j.elecom.2010.08.023.

[131] M. A. Lowe, J. Gao und H. D. Abruña, "In operando X-ray studies of the conversion reaction in Mn_3O_4 lithium battery anodes", *J. Mater. Chem. A*, Jg. 1, Nr. 6, S. 2094–2103, 2013, ISSN: 2050-7488. DOI: 10.1039/C2TA01270G.

[132] K. Zhong, B. Zhang, S. Luo, W. Wen, H. Li, X. Huang und L. Chen, "Investigation on porous MnO microsphere anode for lithium ion batteries", *Journal of Power Sources*, Jg. 196, Nr. 16, S. 6802–6808, 2011. DOI: 10.1016/j.jpowsour.2010.10.031.

[133] S.-Z. Huang, J. Jin, Y. Cai, Y. Li, H.-Y. Tan, H.-E. Wang, G. van Tendeloo und B.-L. Su, "Engineering single crystalline Mn_3O_4 nano-octahedra with exposed highly active (011) facets for high performance lithium ion batteries", *Nanoscale*, Jg. 6, Nr. 12, S. 6819–6827, 2014. DOI: 10.1039/c4nr01389a.

[134] Z. Bai, N. Fan, Z. Ju, C. Guo, Y. Qian, B. Tang und S. Xiong, "Facile synthesis of mesoporous Mn_3O_4 nanotubes and their excellent performance for lithium-ion batteries", *J. Mater. Chem. A*, Jg. 1, Nr. 36, S. 10 985, 2013, ISSN: 2050-7488. DOI: 10.1039/c3ta11910f.

[135] Y. Zhuang, Z. Ma, Y. Deng, X. Song, X. Zuo, X. Xiao und J. Nan, "Sandwich-like Mn_3O_4/carbon nanofragment composites with a higher capacity than commercial graphite and hierarchical voltage plateaus for lithium ion batteries", *Electrochimica Acta*, Jg. 245, S. 448–455, 2017, ISSN: 00134686. DOI: 10.1016/j.electacta.2017.05.171. Adresse: https://www.sciencedirect.com/science/article/pii/s0013468617312021.

[136] H.-J. Peng, G.-X. Hao, Z.-H. Chu, J. Lin, X.-M. Lin und Y.-P. Cai, "Mesoporous Mn_3O_4/C Microspheres Fabricated from MOF Template as Advanced Lithium-Ion Battery Anode", *Crystal Growth & Design*, Jg. 17, Nr. 11, S. 5881–5886, 2017, ISSN: 1528-7483. DOI: 10.1021/acs.cgd.7b00978.

[137] K. Liu, F. Zou, Y. Sun, Z. Yu, X. Liu, L. Zhou, Y. Xia, B. D. Vogt und Y. Zhu, "Self-assembled Mn_3O_4/C nanospheres as high-performance anode materials for lithium ion batteries", *Journal of Power Sources*, Jg. 395, S. 92–97, 2018, ISSN: 0378-7753. DOI: 10.1016/j.jpowsour.2018.05.064.

[138] C. Wang, L. Yin, D. Xiang und Y. Qi, "Uniform carbon layer coated Mn_3O_4 nanorod anodes with improved reversible capacity and cyclic stability for lithium ion batteries", *ACS Applied Materials & Interfaces*, Jg. 4, Nr. 3, S. 1636–1642, 2012, ISSN: 1944-8244. DOI: 10.1021/am2017909.

[139] L. Li, Z. Guo, A. Du und H. Liu, "Rapid microwave-assisted synthesis of Mn_3O_4–graphene nanocomposite and its lithium storage properties", *Journal of Materials Chemistry*, Jg. 22, Nr. 8, S. 3600, 2012, ISSN: 0959-9428. DOI: 10.1039/c2jm15075a.

[140] H. Wang, L.-F. Cui, Y. Yang, H. Sanchez Casalongue, J. T. Robinson, Y. Liang, Y. Cui und H. Dai, "Mn_3O_4-graphene hybrid as a high-capacity anode material for lithium ion batteries", *Journal of the American Chemical Society*, Jg. 132, Nr. 40, S. 13 978–13 980, 2010. DOI: 10.1021/ja105296a.

[141] S. P. Varghese, B. Babu, R. Prasannachandran, R. Antony und M. M. Shaijumon, "Enhanced electrochemical properties of Mn_3O_4/graphene nanocomposite as efficient anode material for lithium ion batteries", *Journal of Alloys and Compounds*, Jg. 780, S. 588–596, 2019, ISSN: 09258388. DOI: 10.1016/j.jallcom.2018.11.394.

[142] B. Wang, F. Li, X. Wang, G. Wang, H. Wang und J. Bai, "Mn_3O_4 nanotubes encapsulated by porous graphene sheets with enhanced electrochemical properties for lithium/sodium-ion batteries", *Chemical Engineering Journal*, Jg. 364, S. 57–69, 2019, ISSN: 1385-8947. DOI: 10.1016/j.cej.2019.01.155.

[143] Y. Wang, "Coprecipitated 3D nanostructured graphene oxide–Mn_3O_4 hybrid as anode of lithium-ion batteries", *Journal of Materials Research*, Jg. 30, Nr. 4, S. 484–492, 2015, ISSN: 0884-2914. DOI: 10.1557/jmr.2014.394.

[144] S.-K. Park, C.-Y. Seong, S. Yoo und Y. Piao, "Porous Mn_3O_4 nanorod/reduced graphene oxide hybrid paper as a flexible and binder-free anode material for lithium ion battery", *Energy*, Jg. 99, S. 266–273, 2016, ISSN: 03605442. DOI: 10.1016/j.energy.2016.01.061.

[145] M. Jing, H. Hou, Y. Yang, Y. Zhang, X. Yang, Q. Chen und X. Ji, "Electrochemically Alternating Voltage Induced Mn_3O_4/Graphite Powder Composite with Enhanced Electrochemical Performances for Lithium-ion Batteries", *Electrochimica Acta*, Jg. 155, S. 157–163, 2015, ISSN: 00134686. DOI: 10.1016/j.electacta.2014.12.170.

[146] Y. Zhao, C. Ma und Y. Li, "One-step microwave preparation of a Mn_3O_4 nanoparticles/exfoliated graphite composite as superior anode materials for Li-ion batteries", *Chemical Physics Letters*, Jg. 673, S. 19–23, 2017, ISSN: 00092614. DOI: 10.1016/j.cplett.2017.02.002.

[147] S. Luo, H. Wu, Y. Wu, K. Jiang, J. Wang und S. Fan, "Mn_3O_4 nanoparticles anchored on continuous carbon nanotube network as superior anodes for lithium ion batteries", *Journal of Power Sources*, Jg. 249, S. 463–469, 2014. DOI: 10.1016/j.jpowsour.2013.10.133.

[148] X. Cui, Y. Wang, Q. Xu, P. Sun, X. Wang, T. Wei und Y. Sun, "Carbon nanotube entangled Mn_3O_4 octahedron as anode materials for lithium-ion batteries", *Nanotechnology*, Jg. 28, Nr. 25, S. 255 402, 2017, ISSN: 0957-4484. DOI: 10.1088/1361-6528/aa7239.

[149] K. Cao, Y. Jia, S. Wang, K.-J. Huang und H. Liu, "Mn_3O_4 nanoparticles anchored on carbon nanotubes as anode material with enhanced lithium storage", *Journal of Alloys and Compounds*, Jg. 854, S. 157 179, 2021, ISSN: 09258388. DOI: 10.1016/j.jallcom.2020.157179.

[150] C. Yuan, H. B. Wu, Y. Xie und X. W. D. Lou, "Mixed transition-metal oxides: design, synthesis, and energy-related applications", *Angewandte Chemie (International ed. in English)*, Jg. 53, Nr. 6, S. 1488–1504, 2014, ISSN: 1433-7851. DOI: 10.1002/anie.201303971.

[151] F. Wu, J. Bai, J. Feng und S. Xiong, "Porous mixed metal oxides: design, formation mechanism, and application in lithium-ion batteries", *Nanoscale*, Jg. 7, Nr. 41, S. 17 211–17 230, 2015. DOI: 10.1039/C5NR04791A.

[152] F. Sharifianjazi, M. Moradi, N. Parvin, A. Nemati, A. Jafari Rad, N. Sheysi, A. Abouchenari, A. Mohammadi, S. Karbasi, Z. Ahmadi, A. Esmaeilkhanian, M. Irani, A. Pakseresht, S. Sahmani und M. Shahedi Asl, "Magnetic $CoFe_2O_4$ nanoparticles doped with metal ions: A review", *Ceramics International*, Jg. 46, Nr. 11, S. 18 391–18 412, 2020, ISSN: 02728842. DOI: 10.1016/j.ceramint.2020.04.202.

[153] R. Alcantara, M. Jaraba, O. Lavela und Tirado J.L., Electrochemical Society meeting in Salt Lake City, 2002.

[154] Y.-Q. Chu, Z.-W. Fu und Q.-Z. Qin, "Cobalt ferrite thin films as anode material for lithium ion batteries", *Electrochimica Acta*, Jg. 49, Nr. 27, S. 4915–4921, 2004, ISSN: 00134686. DOI: 10.1016/j.electacta.2004.06.012.

[155] S. Permien, S. Indris, U. Schürmann, L. Kienle, S. Zander, S. Doyle und W. Bensch, "What Happens Structurally and Electronically during the Li Conversion Reaction of CoFe 2 O 4 Nanoparticles: An Operando XAS and XRD Investigation", *Chemistry of Materials*, Jg. 28, Nr. 2, S. 434–444, 2016, ISSN: 1520-5002. DOI: 10.1021/acs.chemmater.5b01754.

[156] P. Lavela und J. L. Tirado, "$CoFe_2O_4$ and $NiFe_2O_4$ synthesized by sol–gel procedures for their use as anode materials for Li ion batteries", *Journal of Power Sources*, Jg. 172, Nr. 1, S. 379–387, 2007, ISSN: 0378-7753. DOI: 10.1016/j.jpowsour.2007.07.055.

[157] Z. H. Li, T. P. Zhao, X. Y. Zhan, D. S. Gao, Q. Z. Xiao und G. T. Lei, "High capacity three-dimensional ordered macroporous $CoFe_2O_4$ as anode material for lithium ion batteries", *Electrochimica Acta*, Jg. 55, Nr. 15, S. 4594–4598, 2010, ISSN: 00134686. DOI: 10.1016/j.electacta.2010.03.015.

[158] N. Wang, H. Xu, L. Chen, X. Gu, J. Yang und Y. Qian, "A general approach for MFe_2O_4 (M = Zn, Co, Ni) nanorods and their high performance as anode materials for lithium ion batteries", *Journal of Power Sources*, Jg. 247, S. 163–169, 2014, ISSN: 0378-7753. DOI: 10.1016/j.jpowsour.2013.08.109.

[159] S. Yoon, "Facile microwave synthesis of $CoFe_2O_4$ spheres and their application as an anode for lithium-ion batteries", *Journal of Applied Electrochemistry*, Jg. 44, Nr. 9, S. 1069–1074, 2014, ISSN: 0021-891X. DOI: 10.1007/s10800-014-0716-9.

[160] Y. Wang, D. Su, A. Ung, J. H. Ahn und G. Wang, "Hollow $CoFe_2O_4$ nanospheres as a high capacity anode material for lithium ion batteries", *Nanotechnology*, Jg. 23, Nr. 5, S. 055 402, 2012, ISSN: 0957-4484. DOI: 10.1088/0957-4484/23/5/055402.

[161] L. Wu, Q. Xiao, Z. Li, G. Lei, P. Zhang und L. Wang, "$CoFe_2O_4$/C composite fibers as anode materials for lithium-ion batteries with stable and high electrochemical performance", *Solid State Ionics*, Jg. 215, S. 24–28, 2012, ISSN: 0167-2738. DOI: 10.1016/j.ssi.2012.03.044.

[162] S. Ren, X. Zhao, R. Chen und M. Fichtner, "A facile synthesis of encapsulated $CoFe_2O_4$ into carbon nanofibres and its application as conversion anodes for lithium ion batteries", *Journal of Power Sources*, Jg. 260, S. 205–210, 2014, ISSN: 0378-7753. DOI: 10.1016/j.jpowsour.2014.03.012.

[163] Z. Zhang, Y. Wang, M. Zhang, Q. Tan, X. Lv, Z. Zhong und F. Su, "Mesoporous $CoFe_2O_4$ nanospheres cross-linked by carbon nanotubes as high-performance anodes for lithium-ion batteries", *J. Mater. Chem. A*, Jg. 1, Nr. 25, S. 7444, 2013, ISSN: 2050-7488. DOI: 10.1039/c3ta10762k.

[164] F. Badway, I. Plitz, S. Grugeon, S. Laruelle, M. Dollé, A. S. Gozdz und J.-M. Tarascon, "Metal Oxides as Negative Electrode Materials in Li-Ion Cells", *Electrochemical and Solid-State Letters*, Jg. 5, Nr. 6, A115, 2002, ISSN: 10990062. DOI: 10.1149/1.1472303.

[165] M. N. Obrovac und V. L. Chevrier, "Alloy negative electrodes for Li-ion batteries", *Chemical reviews*, Jg. 114, Nr. 23, S. 11 444–11 502, 2014. DOI: 10.1021/cr500207g. Adresse: https://pubs.acs.org/doi/full/10.1021/cr500207g.

[166] D. Bresser, S. Passerini und B. Scrosati, "Leveraging valuable synergies by combining alloying and conversion for lithium-ion anodes", *Energy & Environmental Science*, Jg. 9, Nr. 11, S. 3348–3367, 2016, ISSN: 1754-5692. DOI: 10.1039/C6EE02346K.

[167] M. V. Reddy, G. V. Subba Rao und B. V. R. Chowdari, "Metal oxides and oxysalts as anode materials for Li ion batteries", *Chemical Reviews*, Jg. 113, Nr. 7, S. 5364–5457, 2013, ISSN: 0009-2665. DOI: 10.1021/cr3001884.

[168] Z.-W. Fu, F. Huang, Y. Zhang, Y. Chu und Q.-Z. Qin, "The Electrochemical Reaction of Zinc Oxide Thin Films with Lithium", *Journal of The Electrochemical Society*, Jg. 150, Nr. 6, A714, 2003, ISSN: 0013-4651. DOI: 10.1149/1.1570410. Adresse: https://iopscience.iop.org/article/10.1149/1.1570410.

[169] F. Belliard, P. A. Connor und J. T. S. Irvine, "Doped tin oxides as potential lithium ion battery negative electrodes", *Ionics*, Jg. 5, Nr. 5-6, S. 450–454, 1999, ISSN: 0947-7047. DOI: 10.1007/BF02376012.

[170] C. Q. Zhang, J. P. Tu, Y. F. Yuan, X. H. Huang, X. T. Chen und F. Mao, "Electrochemical Performances of Ni-Coated ZnO as an Anode Material for Lithium-Ion Batteries", *Journal of The Electrochemical Society*, Jg. 154, Nr. 2, A65, 2007, ISSN: 0013-4651. DOI: 10.1149/1.2400609.

[171] G.-L. Xu, Y. Li, T. Ma, Y. Ren, H.-H. Wang, L. Wang, J. Wen, D. Miller, K. Amine und Z. Chen, "PEDOT-PSS coated ZnO/C hierarchical porous nanorods as ultralong-life anode material for lithium ion batteries", *Nano Energy*, Jg. 18, S. 253–264, 2015, ISSN: 22112855. DOI: 10.1016/j.nanoen.2015.10.020.

[172] M.-G. Park, G.-K. Sung, N.-E. Sung, J.-H. Kim und C.-M. Park, "Partially reversible Li_2O formation in ZnO: A critical finding supporting realization of highly reversible metal oxide electrodes", *Journal of Power Sources*, Jg. 328, S. 607–614, 2016. DOI: 10.1016/j.jpowsour.2016.08.053.

[173] C. J. Pelliccione, Y. Ding, E. V. Timofeeva und C. U. Segre, "In Situ XAFS Study of the Capacity Fading Mechanisms in ZnO Anodes for Lithium-Ion Batteries", *Journal of The Electrochemical Society*, Jg. 162, Nr. 10, A1935–A1939, 2015, ISSN: 0013-4651. DOI: 10.1149/2.1011509jes.

[174] Y. Zhang, Z. Wang, Y. Li und K. Zhao, "Lithiation of ZnO nanowires studied by in-situ transmission electron microscopy and theoretical analysis", *Mechanics of Materials*, Jg. 91, S. 313–322, 2015, ISSN: 01676636. DOI: 10.1016/j.mechmat.2015.05.004.

[175] Q. Su, Z. Dong, J. Zhang, G. Du und B. Xu, "Visualizing the electrochemical reaction of ZnO nanoparticles with lithium by in situ TEM: two reaction modes are revealed", *Nanotechnology*, Jg. 24, Nr. 25, S. 255 705, 2013, ISSN: 0957-4484. DOI: 10.1088/0957-4484/24/25/255705.

[176] L. Shen und C. Wang, "ZnO/C microboxes derived from coordination polymer particles for superior lithium ion battery anodes", *RSC Advances*, Jg. 5, Nr. 108, S. 88 989–88 995, 2015, ISSN: 2046-2069. DOI: 10.1039/C5RA18254A.

[177] Q. Xie, X. Zhang, X. Wu, H. Wu, X. Liu, G. Yue, Y. Yang und D.-L. Peng, "Yolk-shell ZnO-C microspheres with enhanced electrochemical performance as anode material for lithium ion batteries", *Electrochimica Acta*, Jg. 125, S. 659–665, 2014, ISSN: 00134686. DOI: 10.1016/j.electacta.2014.02.003.

[178] Z. Bai, Y. Zhang, N. Fan, C. Guo und B. Tang, "One-step synthesis of ZnO@C nanospheres and their enhanced performance for lithium-ion batteries", *Materials Letters*, Jg. 119, S. 16–19, 2014, ISSN: 0167-577X. DOI: 10.1016/j.matlet.2013.12.060.

[179] D. Wang, J. Guo, C. Cui, J. Ma und A. Cao, “Controllable synthesis of CNT@ZnO composites with enhanced electrochemical properties for lithium-ion battery”, *Materials Research Bulletin*, Jg. 101, S. 305–310, 2018, ISSN: 0025-5408. DOI: 10.1016/j.materresbull.2018.01.052. Adresse: http://www.sciencedirect.com/science/article/pii/S0025540817324716.

[180] S. M. Abbas, S. T. Hussain, S. Ali, N. Ahmad, N. Ali und S. Abbas, “Structure and electrochemical performance of ZnO/CNT composite as anode material for lithium-ion batteries”, *Journal of Materials Science*, Jg. 48, Nr. 16, S. 5429–5436, 2013, ISSN: 1573-4803. DOI: 10.1007/s10853-013-7336-3.

[181] E. Quartarone, V. Dall’Asta, A. Resmini, C. Tealdi, I. G. Tredici, U. A. Tamburini und P. Mustarelli, “Graphite-coated ZnO nanosheets as high-capacity, highly stable, and binder-free anodes for lithium-ion batteries”, *Journal of Power Sources*, Jg. 320, S. 314–321, 2016. DOI: 10.1016/j.jpowsour.2016.04.107. Adresse: http://www.sciencedirect.com/science/article/pii/S0378775316304803.

[182] M. Yu, D. Shao, F. Lu, X. Sun, H. Sun, T. Hu, G. Wang, S. Sawyer, H. Qiu und J. Lian, “ZnO/graphene nanocomposite fabricated by high energy ball milling with greatly enhanced lithium storage capability”, *Electrochemistry Communications*, Jg. 34, S. 312–315, 2013, ISSN: 13882481. DOI: 10.1016/j.elecom.2013.07.013.

[183] C.-T. Hsieh, C.-Y. Lin, Y.-F. Chen und J.-S. Lin, “Synthesis of ZnO@Graphene composites as anode materials for lithium ion batteries”, *Electrochimica Acta*, Jg. 111, S. 359–365, 2013, ISSN: 00134686. DOI: 10.1016/j.electacta.2013.07.197. Adresse: http://www.sciencedirect.com/science/article/pii/S0013468613014825.

[184] L.-L. Xu, S.-W. Bian und K.-L. Song, “Graphene sheets decorated with ZnO nanoparticles as anode materials for lithium ion batteries”, *Journal of Materials Science*, Jg. 49, Nr. 18, S. 6217–6224, 2014, ISSN: 1573-4803. DOI: 10.1007/s10853-014-8346-5. Adresse: https://link.springer.com/article/10.1007/s10853-014-8346-5.

[185] J. S. Chen und X. W. Lou, “SnO_2 and TiO_2 nanosheets for lithium-ion batteries”, *Materials Today*, Jg. 15, Nr. 6, S. 246–254, 2012, ISSN: 13697021. DOI: 10.1016/s1369-7021(12)70115-3.

Danksagung

An dieser Stelle möchte ich mich bei allen Menschen bedanken, die zum Gelingen meiner Promotion beigetragen haben.

Allen voran möchte ich Rüdiger Klingeler dafür danken, dass er diese Arbeit ermöglicht hat, für seine uneingeschränkte Unterstützung und für sein stetes Vertrauen in meine Arbeit und Fähigkeiten.

Des Weiteren möchte ich mich bei Christian Enss für die Übernahme des Zweitgutachtens bedanken.

Ich danke allen aktiven und ehemaligen Mitgliedern der F25-Arbeitsgruppe am KIP sowie Galina Zakharova für die tolle Arbeitsatmosphäre und die produktive Zusammenarbeit. Mein besonderer Dank gilt Christoph Neef und Alexander Ottmann für die vielen anregenden Gespräche und Diskussionen sowie das freundschaftliche Miteinander. Danke für die schöne Zeit!

Nicht zu vergessen sind meine fleißigen Studenten Lucas Möller, Jan-Hinrich Nölke, Enzo Moretti, Rouven Zeus, Lennart Singer, Simon Wegener, Lukas Deeg und Viktor Adam, denen ich für die vielen Messungen meinen Dank aussprechen möchte.

Zu guter Letzt möchte ich mich bei meinen Eltern und meinen Schwestern bedanken. „Die wirkungsvollste Energiequelle unseres Lebens ist und bleibt die menschliche Wärme.“ (Ernst Ferstl)

Eidesstattliche Versicherung gemäß §8 der Promotionsordnung für die Naturwissenschaftlich-Mathematische Gesamtfakultät der Universität Heidelberg

Ich erkläre hiermit, dass ich diese Arbeit selbstständig verfasst und keine anderen als die angegebenen Quellen und Hilfsmittel benutzt habe.

Heidelberg, den 06. September 2021

Elisa Thauer